Prediction of No-Load Losses of Stacked 3-Phase, 3-Limb Transformer Cores

by

Manjunath Balehosur

A thesis submitted to the Cardiff University in candidature for the degree of Doctor of Philosophy

Wolfson Centre for Magnetics

Cardiff School of Engineering

Cardiff University

Wales, United Kingdom

November 2012

DECLARATION

This work has not previously been accepted in substance for any degree and is not concurrently submitted in candidature for any degree.

Manjunath Balehosur **15/06/2013**

Signed …… (candidate) Date ……..

STATEMENT 1

This thesis is being submitted in partial fulfilment of the requirements for the degree of PhD.

Manjunath Balehosur **15/06/2013**

Signed …… (candidate) Date ……..

STATEMENT 2

This thesis is the result of my own independent work/investigation, except where otherwise stated. Other sources are acknowledged by explicit references.

Manjunath Balehosur **15/06/2013**

Signed …… (candidate) Date ……..

STATEMENT 3

I hereby give consent for my thesis, if accepted, to be available for photocopying and for inter-library loan, and for the title and summary to be made available to outside organisations.

Manjunath Balehosur **15/06/2013**

Signed …… (candidate) Date ……..

To my mother Mrs. Sushila B. Balehosur

Acknowledgements

This work was carried out at the Wolfson Centre for Magnetics, Cardiff School of Engineering, Cardiff University and financially supported by ThyssenKrupp Electrical Steel UGO, France. I am grateful to Cardiff University and ThyssenKrupp for providing the opportunity and resources needed to complete this project.

I would like to thank Professor Anthony Moses for his invaluable guidance and continuous support throughout the project.

I am grateful to Dr. Jeremy Hall and Dr. Thierry Belgrand of ThyssenKrupp Electrical Steel for their challenging and critical views, which helped me immensely in the project.

I would also like to thank Dr. Yevgen Melikhov, Dr. Philip Marketos, Professor Philip Beckley, Dr. Philip Anderson, Dr. Fatih Anayi and Dr. Turgut Meydan, for various technical suggestions and discussions which helped me in the project.

I am extremely thankful to Dr. Yao, Dr. Sakda Sumkun, Mr. Tomasz Kutrowski, Mr. Teeraphon Phophongviwat, Mr. Mahesh Mani and others for their invaluable suggestions.

I am thankful to Mr. Malcolm Seaborne & Mr. Steve Mead of the mechanical workshop and Mrs. Chris Lee & Mrs. Adeyrn Reid of the research office.

I am very grateful to my beloved Asha who has always supported and encouraged me. My greatest thanks are reserved to my mother Sushila B. Balehosur and father Basavaraj S. Balehosur, for their sacrifice and unconditional love, support and encouragement without which this wouldn't have been possible.

Abstract

The work presented in this thesis can be utilised by electrical steel manufacturers and transformer designers to design energy efficient transformer cores possessing lower life cycle costs, thereby increasing financial gains.

A novel computer based algorithm to predict losses of 3-phase, 3-limb transformer cores built with high permeability grain oriented steel (HGO) and conventional grain oriented steel (CGO) is presented. The algorithm utilises parameters like transformer geometry, global flux distribution, localised loss data and material properties thus enhancing the accuracy of the predicted results which were 1% of the measured values. This algorithm has contributed to new knowledge in the no-load loss prediction approach.

Six, geometrically identical, 350 kVA stacked five packet 3-phase, 3-limb transformer cores assembled with HGO, CGO and four mixed combinations of HGO and CGO laminations in multi step lap (MSL) joint configuration were tested for the global flux density (B_{pk}) distribution and no-load loss.

The B_{pk} investigation results are novel and suggest that the bolt hole diameter (slot width) and lamination width ratio affects the packet to packet variation of B_{pk}. This is a new contribution to the flux distribution regime in transformer cores.

The no-load loss experimental results are novel and suggest that the variation of no-load losses with CGO content in mixed cores was non-linear because of the packet to packet variation of B_{pk}. This is a new contribution of knowledge in the field of mixed core loss behaviour.

Novel data sets of localised specific loss increase and localised relative permeability decrease around different sizes of holes and slots for HGO and CGO were processed from data obtained by two dimensional finite element (FE) analysis. The data sets are a new contribution in the field of predicting localised magnetic properties around holes and slots.

List of Symbols

Abbreviations

2D	Two-dimensional
AC	Alternating current
ACW	Anticlockwise direction
C	Conventional grain-oriented
CGO	Conventional grain-oriented
CW	Clockwise direction
DAQ	Data acquisition
FEM	Finite element method/modelling
GO	Grain-oriented
H	Highly grain-oriented
HGO	Highly grain-oriented
NO	Non-oriented
RD	Rolling direction
RMS	Root mean square
SST	Single strip/sheet tester
TD	Transverse direction
THD	Total harmonic distortion

Subscripts

x	Variables in the RD
y	Variables in the TD

Symbols

ϕ_{pk}	Peak Flux
ϕ_z	Components of peak flux density in the normal direction
μ	Permeability
μ_{eff}	Effective permeability
μ_0	Permeability of the free space

μ_r	Relative permeability
μ_{r_B}	Permeability of the bulk regions
μ_{r_H}	Permeability of the affected region around holes
μ_{r_S}	Permeability of the affected region around slots
μ_z	Components of permeability in the normal direction
θ	Angle between the major magnetisation direction and the RD
ρ	Resistivity of electrical steel laminations
ρ	Mass density of electrical steel
a	Axis ratio of the flux density loci
A	Area
b	Instantaneous flux density
B_x	Peak flux density component along the RD
B_y	Peak flux density component along the TD
B_{pk}	Peak value of flux density
B_g	Peak value of flux density in air gaps
B_H	Peak value of flux density in affected region around holes
B_S	Peak value of flux density in affected region around slots
d	Hole diameter
f	Magnetising frequency
h	Instantaneous magnetic field
h_x	Instantaneous magnetic field component along the RD
h_y	Instantaneous magnetic field component along the TD
H	Magnetic field
H_{pk}	Peak value of magnetic field
H_c	Coercive force
I_1, I_2, I_3	Primary phase currents in 3-phase, 3-limb, transformer core
I_{rms}	Root mean square value of the primary voltage
I_{pk}	Peak magnetizing current
K	Stacking factor
l	Sample length
l_b	Width of b coils

l_B	Mean path length in the bulk regions
l_g	Mean path length in air gaps
l_H	Length of the affected region around holes
l_m	Mean path length of a magnetic circuit
l_o	Overlap length
l_S	Length of the affected region around slots
m	Number of holes
m_{core}	Mass of transformer core
m_s	Mass of specimens
m_a	Active mass of specimens
M	Magnetisation
M_S	Saturation magnetisation
M_r	Remanent magnetisation
n	Number of slots
N_s	Number of step laps
N_p	Number of packets in a transformer core
N_1, N_2	Turn numbers of the primary and secondary windings
P_{cl}	Loss due to eddy currents in electrical steel laminations
P_h	Loss due to hysteresis in electrical steel laminations
P_{exc}	Excess loss in electrical steel laminations
P_c	Measured power loss
P_s	Specific power loss
P_{rot}	Specific rotational loss
P_x	Specific power loss component along the RD
P_y	Specific power loss component along the TD
P_{x+y}	Summation of Specific power loss in the RD & TD around holes / slots
P_T	Specific power loss averaged over the affected regions of holes / slots
R_b	Reluctance of electrical steel in the rolling direction (bulk region)
R_g	Reluctance of air gaps
R_h	Reluctance of affected region around holes
R_{h_s}	Reluctance of affected region around slots

R_s	Shunt resistor
S	Specific apparent power
s_L	Slot length
s_w	Slot width
t	Time
t_s	Sample thickness
T	Time period
T_{core}	Core thickness
T_p	Packet thickness
$u_A(x)$	Type A uncertainty of the variable x
$u_B(x)$	Type B uncertainty of the variable x
$u(x)$	Standard uncertainty of the variable x
$U(x)$	Expanded uncertainty of the variable x
v_2	Instantaneous secondary voltage
V_1, V_2, V_3	Secondary phase voltages in 3-phase, 3-limb, transformer core
V_{R_s}	Voltage across shunt resistor
V_{rms}	Root mean square value of the secondary voltage
V_{av}	Average value of the secondary voltage
V_s	Average value of the secondary voltage
V_L	Overlap region excitation
W_E	Epstein Loss
W	Lamination width

Table of Contents

Chapter 1 Theoretical Background and Aims of the Investigation.

1.1 Introduction

In this chapter, the fundamental background related to the work carried out in the thesis is described. Magnetic materials, Magnetisation and power loss mechanism in grain oriented electrical steel are discussed. Transformer theory and developments in stacked transformer core research are also described. The previous related research work on the effect of bolt holes on power losses in transformer cores, the packet to packet variation of flux density in stacked transformer cores, the effect of mixing different types of electrical steel laminations on power losses in transformer cores and core loss calculation from localised losses are also discussed in this chapter. The aims of this thesis are mentioned at the end of the chapter.

1.2 Basics of Magnetism in Magnetic Materials

Whenever an electric charge is in motion, it produces a magnetic field. It can be detected by a force acting on a current carrying conductor or by a torque on a magnetic dipole [1]. The field strength (H) is measured in Amperes per metre $\left(\frac{A}{m}\right)$. The response of a magnetic medium to H is called flux density (B) and is measured in Webers per metre square $\left(\frac{W}{m^2}\right)$ or Teslas. In free space, the relationship between B and H is written as

$$B = \mu_0 . H \qquad [T] \tag{1.1}$$

Where μ_0 is the permeability of free space ($\mu_0 = 4.\pi.10^{-7} H/m$).

In other magnetic media, B is expressed relative to free space as,

$$B = \mu_0 . \mu_r . H \qquad [T] \tag{1.2}$$

Where μ_r is the relative permeability of the magnetic media and is dimensionless.

The value of μ_r is used to classify magnetic materials. If the value of μ_r is slightly less than one, then the material is called a diamagnet. Copper, gold, silver, bismuth and beryllium are examples of diamagnets. Their magnetic response is in opposition to the applied magnetic field. If the value of μ_r is slightly more than one, then the material is called a paramagnet. Examples of paramagnets include aluminium, platinum and manganese. These materials exhibit weaker magnetisation (M), whose direction is aligned towards the magnetic field. If the value of μ_r is much greater than one, then the material is called a ferromagnetic material. Examples of ferromagnetic materials include iron, cobalt and nickel. The magnetisation process in ferromagnetic materials is discussed in the next section.

1.3 Magnetisation in Ferromagnetic Materials

Even under no external magnetic field, the magnetic moments of atoms in the ferromagnetic material line up, with each magnetic moment similar to a north-south bar magnet shown in Fig. 1-1. A region comprising of all the magnetic moments pointing in the same direction is called a magnetic domain. Layers of atoms known as domain walls separate the domains and are approximately 100 to 1000 atoms thick [1]. When an external magnetic field is applied, the magnetic moments align themselves in the direction of the field. The intensity of magnetic moments per unit volume of a magnetic material, aligned in a particular direction defines the magnetisation of the material.

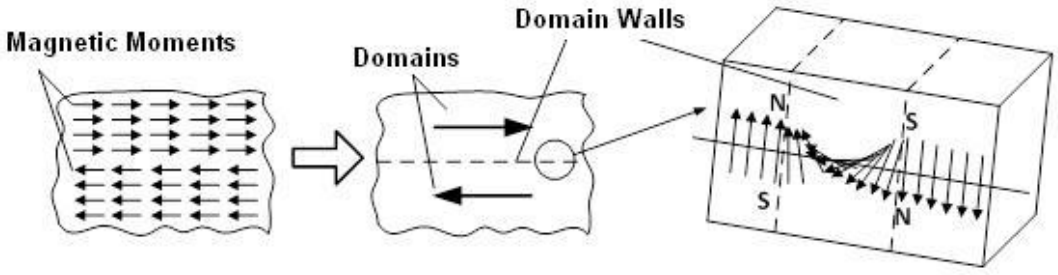

Fig.1-1 Domains and domain walls in ferromagnetic materials [1].

A single domain produces a large external field so domains re-distribute themselves to a state which has no external field and zero magnetisation as shown in Fig. 1-2. The domain walls separating two anti-parallel bar domains are called 180° domain

walls and walls between the main bar domains and the perpendicular flux-closure domains are called as 90° domain walls.

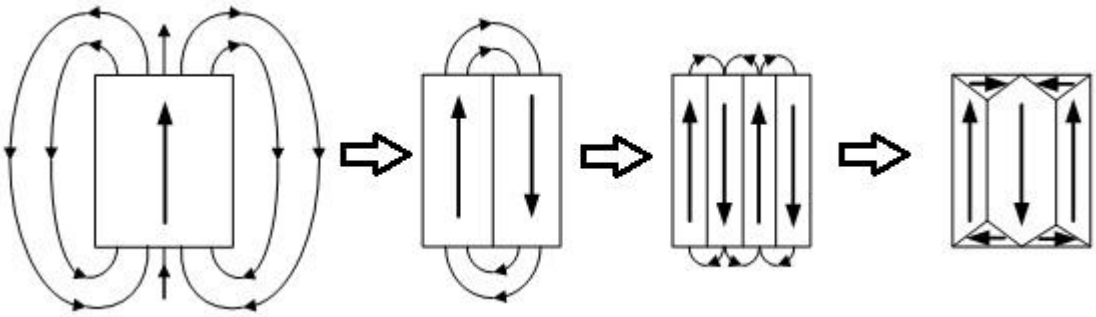

Fig.1-2 Re-distribution of domains to minimise the magneto-static energy [2].

The changes in domain structure of a ferromagnetic material when magnetised, is shown in Fig.1-3. The x-axis represents the magnetic field (H) and the y-axis represents the magnetic flux density (B). The minimised state of energy exhibited by the domain walls under de-magnetised condition (point 1 in Fig.1-3) is altered when an external magnetic field (H) is applied. Net magnetisation is not zero in the material as the domain wall movement produces magneto-static energy to counter the energy created from the increasing H (point 2 in Fig.1-3). At higher H, the flux closure domains disappear and only a single domain appears in the material (point 3 in Fig.1-3). If H is increased even higher, then the magnetisation vectors in the single domain in the material rotate and become parallel to the direction of H (point 4 in Fig.1-3). This condition is termed as magnetic saturation and the flux density at saturation is B_{sat}.

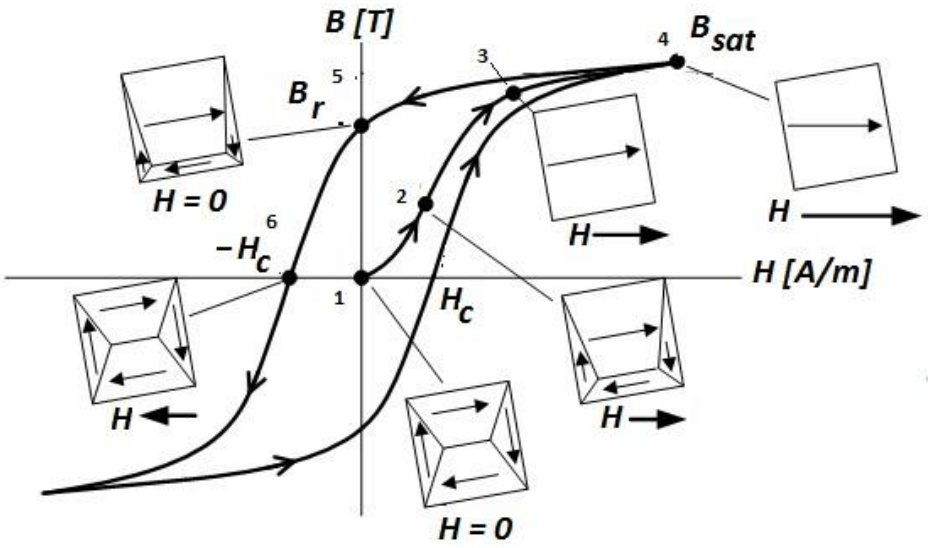

Fig.1-3 The effect of an external magnetic field (H) on the domain structure of a ferromagnetic material [3].

If the H is decreased from saturation to zero (point 5 in Fig.1-3), B traverses a different path because the domain walls do not return to the initial de-magnetised state due to pinning sites like impurities. This magnetisation process is irreversible. The residual flux density at point 5 in Fig.1-3 is called remanent flux density (B_r) or remanence. To reduce the net magnetisation to zero, an opposing field called as coercive field (H_c) or coercivity must be applied (point 6 in Fig.1-4). If the H is increased even higher in the opposite direction, then the material will be saturated (point 6 in Fig.1-3). Thus for one cycle of magnetisation, a B-H loop is obtained. This loop is called the hysteresis loop. The area enclosed by the hysteresis loop is proportional to the total power lost in the material for one cycle of magnetisation. This power loss is called hysteresis loss.

Ferromagnetic materials can be classified based on their coercivities (H_c). If the H_c is more than 10 kA/m [1], then the material is termed 'hard' and if the H_c is less than 1 kA/m [1], then the material is termed as 'soft'. Permanent magnets are examples of hard magnetic materials. Electrical steel is an example of a soft magnetic material and is applicable in electrical devices like transformers and motors.

1.4 Grain Oriented Electrical Steel

1.4.1 History and Development

Early transformer cores were constructed using solid iron cores. To reduce losses due to eddy currents, laminations were employed in the construction of modern transformer cores. In 1903, Hadfield [4] discovered that adding silicon to high purity steels can improve the coercive force and permeability. Since then, improvements in the manufacturing techniques have resulted in production of steels with improved magnetic properties.

Beck [5] in 1918 and Ruder [6] in 1925, demonstrated high magnetic anisotropy in iron and iron silicon. In 1934, N.P. Goss [7] developed a process to produce grain oriented electrical steel based on the work of Beck and Ruder. This process had a combination of heat treatment and cold rolling resulting in a texture with a high proportion of grains having [00l] directions close to the rolling direction (RD) and (110) planes close to the sheet plane. Iron crystals have easy axis magnetisation directions <100> along the cube edges. The Goss structure uses this property. Higher magnetisation at lower magnetic fields and lower power loss can be achieved by this property in grain oriented electrical steel. But if the steel is magnetised in the transverse direction (TD) <110> which is the medium hard direction, power losses increase. The power loss is even more in case of magnetisation in the hard direction <111>.The magnetisation characteristics of iron single crystal along <100>, <110> and <111> directions are shown in Fig. 1-4 (a) and were measured using a superconducting quantum interference device (SQUID) [1]. The Goss grain layout in a strip is shown in Fig. 1-4 (b). The Goss texture in grain oriented electrical steel is shown in Fig. 1-5. ARMCO, an American based company, commercialised the process in 1939. The first mass produced strip of the conventional grain oriented (CGO) steel was 0.32 mm thick, with a power loss of 1.5 W/kg, at 1.5 T, 50 Hz [8]. The angle of misalignment of the crystals with the RD was around 7^{o} in CGO steel. The average grain size diameter was approximately 5 mm.

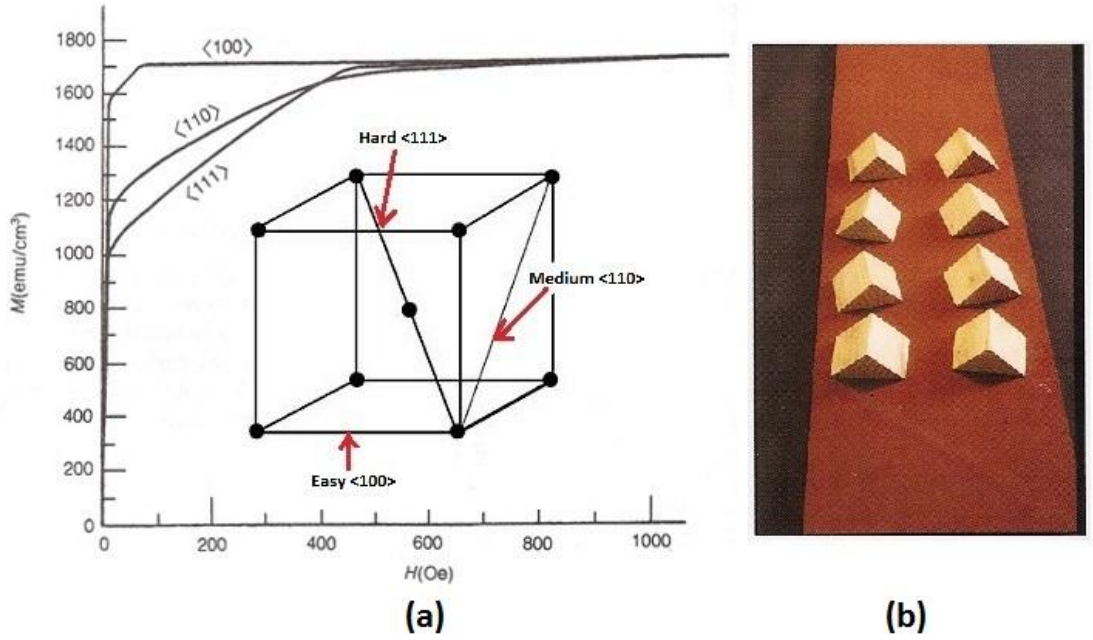

Fig. 1-4 (a) The variation of magnetisation with the applied field for a single crystal iron, magnetised along the <100>, <110> and <111> directions (1 emu/cm^3 = 1000 A/m & 1 Oe = 79.58 A/m) [1] (b) Model of Goss grain layout [9].

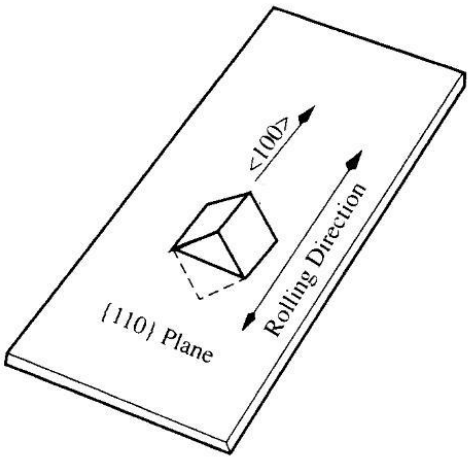

Fig. 1-5 Goss texture of grain oriented electrical steel 10].

Nippon Steel [11-13] developed a high permeability grain-oriented (HGO) steel with 3.25% silicon. HGO steel exhibited lower losses and apparent power as compared to the losses and apparent power of CGO steel. The angle of misalignment of the crystals with the RD was around 3^o in HGO steel and the average grain size diameter was approximately 10 mm. The CGO and HGO steel microstructure along with the early GOSS structure is shown in Fig. 1-6.

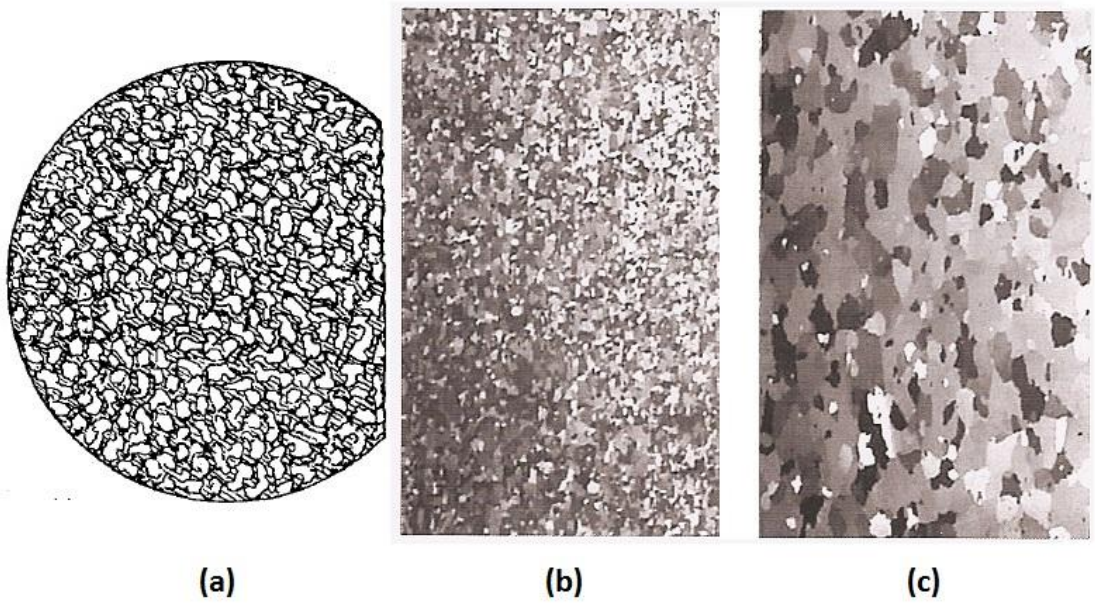

Fig. 1-6 Grain structure (figure not to scale) (a) Goss structure in 1934 [7] (b) Present day CGO [9] (c) Present day HGO [9].

The power loss in the HGO steel was further reduced by domain refinement [14]. The resulting steel was called domain refined steel. The non oriented electrical steels have randomly oriented crystals and are primarily used in motors and generators [8].

Since this investigation is based on HGO and CGO steel, the other mentioned steels are not discussed in detail.

1.4.2 Silicon Content in Electrical Steel

The silicon content in commercial grain oriented electrical steel is around 3.2% by weight. Adding silicon to the electrical steel increases the resistivity and decreases the eddy current losses. It also lowers the hysteresis loss and magnetostriction. Silicon is also beneficial in preventing the aging of the electrical steel. If the silicon content increases, the steel becomes brittle and is hard to machine and assemble.

1.4.3 Coatings

The electrical steel laminations are coated on either side with a thin layer of insulating coating. In a laminated electrical equipment like a transformer, these coatings provide electrical insulation between the adjacent laminations and also prevent corrosion. Coatings can be made of inorganic material, a mixture of

inorganic and organic material, organic material and glass-phosphate. The typical thickness of the coatings varies between 2 µm to 5 µm [15].

The stacking factor of a transformer core is defined as the amount of electrical steel in the core cross sectional area. The stacking factor of transformers is usually around 95.5% to 97 % [15] and is influenced by the thickness of the electrical steel and insulation coating.

1.4.4 Thickness of Electrical Steel

An alternating magnetising current induces an alternating magnetisation in a magnetic material (Faraday's Law). But it also induces an emf in the magnetic material which leads to eddy currents. Eddy currents flow in a closed loop within the cross section of the material and cause power losses in the material due to resistive heating. The power loss due to eddy currents can be minimised by minimising the cross sectional area of the magnetic material.

The eddy current flowing in a closed loop generates its own magnetising field which opposes the main magnetising field. This effect is described by Lenz law. Due to the opposition of the main magnetising field, the central regions of the magnetic material are not magnetised. This phenomenon is called as skin effect. To reduce this skin effect, electrical steel laminations must be thin for maximum utilisation of the material. A typical thickness of grain electrical steel laminations is around 0.3 mm.

1.5 Power Loss in Electrical Steel

1.5.1 Power Loss Measurement in Electrical Steel

Power losses of electrical steel are measured by means of a standard Epstein frame [16] or by a single sheet tester (SST) [17]. The Epstein measurements require more sample preparation, as the 30 mm wide samples require annealing to relieve the cutting stresses. The mean path length of the Epstein frame of 0.94 m, has been empirically obtained from many previous experiments. But the mean path length of magnetic materials changes with permeability and anisotropy for different operating flux densities and frequency [18]. Also the strips used for Epstein measurements are

cut from a small portion of a large sheet, and the measurement results may not accurately represent the actual properties of the magnetic material. The samples tested in a SST are 500 mm x 500 mm in size. The cutting stress has a negligible effect on the measurement results for a large sample size. Sievert [19] presented a detailed survey on measurement methods and standards. He proposed that the results obtained from SST and Epstein Frame can be within 2% of relative standard deviation, if the mean path length of the SST is changed from the fixed 45 mm to values averaged over a number of grades of magnetic materials. This statement was backed by Epstein and SST measurements considering same reference samples sourced from nine different suppliers. The mean values of relative loss difference (δP_{SE}) in percentage between Epstein and SST results were plotted against B_{pk} as shown in Fig. 1-7. For a 2 % relative standard deviation between Epstein and SST measurements, the mean path length of SST should be increased by 3.2 % at B_{pk} = 1.5 T and by 5% at B_{pk} = 1.7 T. The author does not mention the values of percentage increase of mean path length at other B_{pk} values shown in Fig. 1-7.

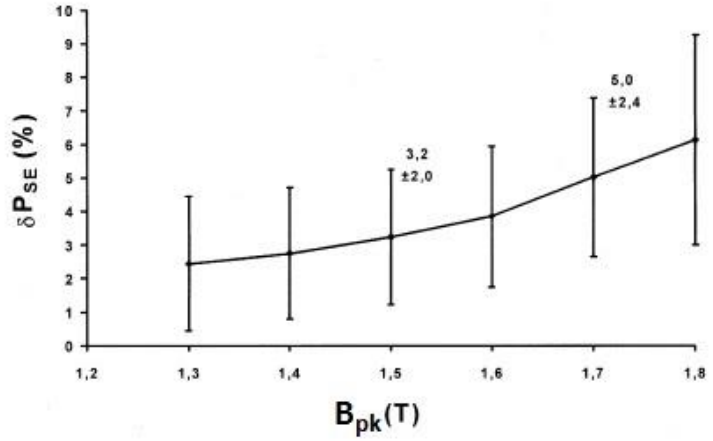

Fig. 1-7 Plot showing δP_{SE} values averaged for B_{pk} = 1.3 T to 1.8 T in steps of 0.1 T [19].

1.5.2 Power Loss Estimation in Electrical Steel

Bertotti [20] presented a model which separates power loss in soft ferromagnetic materials into three components. The loss per cycle P at a particular magnetising frequency f and peak flux density B_{pk} is given by equation (1.3) [20],

$$P = P_h + P_{cl} + P_{exc} = k_0 + k_1.f + k_2.f^{0.5} \quad (1.3)$$

where P_h is the loss component due to hysteresis, P_{cl} is the loss component due to eddy currents, P_{exc} is the excess loss component, k_0, k_1, and k_2 are parameters depending on the material properties of electrical resistivity, density, sheet thickness, shape factor, etc.

The hysteresis loss component (P_h) [21] is independent of frequency and is proportional to the area enclosed by the static B–H loop obtained by measurements. Fig.1-7 shows the variation of the power loss per cycle (P) with magnetising frequency(f). If P is extrapolated to zero then, P_h can be estimated. The parameters which increase P_h are impurities, defects, internal stresses in the sheet and poor surface condition of the sheet. If the sheet is thick and has large grains, P_h is low for a given B_{pk}.

The loss component due to eddy currents (P_{cl}) [21] is proportional to magnetising frequency (f). The parameters which increase P_{cl} are low electrical resistivity of the sheet and thick sheets. If the sheet is thin and has small grains, P_{cl} is low for a given B_{pk}.

The excess loss component (P_{exc}) [21] is proportional to magnetising frequency (f) raised to the power of 0.5. It is the difference between the measured total loss and the sum of P_h and P_{cl} for a particular f & B_{pk}. The parameters which increase P_{exc} are impurities, defects, and internal stress in the sheet. If the sheet has smaller domain width and has small grains, P_{exc} is low. The variation of the components of power losses with magnetising frequency is shown in Fig.1-8.

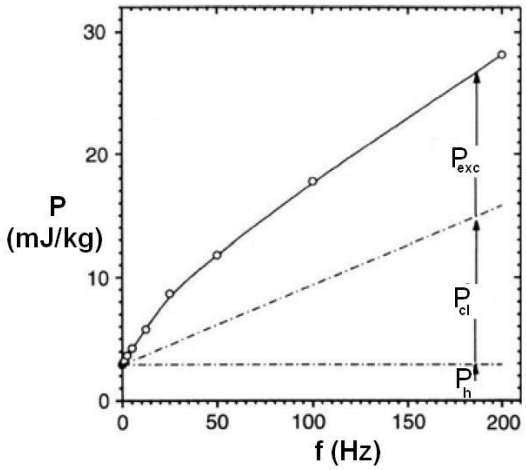

Fig. 1-8 The variation of hysteresis, eddy current and excess loss components of power loss with magnetising frequency in grain oriented 3% silicon steel measured at 1.32 T, 50 Hz [21].

Zirka [22-25] presented a model which separates power loss in soft ferromagnetic materials using viscosity based dynamic Preisach model (DPM). This model solves the diffusion equation (1.4) [25] of a thin ferromagnetic lamination using the finite difference (FD) solver. The diffusion equation relates the magnetic induction (b) and the magnetic field (h) in a homogeneous material of electrical resistivity (σ). If the x-axis is directed into the thin ferromagnetic lamination, the z-axis is directed along the RD and the plane *yz* is coincident with the lamination surface, the diffusion equation is expressed as,

$$\sigma \frac{\partial b}{\partial t} = \frac{\partial^2 h}{\partial x^2} \tag{1.4}$$

Where $h = h_z(x,t)$ and $b = b_z(x,t)$.

The lag of b behind h, termed as magnetic viscosity is used to simulate the excess losses. The thin ferromagnetic lamination is divided into $'n'$ number of node points and equation (1.4) is solved at each node point using finite difference method to obtain the power loss. The total loss in the ferromagnetic lamination is then calculated by the summation of calculated losses at each node point within the thin lamination. This model can be employed to accurately predict total losses in non-oriented and grain-oriented electrical steel within 2% of measured values for

sinusoidal or non-sinusoidal flux waveforms [26]. The DPM technique was also used by many other researchers [27]-[29] to estimate power losses.

1.5.3 Power loss due to Alternating and Rotational Magnetisation

Alternating magnetisation occurs when the magnetic flux varies in magnitude as a function of time in the plane of a lamination. The direction of the alternating magnetisation remains constant in the plane of the lamination [30]. The alternating power losses in the limbs and yokes of transformers mainly occur due to alternating magnetisation.

Rotational magnetisation occurs when the magnitude and direction of the magnetic field and magnetic flux rotate in the plane of a lamination. The rotational losses in the T-joint regions of transformers occur due to rotational magnetisation.

A comparison of the rotational and alternating losses is shown in Fig. 1-9.

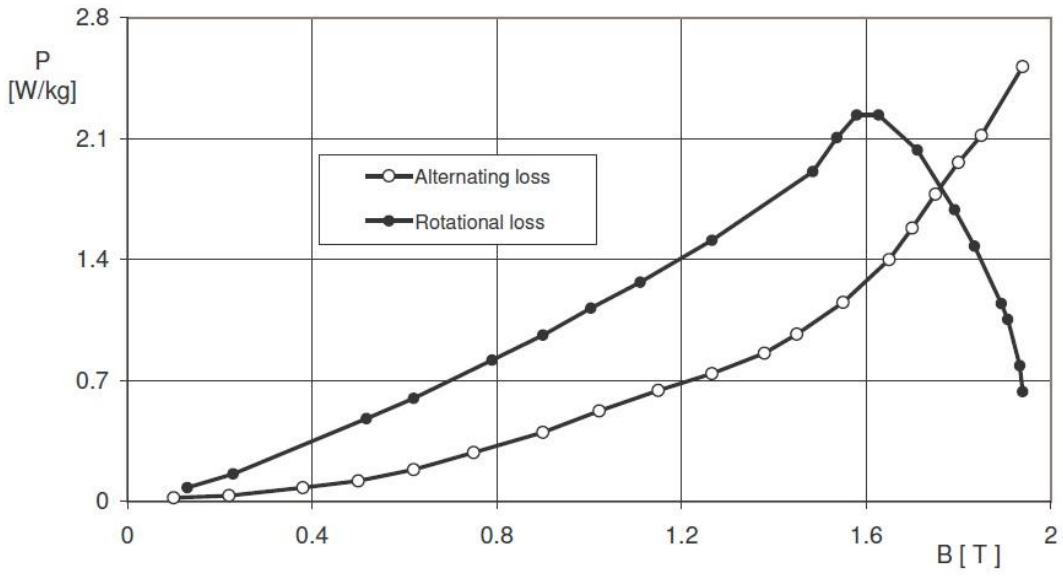

Fig. 1-9 Rotational loss and alternating loss in conventional grain oriented electrical steel [31].

Rotational losses are higher than the alternating losses and drop at higher flux densities. This is because of the absence of domain walls at higher flux densities close to saturation which leads to a drop in hysteresis losses.

1.6 Transformer

1.6.1 History

Michael Faraday discovered that electric energy could be converted into magnetism and vice –versa in 1831. Faraday's first transformer is shown in Fig.1-10a. Gaulard and Gibbs further developed this idea to conceive a power distribution system using alternating current (AC) and transformers and obtained an English patent for it in 1882. Although the system was not successful, the idea to transmit power was established. George Westinghouse acquired the American rights of Gaulard and Gibb's patents in 1885 to develop further the transformer and AC systems. William Stanley was selected to lead this effort in 1886 [32]. William Stanley was successful in his work (Fig.1 -10b) and led the development of early AC transmission systems. These systems were able to transform the low voltage output and high current of electrical generators to a voltage level with low currents that could be transmitted in cables to consumers who were located a mile away or further.

Modern day transmission and distribution systems are more extensive and the transformers are around 99 % efficient. A modern day transformer is shown in Fig.1-11.

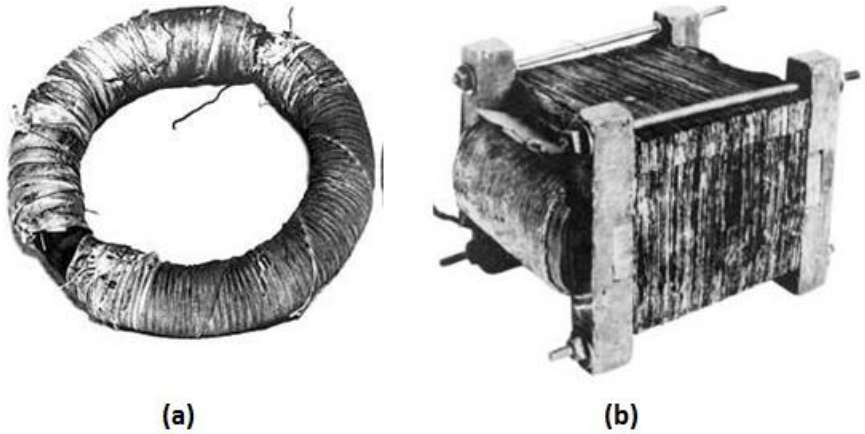

Fig. 1-10 (a) Faraday's original transformer [33] (b) Stanley transformer [33].

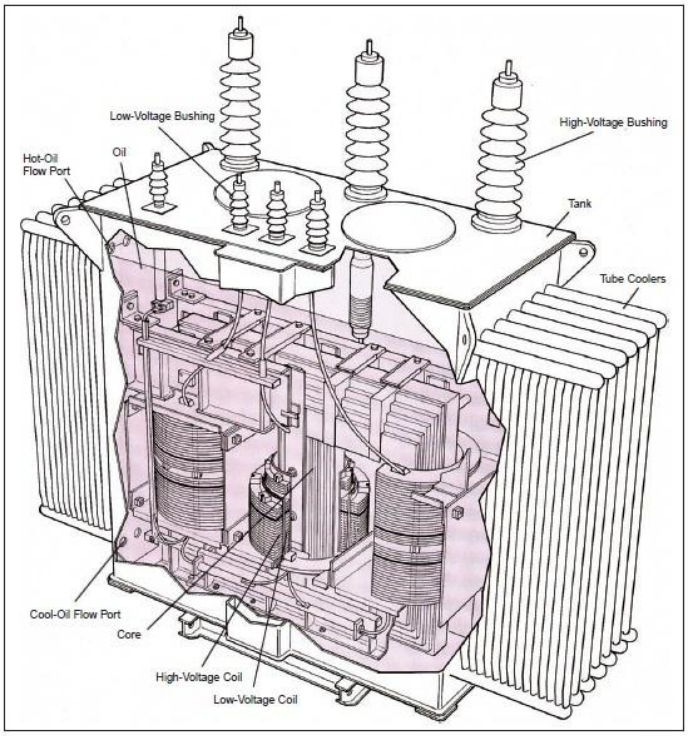

Fig. 1-11 Modern day transformer [33].

1.6.2 Transformer Theory

The secondary voltage required to induce a desired peak flux density in a transformer core under no-load condition can be derived [34] by considering an ideal single phase transformer core shown in Fig.1-12. An ideal transformer core has negligible core and winding losses, infinite magnetic permeability, infinite electrical resistivity and the flux is confined to the core linking the primary and secondary windings.

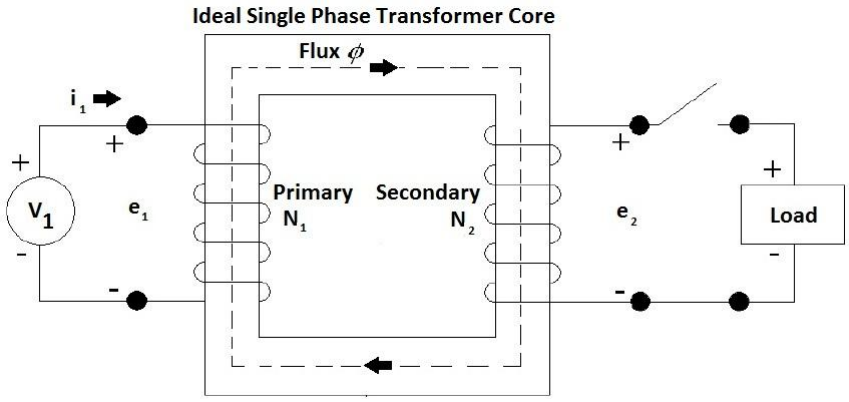

Fig. 1-12 Ideal single phase transformer core [34].

If the primary winding turns (N_1) are equal to the secondary winding turns (N_2), then the voltage induced in the primary and secondary windings are equal. The primary and secondary voltages are directly proportional to the number of winding turns, given by,

$$\frac{V_1}{V_2} = \frac{N_1}{N_2} \tag{1.5}$$

From Faraday's law,

$$e_1 = -\frac{d\lambda_1}{dt} = -N_1 \frac{d\emptyset}{dt} \tag{1.6}$$

$$\text{and } \lambda_1 = N_1 \emptyset \tag{1.7}$$

where e_1 is the *e.m.f* in the primary windings, $\emptyset$ is the magnetic flux in the core, and λ_1 is the flux linkage with the primary windings having N_1 turns.

As there is no leakage flux in an ideal transformer core, the flux in the core $\emptyset$ links all the secondary windings N_2 and produces an *e.m.f* e_2 given by,

$$e_2 = \frac{d\lambda_2}{dt} = N_2 \frac{d\emptyset}{dt} \tag{1.8}$$

If the waveforms of the applied voltage and flux are sinusoidal, then flux as a function of time is expressed as,

$$\emptyset(t) = \emptyset_{pk} sin\omega t \tag{1.9}$$

where $\emptyset_{pk}$ is the peak value of flux and ω is $2\pi f$, with f being the frequency.

Substituting equation (1.9) in equation (1.8), the induced secondary voltage is given by,

$$e_2(t) = N_2 \frac{d\emptyset(t)}{dt} = \omega N_2 \emptyset_{pk} cos\omega t \tag{1.10}$$

The *rms* value of the induced secondary voltage is given by,

$$e_{rms} = N_2 \frac{d\emptyset(t)}{dt} = \frac{2\pi}{\sqrt{2}} f N_2 \emptyset_{pk} = 4.44 f N_2 \emptyset_{pk} \tag{1.11}$$

The peak flux density in the core is given by,

$$B_{pk} = \frac{\emptyset_{pk}}{A} \tag{1.12}$$

where A is the area of cross section of the core.

Substituting equation (1.12) in equation (1.11), the *rms* value of the secondary induced voltage,

$$e_{rms} = 4.44 f N_2 A B_{pk} \tag{1.13}$$

The average value of the secondary voltage over a time period T is given by,

$$e_{av} = \frac{2}{T}\int_0^{T/2} e_2(t)\, dt = 4 f N_2 A B_{pk} \tag{1.14}$$

In order to get a desired peak flux density B_{pk} in a transformer core under sinusoidal excitation, equations (1.11) and (1.14) can be used.

1.6.3 Three – Phase No-Load Loss Measurement Method

The number of wattmeters required and the circuit connections of the voltage and current elements to measure no-load total power loss are governed by Blondel's theorem. The theorem states that to measure the total power supplied through N conductors, N wattmeters are required with a certain kind of connection [35]. The current element of each wattmeter is to be connected to one of the lines, and the corresponding voltage element is to be connected between that line and a common point. The total power loss is then determined by the summation of N wattmeter readings. Thus, to measure the no-load loss of 3-phase transformers cores, three watt meters are required [35] as shown in Fig.1-13.

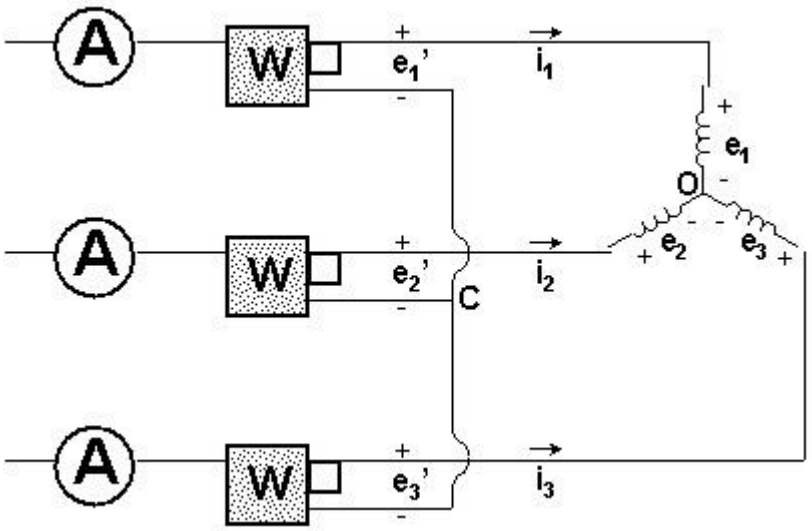

Fig. 1-13 Three wattmeter circuit of a 3-phase transformer [35].

The voltages and currents that define the total instantaneous power and determine the individual wattmeter readings are shown in Fig.1-13. The total instantaneous power is given by,

$$P_{tot} = e_1.i_1 + e_2.i_2 + e_3.i_3 \tag{1.15}$$

The instantaneous power measured by the three wattmeters is given by,

$$P_{sum} = e_1'.i_1 + e_2'.i_2 + e_3'.i_3 \tag{1.16}$$

where e_1, e_2 and e_3 are the instantaneous phase-to-neutral voltages of the three phase transformer, e_1', $e_2'$and e_3' are the instantaneous voltages across the wattmeter voltage elements, i_1, i_2 and i_3 are the instantaneous line currents and currents in the wattmeter current elements.

If the instantaneous voltage between points O and C in Fig. 1-13 is v , then,

$$e_1 = v + e_1' \tag{1.17}$$

$$e_2 = v + e_2' \tag{1.18}$$

$$e_2 = v + e_2' \tag{1.19}$$

Substituting the above equations (1.17), (1.18) and (1.19) in equation (1.16),

$$P_{sum} = e_1.i_1 + e_2.i_2 + e_3.i_3 - v(\,i_1 + i_2 + i_3\,) \tag{1.20}$$

Substituting equation (1.15) in equation (1.20),

$$P_{sum} = \ P_{tot} - v(\,i_1 + i_2 + i_3\,) \tag{1.21}$$

From Fig.1-13, if there is no connection between points O and C, then $(\,i_1 + i_2 + i_3\,)$ is zero, and if point O and C are connected together, then v is zero. In either case, the term $v(\,i_1 + i_2 + i_3\,)$ is always zero, and under all conditions of phase imbalance,

$$P_{sum} = \ P_{tot} \tag{1.22}$$

Thus, the total instantaneous power is equal to the instantaneous power measured by the three wattmeters.

1.6.4 Three – Phase No-Load Loss Measurement Circuits

The transformer windings can be connected in either wye (star or Y) or delta (Δ) configuration. Fig.1-14 (a) shows an energised winding connected in Y and Fig. 1-14 (b) shows an energised winding connected in Δ.

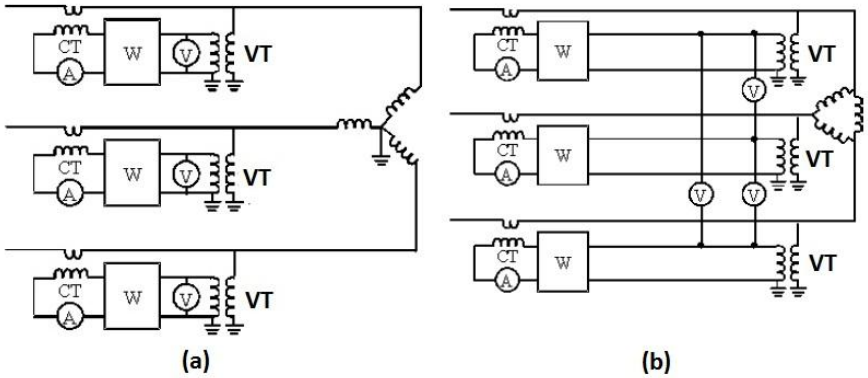

Fig. 1-14 Energised windings (a) Wye configuration [35] (b) Delta configuration [35].

For a 3-phase transformer, four combinations of winding connection configurations are possible. They are Y- Δ, Δ-Y, Δ- Δ and Y-Y.

The Y- Δ connection is used to step down high voltages. The neutral available on the primary winding connected in Y is earthed to avoid distortions and reduce insulation

costs. The secondary winding connected in Δ re-distributes any unbalanced loads. As fewer numbers of primary turns are required, this type of connection is more economical for large step down transformers.

The Δ-Y connection is used to step up low voltages to high voltages. The secondary winding connected in Y provides a neutral for grounding and reduces insulation costs.

The Δ- Δ connection is used in medium voltage transmission systems. In this type of connection, the cross section of windings is less as the phase current is $\frac{1}{\sqrt{3}}$ times the line current. Therefore medium voltage transmission systems are more suited for this type of connection.

The Y-Y connection is used in high voltage (> 1kV) applications. In this type of connection, the cross section of windings is high as the phase current equal to the line current. Therefore high transmission systems are more suited for this type of connection.

1.6.5 Types of Transformers

Transformers are classified on the basis of their core/winding configuration. The two types of transformers are shell type and core type as shown in Fig.1-15.

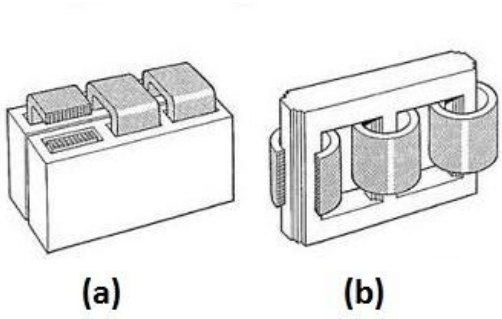

Fig. 1-15 Transformer types (a) Shell type [36] (b) Core type [36].

In the shell type, the windings are surrounded by the core material. Due to the compact design, they are suitable for supplying low voltages at high currents. Arc furnace transformers are an example of shell type cores. In the core type, the

winding surround the core limbs. Both shell type and core type transformers can be built using stacked or wound 3.2 % silicon grain oriented electrical steel laminations.

1.7 Developments and Research in Stacked Transformers

1.7.1 Corner and T-joint Regions

Brailsford [37] investigated the effect of alternating magnetic flux distribution in corner joints of transformers. Two commercially available Fe-Si steel were used in the investigation. Material A was non oriented, 0.35 mm thick, Fe-4%Si with a power loss of 1.63 W/kg at B_{pk} = 1.3T, 50 Hz. Material B was grain oriented, 0.33 mm thick, Fe-3%Si with a power loss of 1.12 $\frac{W}{kg}$ at B_{pk} = 1.5 T, 50 Hz. Single phase cores were built with these materials and flux distribution at right angled corners was measured. Fig 1.16 shows the streamlines of fundamental and 3rd harmonic components of flux for material A and B.

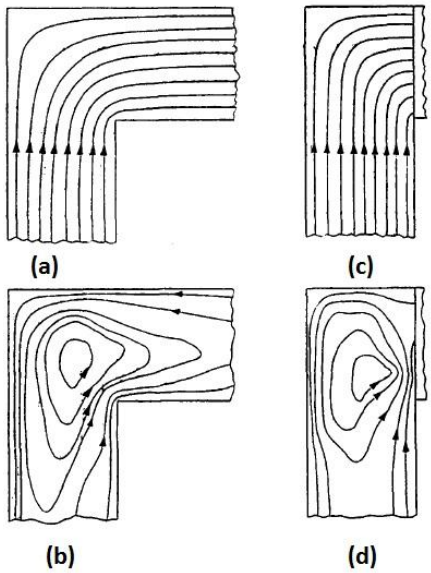

Fig. 1-16 Flux streamlines measured using search coils [37] (a) Fundamental component of flux density at B_{pk}= 1.3 T for material A (b) 3rd harmonic component of flux density at B_{pk}= 1.3 T for material A (c) Fundamental component of flux density at B_{pk}= 1.7 T for material B (d) 3rd harmonic component of flux density at B_{pk}= 1.7 T for material B.

The measured e.m.f waveforms at the corner regions for cores built with material A and B is shown in Fig. 1-17.

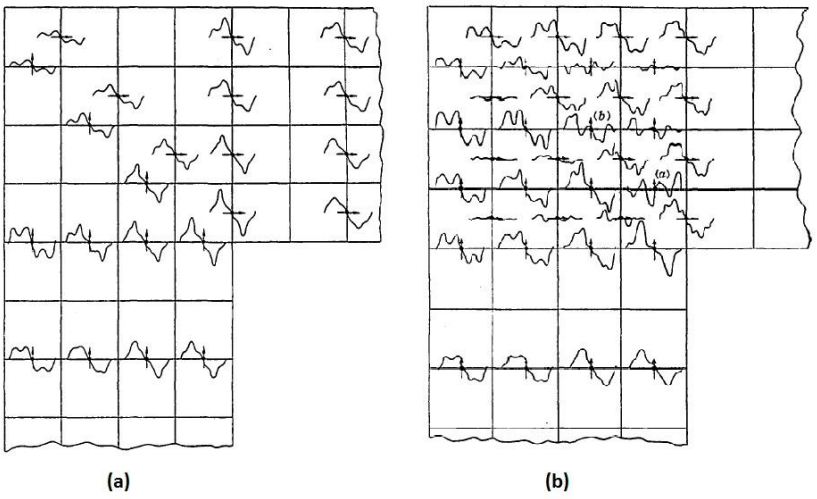

Fig. 1-17 E.M.F. waveforms (a) Material A at B_{pk}= 1.3 T (b) Material B at B_{pk}= 1.7 T [37].

It was found that anisotropy affects the losses in the corner regions of the transformer cores. The stray losses were found to be 24% higher than the losses in the rolling direction. The loss due to flux deviation was 21% and the loss due to harmonics was 3%.

Moses et al [38] investigated the flux and power loss distributions in T-joint regions of a core built with double overlap joints shown in Fig.1-18.

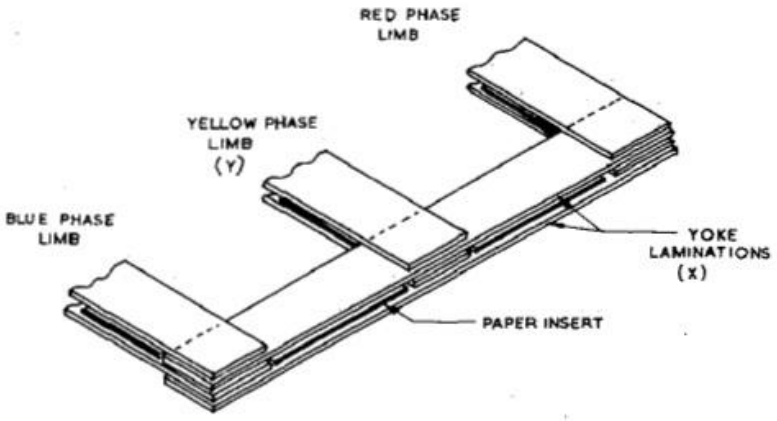

Fig. 1-18 Arrangement of the core built with double overlap joints [38].

An array of search coils was used to measure the local flux density distribution. Miniature thermocouples were used to measure the initial rate of rise of temperature to compute the localised power losses. The inner edges of the yokes and the limbs were found to exhibit 30% more loss than the mean core loss over a

flux density range 1.1 T to 1.6 T. This increase in localised power loss was because of the 3rd harmonic component of the flux density.

Moses and Thomas [39] compared the power losses and flux distribution for cores built with two different T-joint designs, a 45° – 90° mitred and a 45° offset mitred T-joint. The investigated T joints are shown in Fig. 1-19. The cores were built using 150 mm wide, 0.3 mm thick grain oriented Fe-3.2%Si steel. Rotational flux was observed in regions of both types of T joints. The locus of the fundamental component of flux density in both types of T joints is shown in Fig. 1-20.

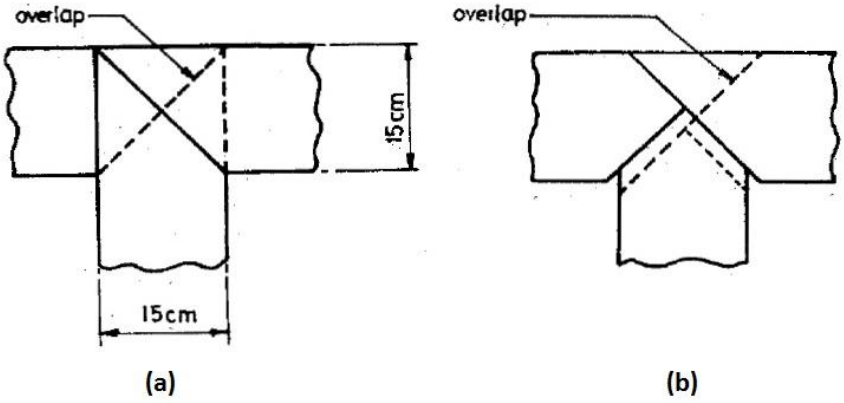

Fig. 1-19 T joint design (a) 45° – 90° joint (b) 45° offset joint [39].

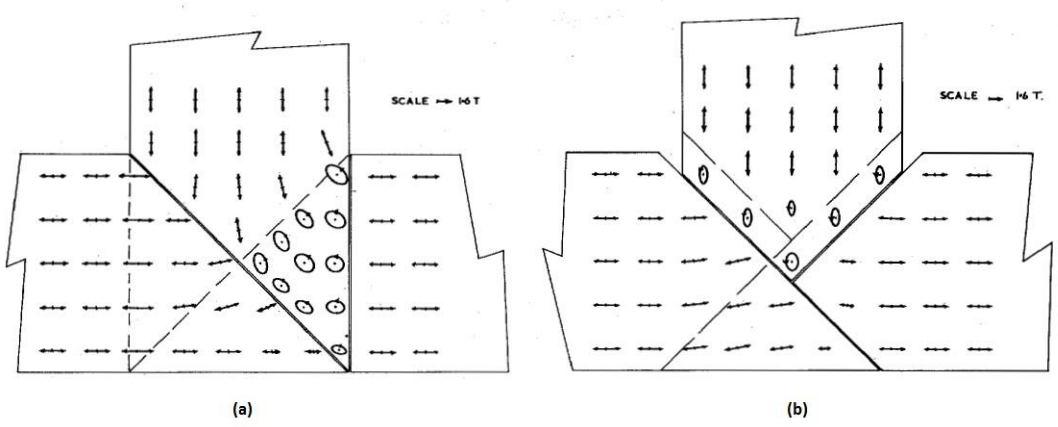

Fig. 1-20 Locus of the fundamental component of flux density (a) 45° – 90° joint at B_{pk}= 1.6 T (b) 45° offset joint at B_{pk}= 1.6 T [39].

In the T joint regions of both cores, the power losses were high because of the combined effect of normal flux, rotating flux and the 3rd harmonic component of flux density. The 45° offset mitred T-joint was found to be 10 -12% more efficient than

the 45^{o} – 90^{o} mitred T joint. The losses in the T joints were reported to be 25% more than the losses in the limbs and yokes.

Jones et al [40] compared two different transformer corner joints, butt-lap and the 45^{o} mitred overlap joint built in two separate cores. The two cores were built using 150 mm wide, 0.3 mm thick grain oriented Fe-3.2%Si steel with a nominal loss of 0.95 W/kg at B_{pk}= 1.5 T, 50 Hz. The two corner joints are shown in Fig.1-21.

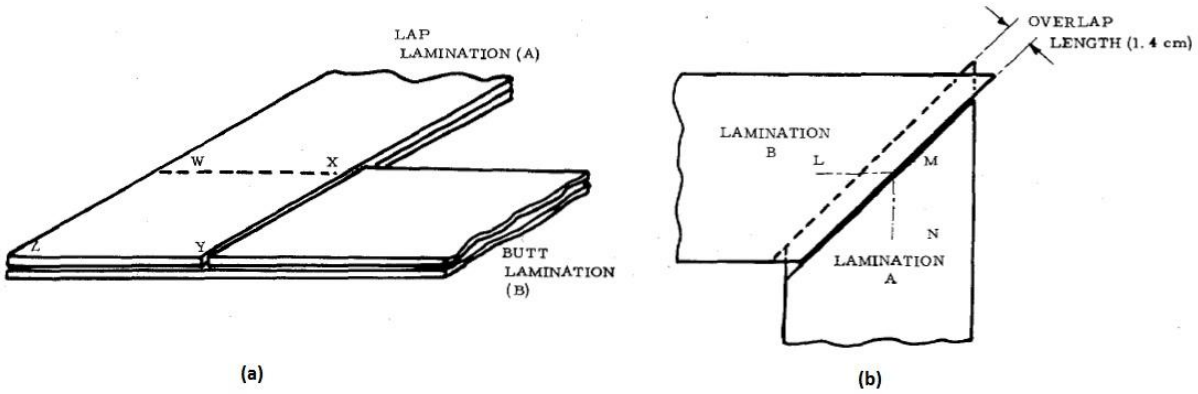

Fig. 1-21 Corner joints (a) Butt and lap joint (b) 45^{o} mitred overlap joint [40].

The variation of longitudinal flux density along the centre of the lap lamination of the butt-lap joint at B_{pk}= 1.1 T, 1.5 T and 1.8 T is shown in Fig.1-22. The variation of longitudinal flux density in two adjacent laminations in the 45^{o} mitred joint at B_{pk}= 1.1 T, 1.5 T and 1.8 T is shown in Fig.1-23. The results indicated that 45^{o} mitred joint was 18% more efficient than the butt-lap joint at B_{pk}= 1.5 T. It was also found that the localised losses in the joint regions of the core built with butt-lap joint were 26 % higher than the mean limb losses. Also, the localised losses in the joint regions of the core built with 45^{o} mitred joint were found to be 7 % higher than the mean limb losses. It was concluded that the reason for higher losses in the butt-lap joint is because of the presence of greater volume of saturated material (due to high longitudinal flux) and rotational flux (measured using search coils).

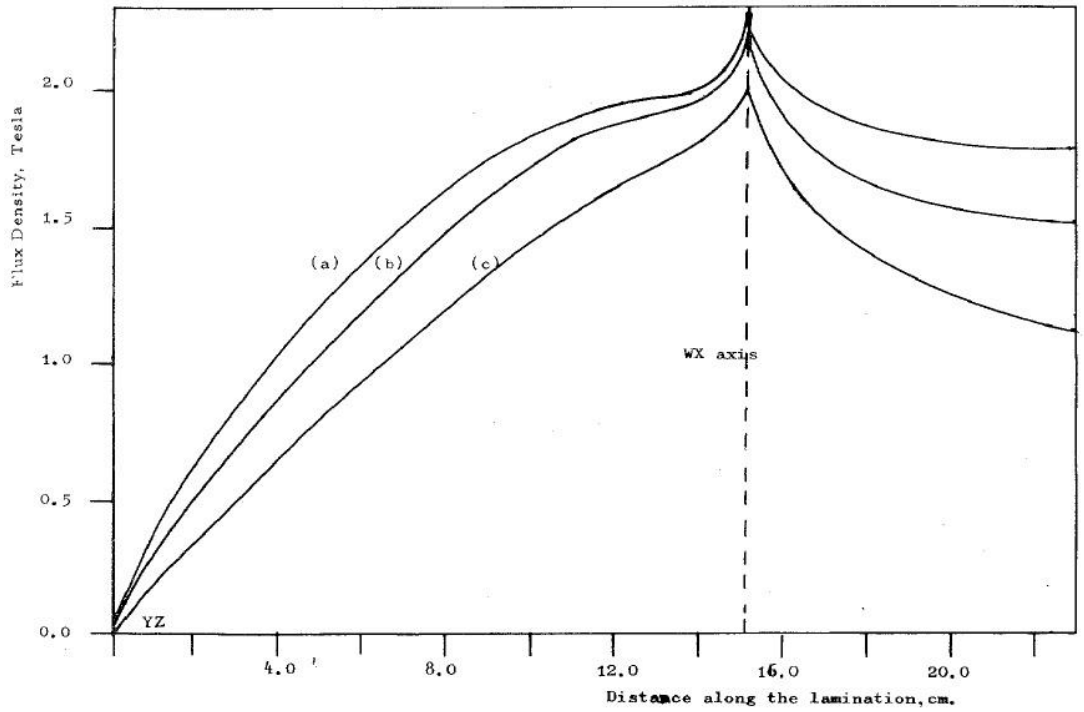

Fig. 1-22 Variation of longitudinal flux density along the centre of the lap lamination of the butt-lap joint (a) B_{pk}= 1.8 T (b) B_{pk}= 1.5 T (c) B_{pk}= 1.1 T [40].

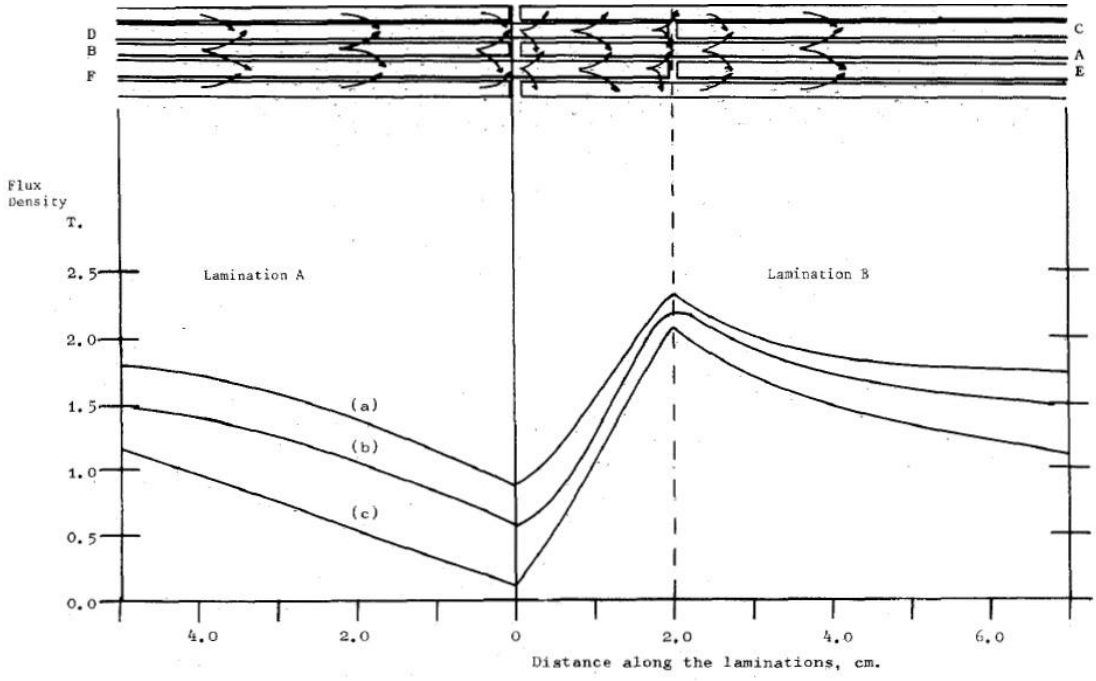

Fig. 1-23 The variation of longitudinal flux density in two adjacent laminations in the 45^o mitred joint (a) B_{pk}= 1.8 T (b) B_{pk}= 1.5 T (c) B_{pk}= 1.1 T [40].

Moses [41] looked into the problems faced by the use of high permeability steel (HGO) in transformer core construction. Although using HGO steel in transformer

cores can reduce the power losses, care should be taken to minimise the localised losses in the corner and T joint regions. At higher flux densities, the power loss and apparent power of HGO steel was reported to be more sensitive to mechanical stress.

Valcovic [42] compared the effect of step-lap design with that of conventional mitre design on the transformer power loss and apparent power, keeping the overlap length constant. The step lap design had five steps. The percentage decrease in total core loss was between 2 to 4.4 %. The percentage decrease in apparent power was between 31 to 37%. It was concluded that step lap design is better than mitred joint design for reducing the power loss and apparent power of transformer cores.

Loffler et al [43] compared full size and model cores built with single step-lap (SSL) joints to those built with multi step-lap (MSL) joints. SSL and MSL joint arrangements are shown in Fig. 1-24 which shows the air gap regions, the overlap length (a) and air gap length (g). The number of step laps (N) for SSL and MSL was 1 and 4 respectively. The authors reported an important finding that a critical induction exists in cores built with MSL joints. If the peak flux density in the core exceeds the critical induction, then there is an increase in power loss and apparent power of the core. This critical induction increases with the number of step laps in the MSL joint. The investigation [43] concluded that cores built with MSL joints have lower local excitation of air gap regions, more homogeneous flux distribution, weaker dependency of power loss and excitation on air gaps, lower normal components of flux density, lower harmonics and lower stray fields in the overlap regions than cores built with SSL joints. The mentioned effects were greater for higher number of step laps. Higher number of step laps must be chosen at higher operating flux densities as it increases the critical induction.

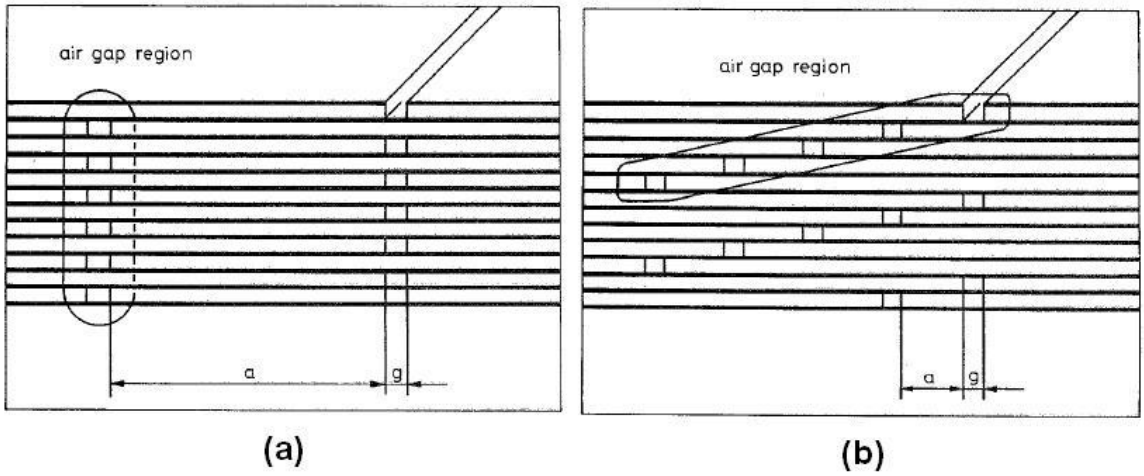

Fig. 1-24 Step Lap configuration showing the air gap region (a) SSL (b) MSL [43].

1.7.2 Effect of Harmonics

Moses and Thomas [44] investigated the problems faced in the design of transformers mainly concentrating on the circulating flux and the rotational flux in the T joints. Arrays of search coils and thermocouples were placed in the T-joint regions of a 45^{o} mitred three-phase transformer core to obtain localised flux density and power loss distribution. It was found that the T-joint design was causing high localised power losses due to the presence of alternating and rotational flux. The rotational loss was found only in T joint regions and was found to be dependent on the T joint design. Circulating flux was found to be present in the limbs and yokes and cause an increase in power loss by 20%. The path of the circulating flux is shown in Fig.1-25. The investigation called for a better T-joint design to reduce the circulating and rotational flux.

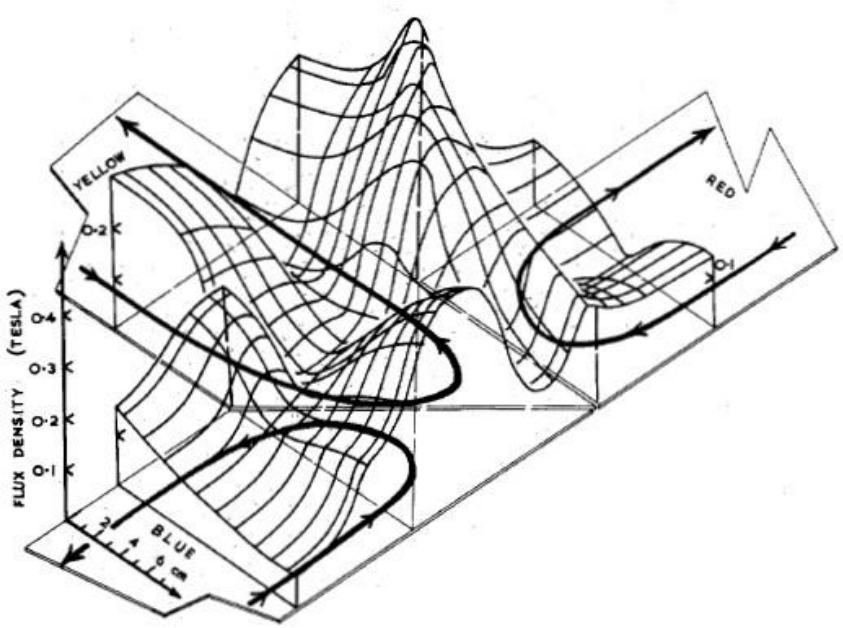

Fig. 1-25 Variation in the magnitude of the 3rd harmonic component of flux density measured at B_{pk}= 1.6 T, showing the path of the circulating flux [44].

Basak and Moses [45] investigated the harmonic losses in a 3-phase, 3-limb transformer core. The losses due to harmonics in the yokes and limbs of the core were calculated by the summation of all the loss, which would be produced if the harmonics were individually present in the electrical steel. The losses in the corner joints were measured. The results showed that the flux distribution in individual laminations was both distorted and non-uniform. The losses in the joints were found to be 17 % of the total loss in the core. The losses due to circulating flux were estimated to be 15 % of the total loss in the core. The losses due to stress and errors in the method of calculating the losses were assumed to be responsible for the rest of the losses in the core.

The effect of distorted flux density on 0.3 mm thick conventional grain oriented silicon steel (CGO), high permeability silicon steel (HGO) and laser scribed high permeability silicon steel (DR) was investigated by Moses and Sakaida [46]. The Epstein losses of the materials were 1.21 $\frac{W}{kg}$ for CGO, 1.01 $\frac{W}{kg}$ for HGO and 0.95 $\frac{W}{kg}$ for DR steel. Three, 3-phase, 3-limb transformer cores were built with each of the mentioned materials. The cores were 500mm x 500mm and the yokes and limbs were 100 mm wide. It was found that the core built with domain refined steel had

the lowest loss while the core built with conventional steel had the lowest building factor. By separate, computer controlled single strip measurements with flux waveforms containing up to 30% 3rd harmonic components, the power losses were measured on each samples of each of the above mentioned materials. The hysteresis and eddy current losses were calculated and it was found that the uniformity of the flux density and the variation of incremental eddy current loss determine the building factor of the cores.

1.7.3 Effect of Clamping Pressure

Basak et al [47] investigated the effect of clamping on the core losses of a model 3-phase, 3-limb transformer core built with 0.14 mm thick amorphous laminations. A similar core was also built with 0.3 mm thick, laser scribed ZDKH silicon steel to compare the core loss increase with clamping. Both the cores had butt lap corner joints. The amorphous core is shown in Fig.1-26 (a) and the core built with silicon steel is shown in Fig. 1-26 (b).

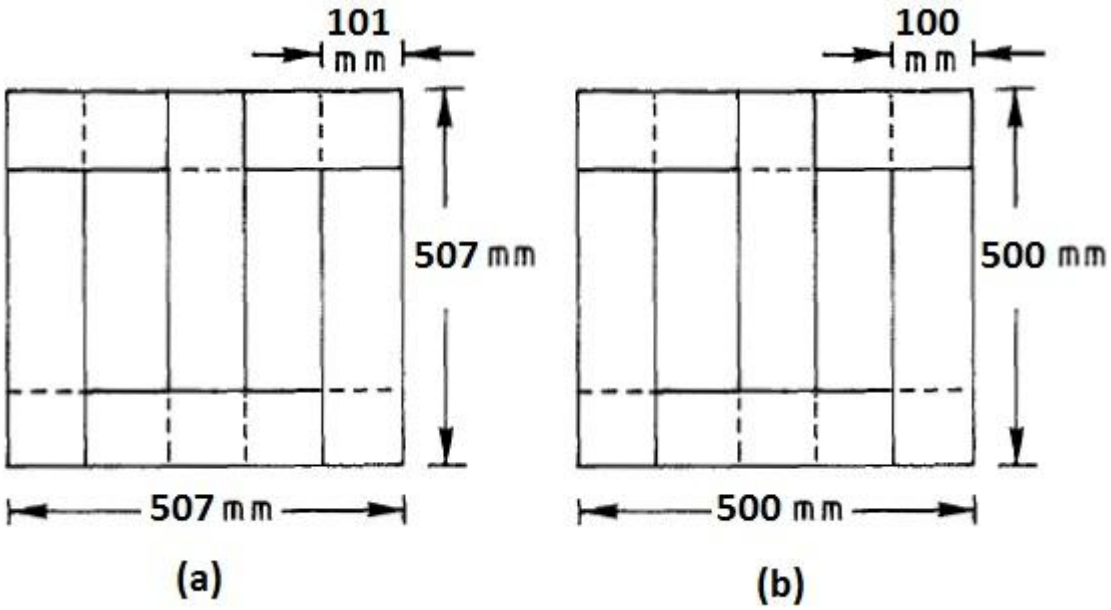

Fig. 1-26 The investigated 3-phase, 3-limb transformer cores (a) Amorphous core (b) Silicon steel core [47].

Two clamping arrangements were used. In the first arrangement, clamps were placed on the yokes. In the second arrangement, clamps were placed on the limbs.

The power loss B_{pk}= 1.35 T for different clamping stresses for the two cores with two different clamping arrangements is shown in Fig. 1.27.

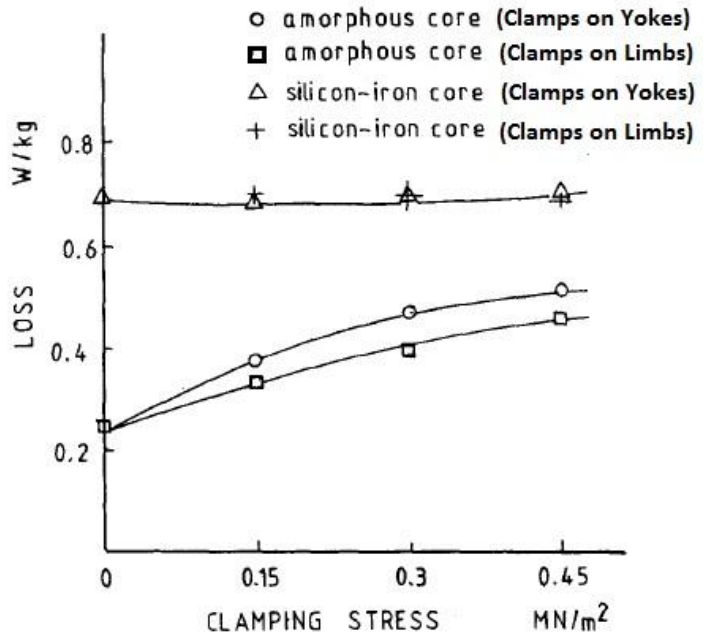

Fig. 1-27 The variation of core loss versus clamping stress in cores built with amorphous core and silicon steel with two clamping arrangements at B_{pk}= 1.35 T [47].

The investigations concluded that the stress due to clamping affects cores built with amorphous cores and has a negligible effect on the losses of cores built with ZDKH silicon steel.

Girgis et. al [48] investigated the effect of clamping pressure on the power loss of two model single phase cores built with CGO and domain refined (DR) steel and two full size transformer cores (16MVA and 63 MVA).The material used in the full sized cores is not mentioned. The building factor increase was 0.15% and 0.30 % respectively for the two full size cores due to clamping pressure. The investigation concluded that the clamping pressure has negligible effect on the power losses of transformer cores.

1.7.4 Effect of Slitting

TeNyenhuis and Girgis [49] investigated the effect of slitting grain oriented electrical steel on the power losses. A total of nine grades of electrical steel sourced from three different electrical steel manufacturers were used in the investigation. The electrical sheet width of 800 mm was chosen as a reference and power loss was measured in a single sheet tester. Then this sheet was slit into equal narrow parts and the loss measurements were repeated. This sequence was repeated until the sheet width was reduced to 30 mm. The sheets were not annealed throughout the sequence. The power loss increase due to slitting from the reference loss at B_{pk}= 1.3 T, 1.5 T and 1.7 T was reported and is shown in Fig. 1-28.

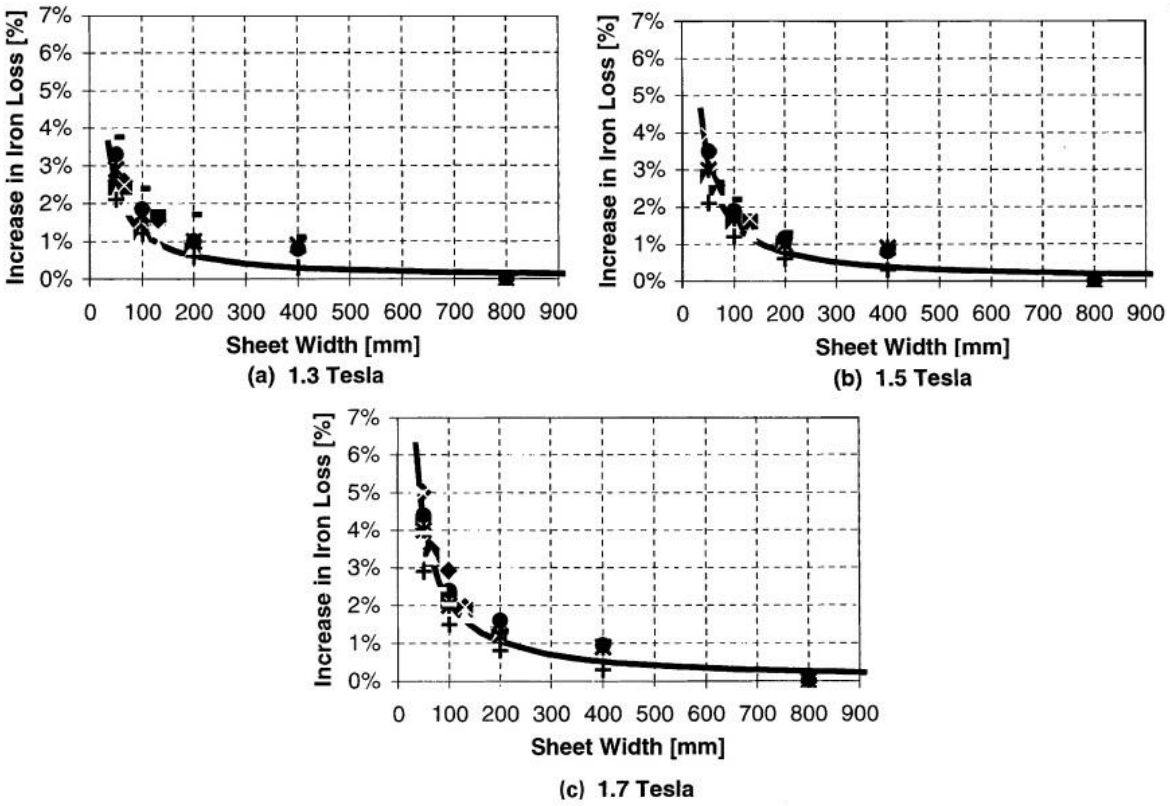

Fig. 1-28 Variation of power loss due to slitting with grain oriented electrical sheet width (a) B_{pk}= 1.3 T (b) B_{pk}= 1.5 T (c) B_{pk}= 1.7 T [49].

The power loss increase due to slitting was very large for narrow sheet width and negligible for sheets which were more than 500 mm wide. For 50 mm wide sheet, the power loss increase due to slitting B_{pk}= 1.7 T was 6 %. The best fit for the measured results were obtained theoretically by considering the width of the

affected region due to slitting being equal to the sheet thickness. It was concluded that the power loss increase due to slitting is dependent on the sheet width and flux density, and independent of the material type.

1.8 Previous Related Work

1.8.1 Packet to packet variation of flux density in stacked transformer cores built with different packet widths

In a multi-packet transformer core, the B_{pk} in each packet can be different to the nominal value. This variation of B_{pk} is termed as packet to packet variation of flux density.

Basak and Qader [50] tested a commercial 100 kVA 3-phase, 3-limb core built with 0.35 mm thick grain oriented electrical steel whose nominal power loss was 1.02 W/kg at B_{pk}= 1.5 T, 50 Hz. The core was built with nine packets of five different widths. The authors do not mention the width of the packets. The cross sectional area for the yokes of packets 1 and 9 was 1.5 times that of the limbs and the cross sectional area for the yokes of packets 2 and 8 was 1.2 times that of the limbs. The authors do not mention specific reasons for the differences in the chosen cross sectional areas of yokes and limbs of packets 1, 2, 8 and 9. The T-joint region was built with 45^o -90^o joint configuration and 45^o mitred overlap joint design was used for the corners. The front and the side views of the core geometry highlighting the dimensions are shown in Fig.1-29. The no-load losses were measured at three different peak flux densities of 0.9 T, 1.3 T and 1.7 T. The peak flux density (B_{pk}) of individual packets of the core was measured using search coils. Packet to packet variation of B_{pk} was measured at all the operating peak flux densities. The centre packet had the lowest B_{pk} whereas the peripheral packets had the highest B_{pk}. The authors do not mention the mechanism of flux transfer between packets but state that the flux transfer in the T-joint regions may be due to air gaps [51]. The largest 3rd and 5th components of B_{pk} were found to be in the middle limb. The percentage of harmonic components of B_{pk} in the T-joint regions was more in the peripheral packets.

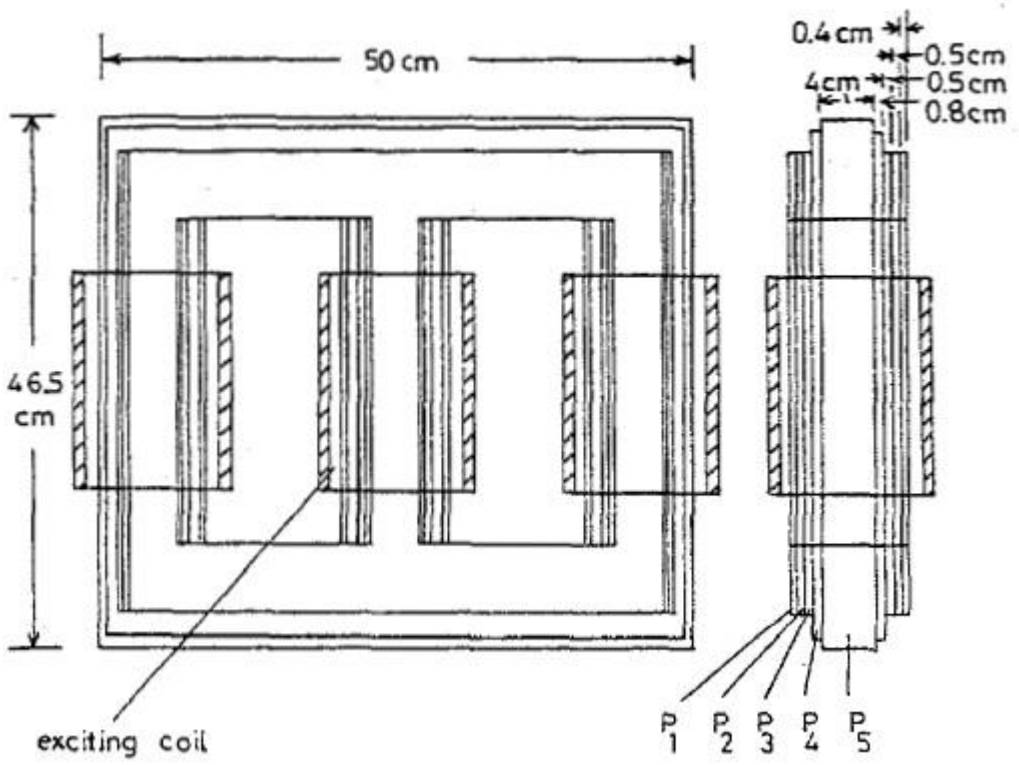

Fig.1-29 The front and side views of the multi-packet 3-phase, 3-limb transformer core [50].

Pfutzner et al. [52] tested a 13 MVA 3-phase, 3-limb core built with 0.3 mm thick M5 material (CGO) and consisting of 29 packets. The core mass was 6.2 tons. The core dimensions are not mentioned by the author. The investigation was done for single step lap corner joints. The flux density (B_{pk}) of individual packets of the core was obtained using a needle probe technique shown in Fig.-1-30. Needle probe technique to obtain B_{pk} in individual packets of a magnetised transformer core involves measurement of average voltage in each packet by means of four needle probes connected to a multi-meter by flexible wires. Each terminal of the multi-meter is connected to two needle probes which in turn are connected to the top and bottom laminations of a packet under investigation as shown in Fig. 1-30. The B_{pk} is then calculated using equation (1.14). The procedure is repeated for all the packets.

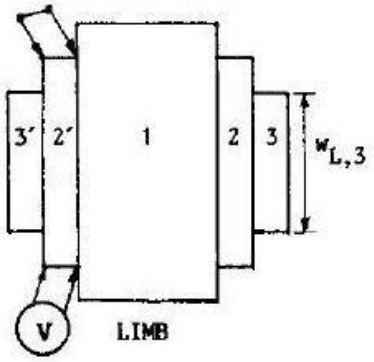

Fig.1-30 The principle of needle probe technique to determine B_{pk} in individual packets illustrated for packet number 2' of a transformer limb with 5 packets. The circuit was closed by the laminations which were in contact with four needle probes as shown [52].

Difference in B_{pk} was observed in the peripheral packets with the central packet exhibiting the minima as shown in Fig. 1-31. These variations in B_{pk} were found to be dependent on localised normal flux components (ϕ_z). High overlap region excitation (V_L) along with shifted overlap regions were found to yield high ϕ_z and cause flux transfer between packets. For multi-step lap joints, these effects are less significant.

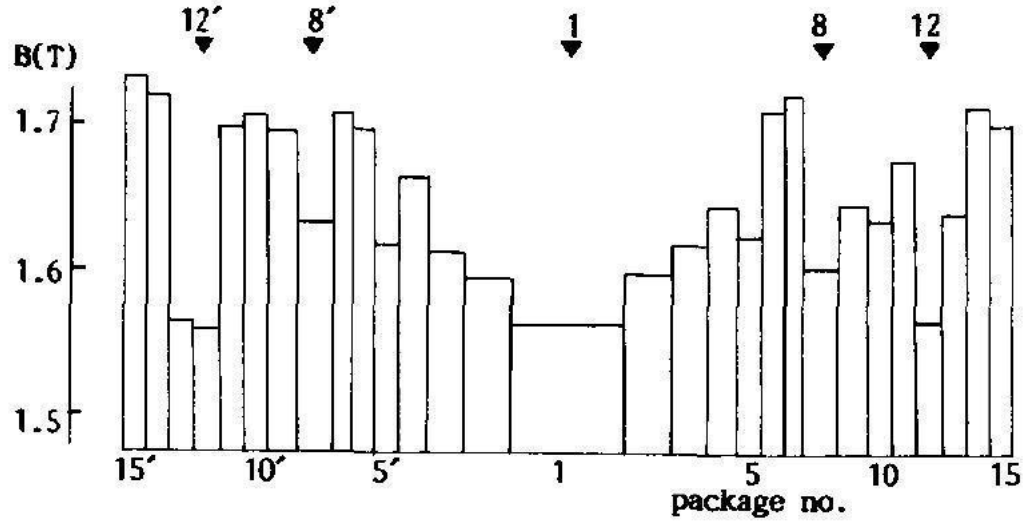

Fig.1-31 The packet to packet variation of B_{pk} in 29 packets in an outer limb of the 12 MVA 3-phase, 3-limb transformer core [52].

1.8.2 The effect of bolt holes on transformer core performance

Valkovic [53] investigated the effect of different T-joint designs and holes in yokes on the magnetic properties of a model 3-phase, 3-limb transformer cores. The model transformer core is as shown in Fig. 1-32. Four cores were built to investigate the effect of different sizes of holes in yokes on the core performance. The yoke and limb width (W) was 60mm. The holes in the yoke lamination are shown in Fig. 1-33. The first core had no holes, and the rest had holes of diameter (d) 5, 7 and 9 mm respectively. There were a total of four holes in the above mentioned cores with holes. The limb laminations were the same for all four cores.

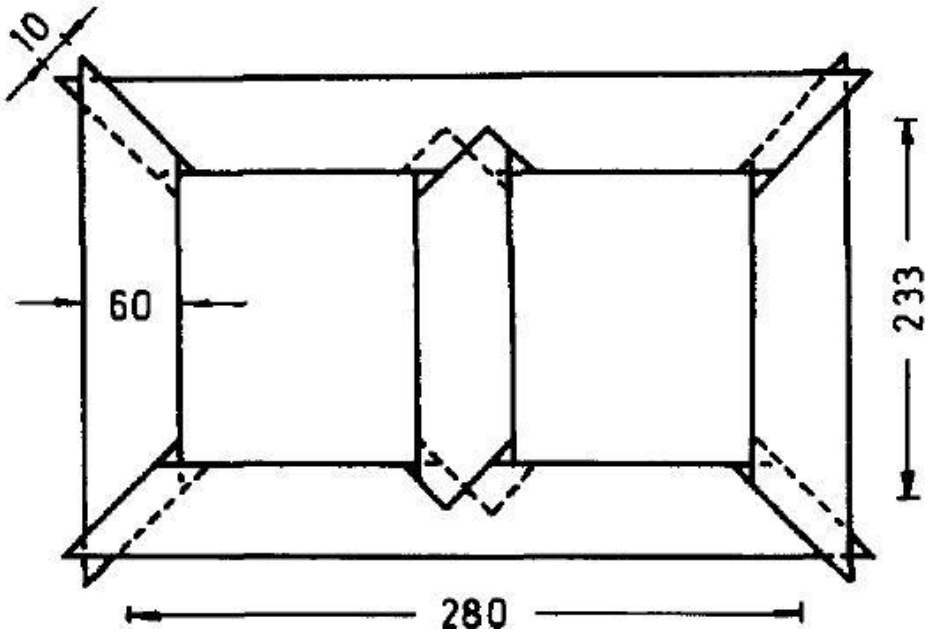

Fig.1-32 The 3-phase, 3-limb transformer core dimensions investigated in [53].

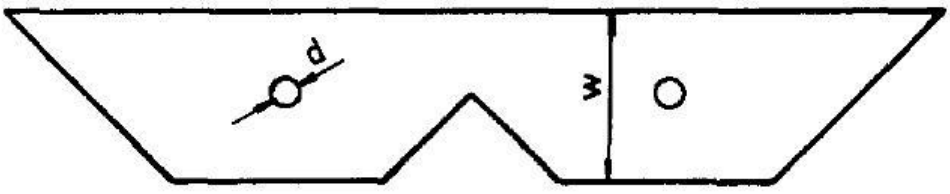

Fig.1-33 The yoke lamination showing the holes [53].

The investigation determined the dependence of power loss increase due to increase in hole diameter to yoke width ratio $\left(\frac{d}{W}\right)$ as shown in Fig. 1-34.

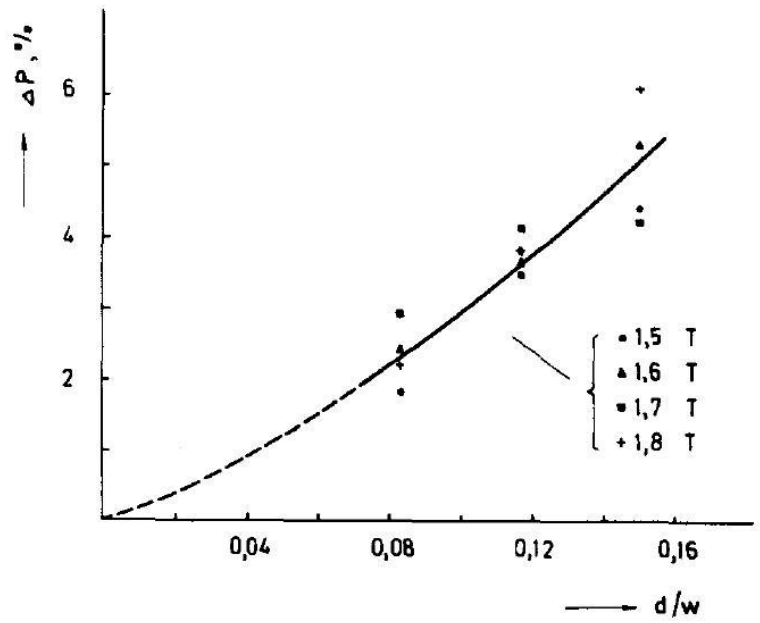

Fig.1-34 Percentage increase in power loss of 3-phase, 3-limb transformer core as a function of $\frac{d}{W}$ of holes present in the yokes [53].

The increase in power losses due to holes in the yokes was reported as between 2 to 8 %.

TeNyenhuis et al [54] used single sheet tester to measure the power loss increase in sample core laminations due to holes. No information is provided on the nominal loss of the laminations and annealing. The punched holes were 10 mm and 15 mm in diameter. The core lamination width was 85 mm. The measurement data was also compared to analytical results evaluated by computational software based on finite difference method. The software is not named in the paper. The authors have mentioned round holes for measurements in the text, but to simulate the flux distribution in 3-phase, 3-limb core geometry, six square holes (one in each limb and each yoke) were used as shown in Fig. 1-35. The square holes are contradictory to the punched round holes used for the measurements.

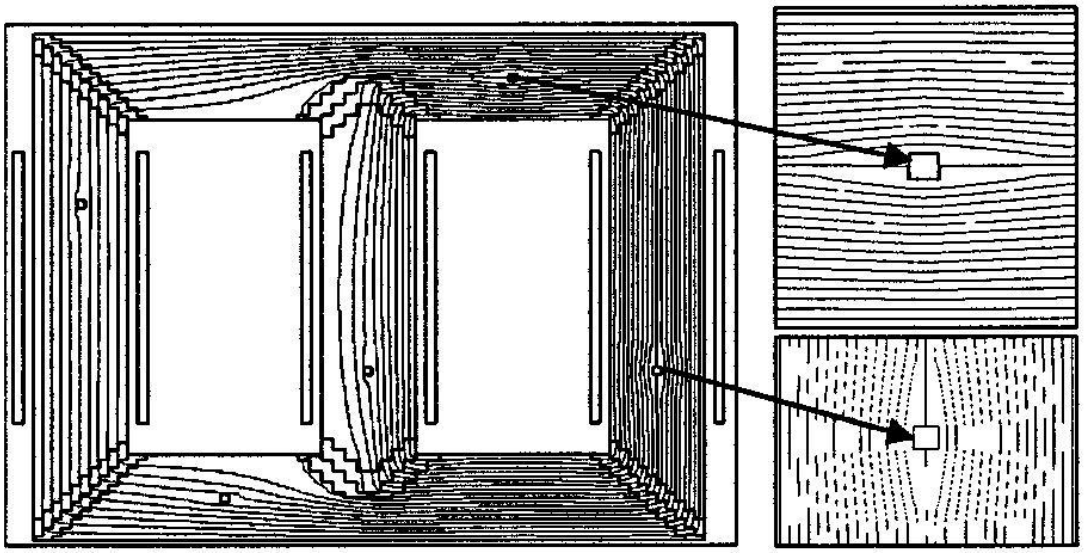

Fig.1-35 Flux (ϕ_{pk}) distribution plot showing the limb and yoke holes [54].

The measured loss increase in percentage against B_{pk} for round holes is shown in Fig 1-36. The calculated loss increase in percentage at B_{pk} = 1.7 T for square holes is also shown.

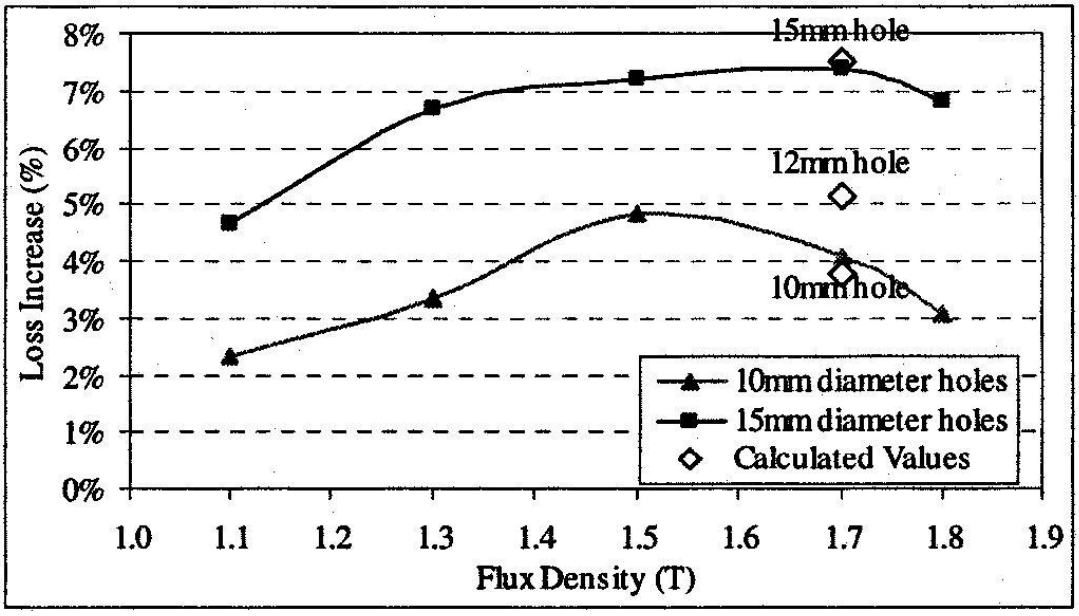

Fig.1-36 Percentage increase in loss in core laminations measured in single sheet tester due to holes [54].

The effect of holes on core loss was found to be position dependant. In the absence of holes, the flux travels along the RD in the limbs and the flux distribution is uniform. The flux distribution is non-uniform in the yokes even in the absence of holes. Thus, when holes are present, the overall loss increase in the limbs is more

than that of the yokes as the loss component in TD is more in the limbs and depends on $\frac{d}{W}$ values. Higher the $\frac{d}{W}$ values, higher will be the loss in the limbs.

It was also found that the percentage increase in loss was highest for B_{pk} = 1.5 T and for higher $\frac{d}{W}$ values.

1.8.3 The effect of mixing different types of magnetic materials on power losses in transformer cores

Joslin et al. [55] investigated the effect of mixing two different grades of 0.33 mm thick 3% silicon grain oriented electrical steel on the power losses of an experimental single phase core design. The power losses were measured under no stress and under normal and longitudinal stresses. The power losses of the two grades used in the mixed cores were 1.0 W/kg (46 grade) and 1.2 W/kg (56 grade) at B_{pk}=1.5 T. Two mixed cores with 10 laminations per limb were built using equal proportions of the two mentioned grades of grain oriented electrical steel. The width of the laminations was 150 mm in both the cases. A double overlap joint configuration was used in both the mixed cores. The first mixed core had 46 grade steel in two adjacent limbs and 56 grade steel in the next two limbs. This mixed core was termed as a series core. The next core was built with the two grades laid out in an alternating manner throughout the four limbs. This mixed core was termed as a parallel core. Under the no stress condition, the power losses of both the mixed cores were approximately equal to the mean losses of the two individual grades. The series core was found to be less stress sensitive than the parallel core. The power losses of the more stress sensitive parallel core, was similar to the power losses of the core built with 56 grade material.

Fukuda et al [56] investigated the effect of the grain texture in grain oriented electrical steel on the building factor of transformer cores. Building factor is defined as the ratio of the actual iron loss of a core to the estimated value based on the nominal loss of the core steel [57]. The two core designs (Type A and B) used for the investigation are shown in Fig. 1-37. Type A core had a 45^{o} offset T-joint design and Type B had 45-90^{o} T-joint design. Both the core designs were built with 90 laminations per limb. The core materials used to build the cores were 0.19mm,

0.23mm, 0.3mm (or 0.35 mm) thick grain oriented electrical steel and 0.35 mm thick non-oriented electrical steel. Each of the materials had different Goss textures which was represented by the flux density (B_{10}) at H_{pk} =1000 A/m. The B_{10} values of the mentioned materials varied between 1.81 T and 1.93 T.

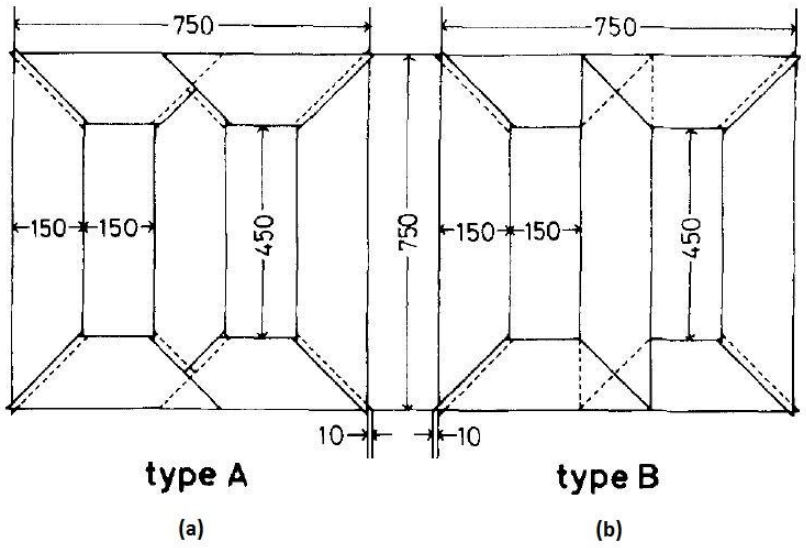

Fig.1-37 The investigated 3-phase, 3-limb transformer core types (a) 45^o offset T-joint design (b) 45-90^o T-joint design [56].

The authors do not disclose the number of cores built for the investigation in the paper. The core losses were measured for the two core designs. The flux penetration in the centre limb of the two core designs at the instant when the flux in the centre limb is zero during a magnetising cycle was also estimated by dc measurements as shown in Fig.1-38.

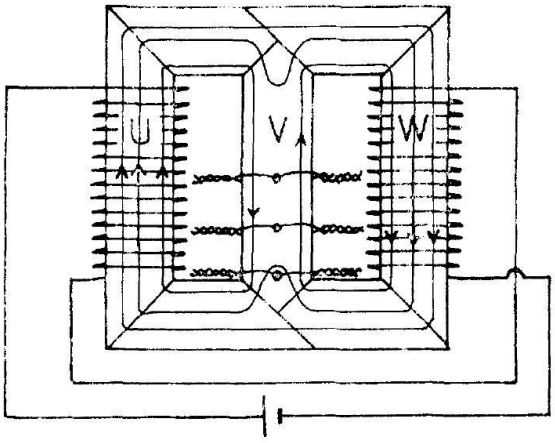

Fig.1-38 Illustration of the dc simulation of flux distribution [56].

Six single turn search coils, wound in the centre layer of the middle limb measured the dc flux when the outer limbs were magnetised using opposite dc currents. The flux penetration for different values of B_{10} of the core material is shown in Fig. 1-39.

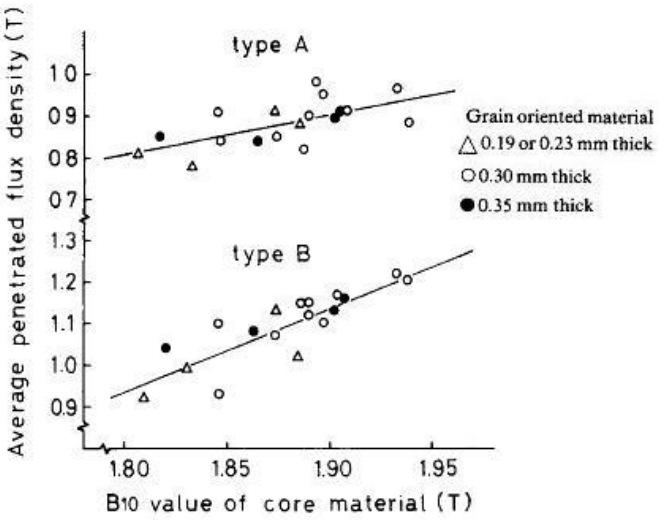

Fig.1-39 The variation of flux penetration for different values of B_{10} of the core material for the two types of cores [56].

The variation of building factor with B_{10} values of grain oriented core material for the two core designs is shown in Fig.1-40. The term $W_{17/50}$ shown in Fig. 1-40 means that the loss was measured at 1.7 T, 50 Hz.

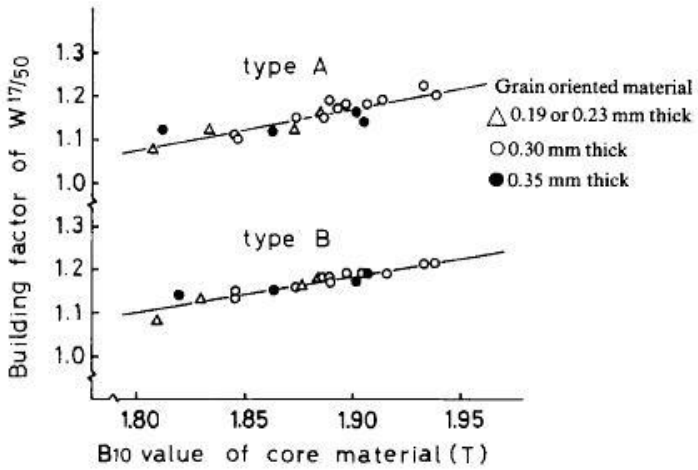

Fig.1-40 The variation of building factor for different values of B_{10} of the core material for the two types of cores [56].

The middle limbs for the two core designs were replaced with core materials having lower values of B_{10} and the core losses were measured. It was found that the

building factor for such cores was lower. It was concluded that the building factor of the cores was greater for higher values of B_{10} of core material and independent of the core design, grade and thickness of the material and peak operating flux density. It was also concluded that replacing the middle limb with core material having lower B_{10} values would reduce the building factor.

Valkovic [58] investigated the effect of mixing HGO (grade MOH) and CGO (grade M4) cores on the power losses of a 3-phase, 3-limb transformer core design shown in Fig. 1-41. The width of the limbs and yoke laminations was 120 mm. The T-joint in the core was of V-45^{o} design.

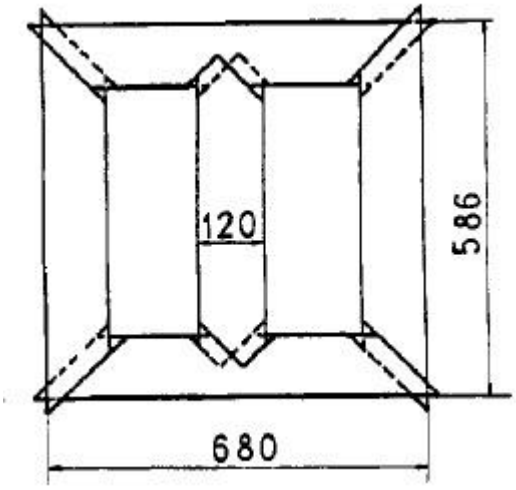

Fig.1-41 The investigated 3-phase, 3-limb transformer core with of V-45^{o} T-joint design [58].

The mixing of materials was in central limb, yokes and side limbs. Eight different cores were built. Two cores were built with HGO and CGO material respectively and six cores were built by mixing HGO and CGO material. For each mixed core, the loss reduction was calculated with respect to the core built with CGO material. It was found that the relative loss reduction in the mixed cores was related to the relative volume of the HGO material in the core. The variation of relative loss reduction with HGO proportion at B_{pk} = 1.7 T is shown in Fig. 1-42. Building the central limb and the side limbs with HGO material proved to be more beneficial than building the yokes with HGO. This was because of the non-uniform flux distribution in the yokes which caused extra losses when the yokes were built with HGO material.

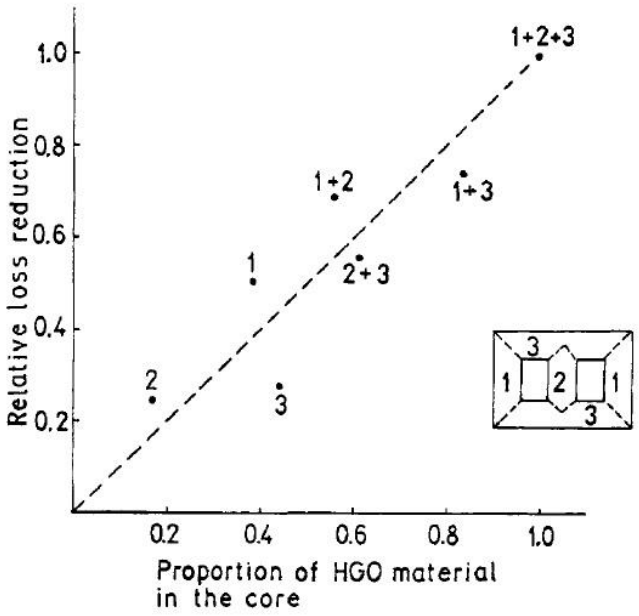

Fig.1-42 Variation of relative loss reduction with the HGO proportion in the 3-phase, 3-limb transformer core at B_{pk} = 1.7 T [58].

Moses and Hamdeh [59] investigated the effect of mixing 0.3 mm thick 3% silicon CGO, HGO and domain refined high permeability (DR) steel in various parts of a model 3-phase, 3-limb transformer core on the building factor. Eighteen cores of the same design were built for the investigation but results of only six cores were reported. The core limbs and yokes were 500 mm long. The limbs and yokes were 100 mm wide. All the cores were 60 layers thick. The six cores reported were 100 % CGO, 100 % HGO, 100 % DR, centre limb CGO rest HGO, centre limb CGO rest DR and limbs CGO & yokes HGO. The no-load measurement range for B_{pk} was 0.5 T to 1.7 T. The nominal loss of CGO, HGO and DR materials were obtained by single strip tester. The building factor for 100% CGO, 100% HGO and the core having centre limb CGO rest HGO is shown in Fig. 1-43.

The core built with 100% CGO steel had the lowest building factor because of lower anisotropy among all the cores. The core built with 100% DR steel had the lowest loss. The core with centre limb CGO and rest HGO improved the building factor as compared to HGO core.

An economic analysis was also done on the six cores to assess the ownership costs by using the core loss (W), material costs (£/kg) and capitalized costs (£/W). The

assumed material costs for CGO, HGO and DR were £1/kg, £1.1/kg and £1.25/kg respectively. The ownership costs were calculated at B_{pk} = 1.5 T and 1.7 T for all the six cores and for three capitalization costs of £1/W, £2/W and £4/W respectively. The ownership cost is the sum of material cost (£) and capitalized core loss cost (£). The capitalized core loss cost is the product of capitalization cost (£/W) and core loss (W). The core built with 100% CGO steel was chosen to be a reference for relative cost calculation for remaining five cores. Relative cost values of the remaining five cores was calculated by dividing their respective ownership costs by the ownership costs of the core built with 100% CGO steel at a particular B_{pk} and capitalization cost (£/W).

For low capitalization costs (£1/W & £2/W), the core with centre limb CGO rest HGO was found to be most economical as it had the least relative cost to that of 100% CGO core. For higher capitalization cost (£4/kg), mixed cores were found to be not economical and the core built with 100% DR was found to be most economical.

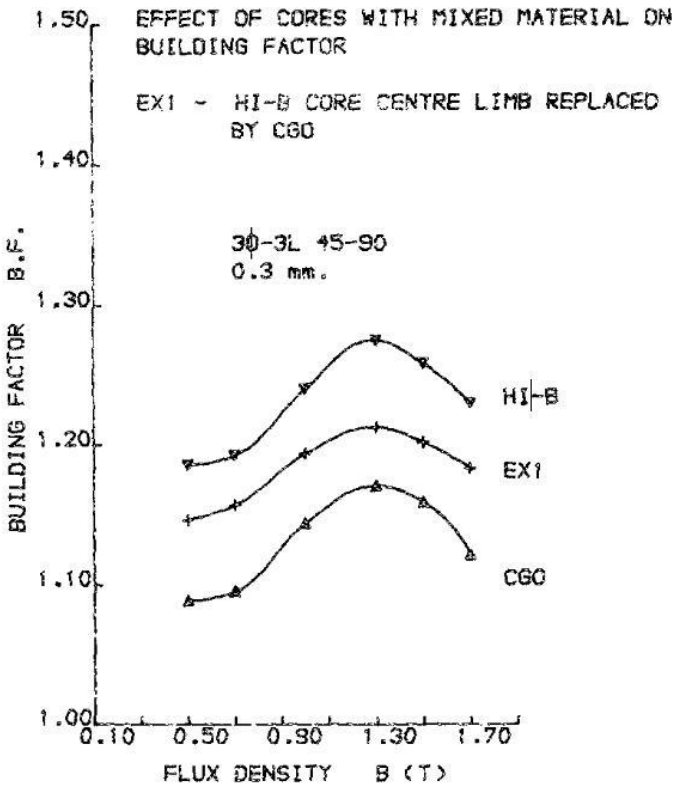

Fig.1-43 The building factor for 100% CGO, 100% HGO and the core having centre limb CGO rest as a function of B_{pk}. (HGO is expressed as HiB and the core having centre limb CGO rest HGO is expressed as EX1) [59].

Megherbi and Basak [60] experimented with the idea of mixing 0.22 mm thick amorphous laminations (Metglas 2605SC) with 0.23 mm thick HGO steel laminations in a stacked model core design of dimensions 260 x 230 x 4 mm^3 and having butt and lap joints. A total of five cores were built with the same design. The cores which were built were 100 % amorphous, 100 % HGO, 25 % amorphous – 75 % HGO, 50 % amorphous – 50 % HGO and 75 % amorphous – 25 % HGO. The lamination width in all the cores was 50 mm. Two, 25 mm wide amorphous laminations were glued together to make a 50 mm wide lamination. For 25 % amorphous – 75 % HGO core, the amorphous lamination stack was sandwiched between two equal HGO lamination stacks. For 50 % amorphous – 50 % HGO, the amorphous lamination stack was placed on top of the HGO lamination stack. For 75 % amorphous – 25 % HGO core, HGO stack was sandwiched between two equal amorphous lamination stacks. The losses were measured and building factor was calculated. The building factor variation with B_{pk} for the five cores is shown in Fig. 1-44.

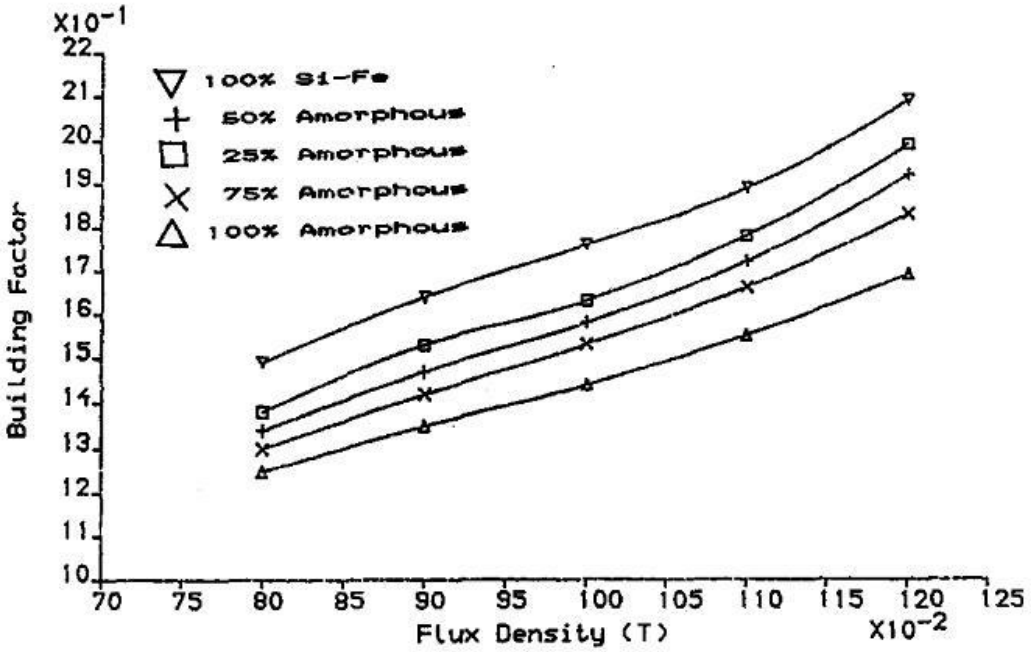

Fig.1-44 Building factor for the five cores as a function of B_{pk}[60].

HGO material has high anisotropy and will have higher losses in the corner and T joints regions. As the percentage of HGO decreased in the core design, the building factor decreased for the B_{pk} range 0.8 T – 1.2 T.

Snell and Coombs [61] investigated the effect of mixing ball unit domain refined (BUDR) and non-domain refined (NDR) steels in a 3-phase, 3-limb transformer core on the core loss. BUDR steel is low loss steel produced by rolling hardened steel balls over HGO steel. The core geometry is shown in Fig.1-45. A total of ten 100 kVA cores were built. No information is given about the corner joint configuration. Among them, five cores were built with different percentage mix of BUDR and NDR steels and five cores were built with different percentage mix of two batches (designated as A and B) of NDR steels. The five cores which were built with BUDR and NDR steels were 100% NDR, 75% NDR-25%BUDR, 50% NDR-50% BUDR, 25% NDR-75% BUDR and 100% BUDR. The five cores which were built with NDR-A and NDR –B steels were 100% NDR-B, 25% NDR-A – 75% NDR-B, 50% NDR-A – 50% NDR-B, 75% NDR-A – 25% NDR-B and 100% NDR-A. NDR-A had lower permeability than NDR-B. All the mixed cores were constructed with one material to a certain height and then the other material was used to complete the core construction. There was no information about the core packet thickness and the lamination thickness. The power losses of all the cores were measured by a computerised loss measurement system.

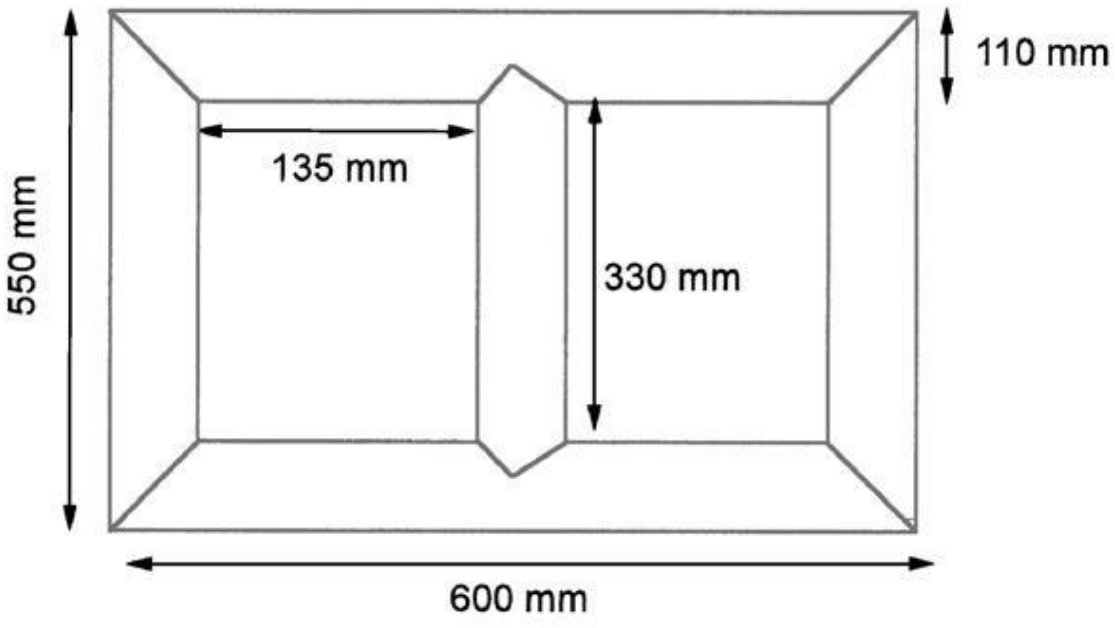

Fig.1-45 The 3-phase, 3-limb transformer core dimensions investigated in [61].

The specific core loss variation of the mixed cores (built with BUDR and NDR) with increasing percentage of BUDR is shown in Fig. 1-46.

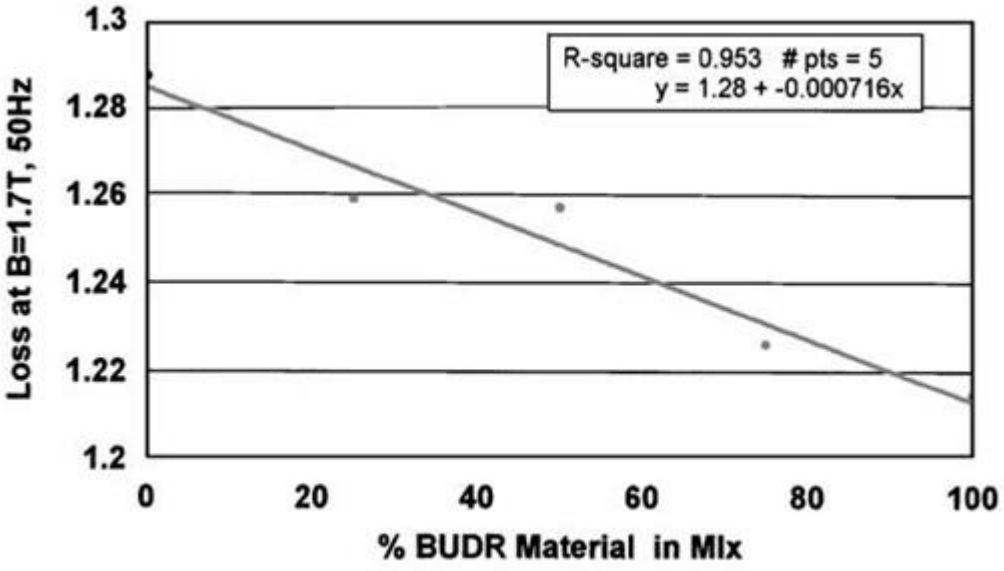

Fig.1-46 Percentage of BUDR in a predominantly NDR core [61].

The specific core loss variation of the mixed cores (built with NDR-A and NDR-B) with increasing percentage of NDR-A is shown in Fig. 1-47.

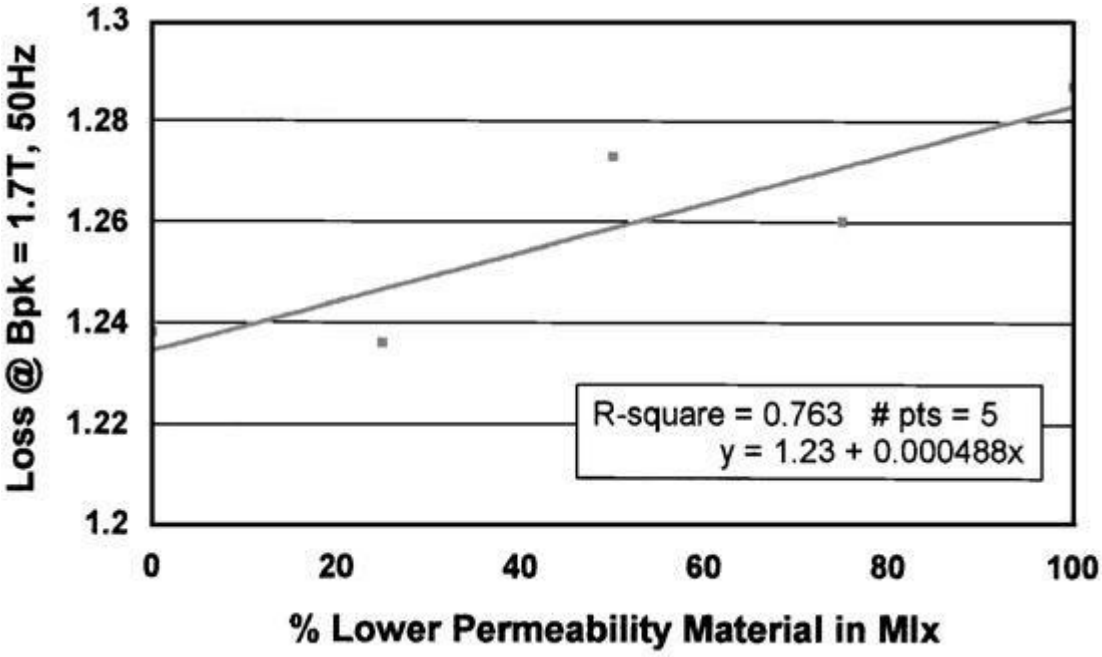

Fig.1-47 Percentage of NDR-A in a predominantly NDR-B core [61].

The mixed core losses are proportional to the losses of the materials used. This investigation has shown that BUDR and NDR steels can be mixed in a single packet 3-phase, 3-limb design without degrading the core performance.

Work on mixed wound distribution transformer cores has been reported by Kefalas et al [62 -64]. Mixed medium voltage instrument transformers were investigated by Pytlech [65] and mixed current transformers were investigated by Lesniewska and Rajchert [66]. The work done by these authors is not discussed in detail as it is not linked to the current investigation. However, it gives information on the mixing of materials to obtain better magnetic properties.

1.8.4 Calculation of Three-Phase, Three-Limb Transformer No-Load Losses from Localised Losses

Moses [57] developed an algorithm to predict the core losses of 3-phase, 3-limb transformers. The algorithm used simple arithmetic summation of localised losses to calculate the total core losses of the transformers. The algorithm used previously published localised loss data due to harmonic flux, rotational flux, inter-laminar flux, stress, bolt holes, corner joints and core geometry. The calculations were not computer based. The algorithm was used to calculate the losses for 20 transformer cores considering the major design aspects like step lap joints, T joint design, with or without oil ducts, with or without increased yoke cross sectional area and different grade of materials. The approximate core weight was 11350 kg. Good agreement was found between the building factor calculated from the predicted losses and the building factor obtained from measurements in the peak flux density (B_{pk}) range 1.5 T to 1.7 T. The results for one of the cores are shown in Fig. 1-48.

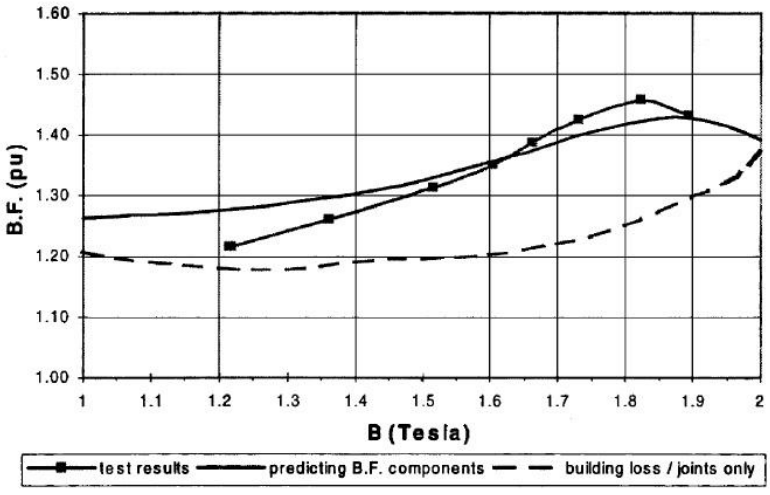

Fig.1-48 The calculated and measured building factor of the investigated 3-phase, 3-limb transformer core [57].

1.9 Aims of the Investigation

Previous research suggests that the power losses of 3-phase, 3-limb transformer cores can be calculated by the summation of losses due to various contributors [57]. Also, electrical steel manufacturers have in-house empirical data sheets to predict the transformer core losses. These data sheets are from years of experience and operation. To supplement these data sheets and to improve upon the previous calculation method [57], a quicker and simpler algorithm which uses the global flux distribution, localised loss data, core geometry and material properties can be a handy tool to predict no-load losses of stacked 3-phase, 3-limb cores built with high permeability grain oriented steel (HGO) and conventional grain oriented steel (CGO).

The packet to packet variation in stacked multi-packet 3-phase, 3-limb transformer cores with single step lap corner joints, is due to high localised normal flux components (ϕ_z) [52]. The reasons for the packet to packet variation of flux density for stacked, multi packet HGO, CGO and mixed 3-phase, 3-limb transformer cores with multi-step lap joints is yet to be investigated.

Previous research on bolt holes is mainly focussed on the power loss increase in transformer cores due to bolt holes [53-54]. Data sets on the localised loss and localised relative permeability around different sizes of holes and slots do not exist for different flux densities. They are valuable in predicting the power loss and effective permeability of transformer cores and need to be processed.

From previous research, experimental, stacked single packet mixed cores built with non - MSL joints tend to possess improved magnetic properties [55-61]. But modern day stacked commercial cores are multi-packet designs with MSL joint configuration. So transformer designers are interested in the variation of no-load specific loss and specific apparent power with increasing CGO content in a multi packet, MSL joint core design predominantly built with HGO material.

This research aims to:

1) Build an algorithm to predict specific losses for 3-phase, 3-limb HGO and CGO cores using the core geometry and material properties in NI LabVIEW software.

2) Investigate the packet to packet variation of flux density, specific loss and specific apparent power for stacked multi packet HGO, CGO and mixed 3-phase, 3-limb transformer cores with (MSL) joints.
3) Quantify the localised losses and relative permeability around different sizes of holes and slots in HGO and CGO steel using FE simulations and post processing of peak flux density distribution.

1.10 Summary

In this chapter, the theoretical background and literature review on magnetic materials, grain oriented electrical steel, power losses and transformers have been presented. Power loss mechanisms and measurement standards in grain oriented electrical steel have been explained. Developments and research on stacked transformers has been discussed. The previous related work to the current investigation has been discussed in detail. Finally, the aims of the investigation have been stated and reasons for why they were taken up have been mentioned.

Chapter 2

Packet to Packet Variation of Flux Density in Three Phase, Three Limb, Power Transformer Cores

2.1 Introduction

In this chapter, the measurement results of the packet to packet variation of flux density in HGO, CGO and four mixed 3-phase, 3-limb multi-packet stacked cores are presented. Six single packet cores (3 HGO and 3 CGO) of 50 mm, 130 mm and 160mm width were built from the limb laminations of the full sized HGO and CGO cores to measure the peak magnetising current. The effective permeability of the single phase packets of 50mm, 130mm and 160mm width were then calculated from the peak magnetising field which was calculated from the peak magnetising currents. An analytical model was deduced to predict the effective permeability of the packets. The results of the effective permeability obtained from measurements and modelling are presented.

2.2 Three Phase Cores

2.2.1 Three Phase, Three Limb Full sized Transformer Cores

Two, 350 kVA 3-phase three limb transformer cores of the same design and dimensions (Fig. 2-1 & Fig. 2-2) were sourced from a commercial transformer manufacturer for the measurements. One was constructed using CGO steel and the other with HGO steel. The lamination thickness was 0.3 mm. Each core comprised 5 packets of two 50 mm, two 130 mm and one 160 mm wide laminations. The core joints were built with multi step lap (MSL) design. Seven step laps were used. Four “mixed” cores assembled with different combinations of the packets of HGO and CGO were also tested. The core specifications are indicated in table 2.1. The notation in table 2.1 indicates the location of HGO (H) and CGO (C) packets. The mixing of packets is shown in Fig. 2-3.

The yokes of each core were clamped using four, insulated, 6 mm diameter bolts, each with a clamping torque of 20 Nm. Each limb and yoke of the cores had one circular hole and one slot. The circular holes were 10 mm in diameter and the slots were 14 mm long and the width of the slots was equal to the diameter of the circular hole.

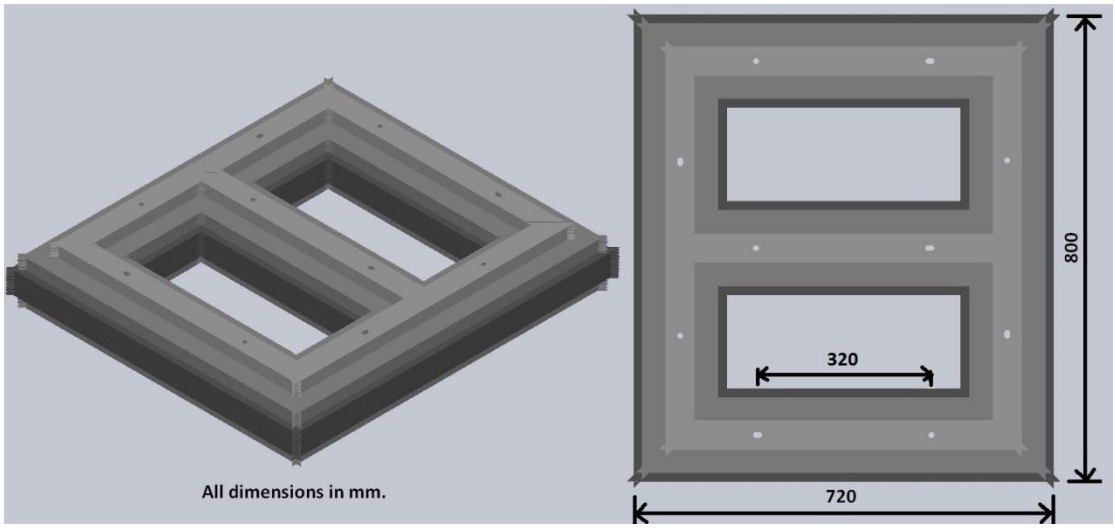

Fig. 2-1 Three phase, three limb full sized core.

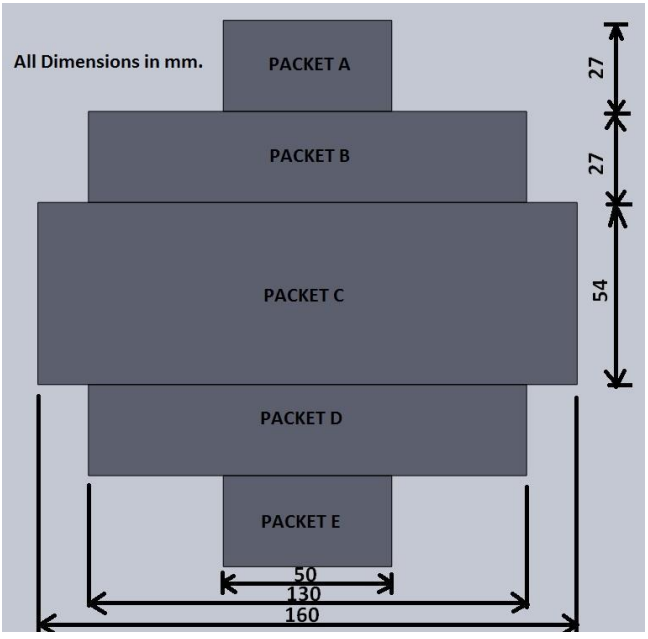

Fig. 2-2 Core cross section.

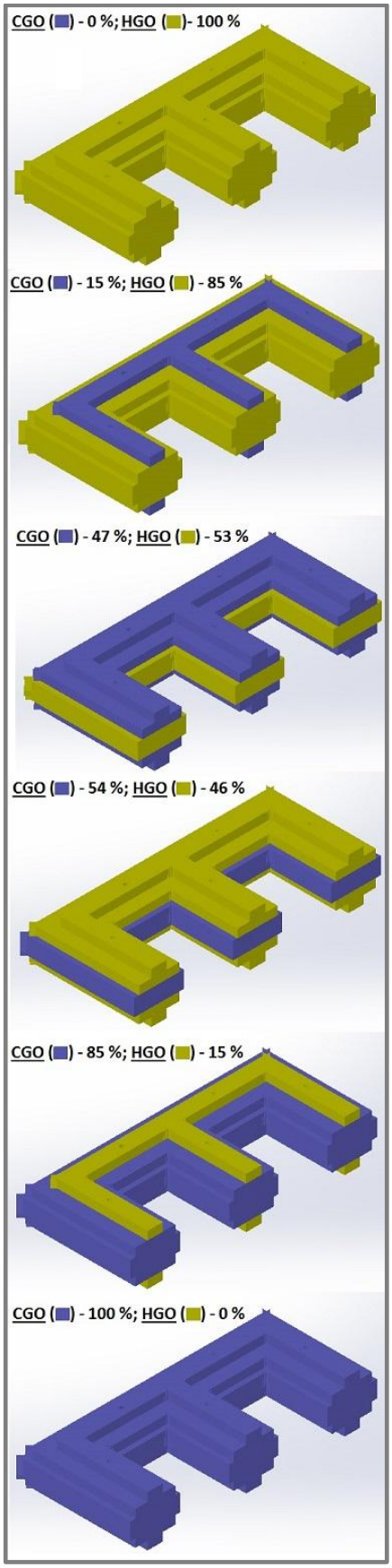

Fig. 2-3 Schematic isometric view of the cores.

Table 2.1 Specifications of 3-Phase, 3-Limb, Full Sized Cores

Core	Designation	% CGO	% HGO	Core Mass (kg.)
1	HGO (50H+130H+160H)	0	100	388.0
2	50C+130H+160H	15	85	386.8
3	50C+130C+160H	47	53	384.9
4	50H+130H+160C	54	46	385.5
5	50H+130C+160C	85	15	383.6
6	CGO (50C+130C+160C)	100	0	382.4

2.2.2 Three Phase Magnetizing System

The HGO, CGO and mixed cores were magnetised using the three wattmeter method and no-load loss, apparent power were recorded for peak flux density (B_{pk}) =1.0 T to 1.8 T in steps of 0.1 T under 50 Hz sinusoidal excitation[68]. The no-load loss and apparent power of the cores are discussed in **Chapter 3**. The cores were magnetised using three variacs, which were separately controlled to provide a balanced, sinusoidal flux density with less than 0.2 % harmonics at 50 Hz. The overall peak flux density was calculated from the average induced voltages in 30 turn secondary windings wound around each limb using equation (2.1).

$$B_{pk} = \frac{V_s}{4.N.A.f} \quad [T] \tag{2.1}$$

where $B_{pk}$is the peak flux density induced in the core, V_s is the average voltage in the secondary windings $[\text{volts}]$, N is the number of secondary windings $[30\ turns\ ]$, A is the area of cross section $[\text{m}^2]$ and f is the magnetising frequency $[\text{Hz}]$.

The calculation for the number of turns required is shown in Appendix **II**. The power loss of the 3-phase, 3-limb HGO core was separately measured using the two sets of variacs (variac A and B) using the magnetising circuit as shown in Fig. 2-4. I_1, I_2 & I_3 are the primary phase currents and V_{1N}, V_{2N} & V_{3N} are the secondary phase to neutral voltages. The harmonic content in the secondary voltage of the 3-phase, 3-limb HGO core was also measured the using the two sets of variacs (variac A and B).

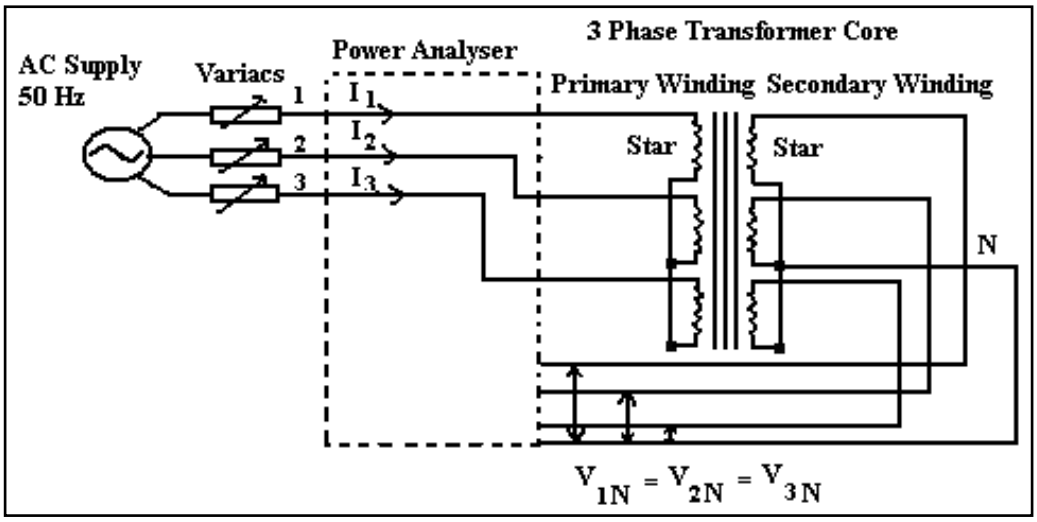

Fig. 2-4 Three phase magnetising circuit.

The harmonic content were mainly 3rd harmonic in the secondary voltage as shown in Fig.2-5. The power analyzer calculated the 3rd harmonic in percentage by discrete Fourier transformation and displayed the results in real time. The variac B was chosen for the investigation as it had less than 0.2% harmonic content.

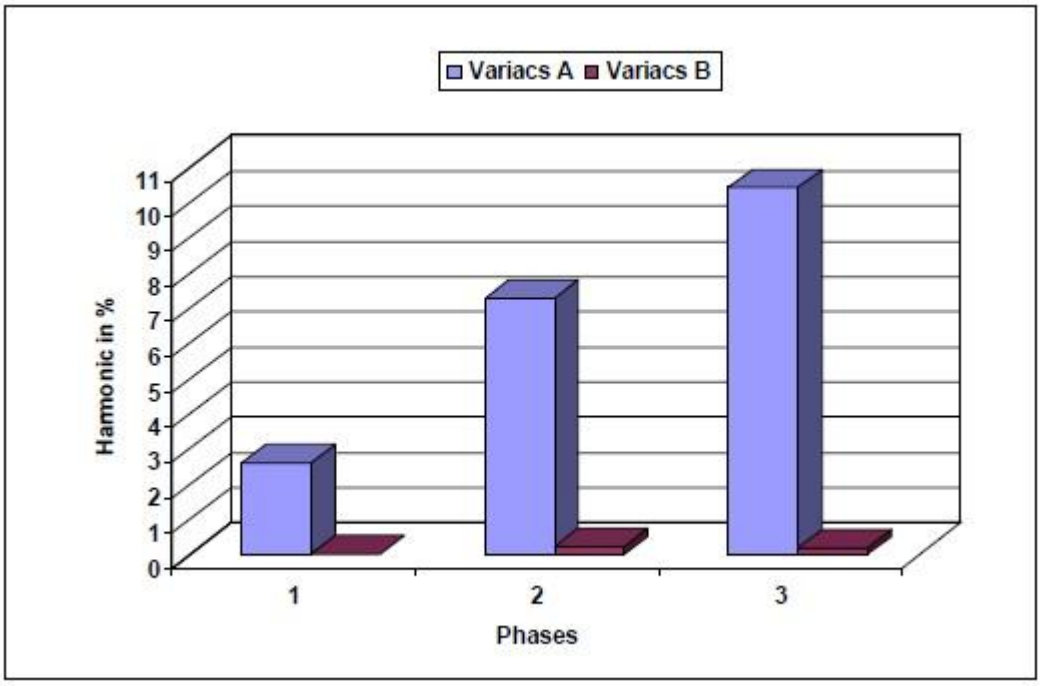

Fig. 2-5 Third harmonic content sourced from Variac A and B.

2.2.3 Packet to Packet Variation of Flux Density Measurement

The flux densities in individual packets of all the cores at B_{pk} = 1.0 T, 1.3 T, 1.5 T and 1.7 T were calculated from the measured average induced voltage between the top and bottom laminations of each packet in a limb using a flexible needle probe technique [52] using the equation (2.2). The measurement was done in the middle portion of the limb. However, the position of the needle probes along the limbs and yokes in individual packets did not affect the measured average voltage.

$$B_{pk} = \frac{V_{packet}}{4.N.A.f} \quad [T] \tag{2.2}$$

where $B_{pk}$is the peak flux density induced in the packet limb, V_{packet} is the average voltage in the single turn needle probes$[\text{volts}]$, N =1, A is the area of cross section of the packet $[\text{m}^2]$ and f is the magnetising frequency $[\text{Hz}]$.

The above mentioned procedure was repeated for the remaining two limbs and two yokes to obtain theB_{pk}. The B_{pk} in the packet was then calculated by averaging the five B_{pk}values obtained from three limbs and two yokes. The whole procedure was repeated three times to obtain the average B_{pk} in individual packets.

2.3 Single Phase Cores

2.3.1 Single Phase, Two Limb Transformer Cores

The individual packets of the full sized 3-phase HGO and CGO cores were used to assemble three single phase HGO and CGO cores whose specifications are given in table 2.2. Each limb of the single phase cores had one 10 mm diameter bolt hole of and one 10 mm diameter, 14 mm long slot in each limb. The core dimensions are given in Fig. 2-6, Fig. 2-7 & Fig. 2-8.

Table 2.2 Dimensions of Individual Single Phase, Two Limb Cores

Material	Packet Width (mm.)	Packet Thickness (mm.)	Mean Magnetic Path Length (mm.)	Mass (kg.)
HGO	50	27	2240	22.5
	130	27	2240	58.7
	160	27	2240	72.3
CGO	50	27	2240	22.2
	130	27	2240	58.0
	160	27	2240	71.3

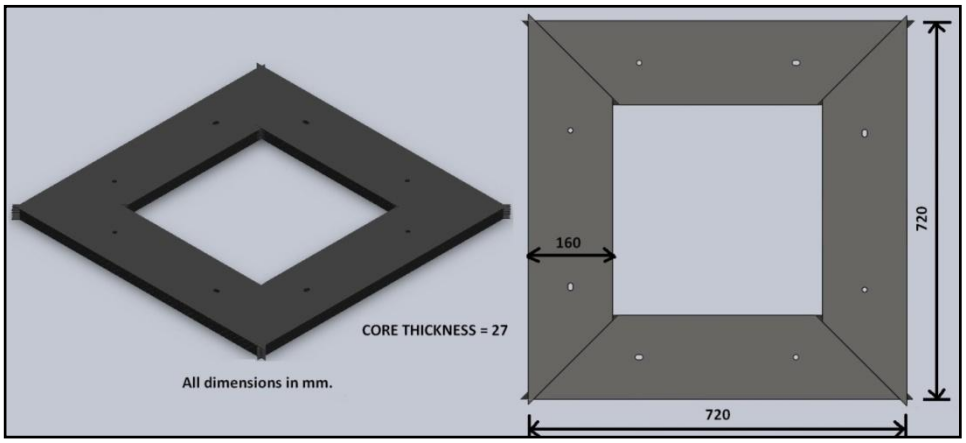

Fig. 2-6 Single phase core built with a single 160mm wide packet.

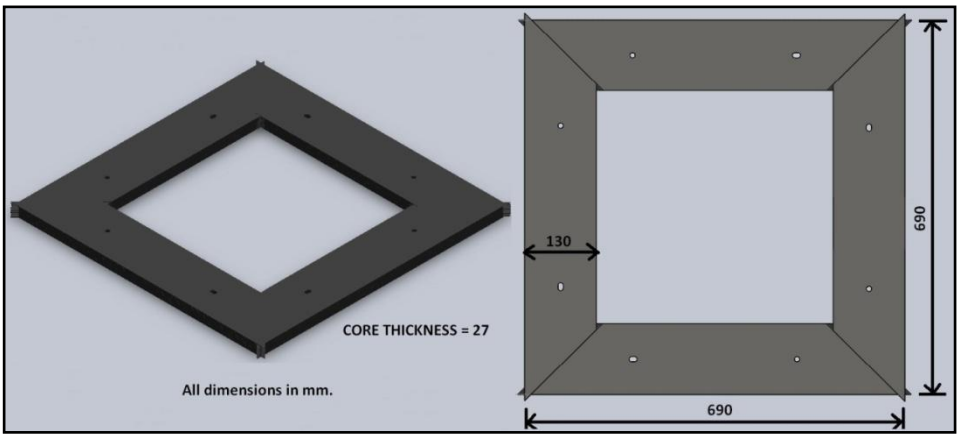

Fig. 2-7 Single phase core built with 130mm wide packet.

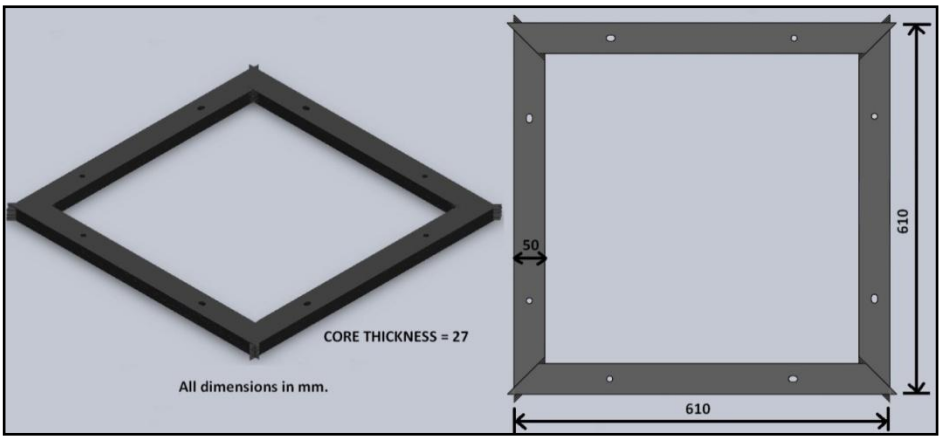

Fig. 2-8 Single phase core assembled from a single 50mm wide packet.

2.3.2 Single Phase Measurements

The single phase cores were tested at B_{pk} = 1.0 T to 1.8 T, 50 Hz and the no load loss, apparent power and magnetising current were recorded. The no-load and apparent power of these cores is discussed in **Chapter 3**. The magnetizing circuit is as shown in Fig.2-9. The overall peak flux density was calculated from the induced average voltages in 30 turn secondary windings wound around each limb using equation (2.1). The effective permeability (μ_{eff}) of each core was obtained from the measured peak magnetising currents (I_{pk}). The peak magnetising field (H_{pk}) was calculated from the measured peak magnetising current (repeatability < $\pm$ 1%), number of secondary winding turns (N_2) and the mean magnetic path length (l_m) using equation (2.3).

$$H_{pk} = \frac{N.I_{pk}}{l_m} \quad \left[\frac{A}{m}\right] \tag{2.3}$$

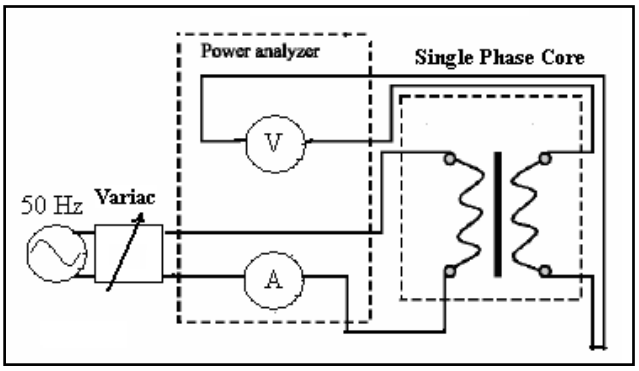

Fig. 2-9 Single phase magnetising circuit.

2.4 Results and Discussion

Packet to packet variation of B_{pk}in the 3 phase cores assembled from HGO and CGO are shown in Fig.2-10 & Fig.2-11 respectively. The repeatability was less than $\pm$ 1% error in all cases. For both HGO and CGO, a reduction in B_{pk} is observed as the packets become narrower.

This phenomenon can be explained by considering the peak magnetising field (H_{pk}) data obtained from the single phase measurements. The H_{pk} required to magnetise the HGO and CGO single phase cores are shown in Fig.2-12 and Fig.2-13 respectively.

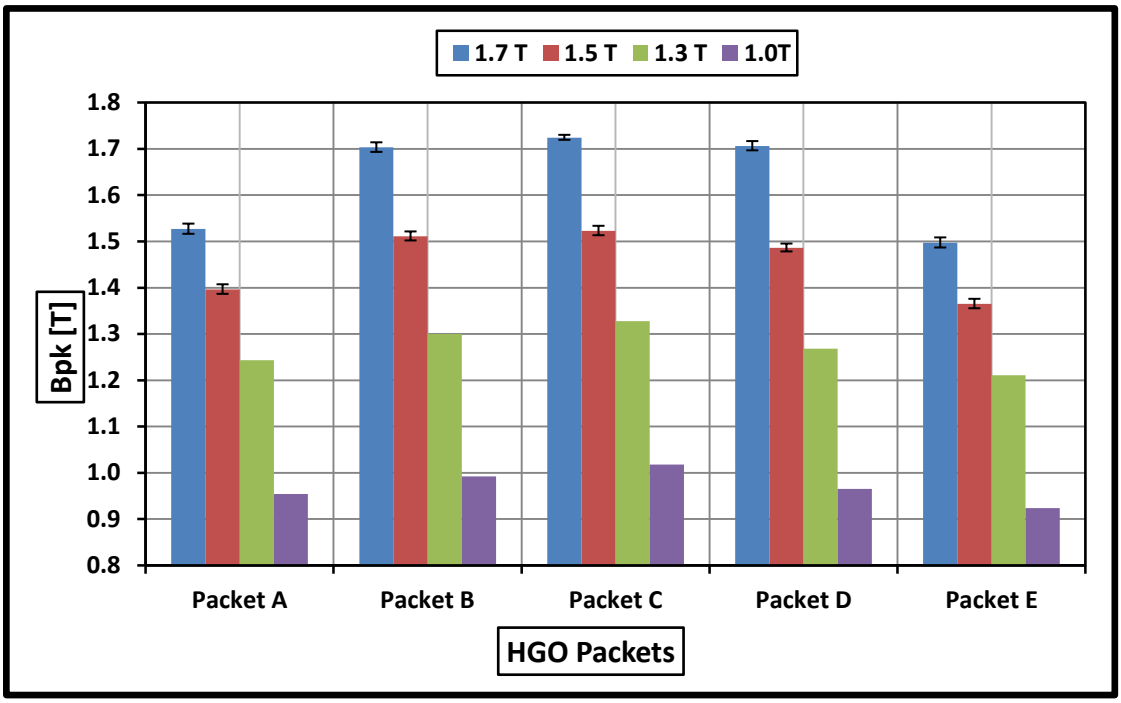

Fig. 2-10 Packet to packet variation of B_{pk} in the 3 phase HGO core at B_{pk} =1.0 T, 1.3 T, 1.5 T and 1.7 T.

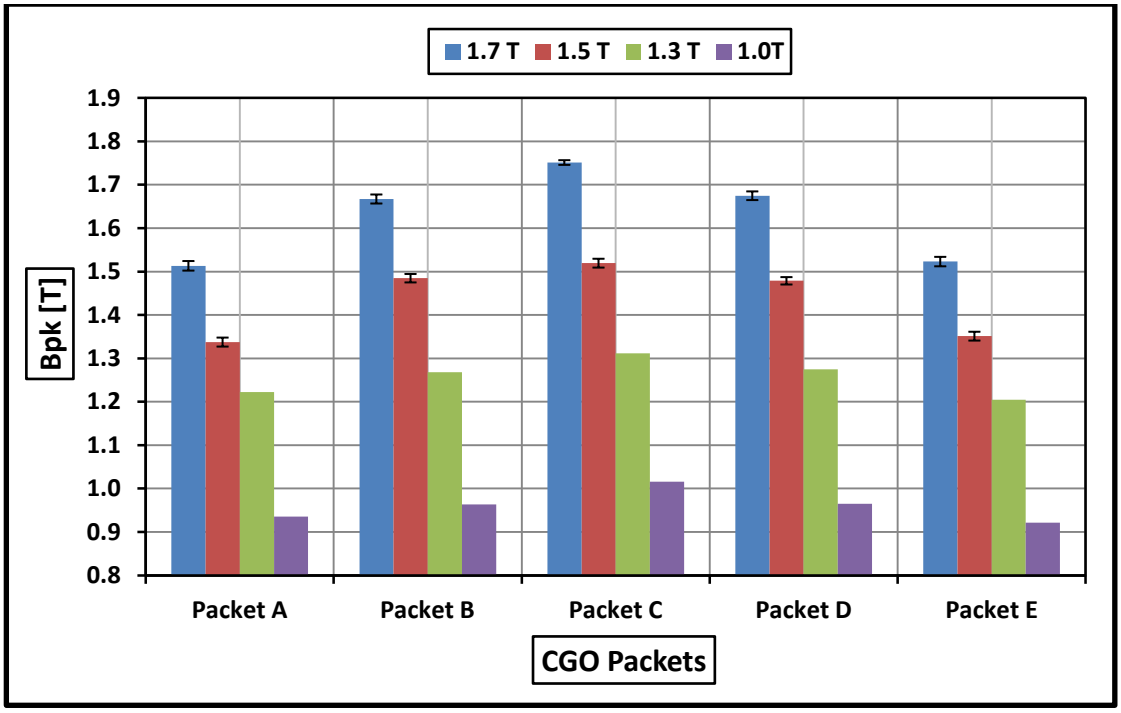

Fig. 2-11 Packet to packet variation of B_{pk} in the 3 phase CGO core at B_{pk} =1.0 T, 1.3 T, 1.5 T and 1.7 T.

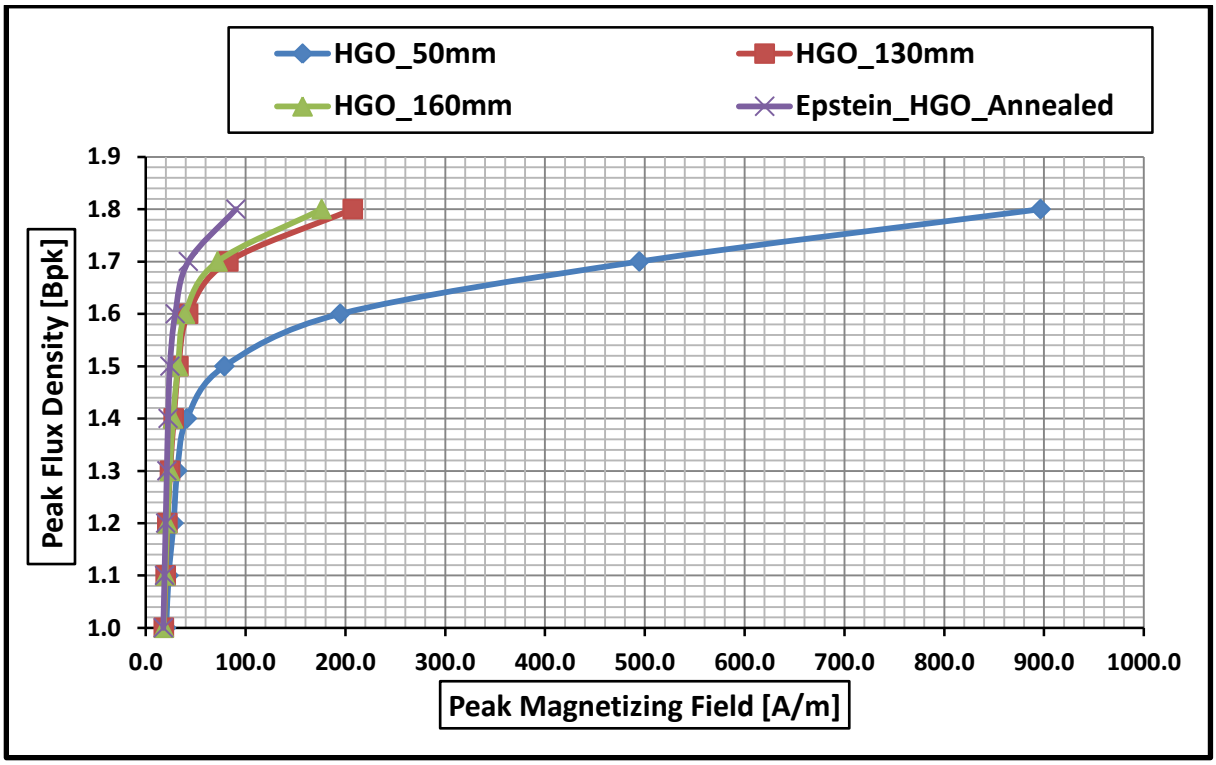

Fig. 2-12 Variation of H_{pk} with B_{pk} for single phase HGO cores.

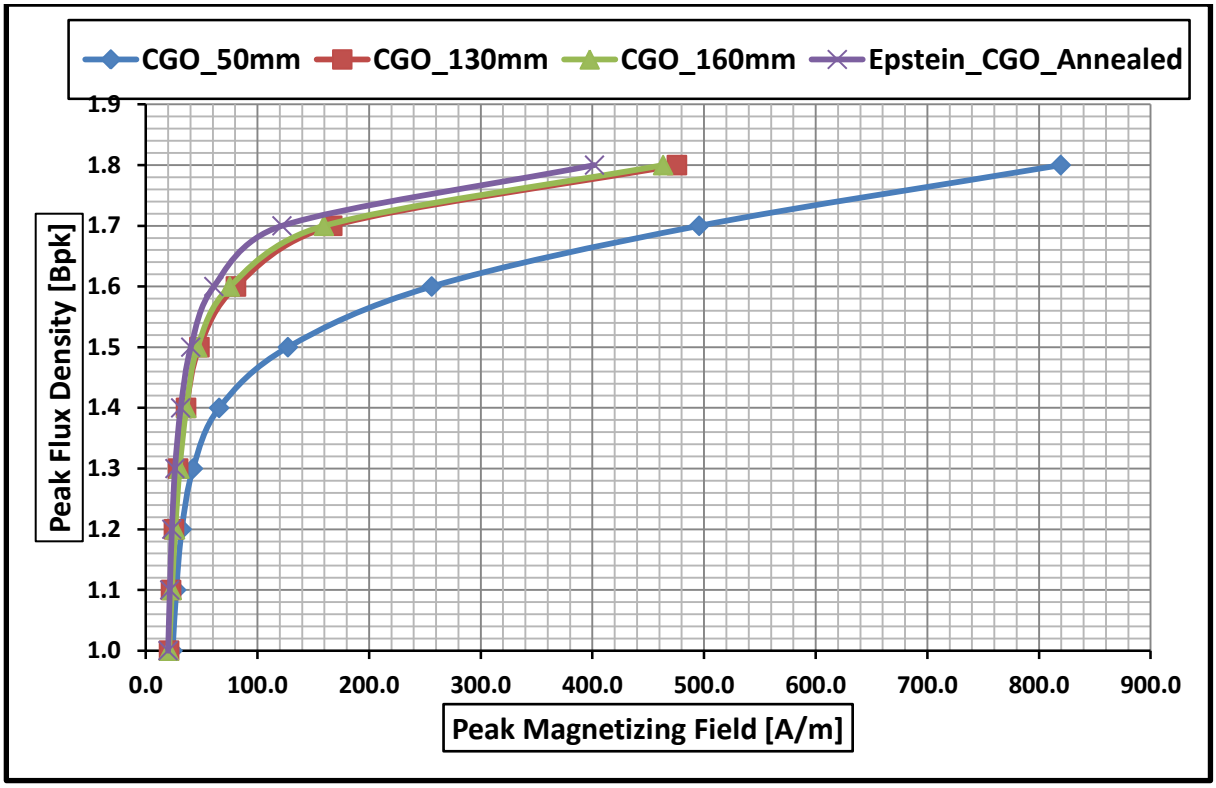

Fig. 2-13 Variation of H_{pk} with B_{pk} for single phase CGO cores.

The effective permeability for the single phase cores was then calculated using the H_{pk} data using equation (2.4).

$$\mu_{eff} = \frac{B_{pk}}{\mu_0 . H_{pk}} \tag{2.4}$$

Also, the effective permeability of one layer of the single phase cores was calculated analytically considering the magnetic circuit shown in Fig.2-14. The reluctances in air gaps, bulk regions and regions adjacent to the circular holes and slot holes are also depicted. Four air gaps are included in the model as they represent the air gaps of the four corner joints of a single phase core.

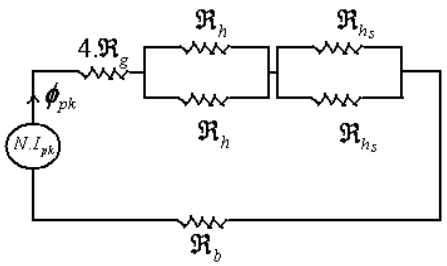

Fig. 2-14 Reluctance circuit of a single layer, single phase core.

From Fig.2-14, the magneto-motive force,

$$N.I_{pk} = \emptyset_{pk}.\left(4.R_g + \frac{R_h}{2} + \frac{R_{h_S}}{2} + R_b\right) \quad [A] \tag{2.5}$$

where $\emptyset_{pk}$ is the peak flux in along the mean path length [Wb], R_g is the reluctance of the corner air gaps $\left[\frac{\text{A}}{\text{Wb}}\right]$, $R_h$is the reluctance of the regions adjacent to the circular hole $\left[\frac{\text{A}}{\text{Wb}}\right]$, $R_{h_s}$is the reluctance of the of the regions adjacent to the slot $\left[\frac{\text{A}}{\text{Wb}}\right]$and $R_b$is the reluctance of the bulk regions $\left[\frac{\text{A}}{\text{Wb}}\right]$.

Also,

$$B_{pk} = \mu_0.\mu_{\,eff}.H_{pk} = \mu_0.\mu_{\,eff}.\frac{N.I_{pk}}{l_m} \qquad [T] \tag{2.6}$$

From equations (2.5) and (2.6), the effective permeability $\left(\mu_{\,eff}\right)$ of a single layer of the single phase core, is given by equation (2.7),

$$\mu_{\,eff} = \frac{1}{\left\{\frac{(4.B_g.l_g)}{(B_{pk}.l_m)}\right\}+\left\{\frac{l_B}{(\mu_{\,rB}.B_{pk}.l_m)}\right\}+\left\{\frac{(B_H.l_H)}{(2.\mu_{\,rH}.B_{pk}.l_m)}\right\}+\left\{\frac{(B_S.l_S)}{(2.\mu_{\,rS}.B_{pk}.l_m)}\right\}} \tag{2.7}$$

where l_g is the mean magnetic path length in the air gaps $[m]$, l_B is the mean magnetic path length of the layer in bulk regions $[m]$ and is calculated using equation (2.8), l_H is the affected length adjacent due to the circular hole $[m]$, l_S is the affected length adjacent due to the slot hole $[m]$, $\mu_{\,rB}$ is the relative permeability of the bulk regions of the layer, $\mu_{\,rH}$ is the relative permeability of the regions with affected hole length l_H, $\mu_{\,rS}$ is the relative permeability of the regions with affected slot length l_S, B_g is the peak flux density in the air gaps $[T]$, B_H is the peak flux density in the affected hole length l_H regions $[T]$ and B_S is the peak flux density in the affected slot length l_S regions $[T]$.

$$l_B = l_m - \left(l_H + l_S + l_g\right) \quad [m] \tag{2.8}$$

For $'n'$ circular holes and $'m'$ slots, the effective permeability is given by

$$\mu_{\,eff} = \frac{1}{\left\{\frac{(4.B_g.l_g)}{(B_{pk}.l_m)}\right\}+\left\{\frac{l_B}{(\mu_{\,rB}.B_{pk}.l_m)}\right\}+\left\{\frac{(n.B_H.l_H)}{(2.\mu_{\,rH}.B_{pk}.l_m)}\right\}+\left\{\frac{(m.B_S.l_S)}{(2.\mu_{\,rS}.B_{pk}.l_m)}\right\}} \tag{2.9}$$

B_H, B_S, l_H, l_S, μ_{rH}, and μ_{rS} were obtained from an investigation involving finite element (FE) simulations discussed in **Chapter 4** and shown in **Appendix III (Section B)**. Four holes and four slots were chosen for the calculations as the single phase cores built for measurements had four holes and four slot holes.

For all the calculations of μ_{eff} of the packets, l_m = 2.24 m and l_g = 0.005 m. μ_{rB} is the relative permeability of the material. The values of B_g were calculated by using equation (2.9). The μ_{eff} values closer to the measured values of μ_{eff} formed the left hand side of the equation (2.9). The other parameters were not changed in the right hand side of the equation (2.9). The equation (2.9) was then solved for B_g. Thus the calculated values of B_g were fitted to obtain the best fit for the calculated values of μ_{eff}.

The μ_{eff} obtained from the measurements and analytical model for the HGO and CGO packets are shown in Fig. 2.15 and Fig. 2.16 respectively.

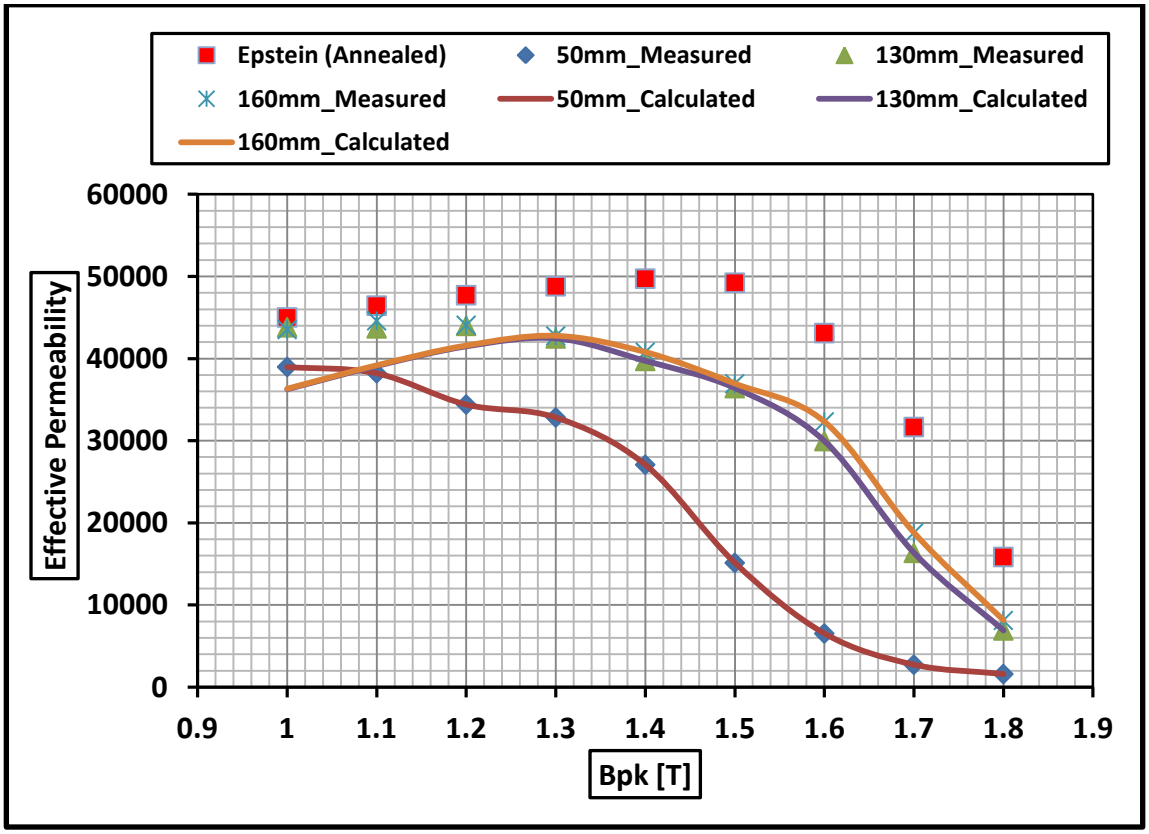

Fig. 2-15 Variation of μ_{eff} with B_{pk} for Single Phase HGO cores.

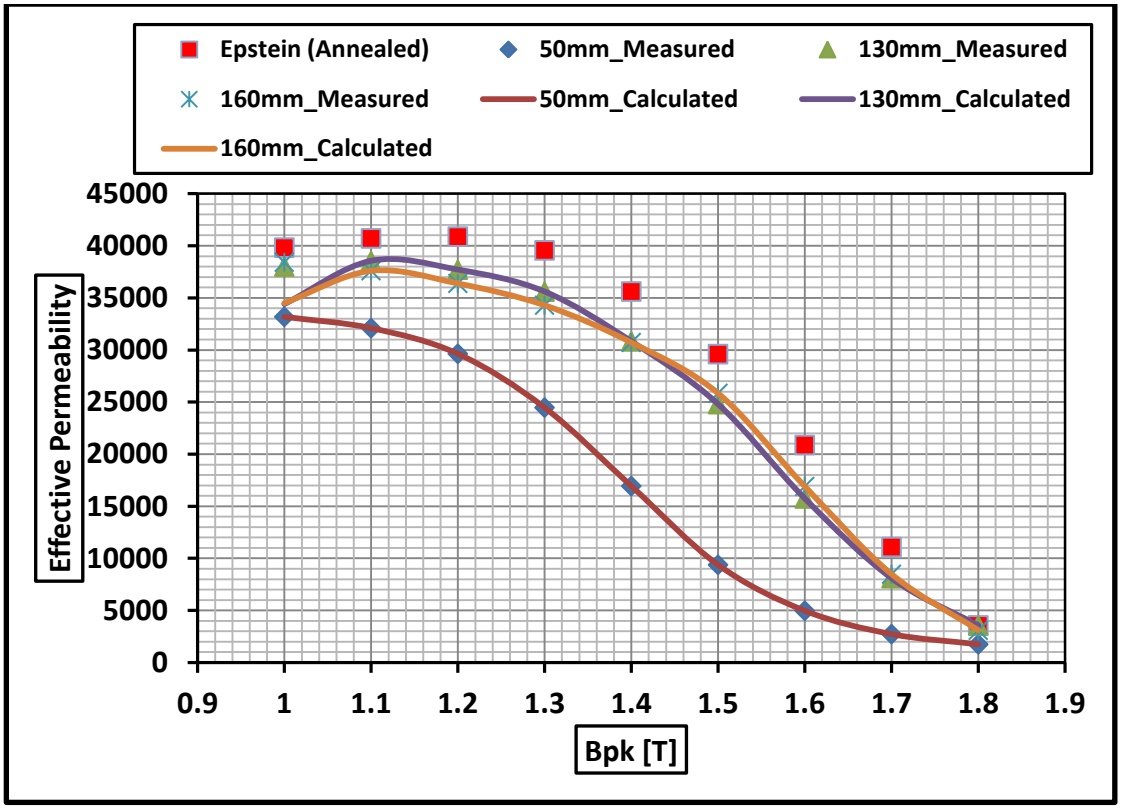

Fig. 2-16 Variation of μ_{eff} with B_{pk} for Single Phase CGO cores.

In the single phase tests, the H_{pk} required to magnetise the HGO 130 mm and HGO 160 mm packets to B_{pk}= 1.7 T was 83 A/m and 72 A/m respectively. But for the HGO 50 mm wide packet, the H_{pk} required was 79 A/m at 1.5 T and 494 A/m at B_{pk}= 1.7 T. Thus, the flux variation (Fig. 2-10) in the HGO 3-phase, 3-limb core can be explained by taking into account the H_{pk} of the packets.

If the H_{pk} in the HGO 3-phase, 3-limb core is in the range of 75 - 85 A/m, then the B_{pk} in the 160 mm wide packet will be approximately 1.72 T and approximately 1.7 T and 1.71 T in the two 130mm wide packets, whereas, the B_{pk} in the two 50 mm wide packets will be approximately 1.53T and 1.50 T. Similarly, the variation in peak flux density in the individual packets of the HGO 3-phase, 3-limb core at B_{pk}= 1.5 T, 1.3 T and 1.0 T is due to differences in H_{pk}.

The H_{pk} required to magnetise the individual packets of HGO depends on the effective permeability (μ_{eff}). The 50 mm wide packet has the lowest μ_{eff} (Fig. 2-11) because the bolt holes reduce the effective cross sectional area leading to

localised saturation of the core and increase in magnetic reluctance.

Similarly, the packet to packet variation of flux density for CGO core and cores built with combinations of HGO and CGO packets is due to the difference in μ_{eff} of the packets.

The 50 mm packet A was chosen as a reference for interpolations of B_{pk} from the H_{pk} curves. The interpolations were done in MATLAB software. This software was chosen because it allows large data sets to be processed with ease. To obtain the interpolations for HGO core at B_{pk} = 1.7 T, the data of the H_{pk} curves of HGO 50 mm, HGO 130 mm and HGO 160 mm packets were used as input. The other input to the MATLAB code was the measured H_{pk} value for HGO 50 mm (packet A) at B_{pk} = 1.7 T. The code executed the problem in two steps. First it plotted the H_{pk} curves ($H_{pk}\ vs\ B_{pk}$) of HGO 50 mm, HGO 130 mm and HGO 160 mm. In the second step the code found out the B_{pk} values for HGO 130 mm and HGO 160 mm in the plot (obtained in the first step) from the reference H_{pk} value of HGO 50 mm (packet A). Thus the interpolated values of B_{pk} in individual packets (50mm, 130mm & 160mm) of the HGO core magnetised at B_{pk} = 1.7 T were found out.

For CGO core, the data of the H_{pk} curves of CGO 50 mm, CGO 130 mm and CGO 160 mm packets were used. The measured H_{pk} value for HGO 50 mm (packet A) at B_{pk} = 1.7 T was the other input to the code.

For 50C+130H+160H core, the data of the H_{pk} curves of CGO 50 mm, HGO 130 mm and HGO 160 mm packets were used. The measured H_{pk} value for CGO 50 mm (packet A) at B_{pk} = 1.7 T was the other input to the code.

For 50C+130C+160H core, the data of the H_{pk} curves of CGO 50 mm, CGO 130 mm and HGO 160 mm packets were used. The measured H_{pk} value for CGO 50 mm (packet A) at B_{pk} = 1.7 T was the other input to the code.

For 50H+130H+160C core, the data of the H_{pk} curves of HGO 50 mm, HGO 130 mm and CGO 160 mm packets were used. The measured H_{pk} value for HGO 50 mm

(packet A) at B_{pk} = 1.7 T was the other input to the code.

For 50H+130C+160C core, the data of the H_{pk} curves of HGO 50 mm, CGO 130 mm and CGO 160 mm packets were used. The measured H_{pk} value for HGO 50 mm (packet A) at B_{pk} = 1.7 T was the other input to the code.

For interpolations at B_{pk} = 1.3 T and B_{pk} = 1.5 T, all the above procedures were repeated.

The measured and interpolated peak flux density variation (from single phase measurements) for all the cores is shown in Figures 2-15 to 2-20. The measured variation of B_{pk} is not symmetrical, maybe because of the errors arising from the construction of the cores.

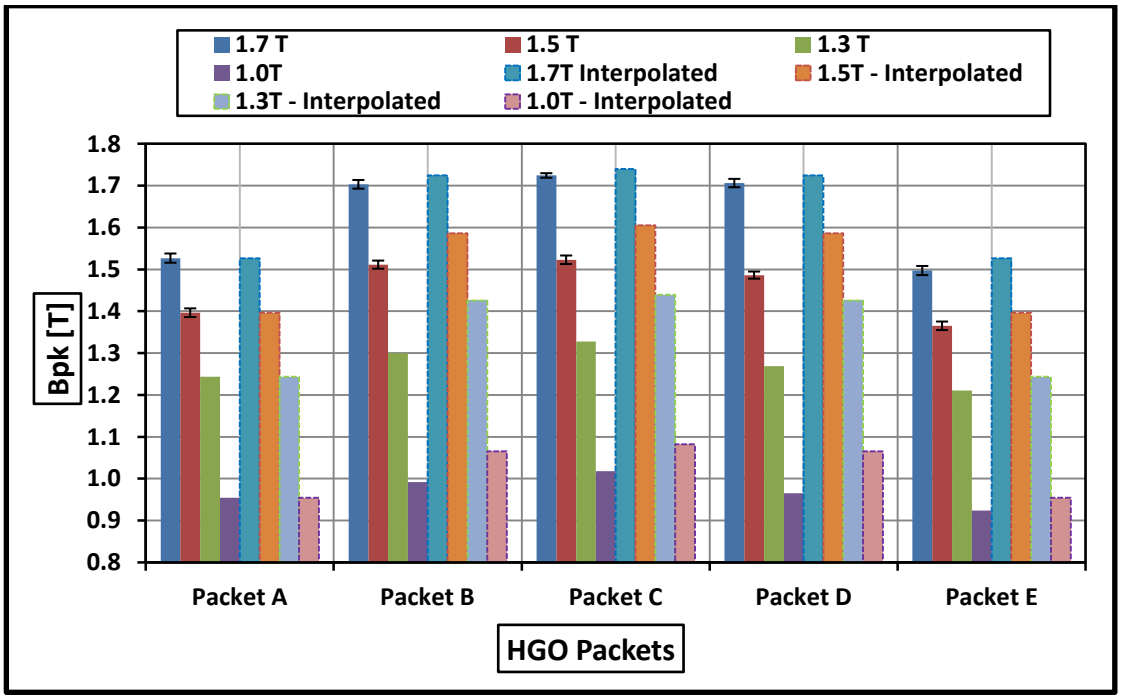

Fig. 2-15 Packet to packet variation of B_{pk} for HGO core at B_{pk} =1.0 T, 1.3 T, 1.5 T and 1.7 T.

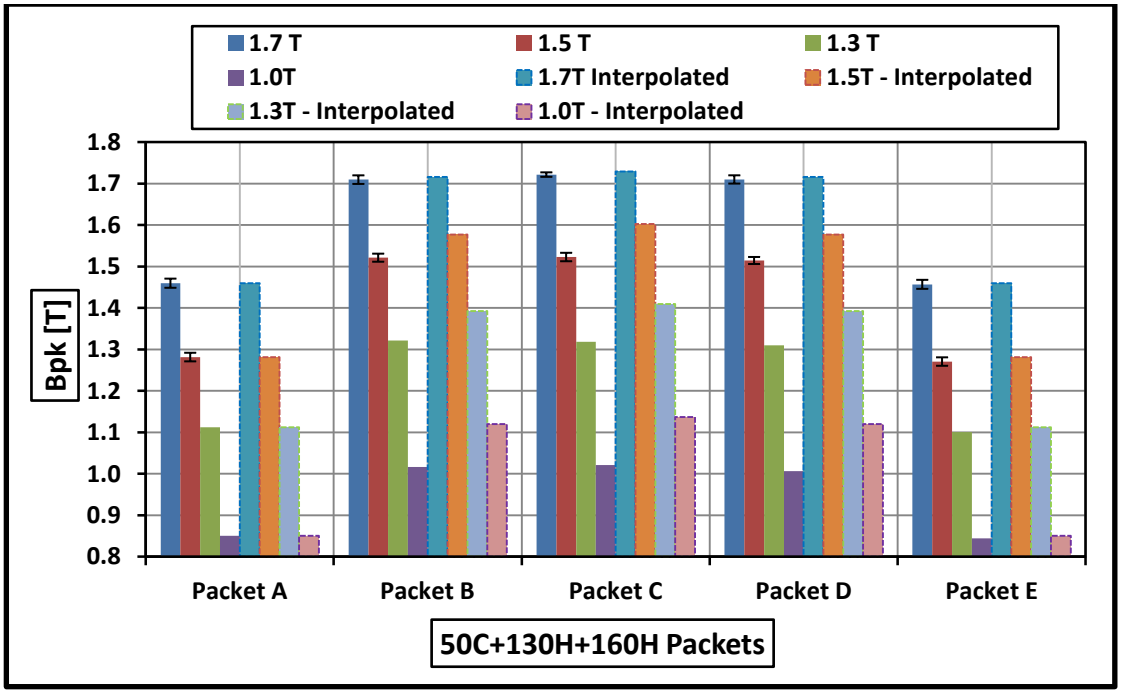

Fig. 2-16 Packet to packet variation of B_{pk} for 50C+130H+160H core at B_{pk} =1.0 T, 1.3 T, 1.5 T and 1.7 T.

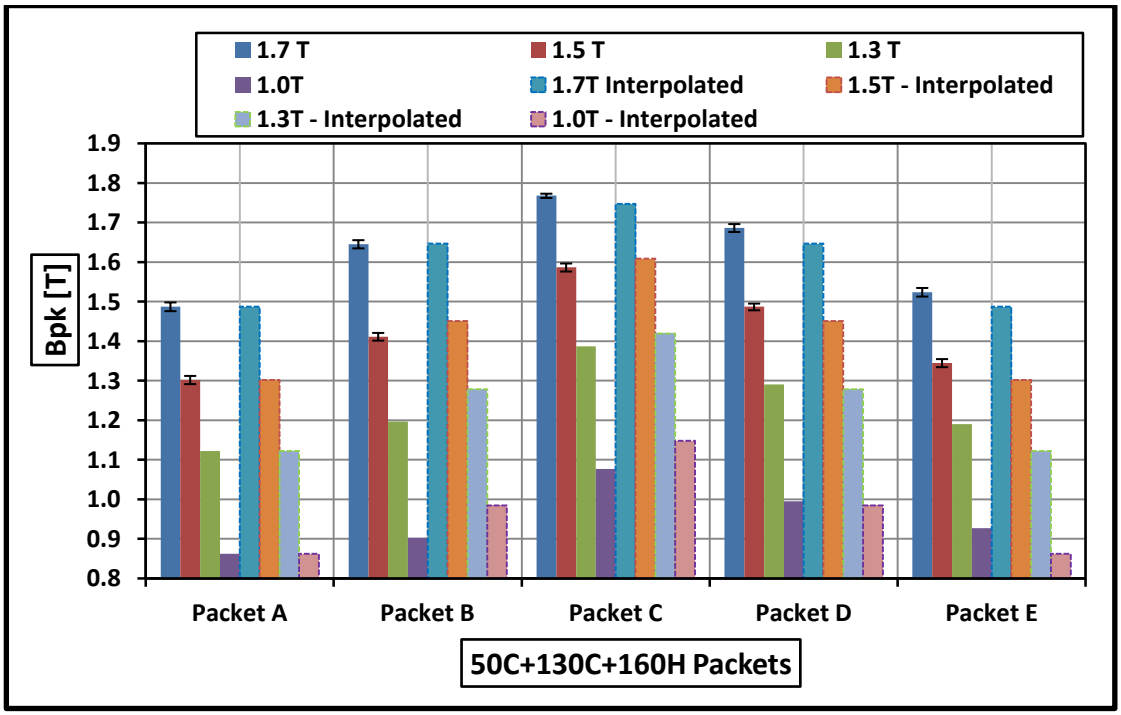

Fig. 2-17 Packet to packet variation of B_{pk} for 50C+130C+160H core at B_{pk} =1.0 T, 1.3 T, 1.5 T and 1.7 T.

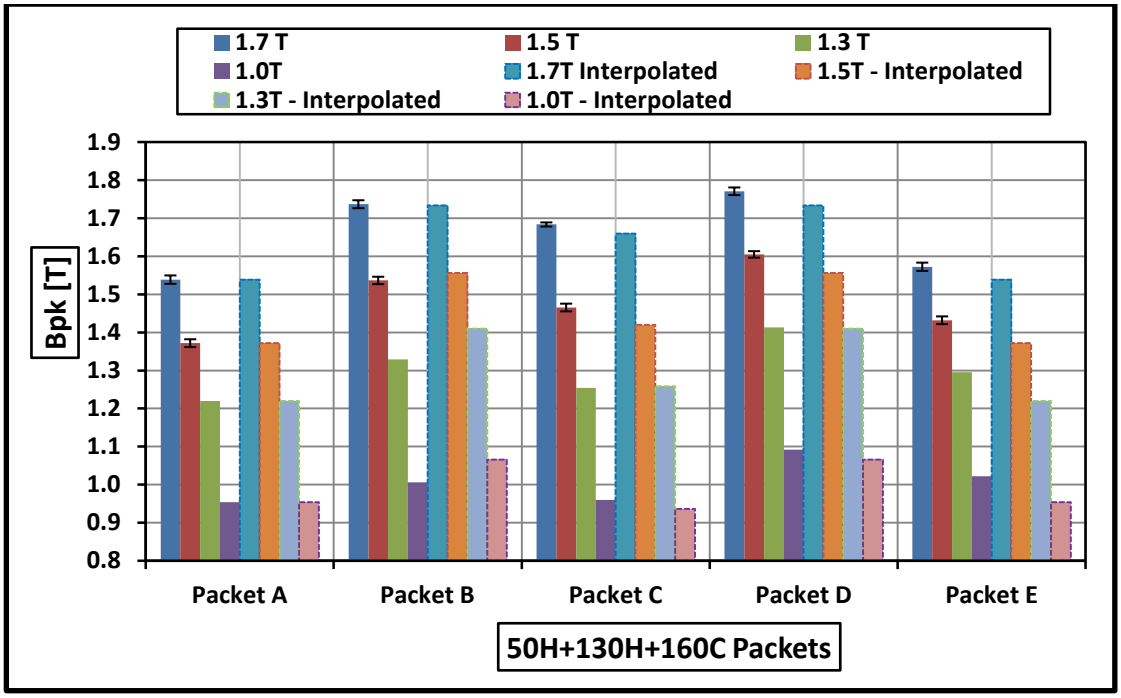

Fig. 2-18 Packet to packet variation of B_{pk} for 50H+130H+160C core at B_{pk} =1.0 T, 1.3 T, 1.5 T and 1.7 T.

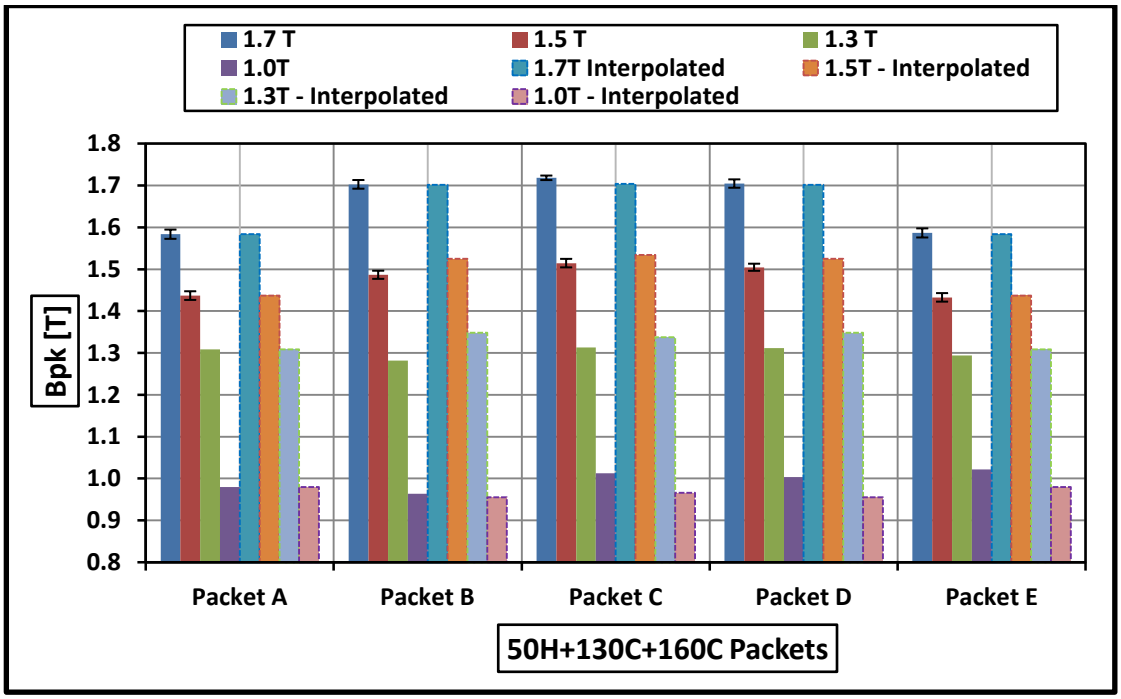

Fig. 2-19 Packet to packet variation of B_{pk} for 50H+130C+160C core at B_{pk} =1.0 T, 1.3 T, 1.5 T and 1.7 T.

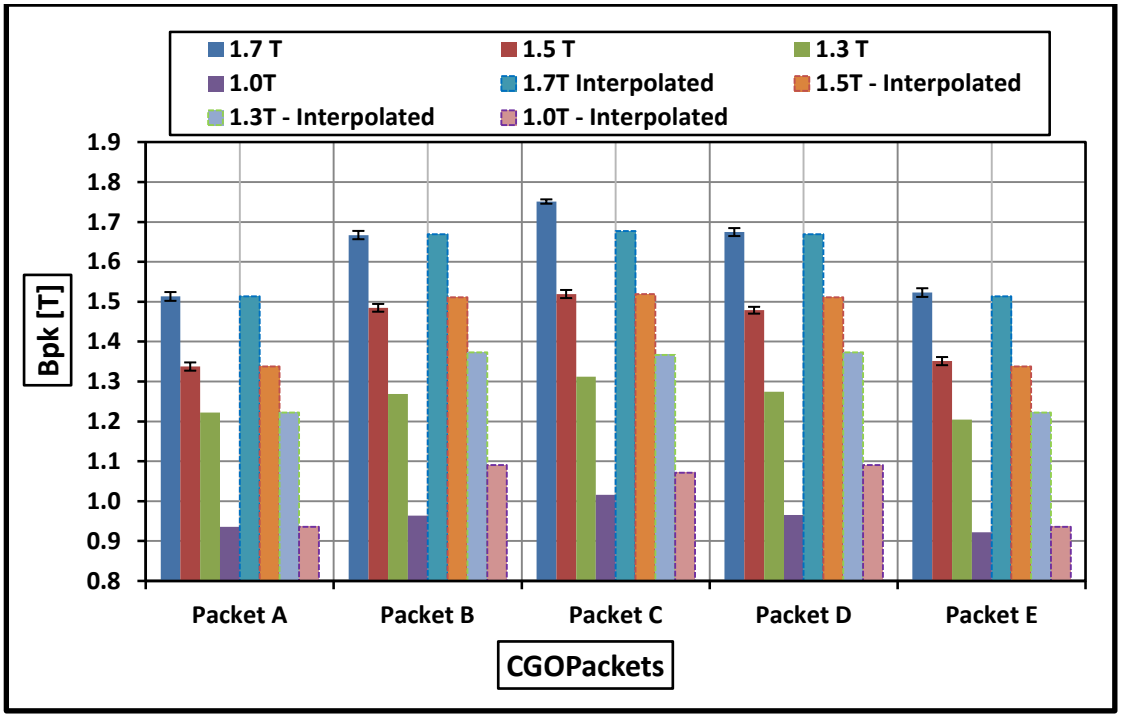

Fig. 2-20 Packet to packet variation of B_{pk} for CGO core at B_{pk} =1.0 T, 1.3 T, 1.5 T and 1.7 T.

The magnetic saturation in MSL joint regions can be explained by a parameter called as lower critical induction(B_c) [68]. In a MSL joint, for B_{pk} < B_c , the flux avoids the air gaps and traverses to the neighbouring laminations which act as a gap bridge (GB). At this stage, the core joint flux transfer operation is not critical. As B_{pk} increases, GBs become overloaded. For B_{pk} > B_c, the flux traverses through the air gaps, thus causing a sudden increase in the apparent power [68].

Another important parameter is the upper critical induction(B'_c). It is the induction at which the MSL core joint ceases to be advantageous to SSL joints and termed as inefficient. Both B_c and B'_c depend on step lap number(N_S) and form the induction window shown in Fig. 2-21.

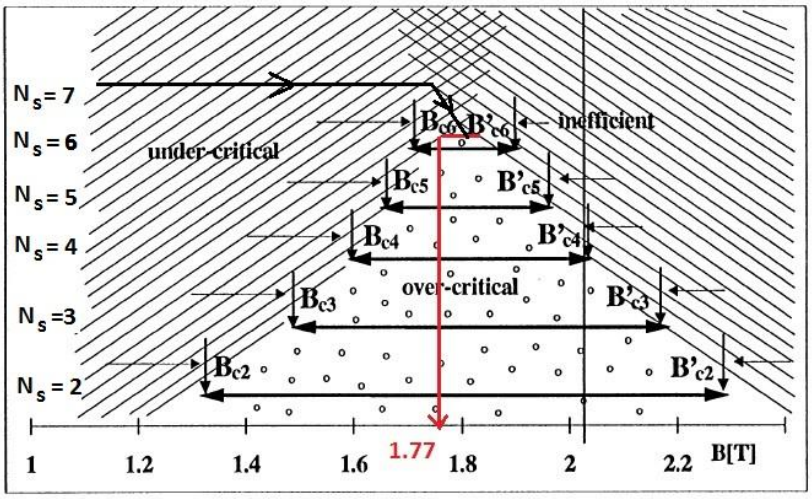

Fig. 2-21 The induction window for MSL joints [68].

The induction window gives information on the state of the MSL joints at different step lap numbers (N_S) for a known B_c (calculated by equation (2.10) [68]) and the operating B_{pk} of the transformer core. The MSL joint can operate in under-critical state, over-critical state and in in-efficient state. For transformer cores built with MSL joints, it is always desired that the joint region must operate in under-critical state. If the $B_{pk} < B_c$, then the transformer core is operating in a under-critical state because of MSL joints. If the $B_{pk} > B_c$, then the transformer core is operating in a over-critical state and the building factor of the transformer core will increase. This operating state is common for cores built with SSL joints. If the $B_{pk} > B'_c$, then the core joint becomes inefficient.

For the current investigation, the B_c for the HGO, CGO and mixed cores depends on N_S used in the joint. Seven step laps were used for this investigation. So the B_c was calculated to be equal to 1.77 T using equation (2.10). This equation was used because B_c is a function of N_S and the saturation flux density (B_{sat}).

$$B_c = \left(\frac{N_S}{N_S+1}\right) . B_{sat} \quad [T] \tag{2.10}$$

where, N_S is the step lap number, B_{sat} is the saturation flux density =2.03 T [8].

From Fig. 2-21, the induction window length ($B'_c - B_c$) decreases with N_S. The B_c for all the packets of the cores was approximately equal to 1.77 T. So the cores have a very small induction window length($B'_c - B_c$). Any increase in induction above B_c

will render the core joints to be at the boundary of the over critical region and inefficient region. Increase in induction above B_c and equal to B'_c will make the MSL joint inefficient causing magnetic flux in the core to traverse a path, which has the highest μ_{eff}. In this investigation, the increase in induction in the MSL joints above B_c and equal to B'_c is caused by the bolt hole diameter (or slot width) and lamination width ratio which reduces the effective cross section of the packet.

In homogeneous cores (HGO and CGO), the centre packet which was 160 mm wide, had the highest μ_{eff}, followed by the 130 mm packets and 50 mm wide packets had the least μ_{eff}. This results in the flux density to be the highest in the 160 mm wide packet, followed by the 130 mm wide packet and lowest in the 50 mm wide packet. This phenomenon is dependent the bolt hole diameter (or slot width) and lamination width ratio which was 0.2 for 50 mm packet, 0.0769 for 130 mm packet, and 0.0625 for 160 mm packet. The lower the ratio in the packets, the higher will be the μ_{eff}.

In the case of mixed cores, the individual packets in the cores are magnetised based on the μ_{eff} and the material type. For example, in the 50H+130H+160C core, the maximum peak flux density is highest in the 130 mm wide packets which are built with HGO laminations rather than the 160 mm packet which is built with CGO laminations. This is because the 130 mm packet built with HGO had higher μ_{eff} than that of the 160 mm wide CGO packet. The 50mm wide packet had the least peak flux density as its μ_{eff} was the least.

Thus, the presence of one hole and one slot in each limb and each yoke in the investigated stacked multi packet 3-phase, 3-limb core design caused global flux density variations. Therefore packet to packet variation of flux density must be considered while designing a transformer core.

2.5 Summary

The packet to packet variation of peak flux density of stacked multi-packet, 3-phase, 3-limb transformer cores built with MSL joints was investigated. The cores were built with HGO, CGO and a mix of both HGO and CGO. HGO and CGO single phase cores were built using the side limb laminations of the 3-phase, 3-limb HGO and CGO cores to obtain the effective permeability of individual packet widths. An analytical model was built considering the reluctances of the holes, slots and the corner joints to explain the variation of flux density in the 3-phase, 3-limb HGO, CGO and mixed cores. It was found that the high bolt hole diameter (or slot width) and lamination width ratio of 0.2 is responsible for the packet to packet variation of flux density in stacked multi-packet, 3-phase, 3-limb transformer cores built with MSL joints.

Chapter 3

Specific Loss and Specific Apparent Power of Three-Phase Cores, Single-Phase Cores and Epstein Sized Cores

3.1 Introduction

In this chapter, the measurement results of the no-load specific loss and specific apparent power of multi-packet 3-phase, 3-limb cores (HGO, CGO & mixed), single packet 3-phase, 3-limb cores (3 HGO and 3 CGO) and single packet two limb, single phase cores (3 HGO and 3 CGO) are presented. The specific loss and specific apparent power of single phase Epstein size mixed cores is also presented. The effect of mixing HGO and CGO on specific power loss and apparent power in multi-packet 3-phase, 3-limb and single phase Epstein sized cores is examined. The combined measurement uncertainty budget (illustration of measurement uncertainty analysis) for measured loss and apparent power is presented in **Appendix VII.**

3.2 Three-Phase, Three-Limb Cores

3.2.1 Three-Phase, Three-Limb Transformer Cores

The no load losses and apparent power of the HGO, CGO, and mixed cores (described in **Chapter 2**) were measured using the three wattmeter method. The no-load loss and apparent power was measured using a Norma D6000 wide band power analyzer. The magnetising circuit is shown in **Chapter 2**. The corrected core loss was obtained from the measured core loss according to [67] using equation (3.1),

$$P = P_m \left(1 + \left[\frac{U' - V_{rms}}{U'}\right]\right) \quad [W] \tag{3.1}$$

where P_m is the measured core loss $[W]$, U' is average secondary voltage scaled to *rms* voltage ($V_s * 1.1107$) $[V]$ and V_{rms} is the secondary *rms* voltage $[V]$.

The corrected specific loss, of each core was then calculated by dividing the corrected no load loss by its mass, over the peak flux density range. The specific apparent power of each core was calculated by dividing the measured apparent power by the core mass over the peak flux density range.

3.2.2 Three Phase, Three Limb Individual packet Transformer Cores

The full sized HGO and CGO cores were disassembled after 3-phase measurements and 6 smaller and rectangular section 3-phase cores were assembled from individual packets, each corresponding to a particular layer type and grade of the initial transformer. Their dimensions are given in table 3-1 and depicted in Fig. 3-1, Fig. 3-2 & Fig.3-3. Three phase measurements similar to that for full cores were conducted over a flux density range of 0.8 T to 1.8 T in steps of 0.1 T and the no-load loss and apparent power were recorded. The specific loss and specific apparent power were calculated in a similar way as that of the multi-packet cores mentioned in **section 3.2.1.**

Table 3-1 Dimensions and Mass of Individual 3-Phase, 3-Limb, Single Packet Cores

Material	Yoke and Limb Width (mm.)	Packet Thickness (mm.)	Weight (kg.)
HGO	50	27	29.1
	130	27	74.1
	160	54	180.7
CGO	50	27	28.8
	130	27	73.2
	160	54	178.1

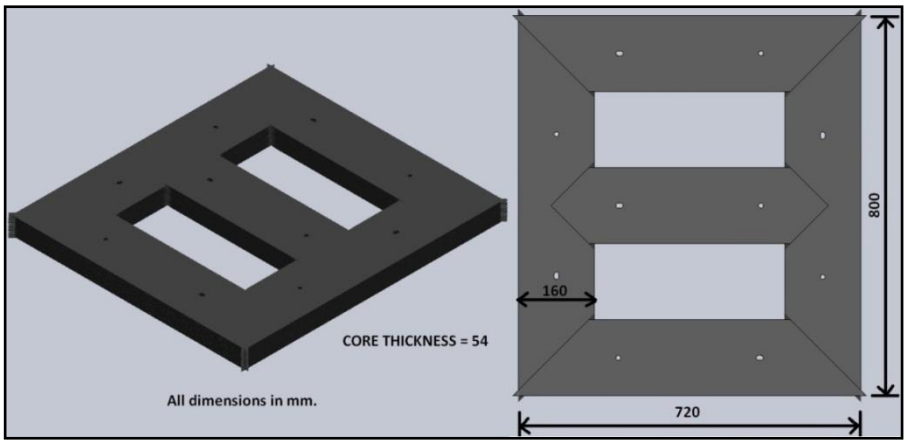

Fig. 3-1 Three phase core built with a single 160mm wide packet.

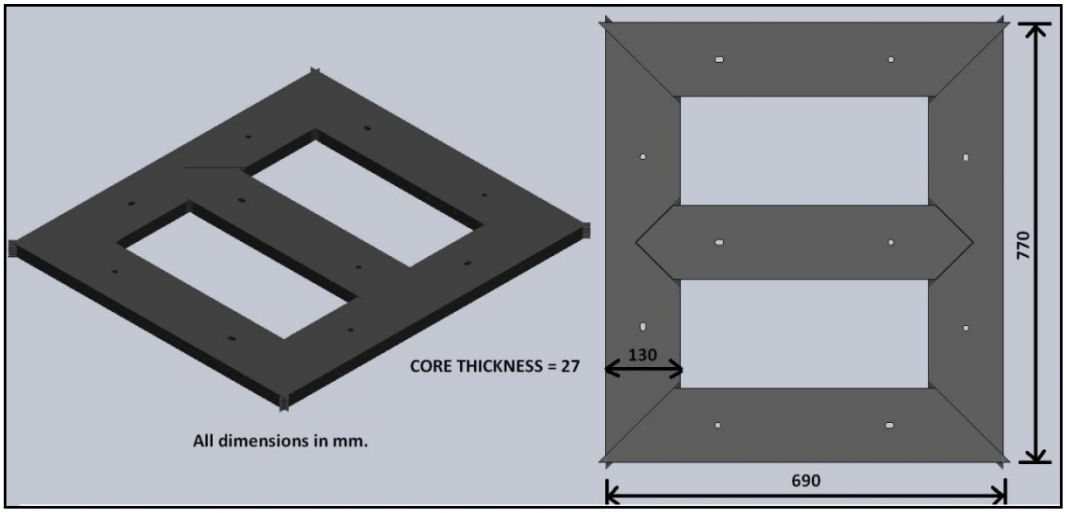

Fig.3-2 Three phase core built with a single 130mm wide packet.

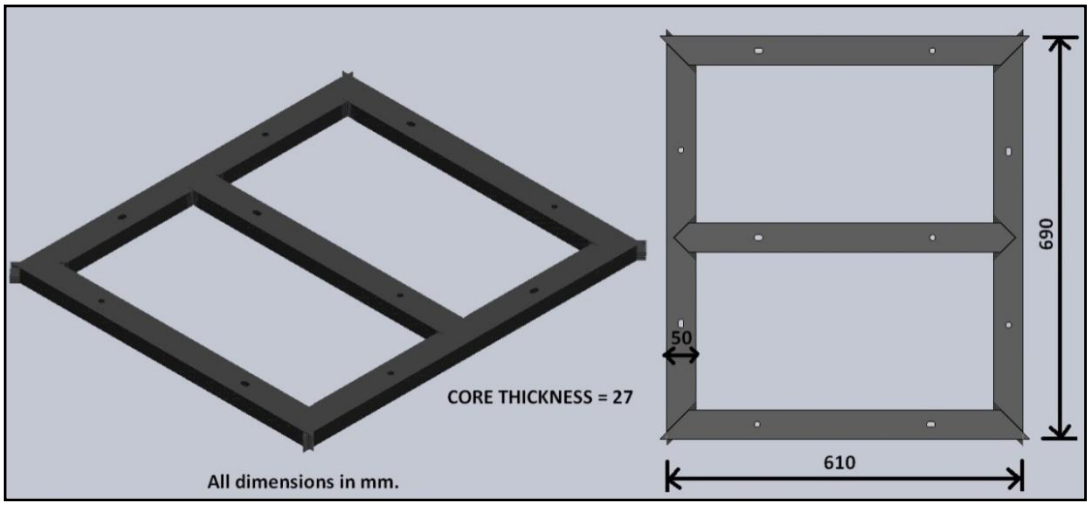

Fig. 3-3 Three phase core built with a single 50mm wide packet.

3.3 Single Phase, Two Limb Transformer Cores

The no load losses and apparent power of the HGO and CGO single phase cores (described in **Chapter 2**) were measured. The cores were magnetised using a single variac. The no-load loss and apparent power were measured using a Norma D6000 wide band power analyzer. The magnetizing circuit is shown in **Chapter 2**.
The specific loss and specific apparent power of each core were calculated in a similar manner as described for the 3-phase, 3-limb cores.

3.4 Single Phase, Epstein Size Cores

3.4.1 Epstein Frame Measurement System

The losses and apparent power of as-cut and annealed stacks of 24 Epstein strips (30 mm x 290 mm), cut from the same batches of steel used to construct the HGO & CGO cores, were measured at 50 Hz sinusoidal excitation, over a flux density range from 0.1 T to 1.8 T in a computerised Epstein square[16].

A schematic diagram of the system is shown in Fig.3-4. It consists of a computer pre-installed with LabVIEW version 8.5 software from National Instruments, a NI PCI-6120 data acquisition (DAQ) card [69], a power amplifier, a 1 Ω shunt resistor (R_s), and an Epstein square. The components of the measurement system are shown in Fig-3.5. LabVIEW was used because it is a specialised data acquisition software which uses mathematical analysis in real time to process the measurement data and displays the desired output in real time. It also allows the user to save the data.

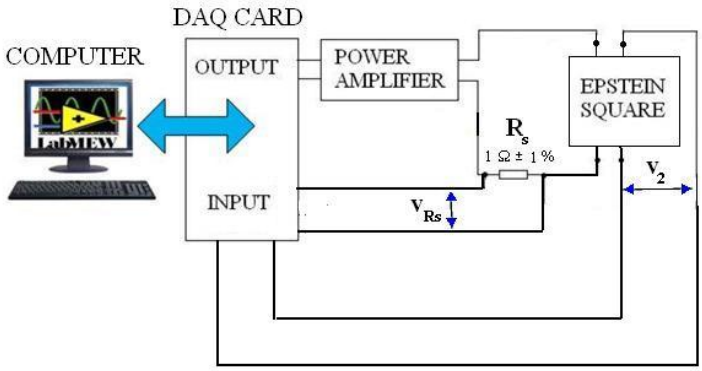

Fig. 3-4 Schematic diagram of the computer-controlled Epstein measurement system.

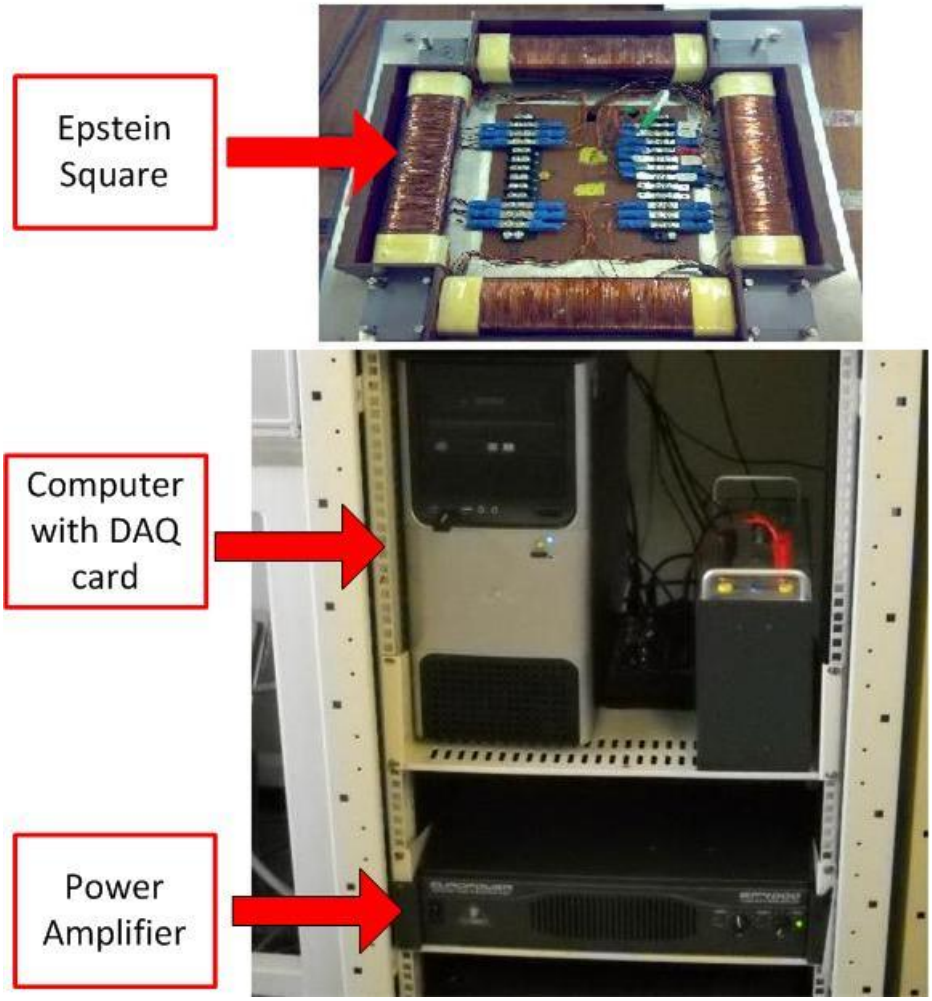

Fig. 3-5 Components of the Epstein measurement system [68].

The magnetising voltage was generated by the LabVIEW program via a voltage output of the DAQ card. The instantaneous voltage across the shunt resistor (v_{Rs}), and the instantaneous secondary voltage (v_2) were measured for calculation of magnetic field and flux density respectively. The instantaneous magnetic field (h) was calculated by the LabVIEW program from equation (3.2),

$$h = \frac{N_1.v_{Rs}}{l_m.R_s} \quad \left[\frac{A}{m}\right] \tag{3.2}$$

where l_m is the mean path length (0.94 m) and N_1 is the number of primary winding turns in the Epstein square (700).

The instantaneous flux density (b) was calculated by LabVIEW program from equation (3.3),

$$b = \frac{1}{N_2.A} . \int v_2 . dt \quad [T] \tag{3.3}$$

where N_2 is the number of secondary winding turns in the Epstein square (700) and A is the area of cross section of the specimen.

The cross section of area (A) used in equation (3.3), was calculated from equation (3.4)

$$A = \frac{m}{4.\rho_m.l} \quad [m^2] \tag{3.4}$$

where m is the mass of the specimen in kg and ρ_m is the density of the specimen (7650 kg/m^3) [15].

The specific power loss (P_s) was calculated from equation (3.5),

$$P_s = \frac{1}{T.\rho_m} . \int_0^T h . \frac{\mathrm{db}}{\mathrm{dt}} . dt \quad \left[\frac{W}{kg}\right] \tag{3.5}$$

where T is the magnetising cycle time period.

The specific apparent power (S) was calculated from equation (3.6),

$$S = \frac{V_{rms}.I_{rms}}{m_a} . \frac{\mathrm{N_1}}{\mathrm{N_2}} \quad \left[\frac{VA}{kg}\right] \tag{3.6}$$

where V_{rms} is the *rms* value of the secondary voltage, I_{rms} is the *rms* value of the primary current and m_a is the active mass in kg.

The active mass (m_a) was calculated from equation (3.7),

$$m_a = \frac{m.l_m}{4.l} \quad [kg] \tag{3.7}$$

3.4.2 Mixed Epstein Combinations

Strips of the HGO and CGO materials (30mm x 290 mm) were magnetised in various combinations in the Epstein square. No holes were punched in the strips. These assemblies are referred to here as “mixed cores”. Mixed cores assembled from annealed laminations were tested in three trials, in two combinations. In Combination 1, HGO strips were placed in the lower part of each arm of the square below CGO strips. In Combination 2, HGO and CGO strips were stacked alternatively in each of the four limbs. The percentage (volume) of each material in each stack is shown in table 3.2. The percentage mix chosen was closer to the percentage mix in the full size three phase mixed cores. The position of the arranged strips in the 46% CGO and 54 % HGO core using Combination 1 and Combination 2 assemblies are shown in Fig. 3-6 and Fig.3-7 respectively. The position of the arranged strips in all other cores is shown in **Appendix IV**.

Table 3-2 Material Combinations Measured in the Epstein Frame

Combination	% CGO	% HGO
1	0	100
	17	83
	46	54
	54	46
	83	17
	100	0
2	0	100
	17	83
	46	54
	54	46
	83	17
	100	0

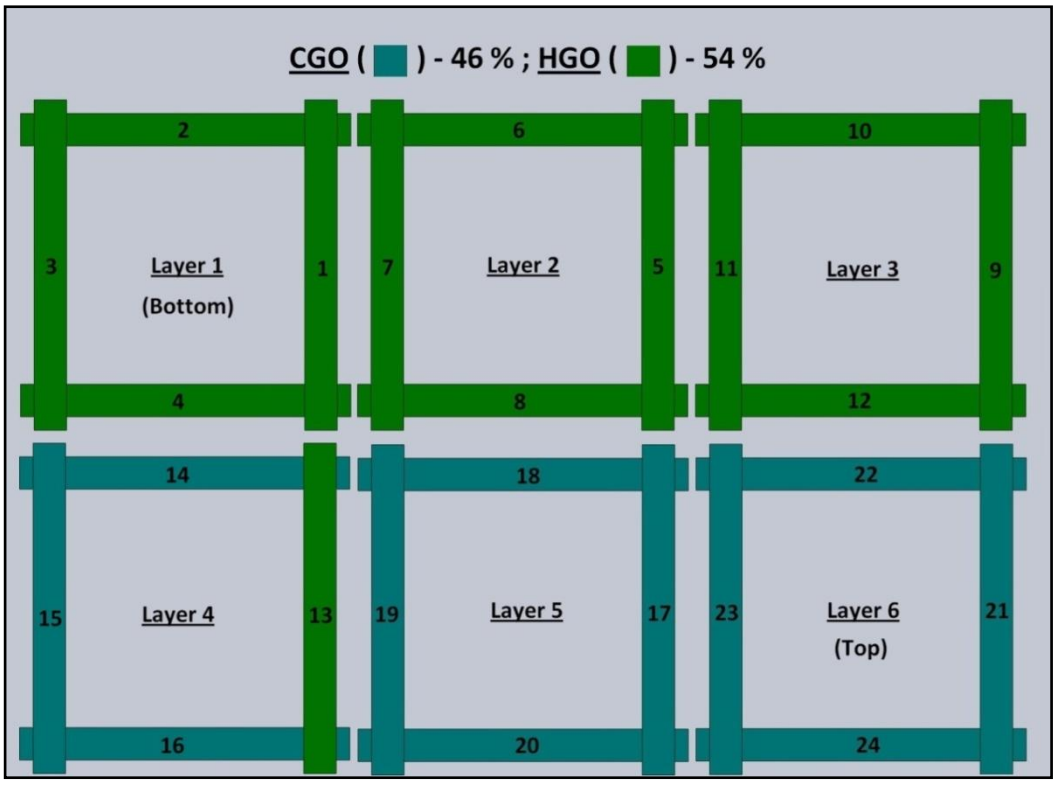

Fig. 3-6 Position of laminations in the 6 layers of strips in Combination 1 (CGO-46%, HGO -54%).

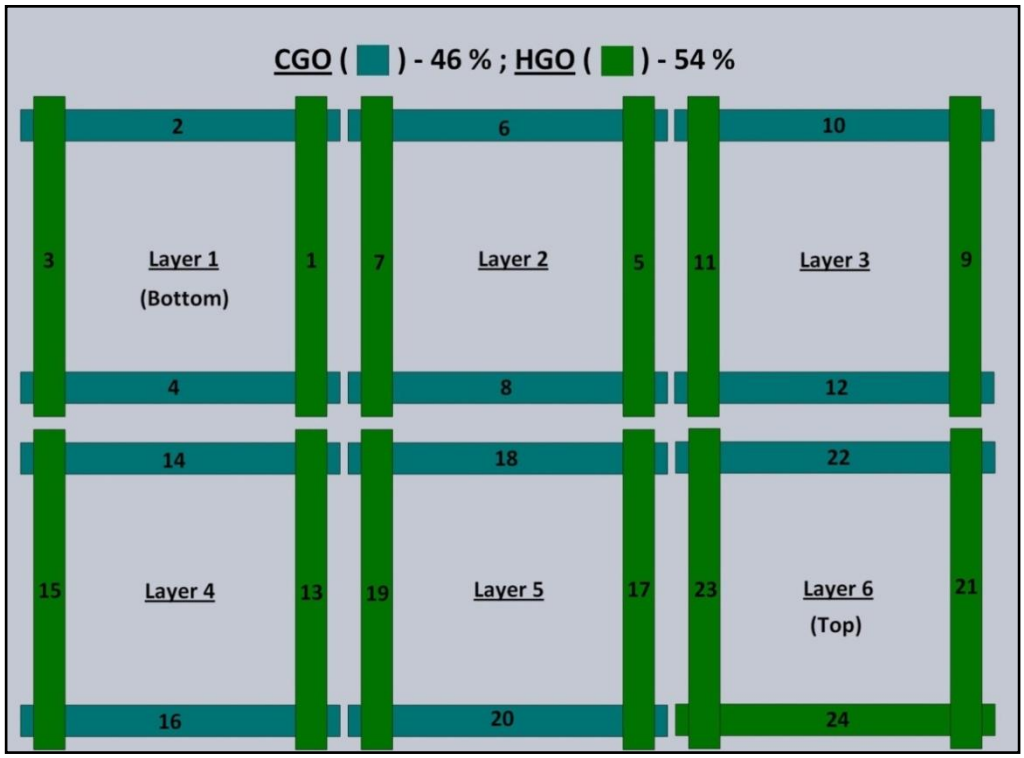

Fig. 3-7 Position of laminations in the 6 layers of strips in Combination 2 (CGO-46%, HGO -54%).

3.5 Results

3.5.1 Specific Loss of Three-Phase, Three-Limb Cores

The variation of specific loss with peak flux density for the full sized cores is shown in Fig. 3-8. The variation of specific loss with peak flux density for single packet HGO and CGO cores is shown in Fig. 3-9 and Fig. 3-10 respectively. The error bars indicate the declared uncertainty values estimated by the uncertainty budgets [70]. The measured values lie within the upper and lower limits of the error bars. The practical application of uncertainty analysis lies in characterising errors for any experimental results. The uncertainty budgets of specific loss for all full sized cores and single phase cores are shown in **Appendix VII**.

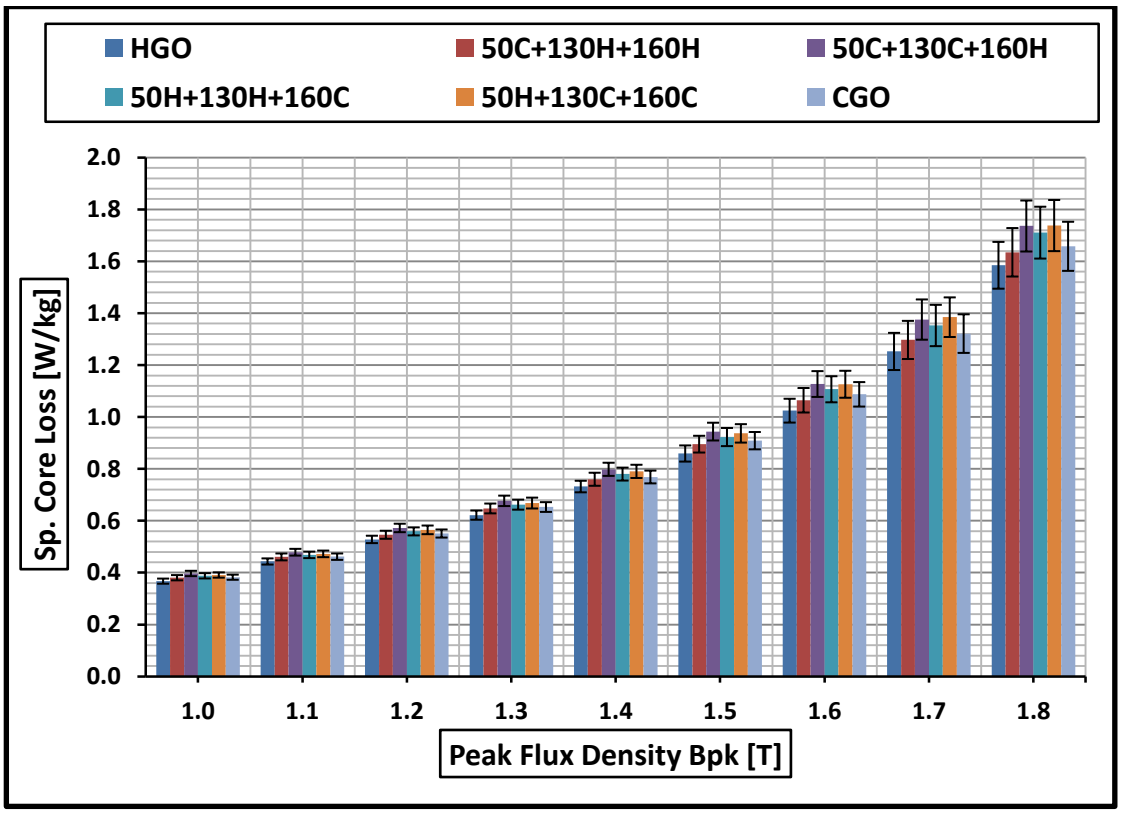

Fig. 3-8 Variation of Specific Loss with Flux Density for Three Phase Three Limb cores for a flux density range of 1.0 T to 1.8 T.

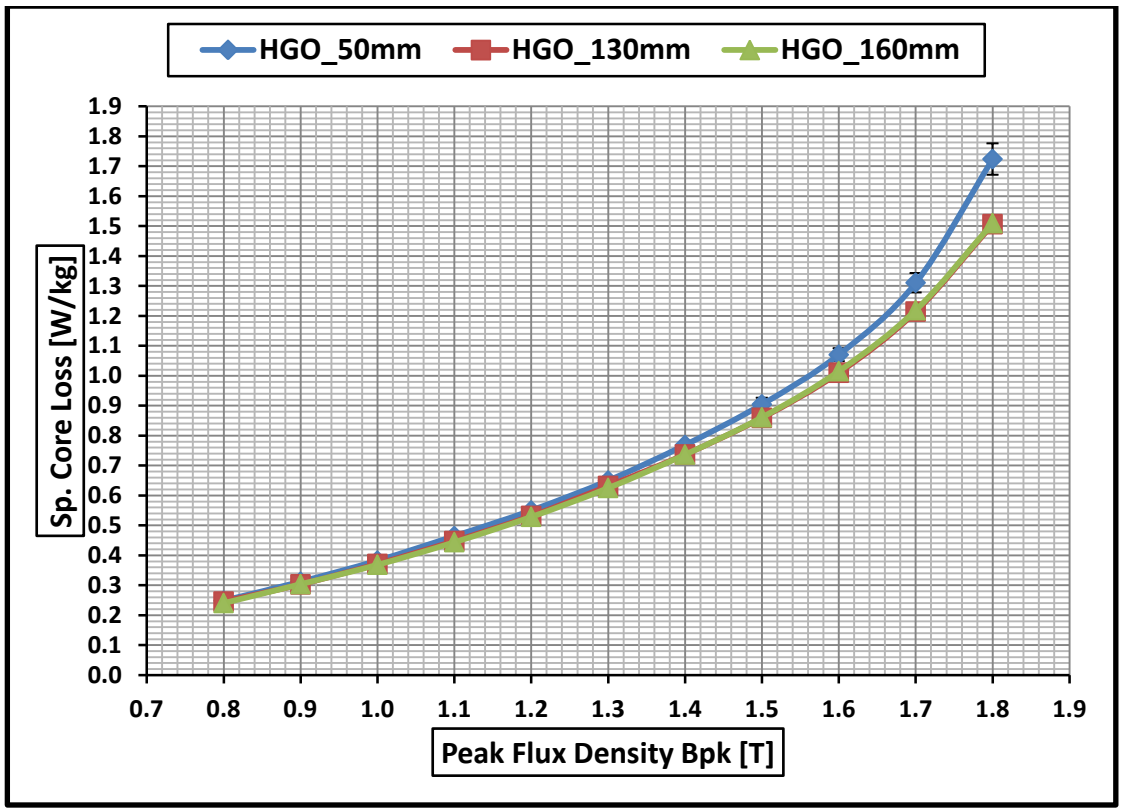

Fig. 3-9 Variation of Specific Loss with Flux Density for HGO Individual Three-Phase, Three-Limb Cores for a flux density range of 0.8 T to 1.8 T.

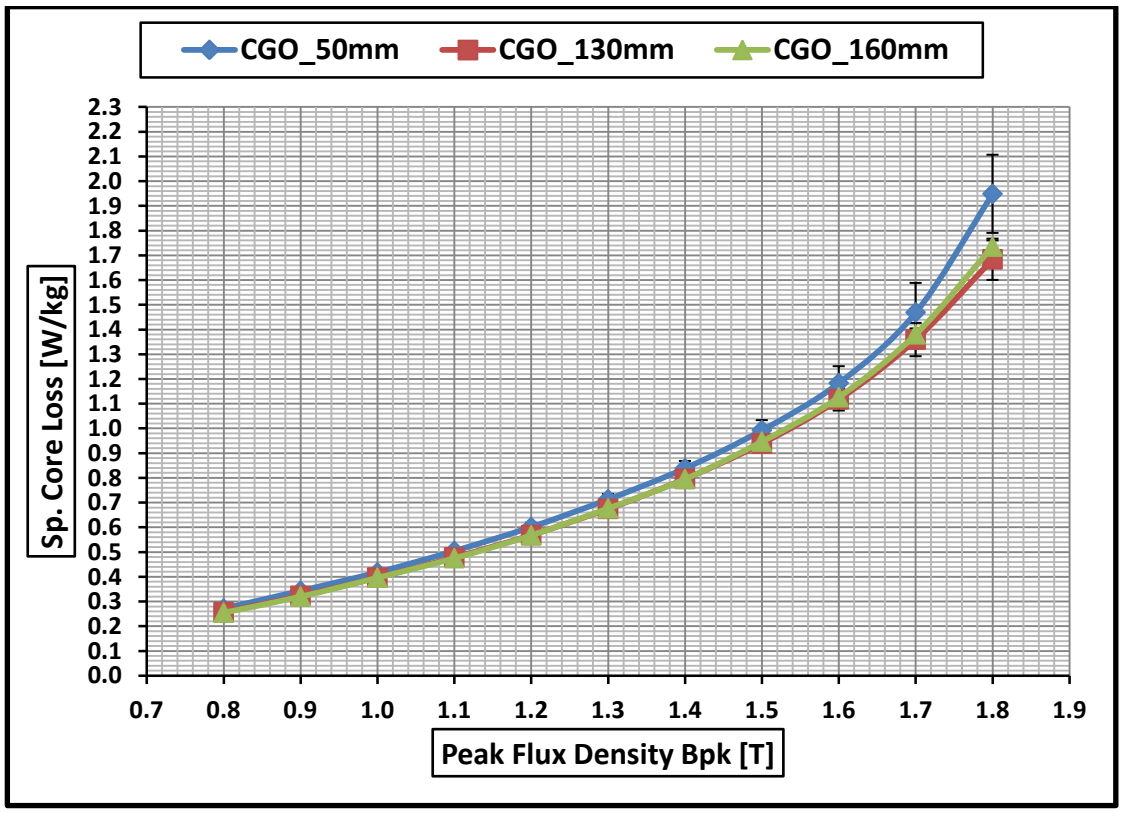

Fig. 3-10 Variation of Specific Loss with Flux Density for CGO Individual Three-Phase, Three-Limb Cores for a flux density range of 0.8 T to 1.8 T.

3.5.2 Specific Apparent Power of Three-Phase, Three-Limb Cores

The variation of specific apparent power with peak flux density for the HGO and CGO cores is shown in Fig. 3-11. The variation of specific apparent power with peak flux density for single packet HGO and CGO cores is shown in Fig. 3-12 and Fig. 3-13 respectively. The high error bars at B_{pk}= 1.8 T are because high values of sensitivity co-efficient of the measurements [70].

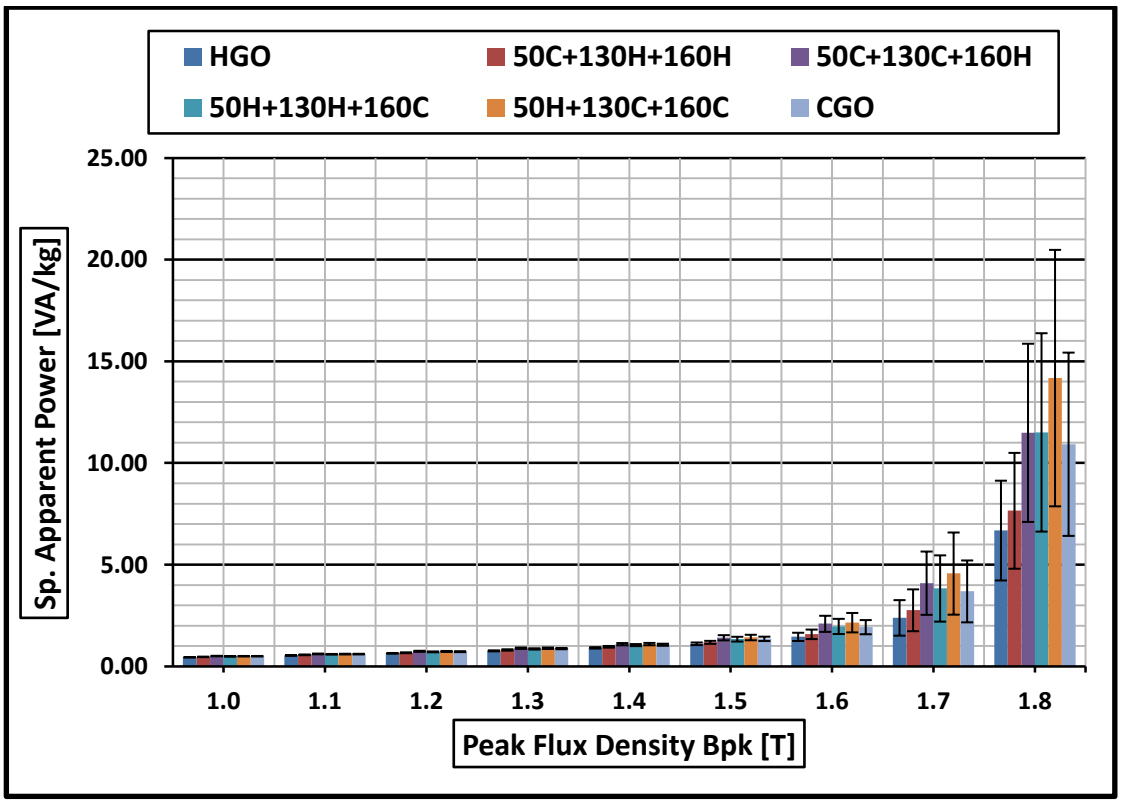

Fig.3-11 Variation of Specific Apparent Power with Flux Density for Three Phase Three Limb cores for a flux density range of 1.0 T to 1.8 T.

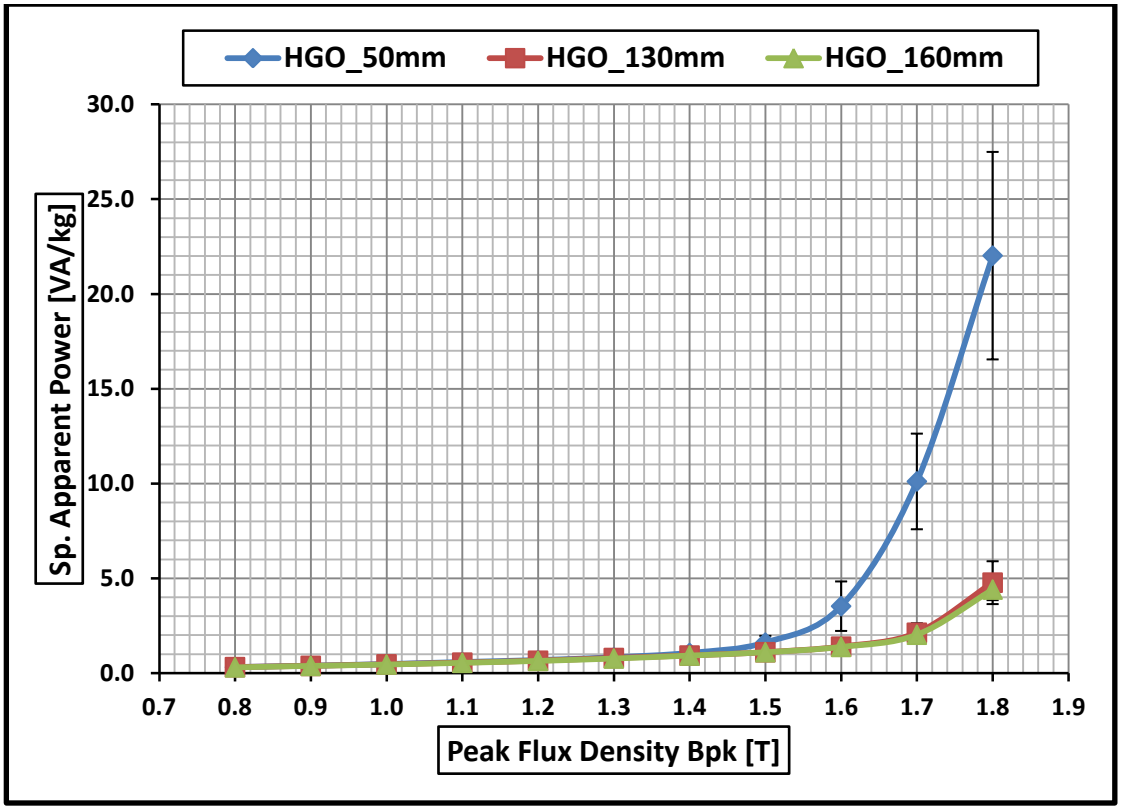

Fig. 3-12 Variation of specific apparent power with flux density for HGO individual three-phase, three-limb cores for a flux density range of 0.8 T to 1.8 T.

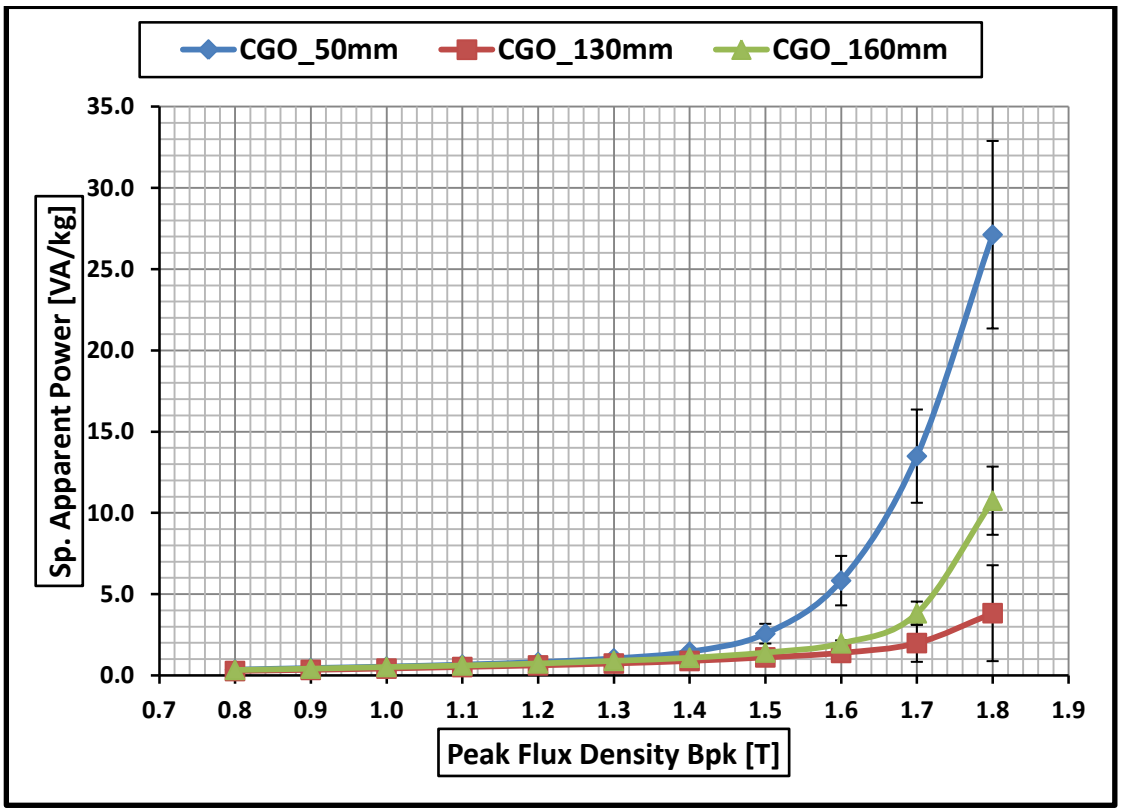

Fig. 3-13 Variation of specific apparent power with flux density for CGO individual three-phase, three-limb cores for a flux density range of 0.8 T to 1.8 T.

3.6 Single Phase, Two Limb Transformer Cores

3.6.1 Specific Power Losses and Apparent Power

The specific core loss for HGO single phase cores is as shown in Fig. 3-14. The specific core loss for CGO single phase cores is shown in Fig. 3-15.

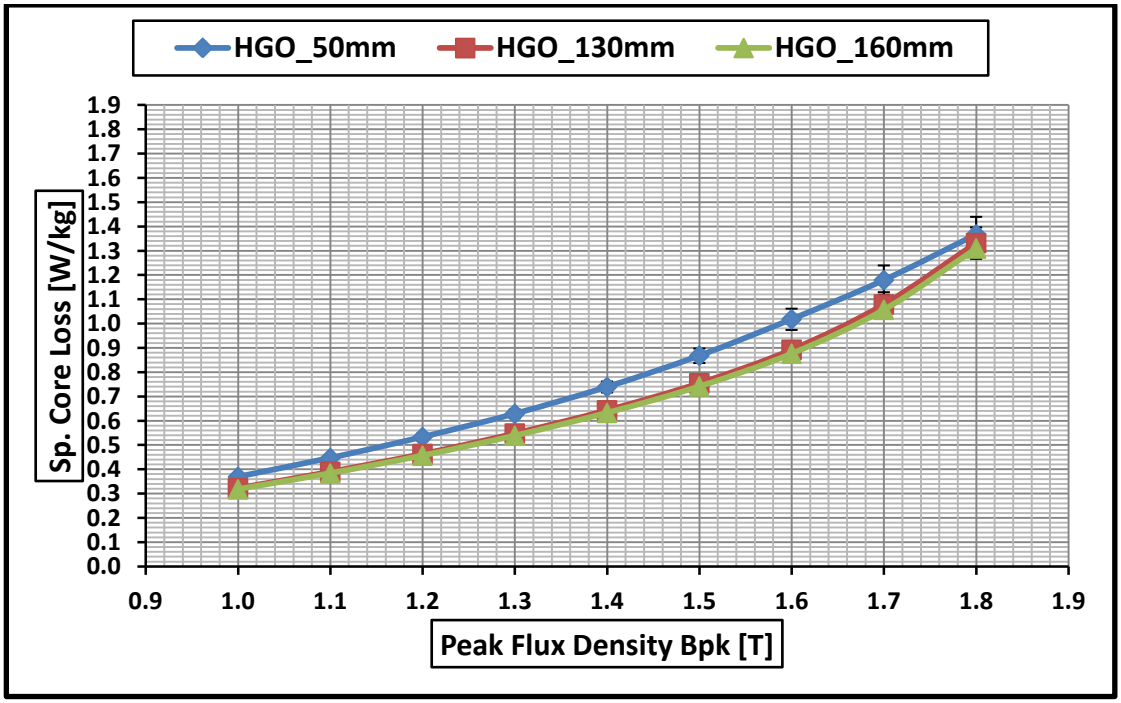

Fig. 3-14 Variation of specific power loss with flux density for single phase HGO cores.

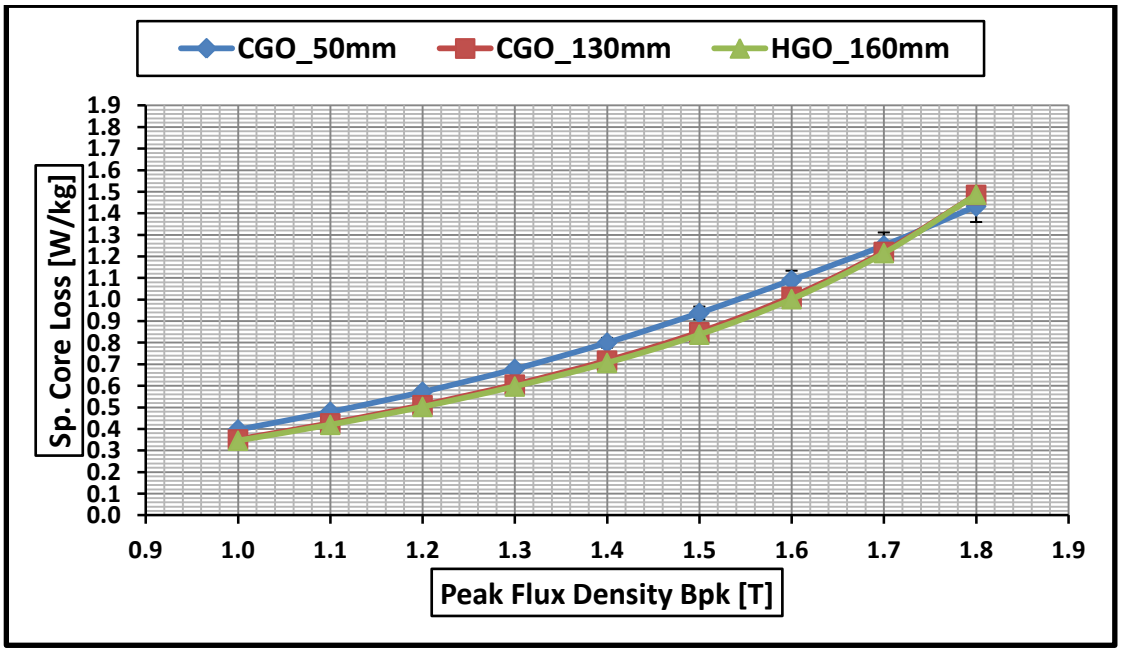

Fig. 3-15 Variation of specific power loss with flux density for single phase CGO cores.

The specific apparent power of the HGO single phase cores is as shown in Fig. 3-16.

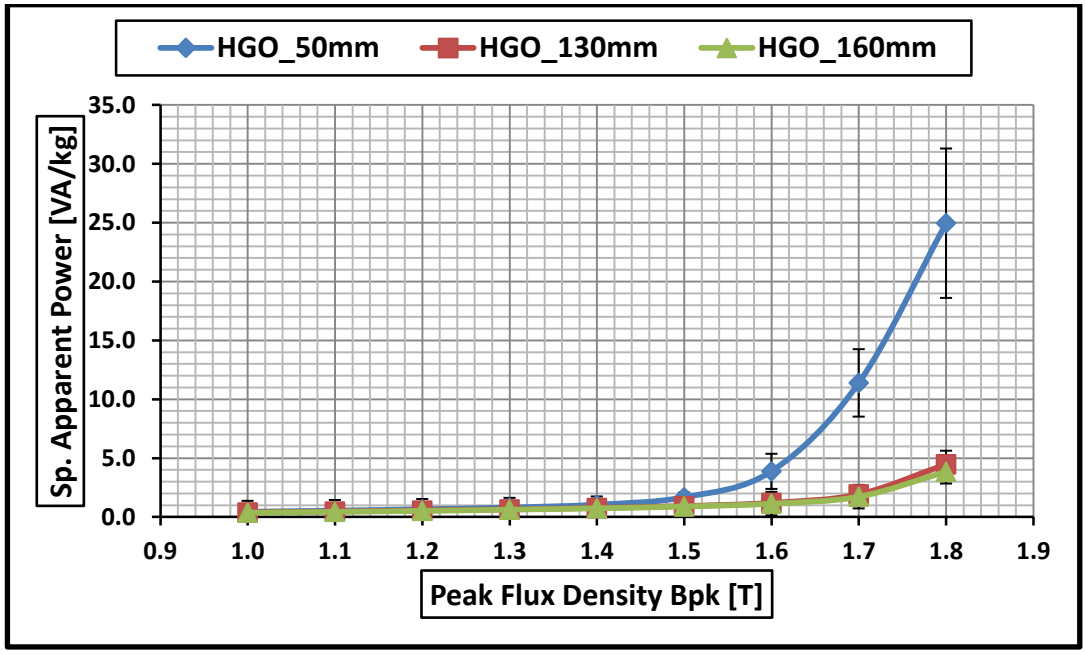

Fig. 3-16 Variation of specific apparent power with flux density for single phase HGO cores.

The specific apparent power of the CGO single phase cores is as shown in Fig. 3-17.

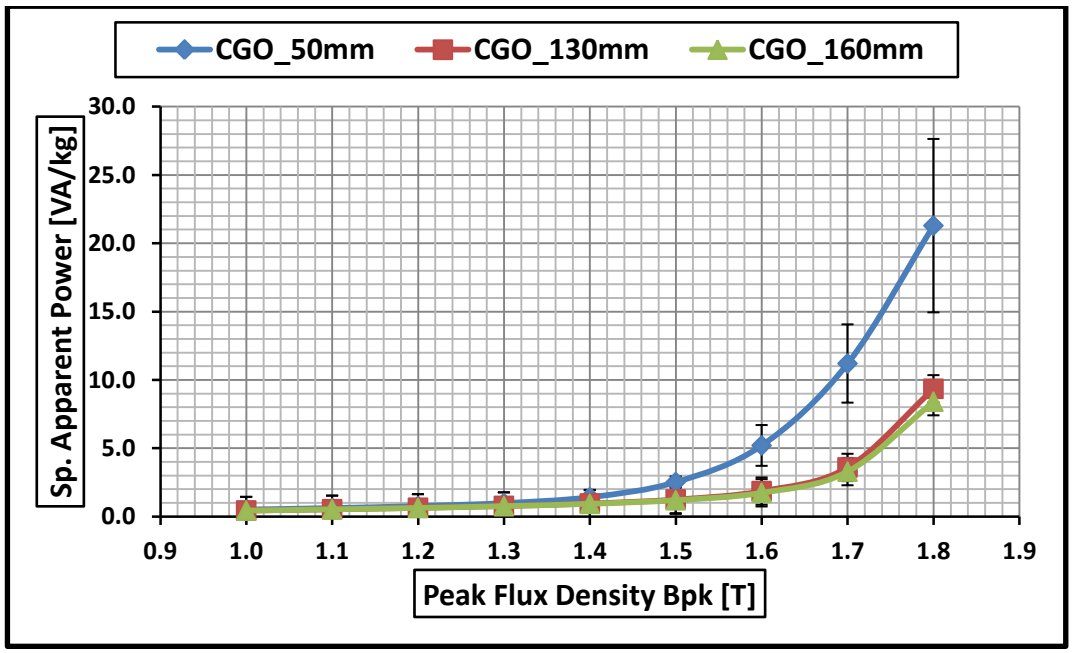

Fig. 3-17 Variation of specific apparent power with flux density for single phase CGO cores.

3.7 Single Phase, Epstein Size Cores

3.7.1 Specific Power Losses and Apparent Power

The specific losses of the HGO, CGO and mixed cores assembled in combinations 1 and 2 are shown in Fig. 3-18 and Fig.3-19 respectively.

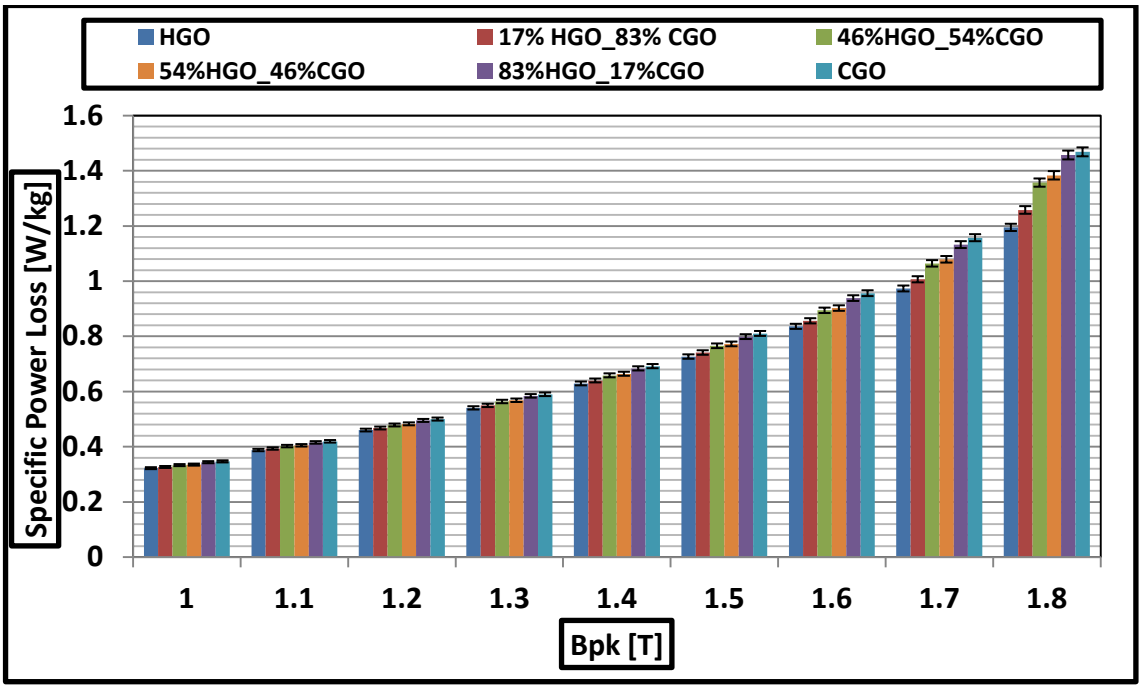

Fig. 3-18 Variation of specific loss with flux density of HGO and CGO strips assembled in the Epstein frame using combination 1.

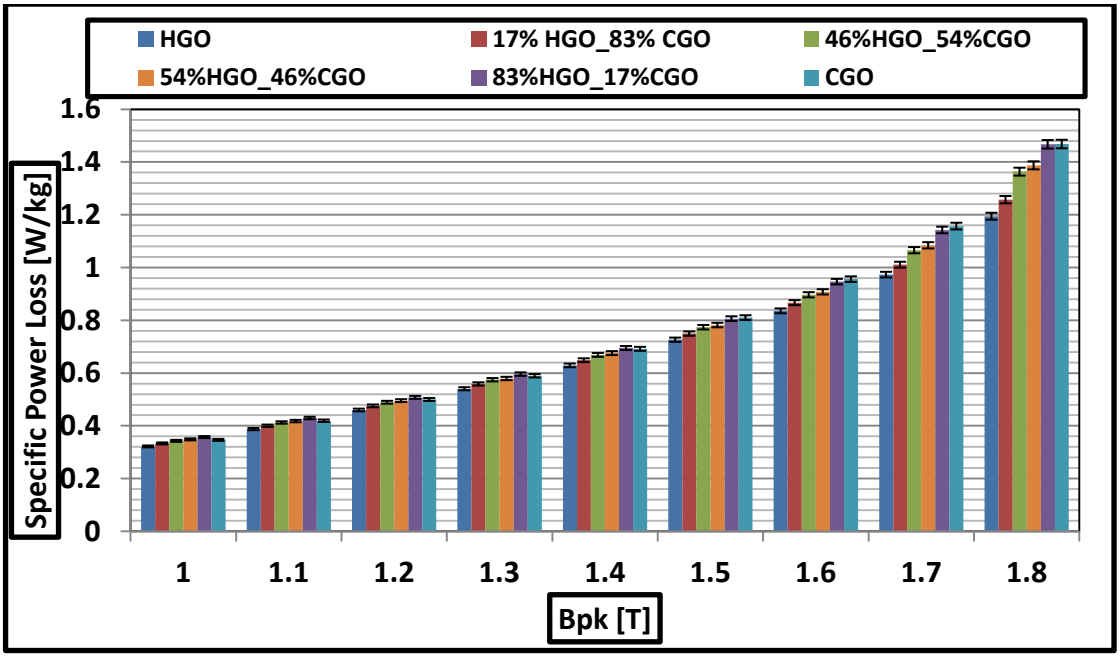

Fig. 3-19 Variation of specific loss with flux density of HGO and CGO strips assembled in the Epstein frame using combination 2.

The measured specific apparent power of HGO, CGO and mixed cores assembled in combinations 1 and 2 are shown in Fig. 3-20 and Fig. 3-21 respectively. The error bars are smaller in Fig.3-20 and Fig. 3-21 as compared to the error bars in Fig. 3-17 because of smaller sensitivity co-efficient of the measurements [70].

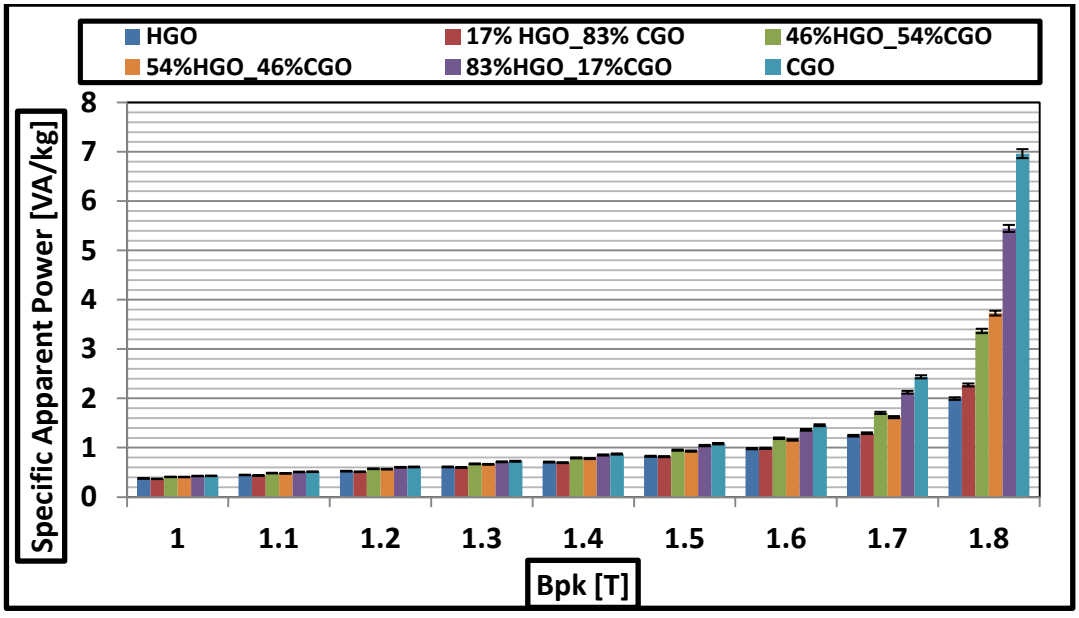

Fig. 3-20 Variation of specific apparent power with flux density of HGO and CGO strips assembled in the Epstein Frame using combination 1.

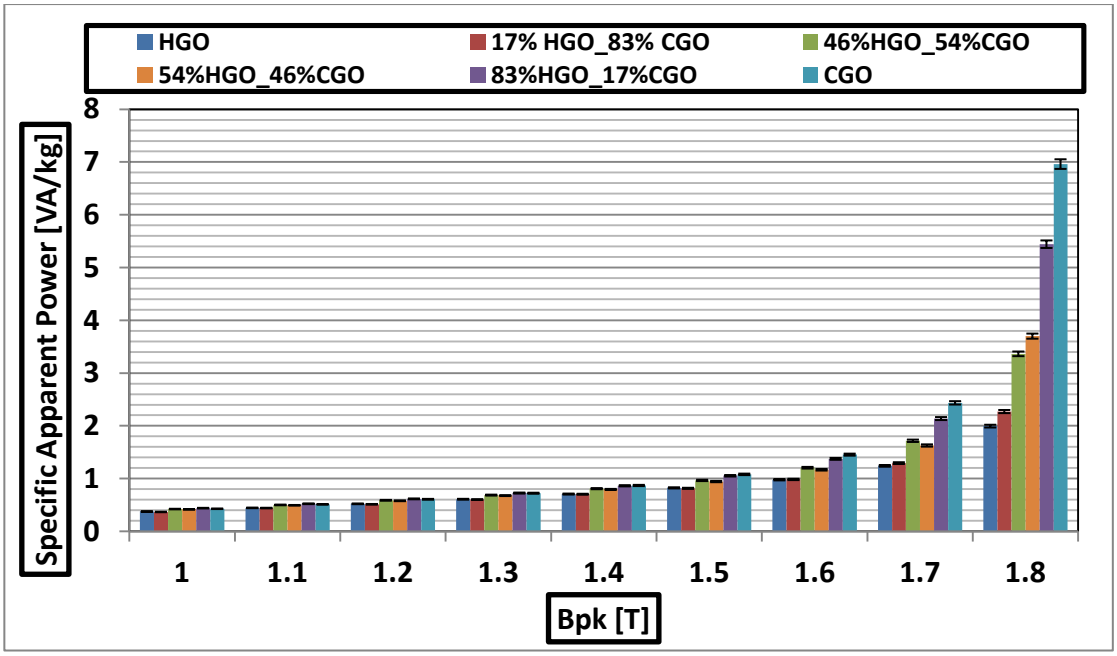

Fig. 3-21 Variation of specific apparent power with flux density of HGO and CGO strips assembled in the Epstein Frame using combination 2.

3.8 Discussion

3.8.1 No-Load Specific Losses and Specific Apparent Power of Three-Phase, Three-Limb and Single Phase, Two Limb Cores

In evaluating the energy expenses, the no-load specific losses must be considered as they are continuous over the designed lifetime of a transformer. The no-load specific losses occur in the core material. They are due to hysteresis and eddy currents. The factors affecting the no-load losses are flux density, excitation waveform, core type, core material, core assembly, core joint design, bolt holes, slots and operating frequency.

In the results, the losses for 3-phase, 3-limb cores and single phase two limb cores built with HGO is lower than that of CGO. This is because of superior grain orientation along the RD in the HGO material. The no-load losses for 3-phase, 3-limb cores are more than single phase, two limb cores because of the 'T' joint region which contributes towards higher losses in both HGO and CGO cores. The no-load losses for single packet 3-phase, 3-limb and single phase , two limb cores built with

HGO and CGO 50 mm wide laminations are higher than those built with 130 mm and 160 mm wide laminations because of the lower effective permeability (**Chapter 2**).

The no-load specific apparent power is the product of the primary current and secondary induced voltage. It is related to the no-load loss by a parameter called as power factor. In the results, the specific apparent power for single packet 3-phase, 3-limb and single phase , two limb cores built with HGO and CGO 50 mm wide laminations is higher than those built with 130 mm and 160 mm wide laminations because of the lower effective permeability (**Chapter 2**). Previous research shows that the sudden increase in specific apparent power of cores built with MSL joints was because of the saturation of the joint regions [68]. The increase in specific apparent power for HGO and CGO cores built with 50mm wide laminations after 1.4 T was observed in the current investigation. Considering the fact that the HGO and CGO cores built with 50mm packets, 130 mm packets and 160 mm packets were all assembled with seven step lap joints, the only difference was the ratio of hole diameter (or slot width) and lamination width. Therefore the high ratio of hole diameter (or slot width) and lamination width of 0.2 for the HGO and CGO 50 mm packet causes the specific apparent power to increase after 1.4 T indicating saturation of the corner joints in accordance with [68].

3.8.2 Effect of Mixing HGO and CGO material on the Specific Loss and Apparent Power of Single Phase Epstein Sized Mixed Cores

The variation of specific losses of all the cores with CGO content at B_{pk} =1.7 T are shown in Fig. 3-22 and Fig.3-23. The measured losses of HGO and CGO cores were multiplied by their respective material content (in percentage) in the mixed cores. The results were added to obtain the calculated losses of the mixed cores. The coefficient of determination (R^2) for linear fitting of the specific power loss data points for B_{pk} = 1.3 T, 1.5 T and 1.7 T is depicted in table 3.3. The values were obtained from Microsoft Excel software. If the R^2 value for a linear fitting of data points, is in between 0.9 and 1, then it is considered as a best fit.

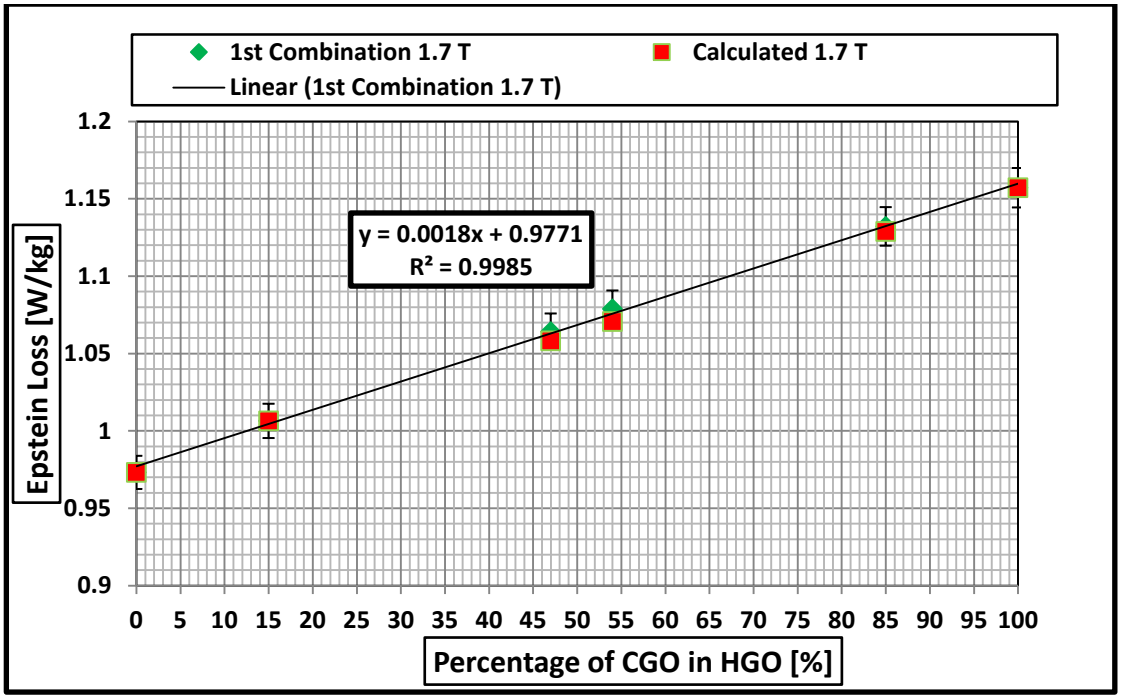

Fig. 3-22 Variation of Specific Loss with CGO content in the Epstein frame at B_{pk} = 1.7T for combination 1.

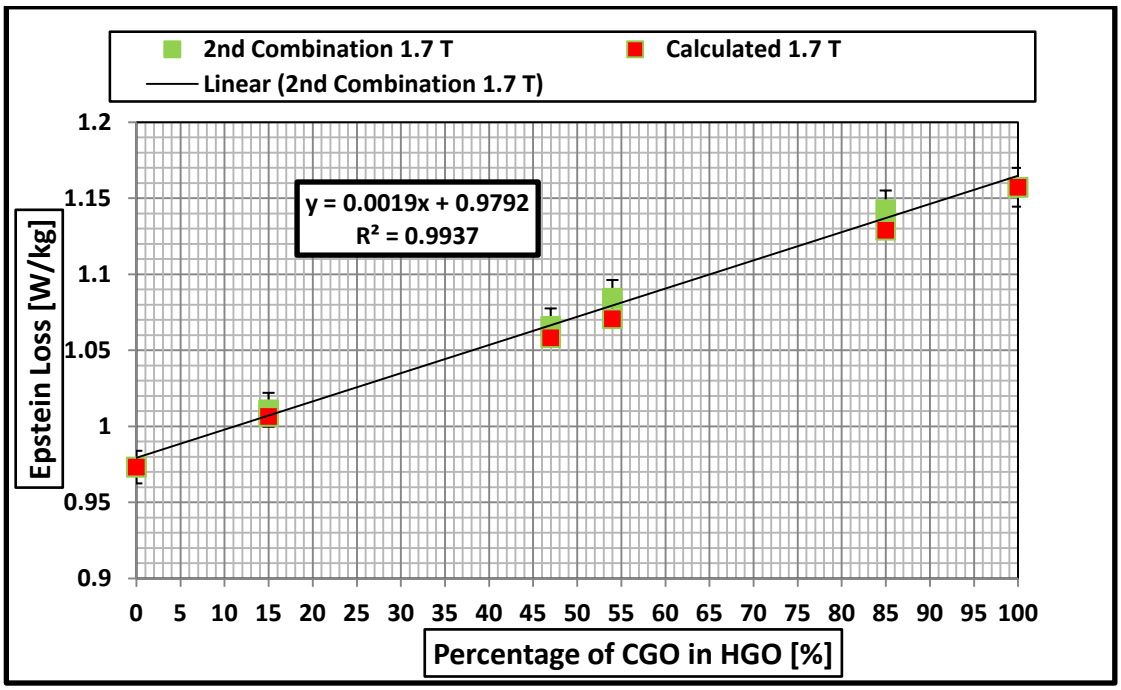

Fig. 3-23 Variation of Specific loss with CGO content in the Epstein frame at B_{pk} = 1.7T for combination 2.

Table 3.3 Coefficient of Determination (R^2) for Linear Fitting of Specific Loss data points of Mixed Epstein Sized Cores

Combination	Peak Flux Density (B_{pk}) [T]	(R^2)
Comb. 1	1.3	0.9981
	1.5	0.9993
	1.7	0.9985
Comb. 2	1.3	0.9074
	1.5	0.9768
	1.7	0.9937
Calculated	1.3	0.9986
	1.5	0.9991
	1.7	0.9987

The measured and calculated results indicate that the specific losses of the mixed single phase Epstein sized cores are dependent on the proportion of the mixed materials and vary linearly with the addition of higher loss material in a core built predominantly with lower loss material and vice versa. This is consistent with the previous research in this field. [55]-[61].

The variation of specific apparent power of all the cores with CGO content at B_{pk} =1.7 T are shown in Fig. 3-24 and Fig.3-25. The coefficient of determination (R^2) for linear fitting of the specific apparent power data points for B_{pk} = 1.3 T, 1.5 T and 1.7 T is depicted in table 3.4.

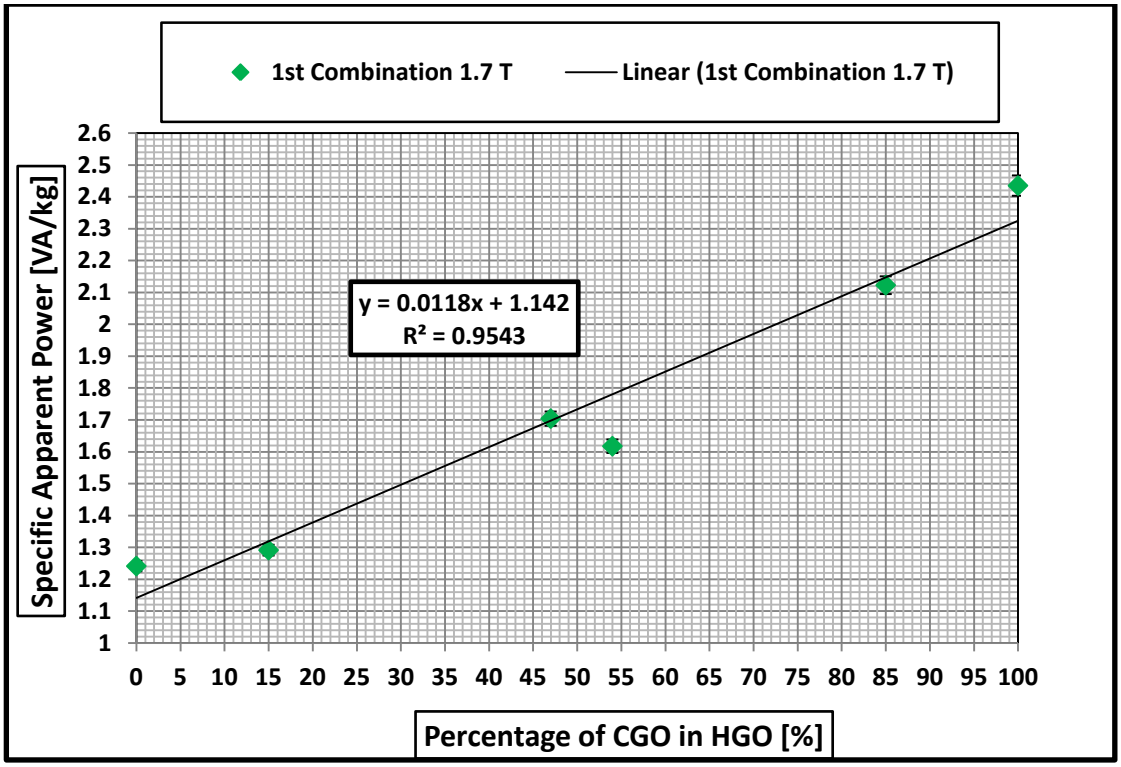

Fig. 3-24 Variation of Specific Apparent Power with CGO content in the Epstein Frame at B_{pk} = 1.7 T for combination 1.

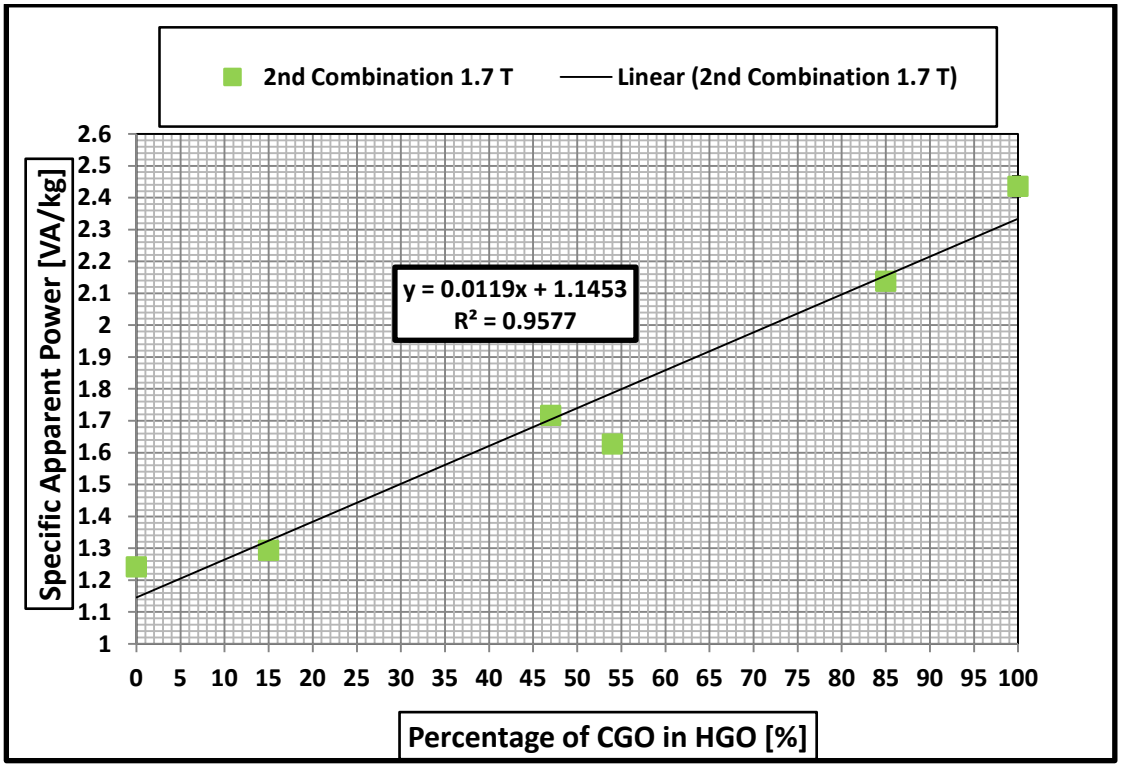

Fig. 3-25 Variation of Specific Apparent Power with CGO content in the Epstein Frame at B_{pk} = 1.7T for combination 2.

Table 3.4 Coefficient of Determination (R^2) for Linear Fitting of Specific Apparent Power data points of Mixed Epstein Sized Cores

Combination	Peak Flux Density (B_{pk}) [T]	(R^2)
Comb. 1	1.3	0.9432
	1.5	0.9665
	1.7	0.9543
Comb. 2	1.3	0.905
	1.5	0.9617
	1.7	0.9577

Similar to the specific power loss, the specific apparent power of mixed cores is also dependent on the proportion of the mixed materials and varies linearly with the addition of higher loss material in a core built predominantly with lower loss material and vice versa.

3.8.3 Effect of Mixing CGO in Predominantly HGO core on the Core Performance

The variation of measured and calculated specific losses of the mixed 3-phase, 3-limb cores at B_{pk} =1.7 T with CGO content is shown in Fig. 3-26. The measured, packet to packet flux distribution (**Chapter 2**) in the full sized cores was used to interpolate the corresponding specific losses of individual packets (Fig.3-9 & Fig.3-10) from individual packet cores shown in Fig. 3-1, Fig. 3-2 and Fig.3-3. The no-load loss in watts was obtained by multiplying the specific no-load loss in watts per kilogram by the corresponding mass in kilogram of the individual cores. The no-load loss values of individual packet cores were added to obtain the total no-load loss of each whole core in watts. The total no-load loss in watts was then divided by the whole core mass to obtain the no-load loss in watts per kilogram. The variation of measured and calculated specific loss for all the cores with CGO content at 1.7 T is shown in Fig. 3-26.

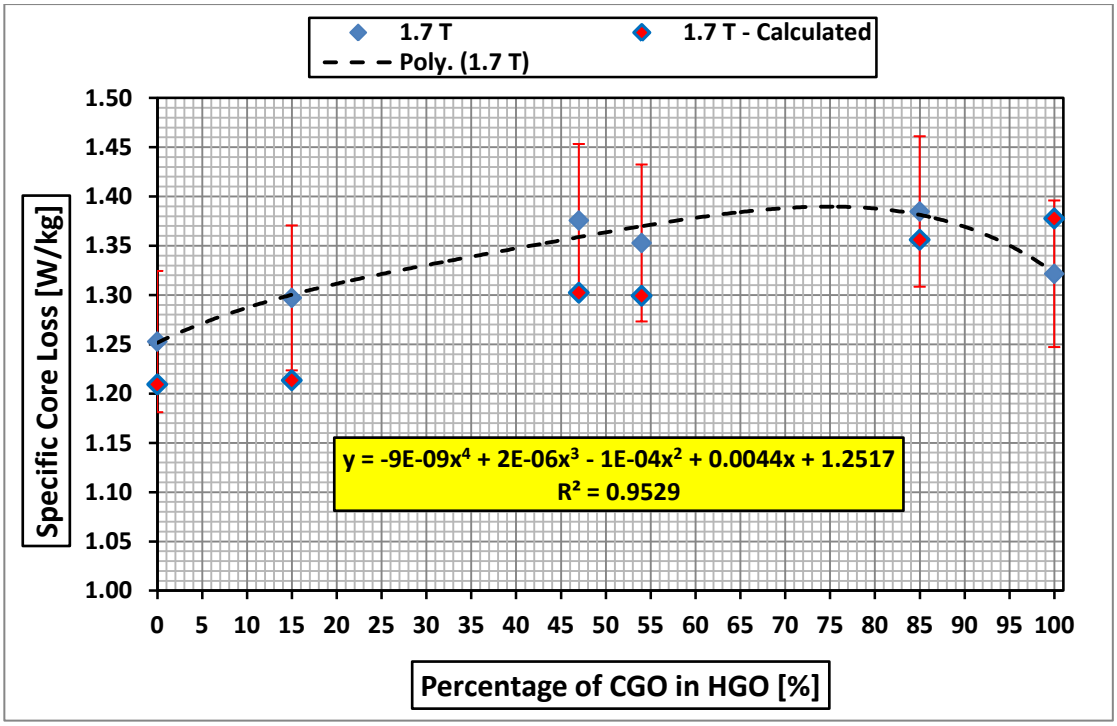

Fig. 3-26 Variation of specific loss with CGO content in the full sized core design at 1.7T.

The measured results indicate that the specific losses of the mixed 3-phase, 3-limb cores are dependent on the proportion of the mixed materials and but do not vary linearly with the addition of higher loss material in a core built predominantly with lower loss material and vice versa. The variation is polynomial. The calculated values are within the error limits of the measured values.

The difference in losses between measured and calculated values of losses is around 6%. The non-linear variation of power loss and apparent power with material content in 3-phase, 3-limb transformer cores was because of the inefficiency of the MSL joints in the packet containing the highest bolt hole (or slot width) and lamination width ratio (**Chapter 2**). Previous research [68] indicates that when the MSL joint becomes inefficient, it generates global flux harmonics which cause additional losses. The power losses and apparent power of cores with inefficient MSL joints also become more sensitive to constructional errors. [52].

The mass of 160 mm, 130 mm and 50 mm packets in all the cores is shown in Fig. 3-27.

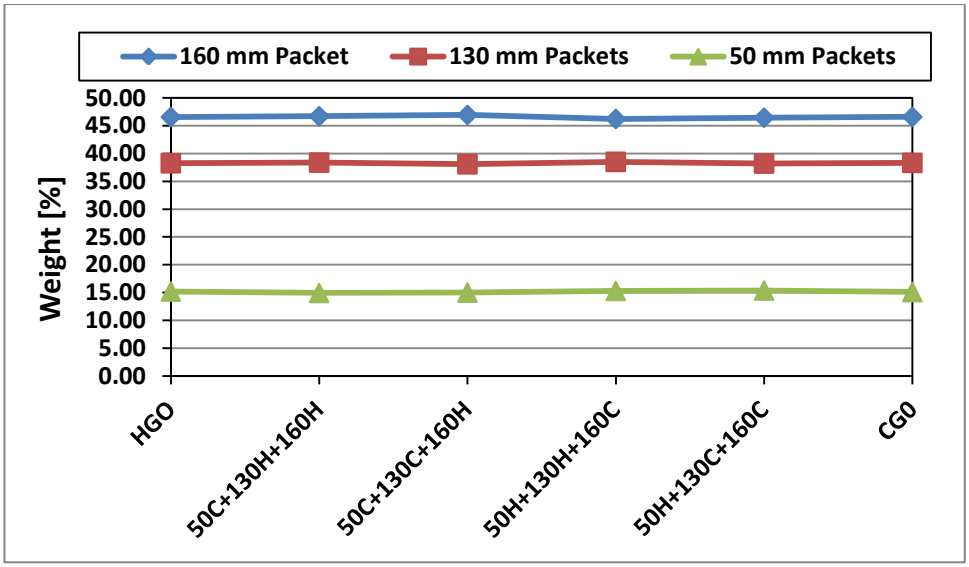

Fig. 3-27 Percentage of the 50mm, 130mm and 160 mm wide packets in the full size cores.

The specific losses of the packets used in calculations are shown in Fig. 3-28.

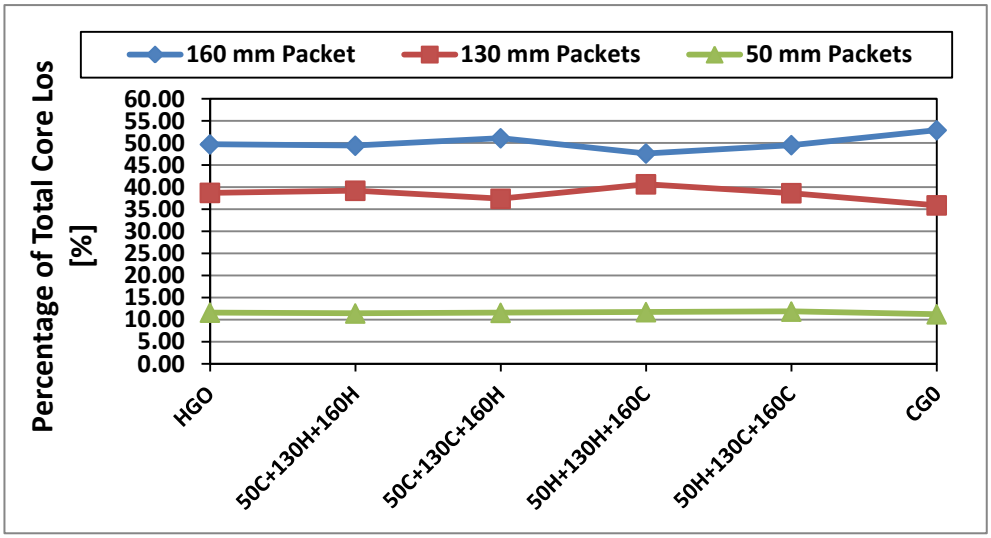

Fig. 3-28 Percentage of specific losses in the 50mm, 130mm and 160 mm wide packets of the full size cores

Around 45-55% of the specific core losses occur in the 160 mm wide central packet which constitutes 45 % of the core mass. The 130 mm wide packets weighing around 35 - 40 % of the core mass together contribute to around 35-40 % of the core losses. The 50 mm wide packets weigh around 15 % of the core mass and contribute 10 % of the core losses. These values indicate that the 160 mm wide packet in all the cores is over utilised by around 5% and the 50 mm wide packets are under utilised by around 5%. The over utilisation of the 160 mm wide packet is because it has the highest

effective permeability. The under utilisation of 50 mm wide packet is because it has the lowest effective permeability. Therefore the packet to packet variation of flux density affects the core losses.

Similarly the variation of apparent power with CGO content in mixed cores can be explained as above. The variation of apparent power with CGO content is shown in Fig. 3-29.

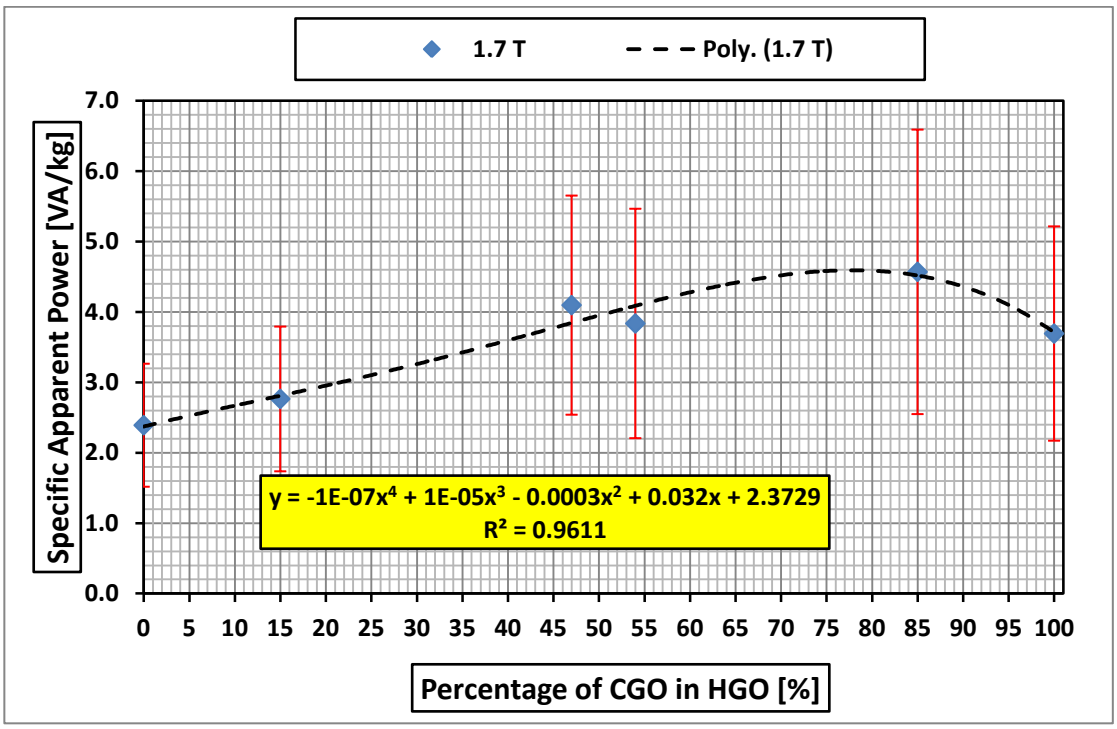

Fig. 3-29 Variation of specific apparent power with CGO content in the full sized core design at 1.7T.

3.9 Summary

The effect of mixing HGO and CGO laminations in Epstein size cores were investigated. The variation of power loss and apparent power was found to be proportional to the material content. The effect of mixing CGO and HGO content on the power losses and apparent power in the 3-phase, 3-limb transformer core design was investigated. The variation of power loss and apparent power was found to be non-linear. Single packet CGO and HGO 3-phase, 3-limb cores of different packet widths were built to obtain the power loss and apparent power.

The non-linear variation of power loss and apparent power with material content in 3-phase, 3-limb transformer cores was because of the additional losses in the cores due to the global flux harmonics generated in the packet containing the highest bolt hole (or slot width) and lamination width ratio.

Chapter 4

Effect of Bolt Holes and Slots on Localised Magnetic Properties of Electrical Steel Laminations using Finite Element (FE) Simulations and Post Processing

4.1 Introduction

In this chapter, the localised specific loss increase (building factor) and relative permeability decrease around holes and slots are quantified by 2-D FE simulations and post processing. Specific power loss and peak magnetising field in the RD were measured for HGO and CGO strips in a standard Epstein Frame. Specific losses and peak magnetising field in the TD were measured in a single strip tester. The measured magnetising fields in RD and TD formed the input to 2-D FE simulations around 2mm, 4mm and 6mm diameter holes and slot widths in a single phase core geometry for HGO and CGO materials at 1.3 T, 1.5 T and 1.7 T. All the simulations were carried out in Infolytica MAGNET software. The spatial variation of flux distribution data around holes and slots was imported to MATLAB for further processing. Data sets for specific power loss increase and relative permeability decrease around holes and slots for various sizes in HGO and CGO were estimated.

4.2 Magnetic Field and Power Loss Measurements for Simulations

The B-H characteristics and losses of annealed Epstein strips (30 mm x 305 mm) magnetised along the rolling direction (RD) were measured by means of an Epstein measurement system [16] over a flux density range from 1.0 T to 1.8 T in steps of 0.1 T. The repeatability was less than 1% for all measurements. A schematic diagram of the system is shown in Fig. 4-1. It consists of a signal generator, a pre-amplifier, a power amplifier, a power analyzer and an Epstein square. The components of the measurement system are shown in Fig. 4-2.

The overall peak flux density (B_{pk}) was calculated from the induced average voltages in 700 turn secondary windings wound around each limb of the frame from equation (2.1),

$$B_{pk} = \frac{V_s}{4.N.A.f} \quad [T] \tag{2.1}$$

where the area of cross-section (A) of the arranged Epstein strips, was calculated from equation (3.4),

$$A = \frac{m}{4.\rho_m.l} \quad [m^2\,] \tag{3.4}$$

The active mass (m_a) was calculated from equation (3.7),

$$m_a = \frac{m.l_m}{4.l} \quad [\,kg\,] \tag{3.7}$$

where (l_m) is the conventional mean magnetic path length in metres (m).

The Epstein loss (W_E) at a particular flux density was then calculated by dividing the measured power loss (P_c) at that flux density by m_a from equation (4.1),

$$W_E = \frac{P_c}{m_a} \quad \left[\frac{W}{kg}\right] \tag{4.1}$$

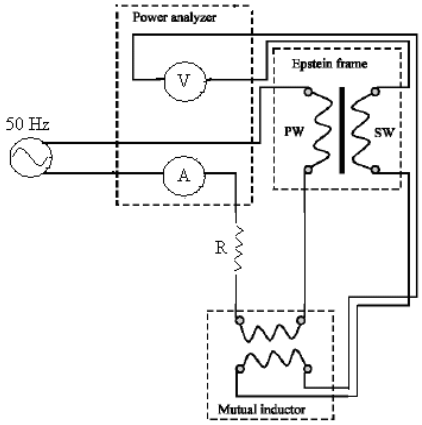

Fig. 4-1 Schematic diagram of Epstein measurement system [16].

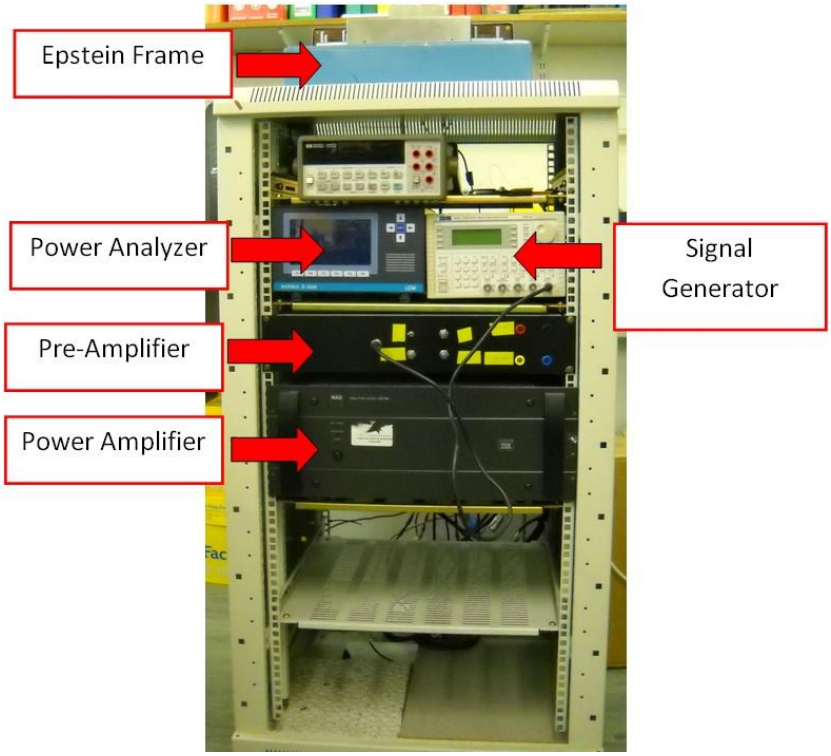

Fig.4-2 Components of the Epstein measurement system [16].

The B-H characteristics and losses of annealed Epstein strips cut in the transverse direction (TD) were measured in a computerised Single Strip Tester (SST) [17]. The repeatability was less than 1% for all the measurements. A schematic diagram of the system is shown in Fig. 4-3. It consists of a computer pre-installed with LabVIEW version 8.5 software from National Instruments, a NI PCI-6120 data acquisition (DAQ) card [69], a power amplifier, a 1 Ω shunt resistor (R_s), and an SST. The components of the measurement system are shown in Fig. 4-4.

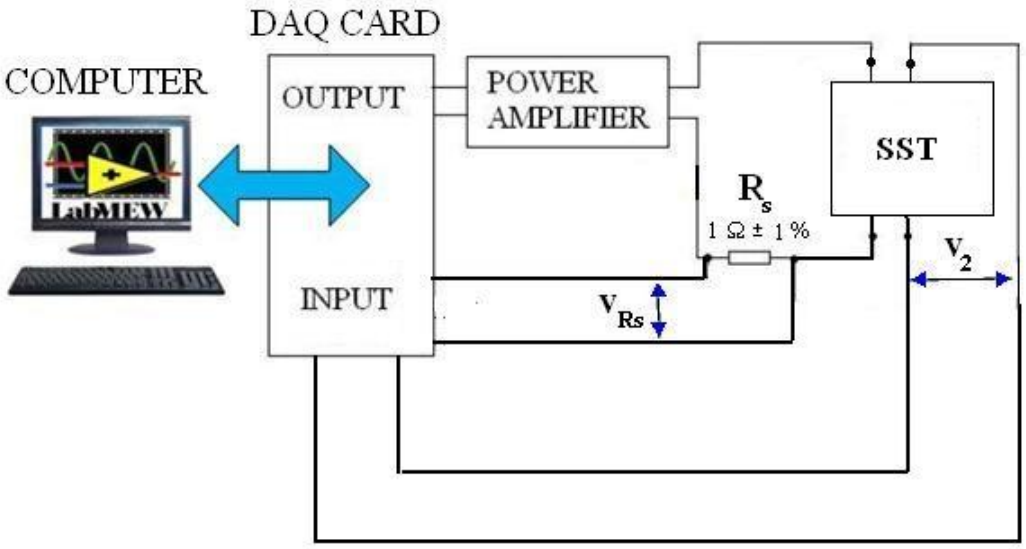

Fig. 4-3 Schematic diagram of computer-controlled SST measurement system [17].

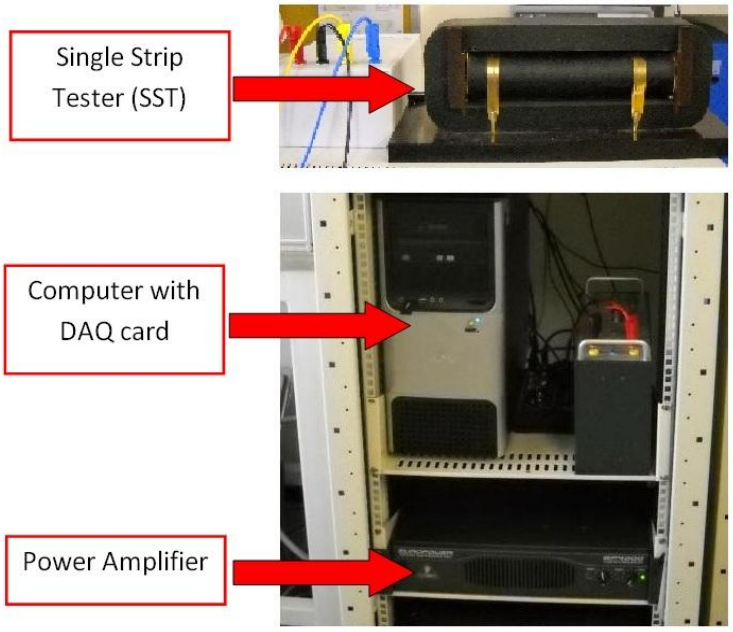

Fig. 4-4 Components of the computer-controlled SST measurement system [17].

The magnetising voltage was generated by the LabVIEW program via a voltage output of the DAQ card. The instantaneous voltage across the shunt resistor (v_{Rs}), and the instantaneous secondary voltage (v_2) were measured for calculation of flux density and magnetic field respectively. The instantaneous magnetic field (h), calculated by the LabVIEW program by equation (3.2),

$$h = \frac{N_1.v_{Rs}}{l_m.R_{sh}} \quad \left[\frac{A}{m}\right] \tag{3.2}$$

where l_m is the mean path length, which is the distance between the inner edges of the yoke (0.255 m).

The instantaneous flux density (b) was calculated by the LabVIEW program by equation (3.3),

$$b = \frac{l.\rho_m}{N_2.m} . \int v_2 . dt \quad [T] \tag{3.3}$$

where, l is the strip length, m is its mass and ρ_m is the density. The specific power loss (P_s) was calculated from equation (3.5),

$$P_s = \frac{1}{T.\rho_m} . \int_0^T h \frac{\mathrm{db}}{\mathrm{dt}} . dt \quad \left[\frac{W}{kg}\right] \tag{3.5}$$

4.3 Finite Element Analysis

4.3.1 Simulation Methodology

The two - dimensional (2D) geometry of the Epstein square shown in Fig.4-5 was constructed for simulations carried out in INFOLYTICA MAGNET which is a specialised electromagnetic software widely used in the industry. The strip width (W) (shown in green) was fixed at 30 mm and the hole diameters and slot widths were varied. The hole diameters and slot widths chosen for the simulations were 2 mm, 4mm and 6 mm respectively. The hole diameter (slot width) and lamination width ratio for the chosen dimensions were 0.066, 0.133 and 0.2 respectively. The maximum hole diameter (slot width) and lamination width ratio in the transformer cores (**Chapter 2 and 3**) was 0.2. Therefore the maximum hole diameter and slot width ratio of 0.2 was chosen for the simulations to correlate the results (Fig.4-6).

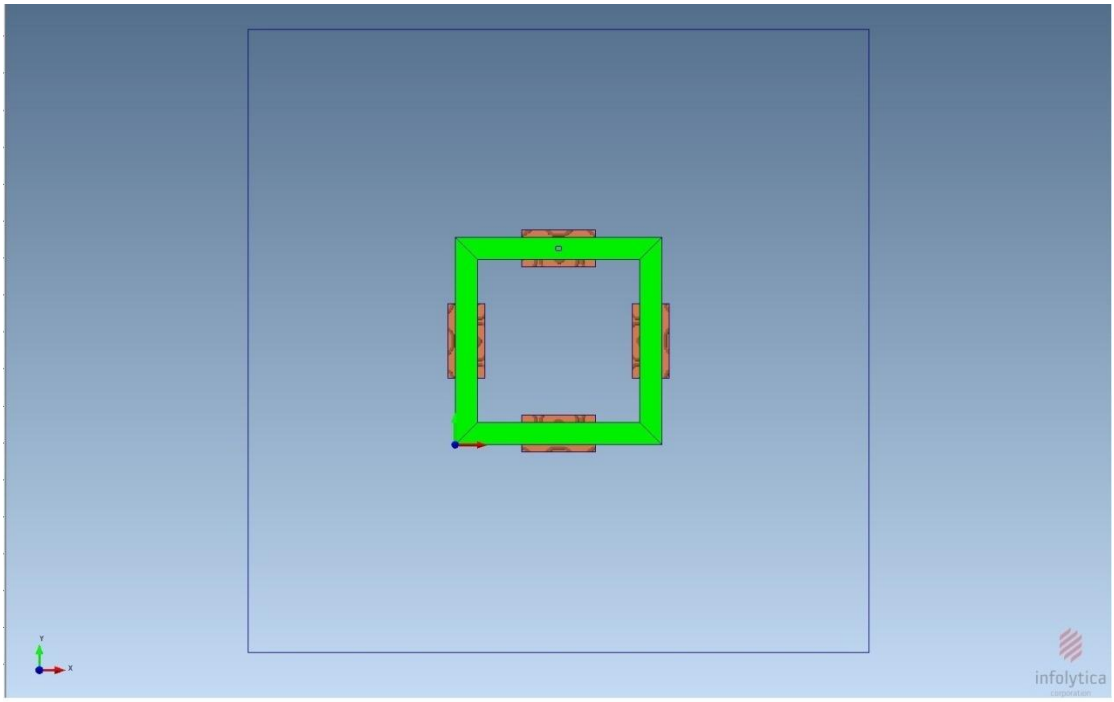

Fig. 4-5 Two-dimensional geometry used for the simulations.

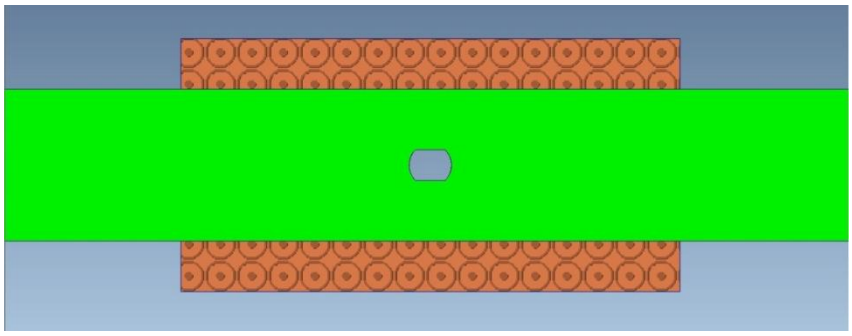

Fig. 4-6 Two-dimensional geometry showing a 6mm wide slot in a 30 mm wide strip.

The measured B-H characteristics when magnetised along the RD (Fig.4-7) and TD (Fig. 4-8) were used as input for the simulations carried out for HGO and CGO material at flux densities 1.3 T, 1.5 T and 1.7 T.

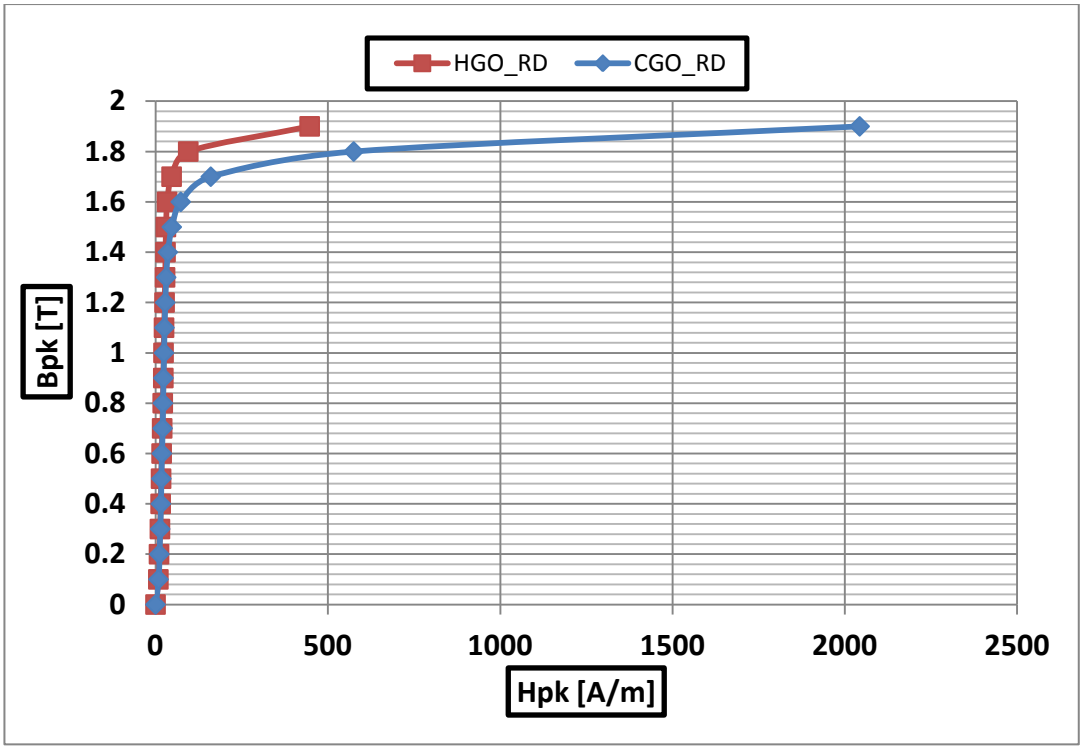

Fig. 4-7 B-H characteristics of 0.3mm thick HGO and CGO strips in RD measured in Epstein Frame for B_{pk} = 0.1 T – 1.9 T.

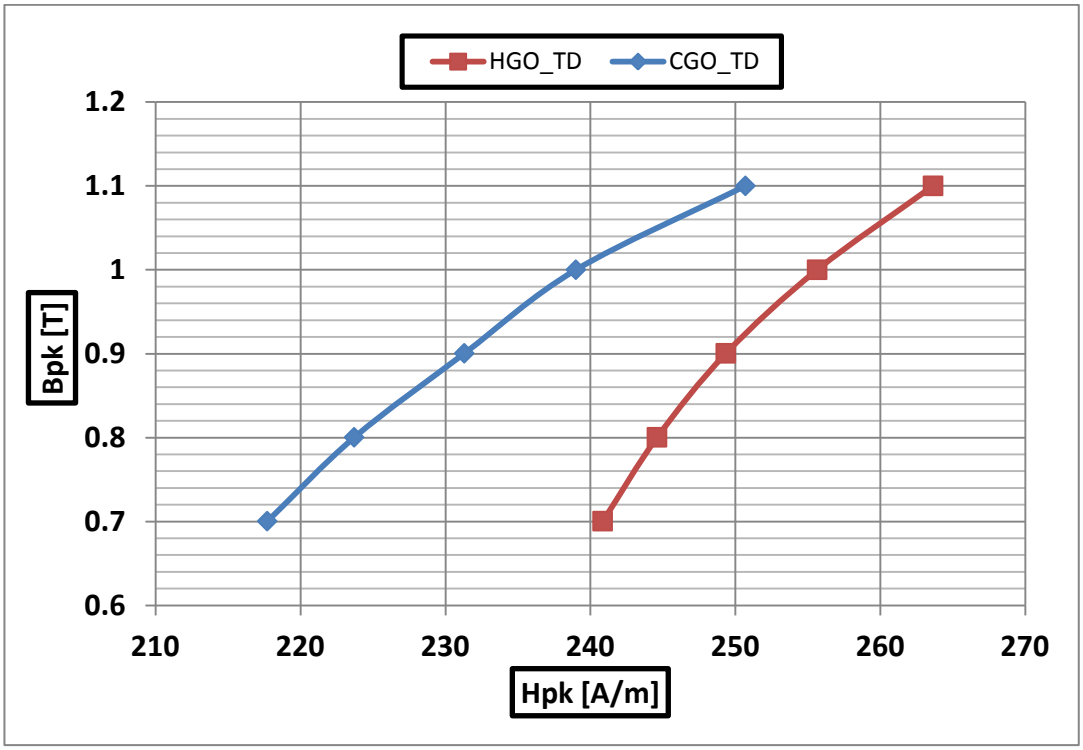

Fig. 4-8 B-H characteristics of 0.3mm thick HGO and CGO strips in TD measured in SST for B_{pk} = 0.7T – 1.1 T.

The excitation current was varied to obtain the desired flux density (B_{pk}). The region where the flux re-distributes across holes- slots was designated as the affected region. The length of this region was designated as affected length (l_H) for holes and (l_S) for slots as shown in Fig. 4-9. It is easier to work with the numerical data in MATLAB, so the B_{pk} distribution data points around the holes and slots in the affected region were exported to Microsoft Excel files and then re-plotted in MATLAB. The affected region area was ($l_H * W$) for holes and ($l_S * W$) for slots.

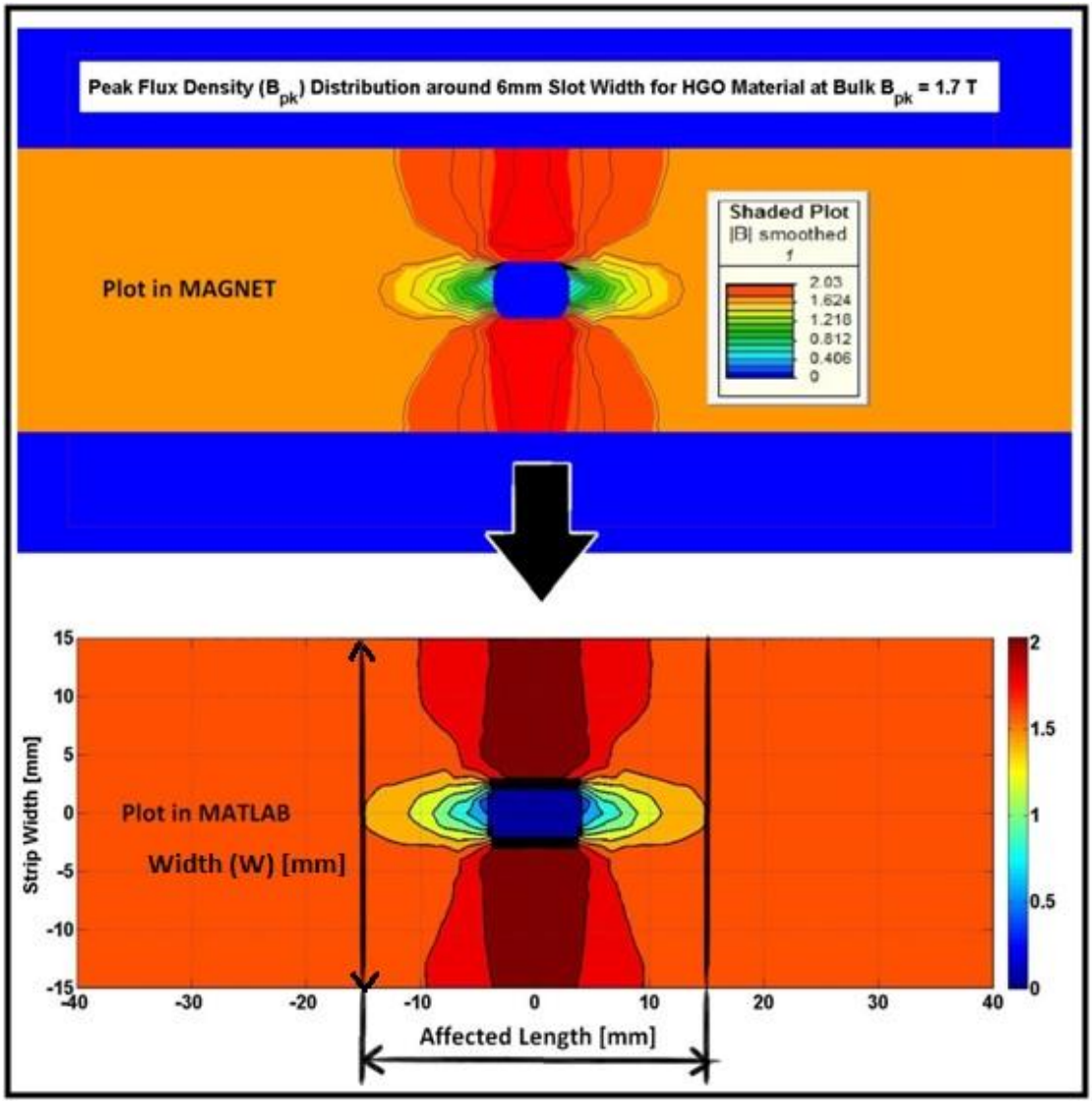

Fig. 4-9 B_{pk} distribution contour graph around a 6mm wide slot in HGO material at B_{pk} = 1.7 T plotted in MAGNET (top) and in MATLAB (bottom) showing affected length l_S.

4.4 Simulation Data Processing and Results

4.4.1 Affected Length – Hole Diameter Ratio for varying Hole diameter – Lamination Width Ratio and Affected Length – Slot Length Ratio for varying Slot Width – Lamination Width Ratio in HGO and CGO

The affected length - hole diameter ratio $\left(\frac{l_H}{d}\right)$ and the affected length – slot length ratio $\left(\frac{l_S}{s_l}\right)$ values for respective hole diameter –lamination width ratio $\left(\frac{d}{W}\right)$ and slot width – lamination width ratio $\left(\frac{s_w}{W}\right)$ values of 0.067, 0.133 and 0.2 at 1.3 T, 1.5 T and 1.7 T for HGO and CGO (**Appendix V**) were extrapolated to saturation B_{pk} (2.03T) and interpolated for flux densities from 0.01 T to 2.03 T in steps of 0.01 T. The resulting $\frac{l_H}{d}$ and $\frac{l_S}{s_l}$ data was then interpolated for $\frac{d}{W}$ and $\frac{s_w}{W}$ respectively from 0 to 0.2 in steps of 0.001667. The resulting data sets of $\frac{l_H}{d}$ for varying $\frac{d}{W}$ and B_{pk} for HGO and CGO are shown in Fig 4-10 and Fig 4-11 respectively. The resulting data sets of $\frac{l_S}{s_l}$ for varying $\frac{s_w}{W}$ and B_{pk} for HGO and CGO are shown in Fig 4-12 and Fig 4-13 respectively.

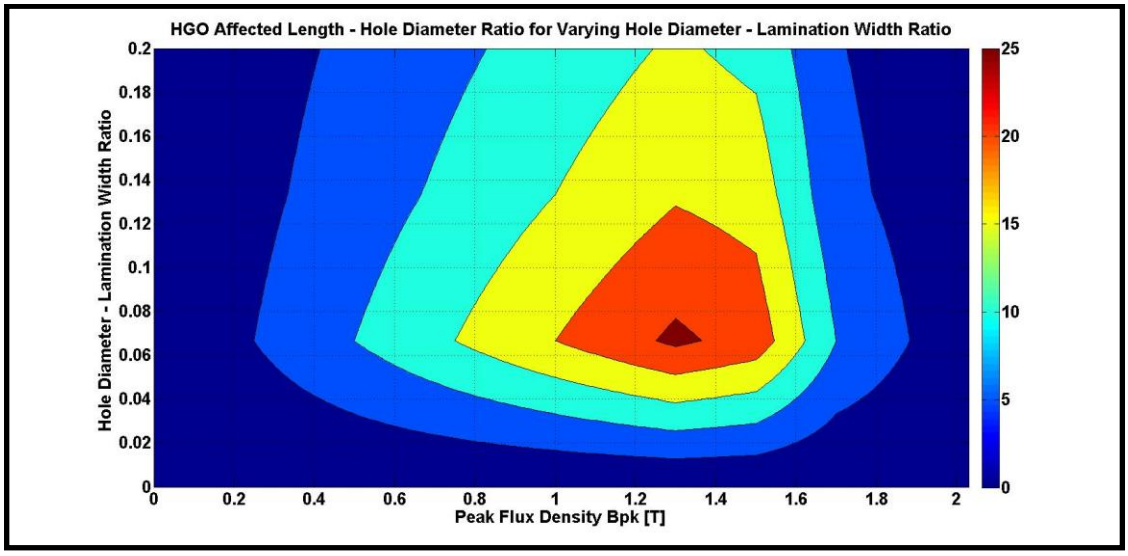

Fig. 4-10 Contour graph of $\frac{l_H}{d}$ for varying $\frac{d}{W}$ and B_{pk} in HGO material.

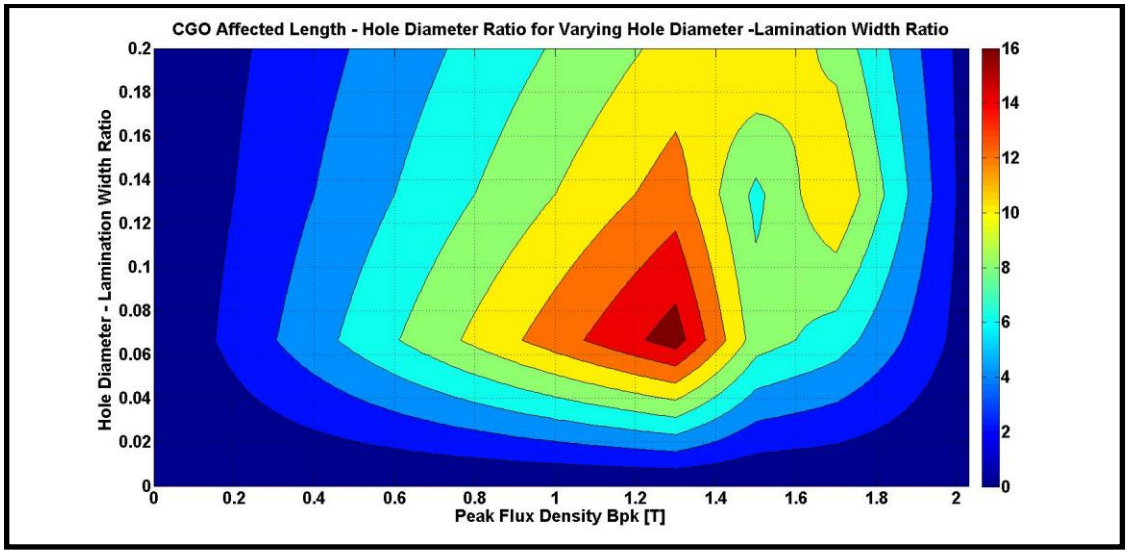

Fig. 4-11 Contour graph of $\frac{l_H}{d}$ for varying $\frac{d}{W}$ and B_{pk} in CGO material.

The contour graphs in Fig. 4-10 and Fig. 4-11 show the $\frac{l_H}{d}$ values for varying $\frac{d}{W}$ and B_{pk} values for HGO and CGO respectively. This data set can be used to compute the affected region length around holes at any B_{pk} value if the hole diameter d and lamination width W is known.

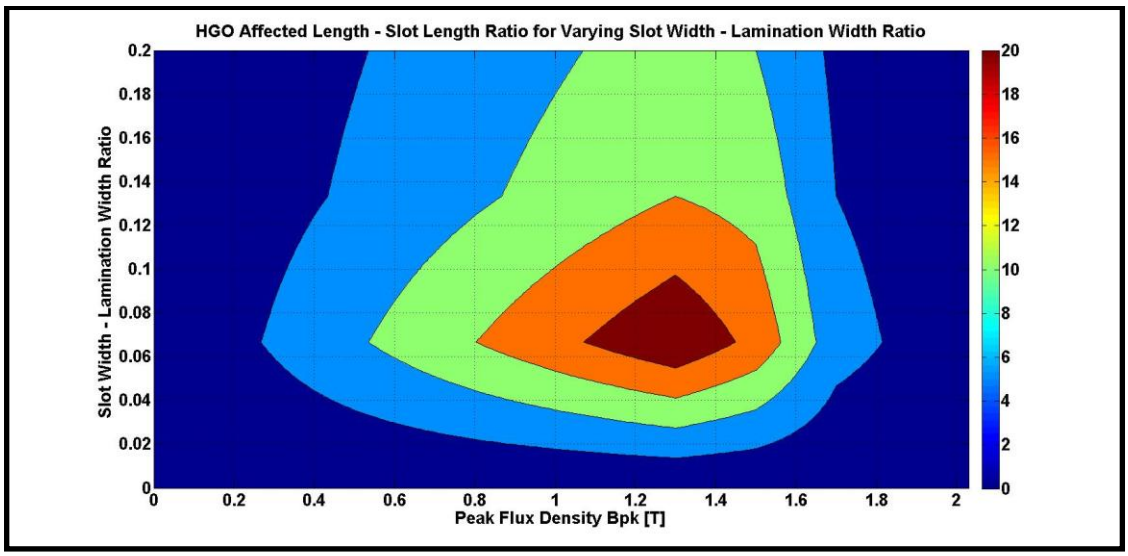

Fig. 4-12 Contour graph of $\frac{l_S}{s_l}$ for varying $\frac{s_w}{W}$ and B_{pk} in HGO material.

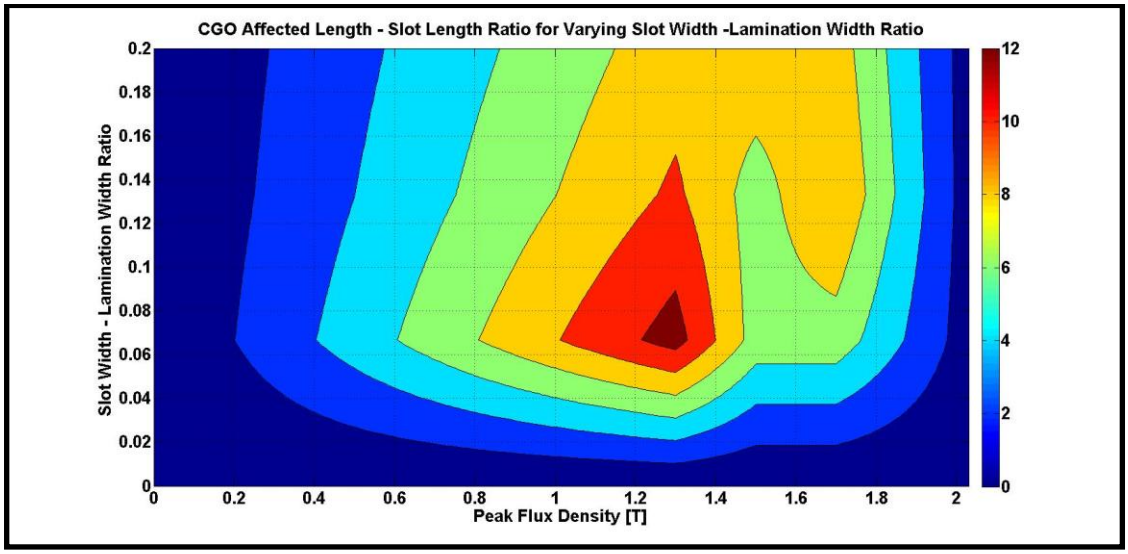

Fig. 4-13 Contour graph of $\frac{l_S}{s_l}$ for varying $\frac{s_w}{W}$ and B_{pk} in HGO material.

The contour graphs in Fig. 4-12 and Fig. 4-13 show the $\frac{l_S}{s_l}$ values for varying $\frac{s_w}{W}$ and B_{pk} values for HGO and CGO respectively. This data set can be used to compute the affected region length around slots at any B_{pk} value if the slot width s_W and lamination width W is known.

4.4.2 Percentage Increase in Peak Flux Density in the Affected Regions around Holes and Slots for HGO and CGO

The B_{pk} distribution data points around the holes and slots were used to calculate the percentage increase in B_{pk} around holes and slots in HGO and CGO for respective $\frac{d}{W}$ and $\frac{s_w}{W}$ values of 0.067, 0.133 and 0.2 at 1.3 T, 1.5 T and 1.7 T (**Appendix V**). The B_{pk} distribution data points around the holes were averaged over the affected region of area $l_H * W$ to obtain $B_{H_{pk}}$. The B_{pk} distribution data points around the slots were averaged over the affected region of area $l_S.W$ to obtain $B_{S_{pk}}$. Equation (4.2) was used to calculate the percentage increase in B_{pk} around holes and equation (4.3) was used to calculate the percentage increase in B_{pk} around slots.

$$\%\ \text{increase in}\ B_{pk}\ \text{around the holes} = \left(\frac{B_{H_{pk}} - B_{pk}}{B_{pk}}\right) * 100 \qquad (4.2)$$

$$\%\ \text{increase in } B_{pk} \text{ around the slots } = \left(\frac{B_{S_{pk}} - B_{pk}}{B_{pk}}\right) * 100 \quad (4.3)$$

The percentage increase in B_{pk} around holes and slots in HGO and CGO for respective $\frac{d}{W}$ and $\frac{s_w}{W}$ values of 0.067, 0.133 and 0.2 at 1.3 T, 1.5 T and 1.7 T were extrapolated to saturation B_{pk} (2.03T) and interpolated for flux density values from 0.01 T to 2.03 T in steps of 0.01 T. The resulting data of percentage increase in $B_{pk}$was then interpolated for $\frac{d}{W}$ and $\frac{s_w}{W}$ range from 0 to 0.2 in steps of 0.001667. The results for percentage increase in B_{pk} around holes for varying $\frac{d}{W}$ and B_{pk}, for HGO and CGO is shown in Fig. 4-14 and Fig. 4-15 respectively. The results for percentage increase in B_{pk} around slots for varying $\frac{s_w}{W}$ and B_{pk}, for HGO and CGO is shown in Fig. 4-16 and Fig. 4-17 respectively.

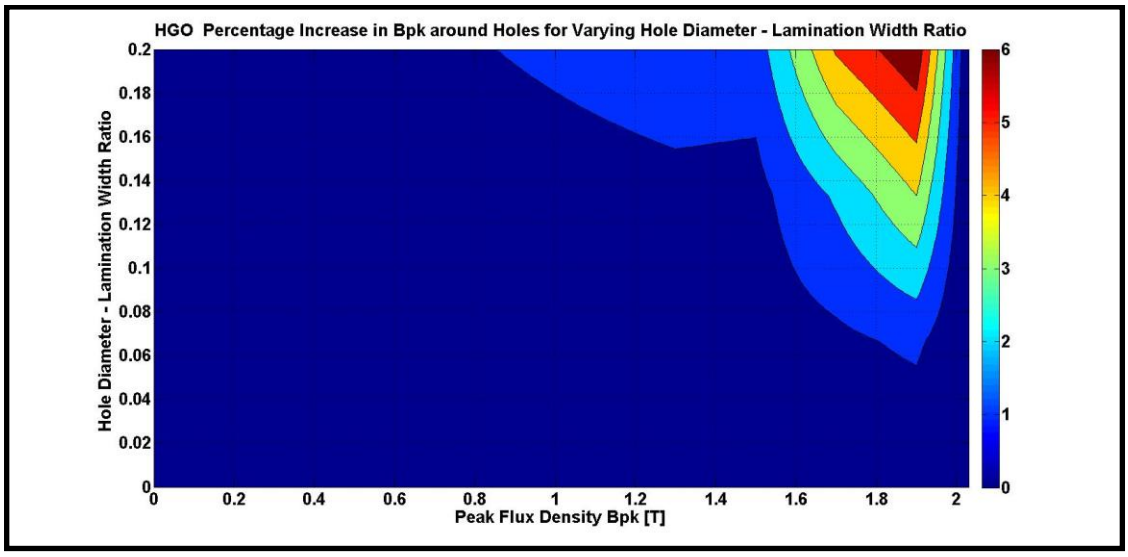

Fig. 4-14 Contour graph of percentage increase in B_{pk} around holes for varying $\frac{d}{W}$ and B_{pk} in HGO material.

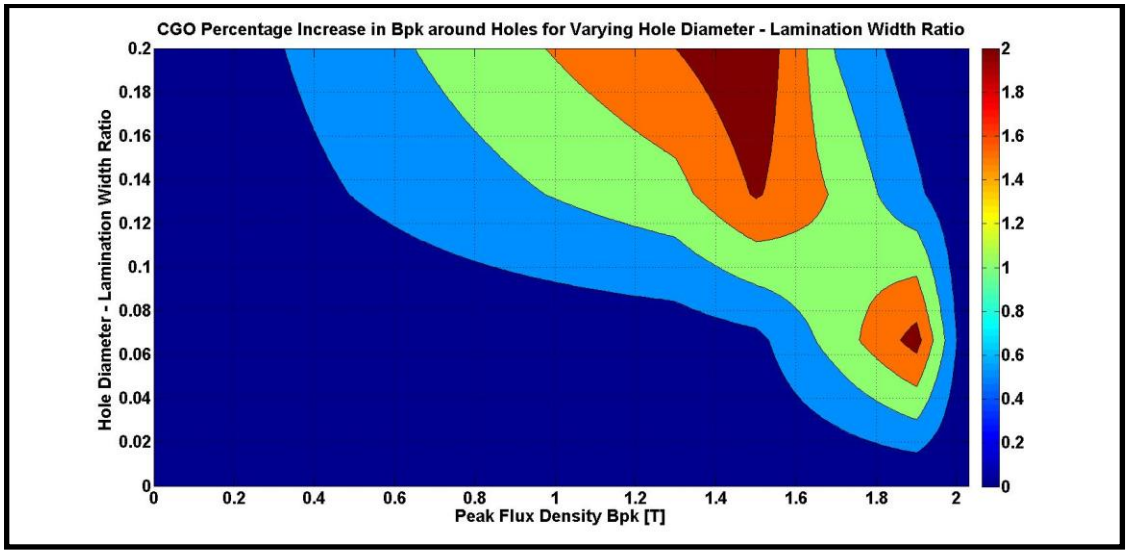

Fig. 4-15 Contour graph of percentage increase in B_{pk} around holes for varying $\frac{d}{W}$ and B_{pk} in CGO material.

The contour graphs in Fig. 4-14 and Fig. 4-15 show the percentage increase in B_{pk} for varying $\frac{d}{W}$ and B_{pk} values for HGO and CGO respectively. This data set can be used to compute the B_{pk} averaged over the affected region length around holes at any B_{pk} value if the hole diameter d and lamination width W is known.

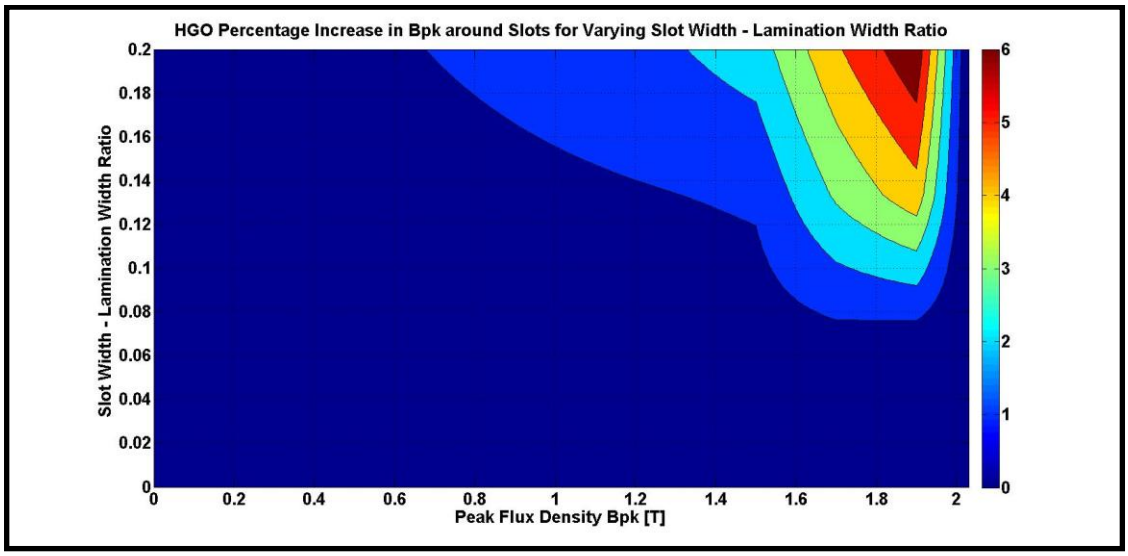

Fig. 4-16 Contour graph of percentage increase in B_{pk} around slots for varying $\frac{s_w}{W}$ and B_{pk} in HGO material.

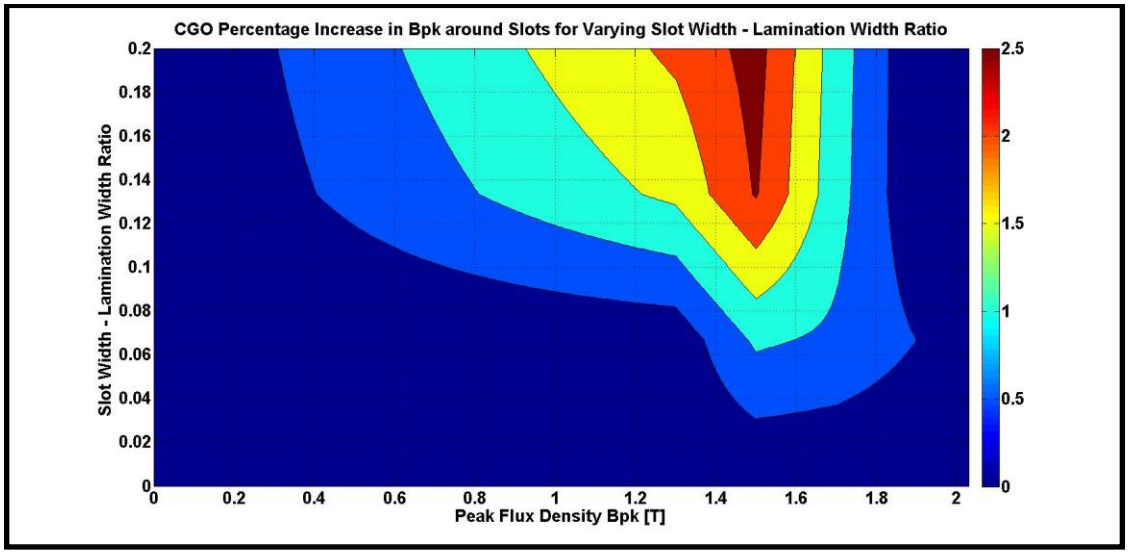

Fig. 4-17 Contour graph of percentage increase in B_{pk} around slots for varying $\frac{s_w}{W}$ and B_{pk} in CGO material.

The contour graphs in Fig. 4-16 and Fig. 4-17 show the percentage increase in B_{pk} for varying $\frac{s_w}{W}$ and B_{pk} values for HGO and CGO respectively. This data set can be used to compute the B_{pk} averaged over the affected region length around slots at any B_{pk} value if the slot width s_W and lamination width W is known.

4.4.3 Percentage Increase in Specific Loss in the Affected Regions around Holes and Slots for HGO and CGO

The specific power losses, when magnetised along the RD and TD were obtained by interpolating the flux density values for specific loss from the peak flux density versus specific loss curves in the RD (Fig.4-18) and TD (Fig.4-19) respectively.

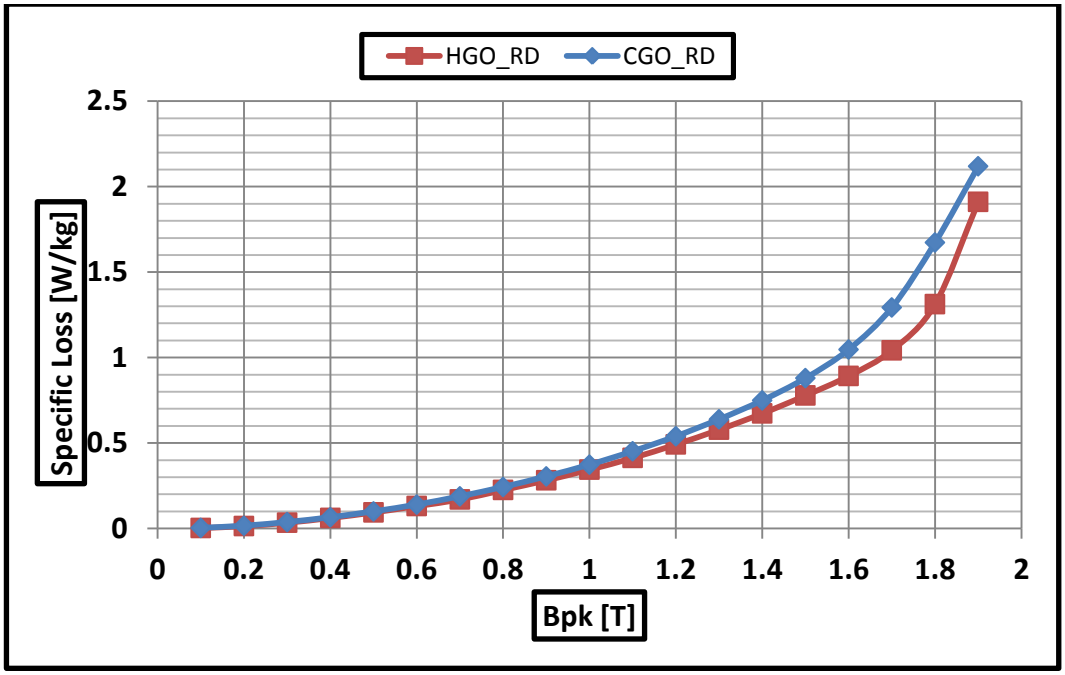

Fig. 4-18 The specific loss for HGO and CGO in RD measured in Epstein frame for B_{pk} = 0.01T – 1.9 T.

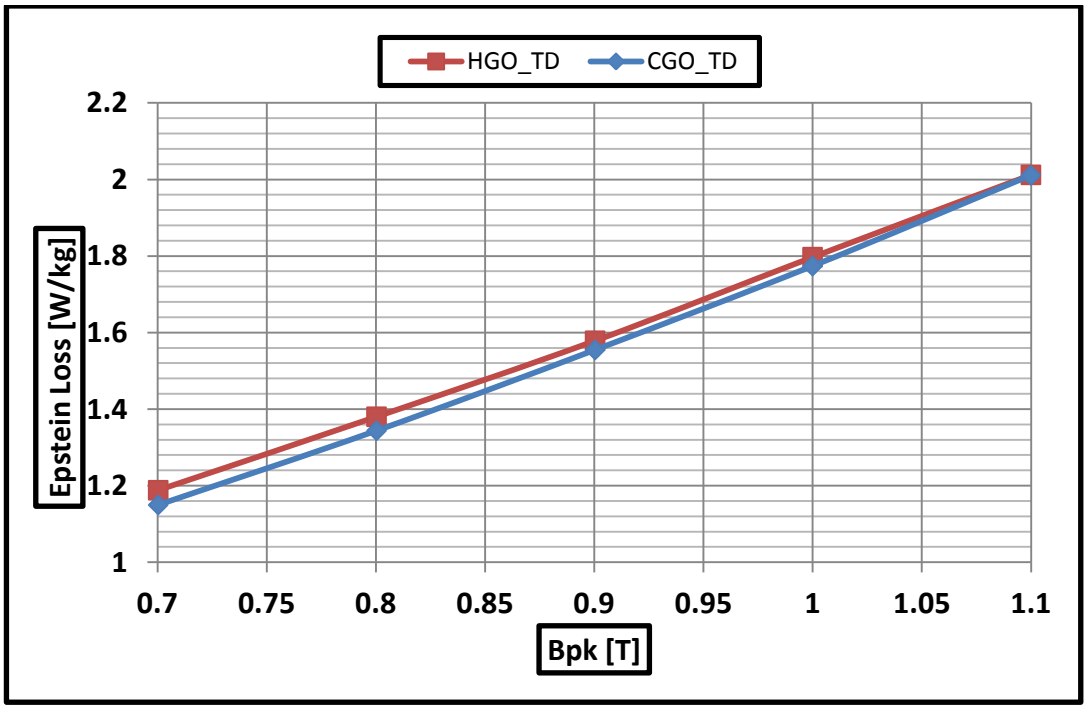

Fig. 4-19 The specific loss for HGO and CGO in TD measured in SST for B_{pk} = 0.7T – 1.1 T.

The interpolation of components of specific loss in RD (P_x) from components of flux density in the RD (B_x) around a 6 mm wide slot at B_{pk} = 1.7 T is shown in Fig. 4-20. The interpolation of components of specific loss in TD (P_y) from components of flux density in the TD (B_y) around a 6 mm wide slot at B_{pk} = 1.7 T is shown in Fig. 4-21.

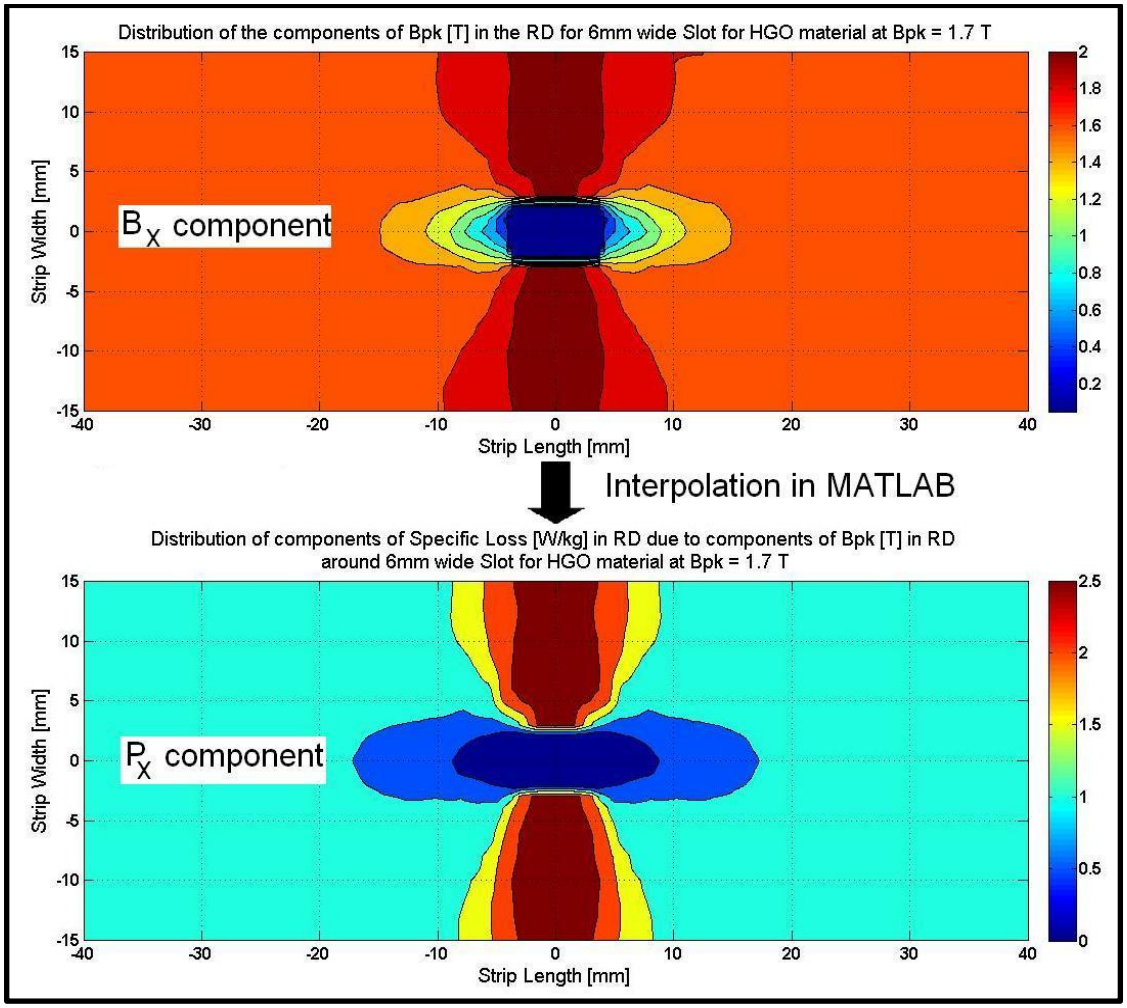

Fig. 4-20 Distribution of components of specific loss in RD interpolated from the components of B_{pk} in RD (Fig. 4-18) around 6mm wide slot ($\frac{s_w}{W}$ =0.2) at B_{pk} = 1.7 T in HGO material.

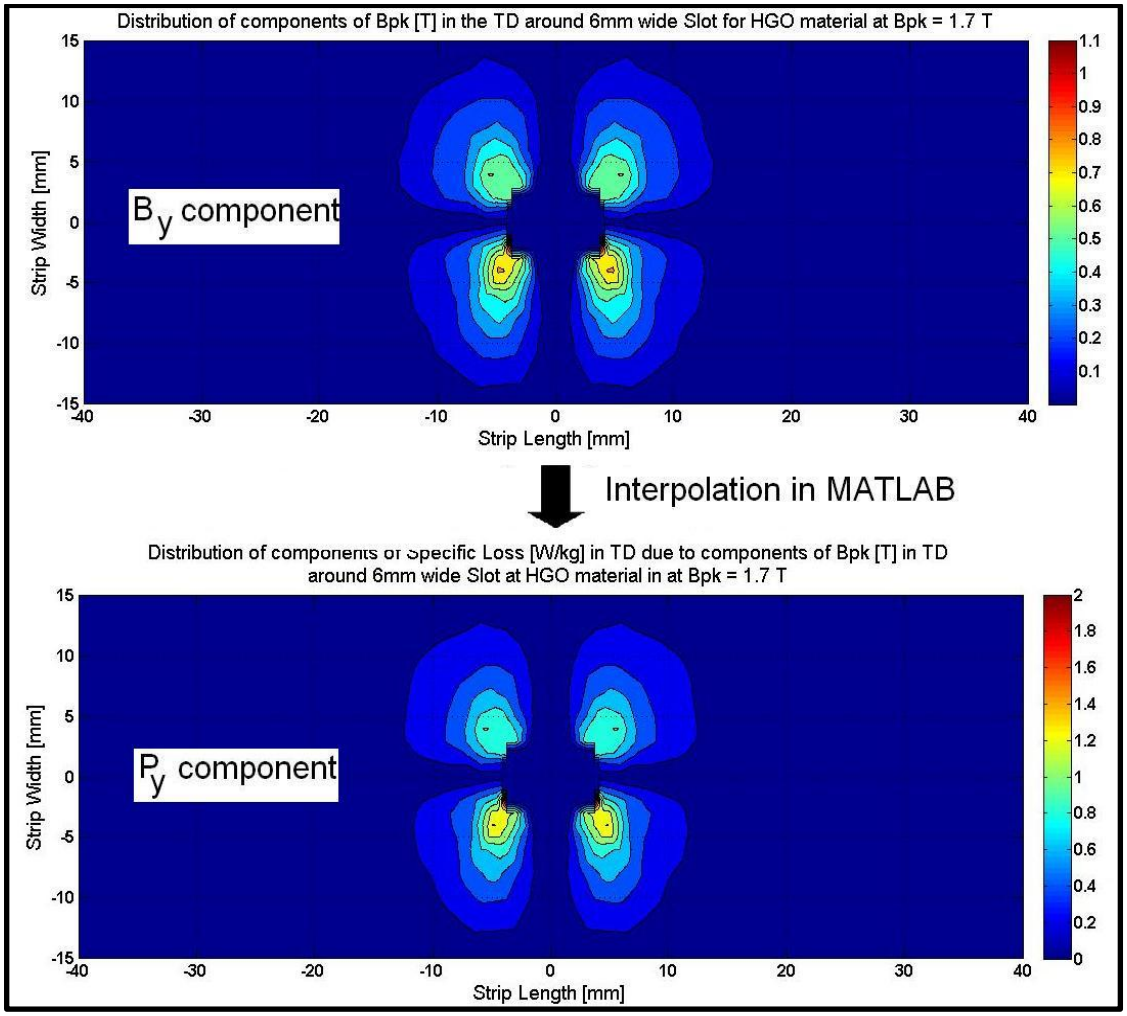

Fig. 4-21 Distribution of components of specific loss in TD interpolated from the components of B_{pk} in TD (Fig.4-19) around 6mm wide slot ($\frac{s_w}{W}$ =0.2) at B_{pk} = 1.7 T in HGO material.

Specific loss (P_s) in HGO and CGO for $\frac{d}{W}$ and $\frac{s_w}{W}$ values of 0.067, 0.133 and 0.2 at 1.3 T, 1.5 T and 1.7 T was calculated by arithmetic addition of P_x and P_y using equation (4.4) [54].

$$P_s = P_x + P_y \quad \left[\frac{W}{kg}\right] \tag{4.4}$$

P_s at $\frac{s_w}{W}$ value of 0.2 and B_{pk} = 1.7 T for HGO material is shown in Fig.4-22.

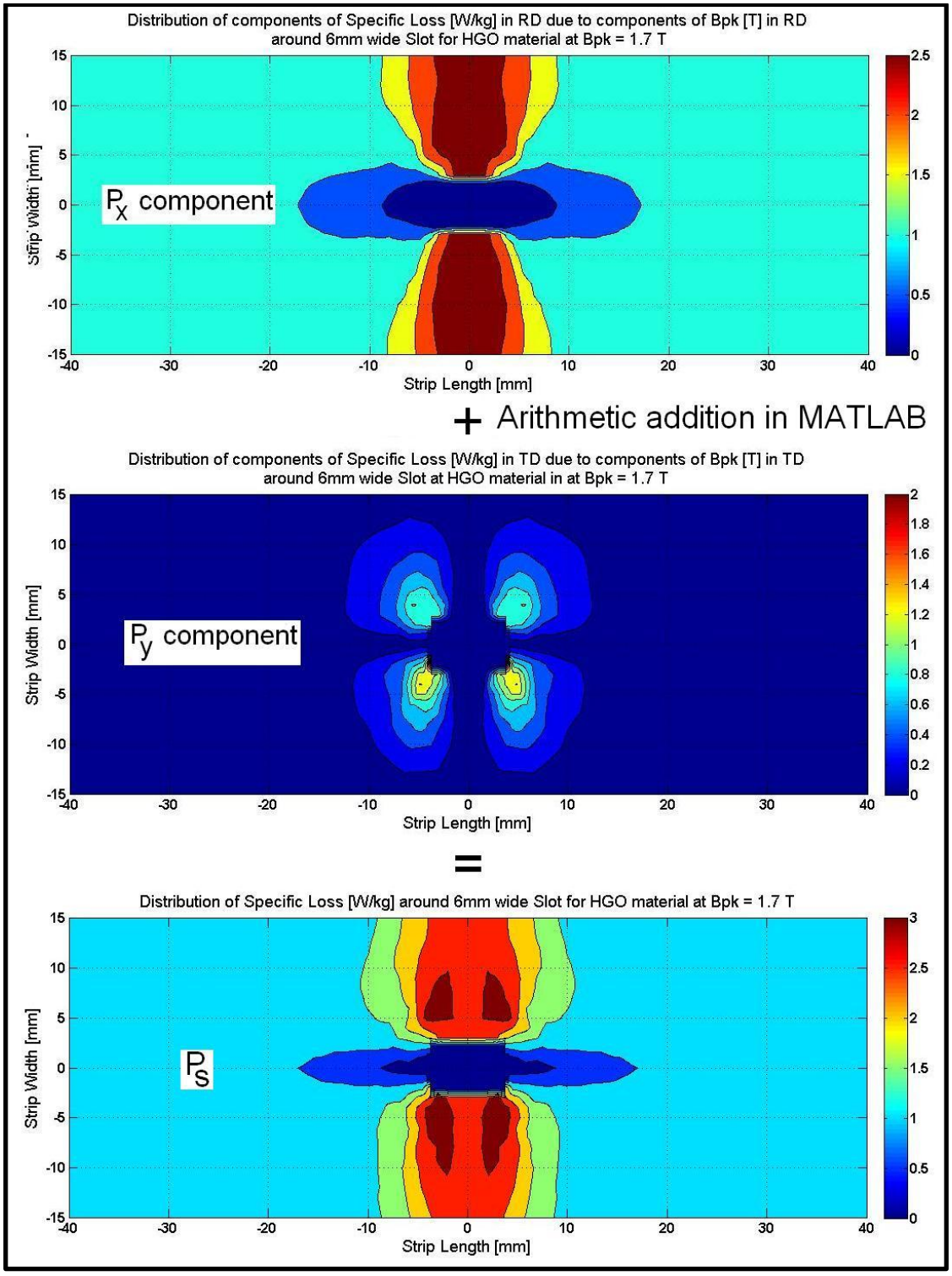

Fig. 4-22 Distribution of specific power loss around 6mm wide slot ($\frac{s_w}{W}$ =0.2) obtained from the arithmetic sum of the components of specific loss in RD and TD at B_{pk} = 1.7 T in HGO material.

The P_s distribution data points around the holes and slots were used to calculate the percentage increase in P_s around holes and slots in HGO and CGO for respective $\frac{d}{W}$

and $\frac{s_w}{W}$ values of 0.067, 0.133 and 0.2 at 1.3 T, 1.5 T and 1.7 T (**Appendix V**). The P_s distribution data points around the holes were averaged over the affected region of area $l_H * W$ to obtain P_{T_h}. The P_s distribution data points around the slots were averaged over the affected region of area $l_S . W$ to obtain P_{T_s}. Equation (4.5) was used to calculate the percentage increase in P_s around holes and equation (4.6) was used to calculate the percentage increase in P_s around slots.

$$\% \text{ increase in } P_s \text{ around the holes} = \left(\frac{P_{T_h} - P_s}{P_s}\right) . 100 \quad (4.5)$$

$$\% \text{ increase in } P_s \text{ around the slots} = \left(\frac{P_{T_s} - P_s}{P_s}\right) . 100 \quad (4.6)$$

The percentage increase in P_s around holes and slots in HGO and CGO for respective $\frac{d}{W}$ and $\frac{s_w}{W}$ values of 0.067, 0.133 and 0.2 at 1.3 T, 1.5 T and 1.7 T were extrapolated to saturation B_{pk} (2.03T) and interpolated for B_{pk} values from 0.01 T to 2.03 T in steps of 0.01 T. The resulting data of percentage increase in P_s was then interpolated for $\frac{d}{W}$ and $\frac{s_w}{W}$ range from 0 to 0.2 in steps of 0.001667. The results for percentage increase in P_s around holes for varying $\frac{d}{W}$ and B_{pk}, for HGO and CGO is shown in Fig. 4-23 and Fig. 4-24 respectively. The results for percentage increase in P_s around slots for varying $\frac{s_w}{W}$ and B_{pk}, for HGO and CGO is shown in Fig. 4-25 and Fig. 4-26 respectively.

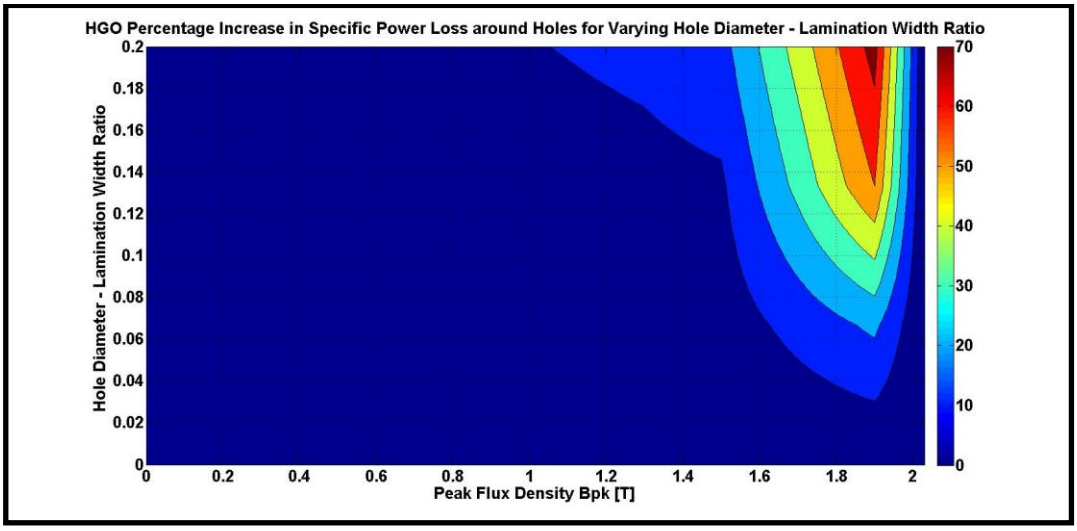

Fig. 4-23 Contour graph of percentage increase in P_s around holes for varying $\frac{d}{W}$ and B_{pk} in HGO material.

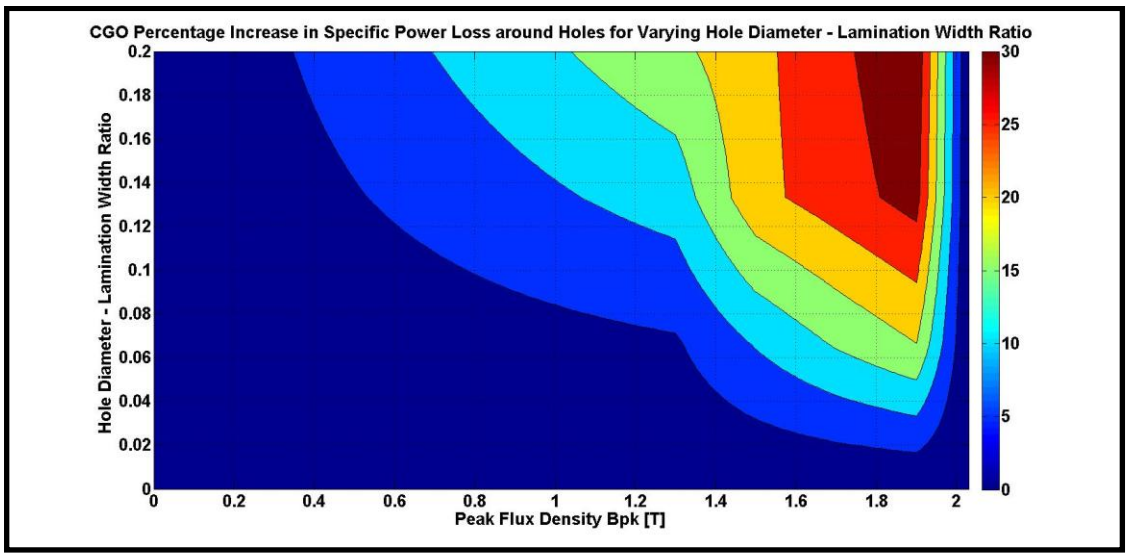

Fig. 4-24 Contour graph of percentage increase in P_s around holes for varying $\frac{d}{W}$ and B_{pk} in CGO material.

The contour graphs in Fig. 4-23 and Fig. 4-24 show the percentage increase in P_s for varying $\frac{d}{W}$ and B_{pk} values for HGO and CGO respectively. This data set can be used to compute the P_s averaged over the affected region length around holes at any B_{pk} value if the hole diameter d and lamination width W is known.

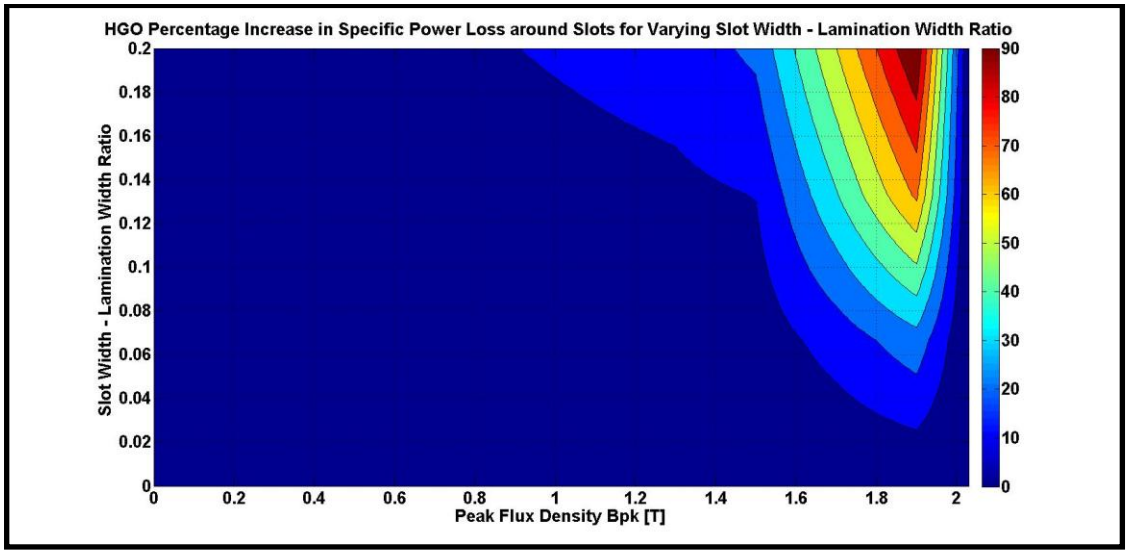

Fig. 4-25 Contour graph of percentage increase in P_s around slots for varying $\frac{s_w}{W}$ and B_{pk} in HGO material.

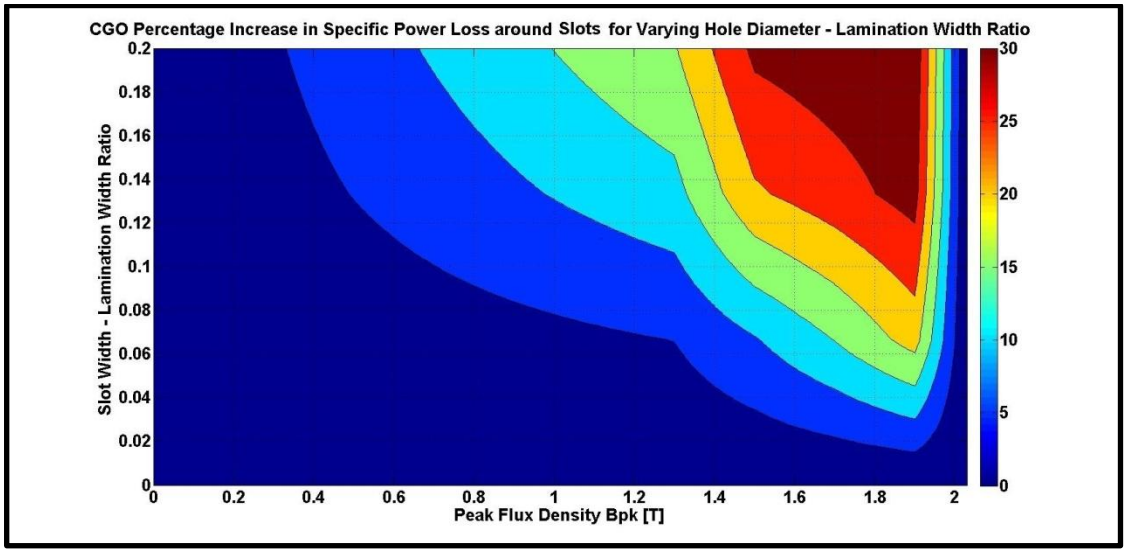

Fig. 4-26 Contour graph of percentage increase in P_s around slots for varying $\frac{s_w}{W}$ and B_{pk} in CGO material.

The contour graphs in Fig. 4-25 and Fig. 4-26 show the percentage increase in P_s for varying $\frac{s_w}{W}$ and B_{pk} values for HGO and CGO respectively. This data set can be used to compute the P_s averaged over the affected region length around slots at any B_{pk} value if the slot width s_W and lamination width W is known.

4.4.4 Percentage Decrease in Relative Permeability

The H_{pk} was obtained by interpolating the B_{pk} values for the H_{pk} values from the measured B_{pk} versus H_{pk} curve. The relative permeability (μ_r) was calculated from equation (4.7).

$$\mu_r = \frac{B_{pk}}{(\mu_o . H_{pk})} \tag{4.7}$$

The μ_r distribution data points around the holes were averaged over the affected region of area $l_H * W$ to obtain μ_{rH}. The μ_r distribution data points around the slots were averaged over the affected region of area $l_S * W$ to obtain μ_{rS}**.** Equation (4.8) was used to calculate the percentage decrease in μ_r around holes and equation (4.9) was used to calculate the percentage decrease in μ_r around slots.

$$\%\ \text{decrease in}\ \mu_r\ \text{around the holes} = \left(\frac{\mu_r - \mu_{rH}}{\mu_r}\right).100 \tag{4.8}$$

$$\%\ \text{decrease in}\ \mu_r\ \text{around the slots} = \left(\frac{\mu_r - \mu_{rS}}{\mu_r}\right).100 \tag{4.9}$$

The percentage decrease in μ_r around holes and slots in HGO and CGO for respective $\frac{d}{W}$ and $\frac{s_w}{W}$ values of 0.067, 0.133 and 0.2 at 1.3 T, 1.5 T and 1.7 T (**Appendix V**) were extrapolated to saturation B_{pk} (2.03T) and interpolated for B_{pk} values from 0.01 T to 2.03 T in steps of 0.01 T. The resulting data of percentage decrease in μ_r was then interpolated for $\frac{d}{W}$ and $\frac{s_w}{W}$ range from 0 to 0.2 in steps of 0.001667. The results for percentage decrease in μ_r around holes for varying $\frac{d}{W}$ and B_{pk}, for HGO and CGO is shown in Fig. 4-27 and Fig. 4-28 respectively. The results for percentage decrease in μ_r around slots for varying $\frac{s_w}{W}$ and B_{pk}, for HGO and CGO is shown in Fig. 4-29 and Fig. 4-30 respectively.

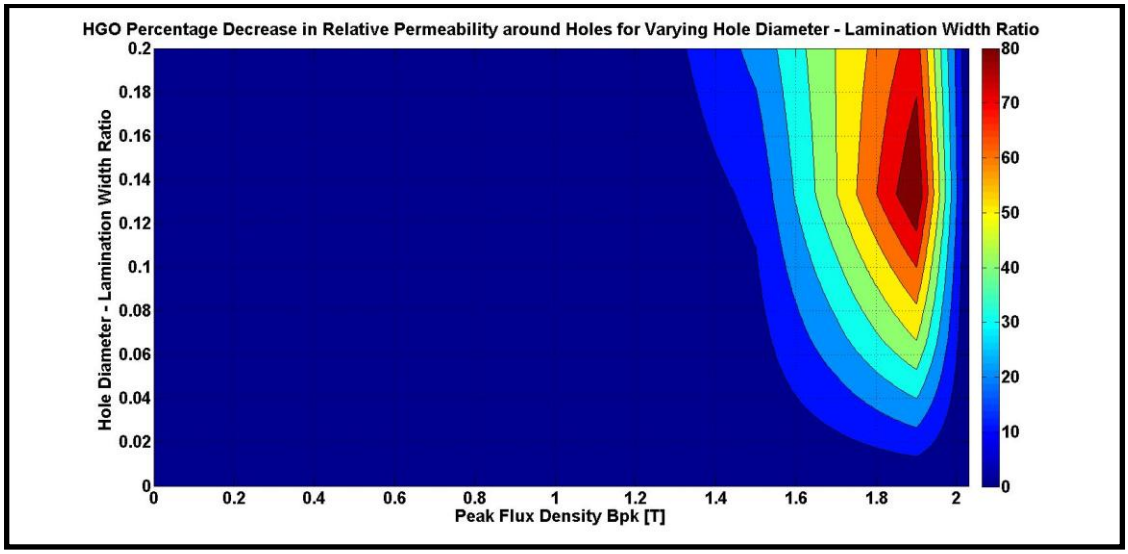

Fig. 4-27 Contour graph of percentage decrease in μ_r around holes for varying $\frac{d}{W}$ and B_{pk} in HGO material.

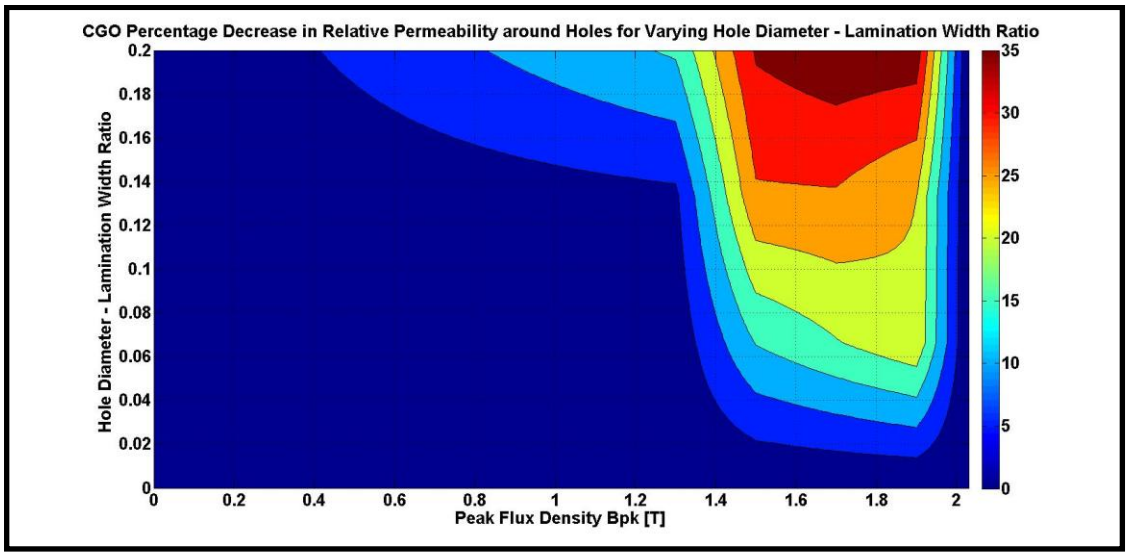

Fig. 4-28 Contour graph of percentage decrease in μ_r around holes for varying $\frac{d}{W}$ and B_{pk} in CGO material.

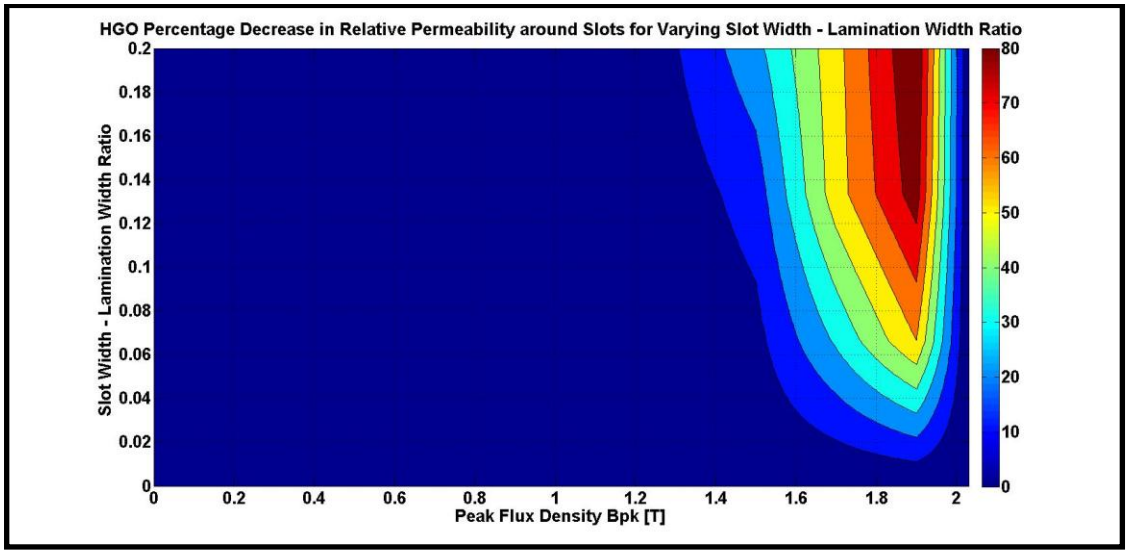

Fig. 4-29 Contour graph of percentage decrease in μ_r around slots for varying $\frac{s_w}{W}$ and B_{pk} in HGO material.

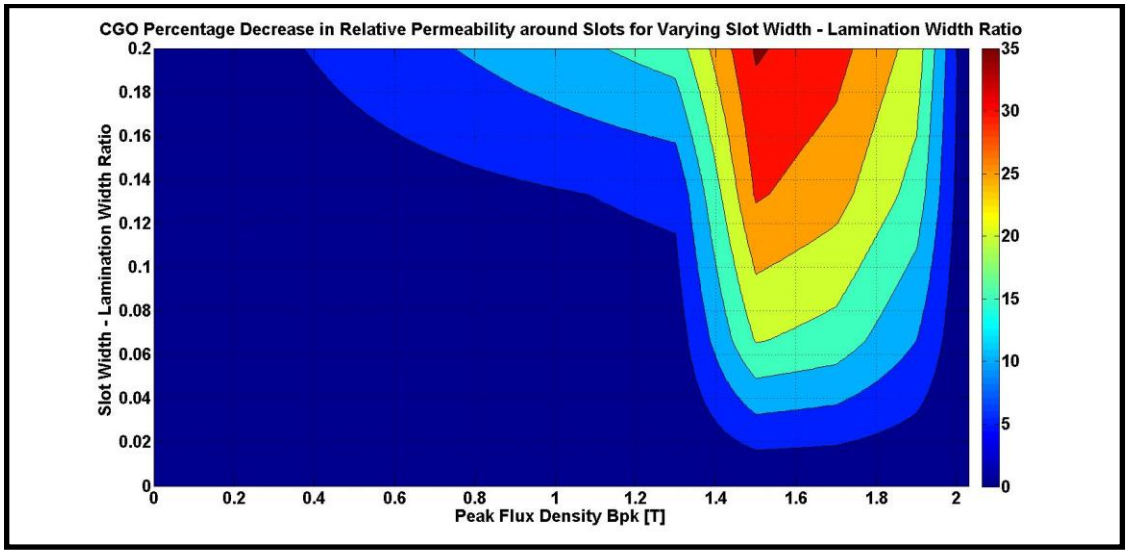

Fig. 4-30 Contour graph of percentage decrease in μ_r around slots for varying $\frac{s_w}{W}$ and B_{pk} in CGO material.

4.5 Discussion

4.5.1 Local Building Factor around Holes in HGO and CGO material

The percentage increase in P_s around holes in electrical steel laminations is a function of $\frac{d}{W}$, and B_{pk} in the HGO and CGO material and is shown in Fig.4-23 and Fig.4-24 respectively. The P_s increases as $\frac{d}{W}$ and B_{pk} increase for both HGO and CGO material because local saturation zones around holes and slots increase in area and magnitude due to flux crowding effect.

The local power loss was calculated using the derived data sets (Fig.4-23 and Fig.4-24) for the holes in the 50 mm, 130 mm and 160 mm packets of the full sized HGO and CGO 3-phase, 3-limb transformer cores.

The local building factor was obtained by dividing the local power loss by the nominal power loss of the material. The local building factors for a 10 mm hole in 50mm, 130mm and 160 mm wide packets for HGO and CGO is shown in Fig.4-31 and Fig.4-32.

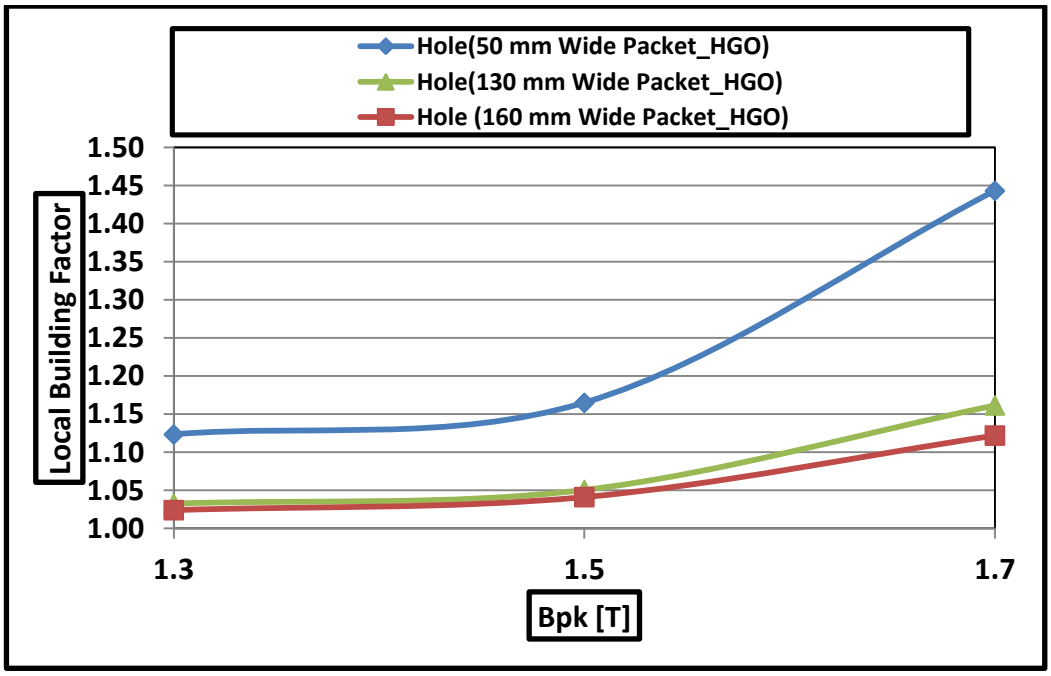

Fig. 4-31 Local building factor for a 10mm diameter hole in 50mm, 130 mm and 160 mm wide HGO transformer packets.

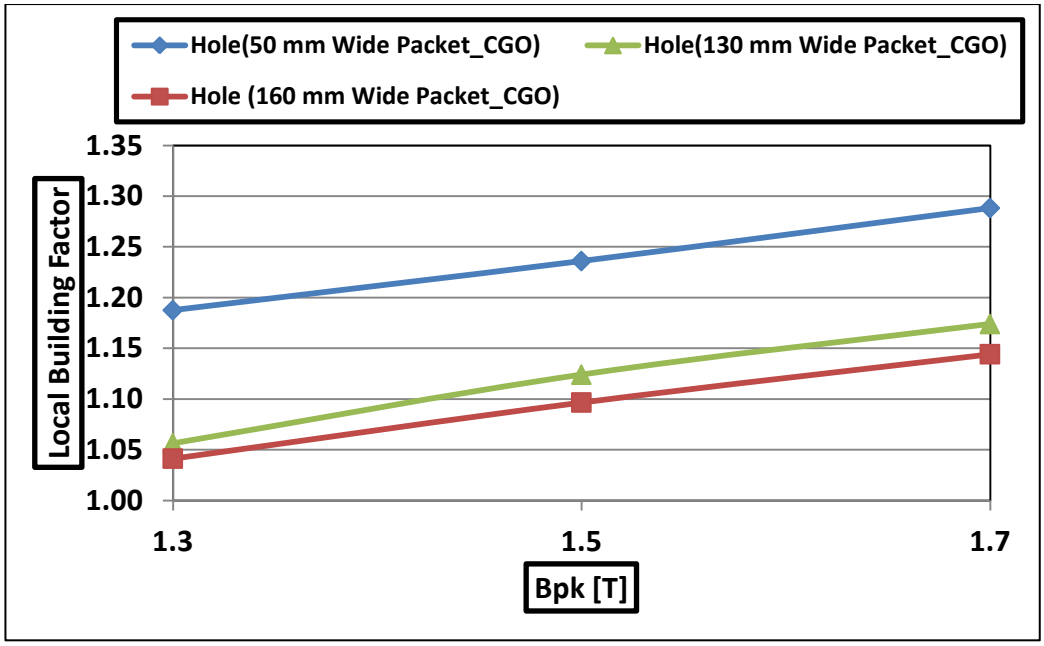

Fig. 4-32 Local building factor for a 10mm diameter hole in 50mm, 130 mm and 160 mm wide CGO transformer packets.

The local building factor due to a 10 mm hole is 24% and 28% higher for the 50 mm wide packet than that of the 130 mm and 160 mm wide packets in HGO material at 1.7 T. For CGO material, at 1.7 T, the local building factor of 50 mm wide packet was 10% and 12% higher than that of the 130 mm and 160 mm wide packets. The difference in local building factor around a 10 mm hole in 130 mm wide packet and 160 mm wide packet is marginal for low and medium flux densities in HGO material, but the difference increases by around 4% at 1.7 T. In CGO material, the difference between the local building factors in 130 mm and 160 mm wide packets is between 1-3% at low and medium flux densities.

The local building factor around holes in HGO material is higher than that of CGO at 1.7 T for higher $\frac{d}{W}$ because of lower affected region length (**Appendix V-section A & B**) which leads to higher losses. For lower $\frac{d}{W}$ ratios, the local building factor around holes in CGO is higher than HGO because of lower affected region length (**Appendix V-section A & B**). The affected region length around a 10mm hole in the 50 mm, 130 mm and 160 mm lamination width packets of the HGO and CGO cores was calculated using the data sets shown in Fig. 4-10 and Fig.4-11 respectively. The affected length at B_{pk} = 1.3 T, 1.5 T and 1.7 T is shown in Fig. 4-33, Fig. 3-34 and Fig. 4-35

respectively. The affected region length can be measured using thermal sensors and thermal imaging techniques [71].

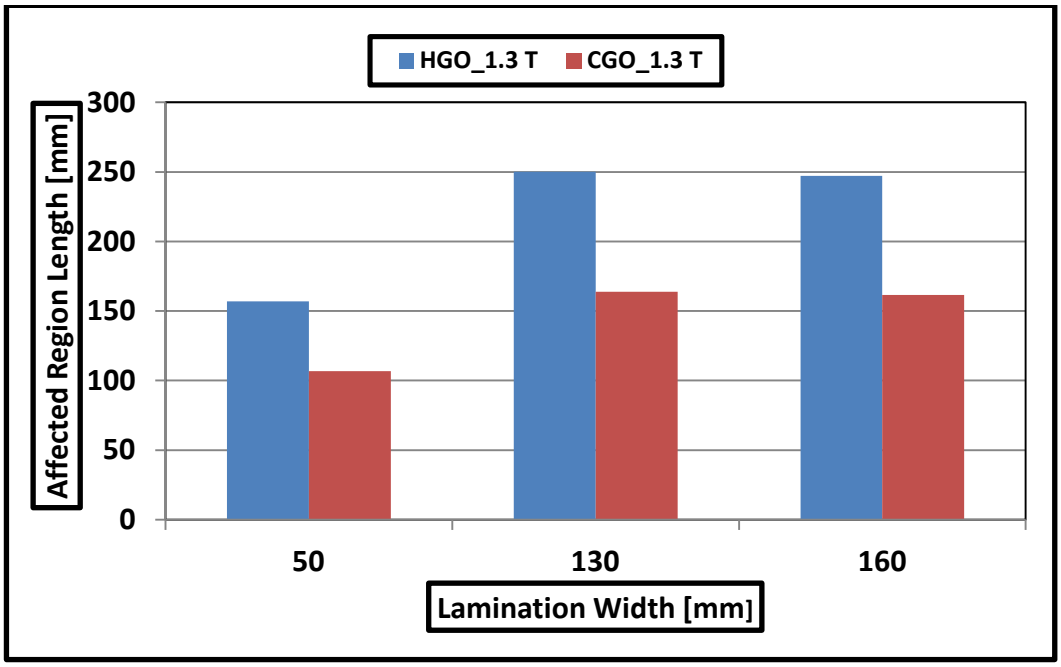

Fig. 4-33 Affected region length for a 10mm diameter hole in 50mm, 130 mm and 160 mm wide HGO and CGO transformer packets at B_{pk} = 1.3 T.

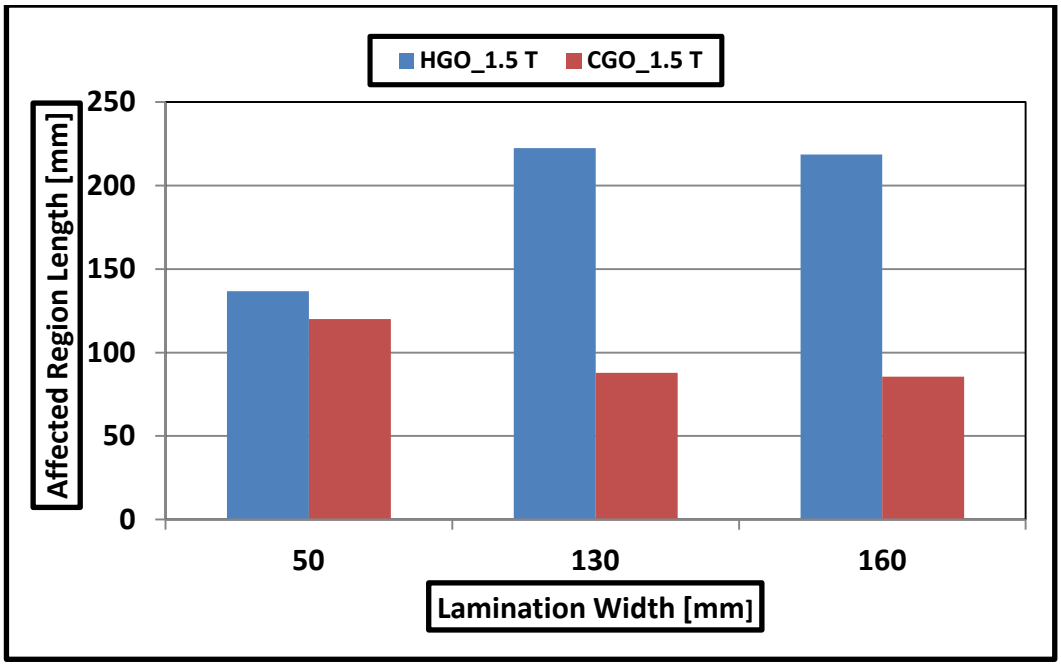

Fig. 4-34 Affected region length for a 10mm diameter hole in 50mm, 130 mm and 160 mm wide HGO and CGO transformer packets at B_{pk} = 1.5 T.

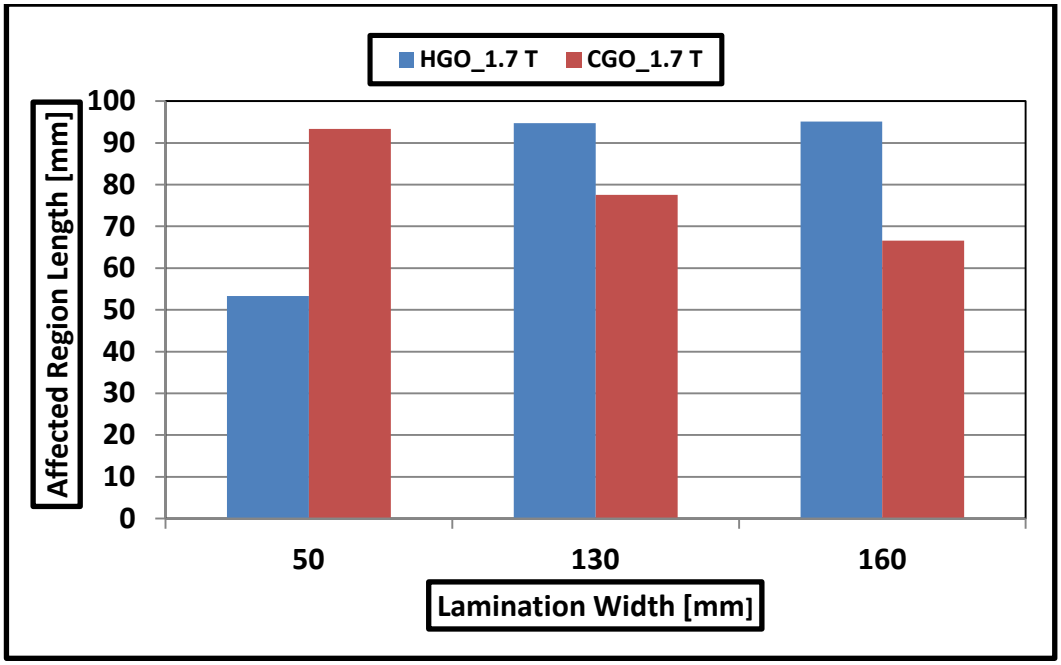

Fig. 4-35 Affected region length for a 10mm diameter hole in 50mm, 130 mm and 160 mm wide HGO and CGO transformer packets at B_{pk} = 1.7 T.

4.5.2 Local Building Factor around Slots in HGO and CGO material

The percentage increase in P_s around slots in electrical steel laminations is a function of $\frac{s_w}{W}$ and B_{pk} in the HGO and CGO material and is shown in Fig.4-25 and Fig.4-26 respectively. The P_s increases as $\frac{s_w}{W}$ and B_{pk} increase for both HGO and CGO material.

Similar to the holes, the P_s increase for HGO material due to slots is more than the P_s increase in CGO material as components of P_s in TD (P_y) in HGO is higher.

The local power loss and building factor was calculated using the data sets (Fig.4-25 and Fig.4-26) in a similar way to holes. The local building factors for a 10 mm wide slot in 50mm, 130mm and 160 mm wide packets for HGO and CGO is shown in Fig. 4-36 and Fig. 4-37.

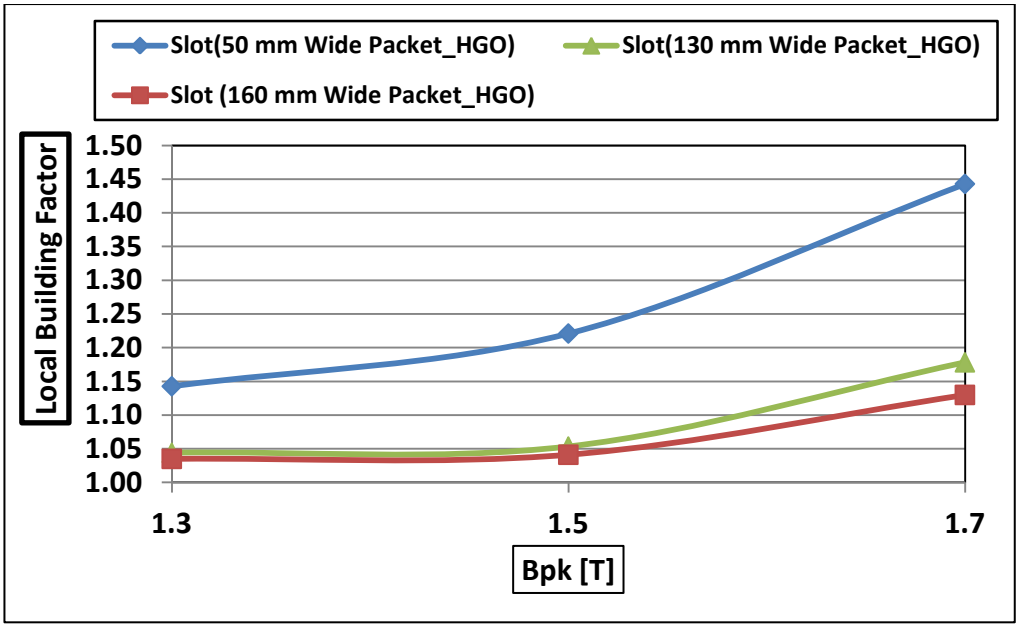

Fig. 4-36 Local building factor for a 10mm wide slot in 50mm, 130 mm and 160 mm wide HGO transformer packets.

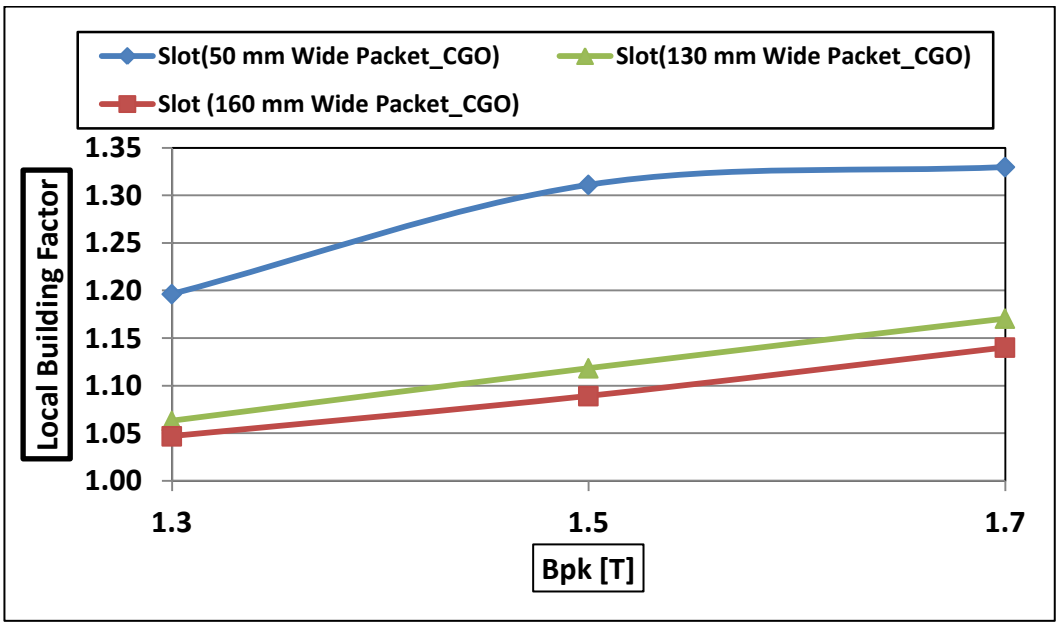

Fig. 4-37 Local building factor for a 10mm wide slot in 50mm, 130 mm and 160 mm wide CGO transformer packets.

The local building factor due to a 10 mm wide slot is 22% and 28% higher for the 50 mm wide packet than that of the 130 mm and 160 mm wide packets in HGO material at 1.7 T. For CGO material, at 1.7 T, the local building factor of 50 mm wide packet was 14% and 17% higher than that of the 130 mm and 160 mm wide packets. The

difference in local building factor around a 10 mm wide slot in 130 mm wide packet and 160 mm wide packet is marginal for low and medium flux densities in HGO material, but the difference increases by around 3% at 1.7 T. In CGO material, the difference between the local building factors in 130 mm and 160 mm wide packets is between 1-3% at low and medium flux densities.

The P_s increase due to slots in HGO and CGO material slightly is higher as compared to P_s increase due to holes for similar $\frac{s_w}{W}$ and $\frac{d}{W}$ as the length of the slot $\left(\sqrt{2}.s_w\right)$ is longer than the diameter of the hole (d). The local saturation zones around slots are longer as compared to holes and thus yield higher P_s.

The local building factor around slots in HGO material is higher than that of CGO at 1.7 T for higher $\frac{s_w}{W}$ because of lower affected region length (**Appendix V-section A & B**) which leads to higher losses. Similar to the observed local building factors around holes in HGO and CGO materials, for lower $\frac{s_w}{W}$ ratios the local building factor around slots in CGO is higher than HGO because of lower affected region length (**Appendix V-section A & B**). The affected region length around a 10mm wide slot in the 50 mm, 130 mm and 160 mm lamination width packets of the HGO and CGO cores was calculated using the data sets shown in Fig. 4-12 and Fig.4-13 respectively. The affected length at B_{pk} = 1.3 T, 1.5 T and 1.7 T is shown in Fig. 4-38, Fig. 4-39 and Fig. 4-40 respectively.

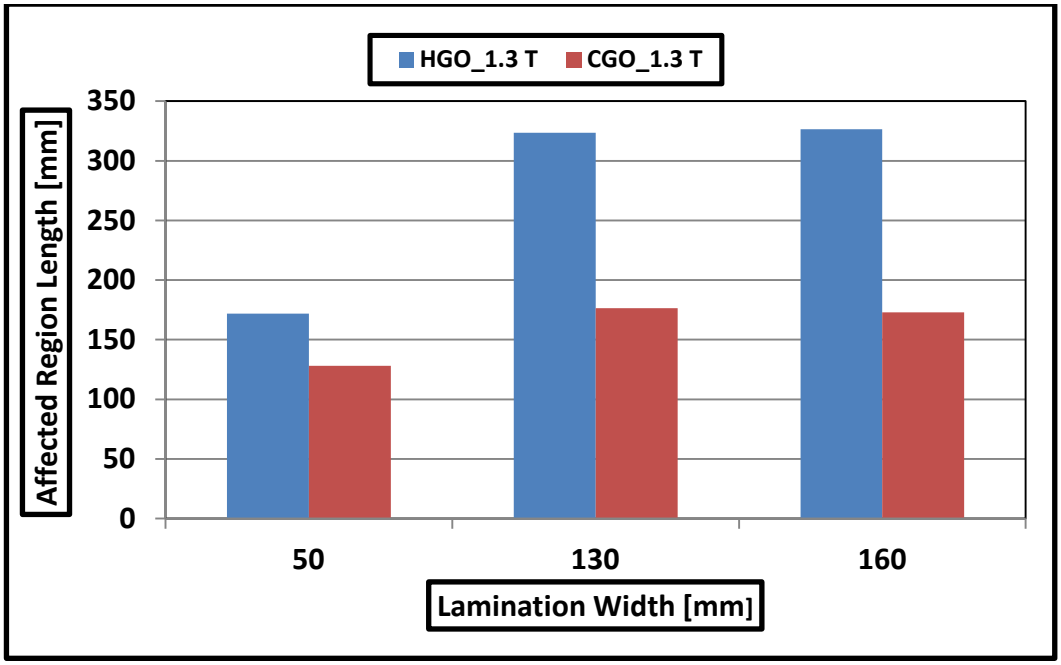

Fig. 4-38 Affected region length for a 10mm wide slot in 50mm, 130 mm and 160 mm wide HGO and CGO transformer packets at B_{pk} = 1.3 T.

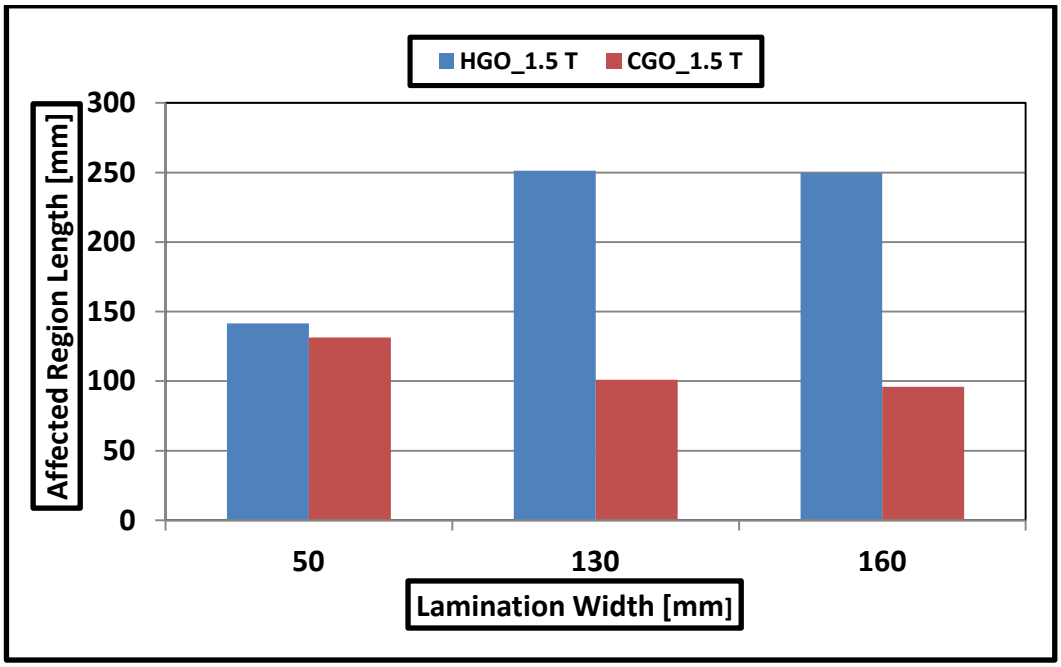

Fig. 4-39 Affected region length for a 10mm wide slot in 50mm, 130 mm and 160 mm wide HGO and CGO transformer packets at B_{pk} = 1.5 T.

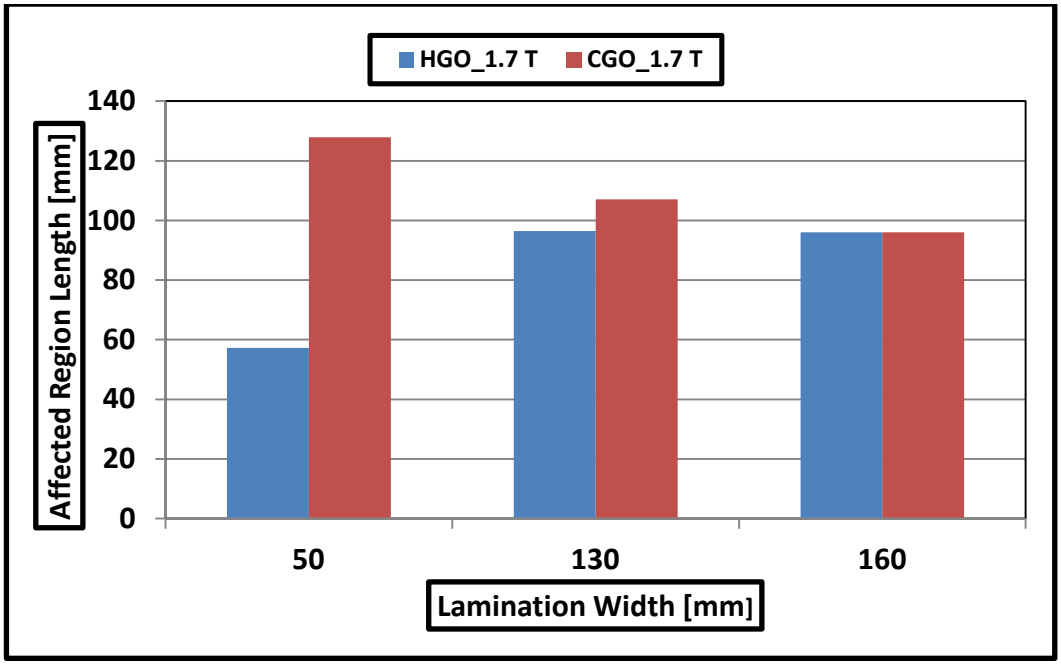

Fig. 4-40 Affected region length for a 10mm wide slot in 50mm, 130 mm and 160 mm wide HGO and CGO transformer packets at B_{pk} = 1.7 T.

4.5.3 Local Relative Permeability around Holes in HGO and CGO material

The percentage decrease in μ_r around holes in electrical steel laminations is a function of $\frac{d}{W}$ and B_{pk} in the HGO and CGO material and is shown in Fig.4-27 and Fig.4-28 respectively. The local relative permeability was calculated using the derived data sets (Fig.4-27 and Fig.4-28). The calculated local relative permeability values for a 10 mm diameter hole in 50mm, 130mm and 160 mm lamination width packets for HGO and CGO cores are shown in Fig. 4-41 and Fig. 4-42.

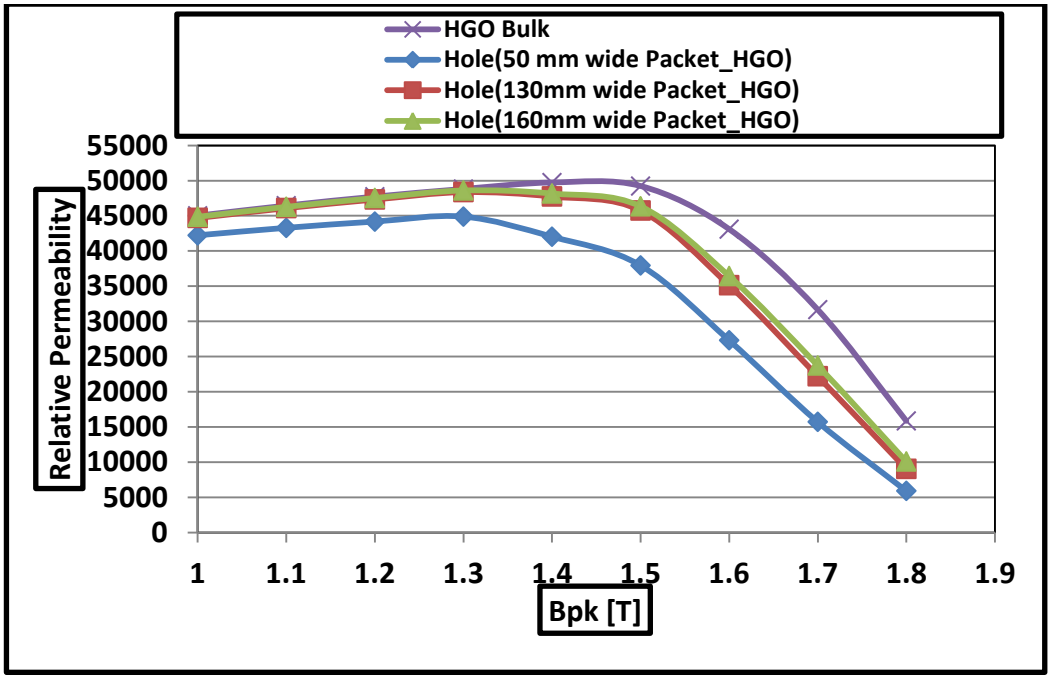

Fig. 4-41 Bulk permeability versus local relative permeability (due to 10mm diameter hole in 50mm, 130 mm and 160 mm wide HGO transformer packets).

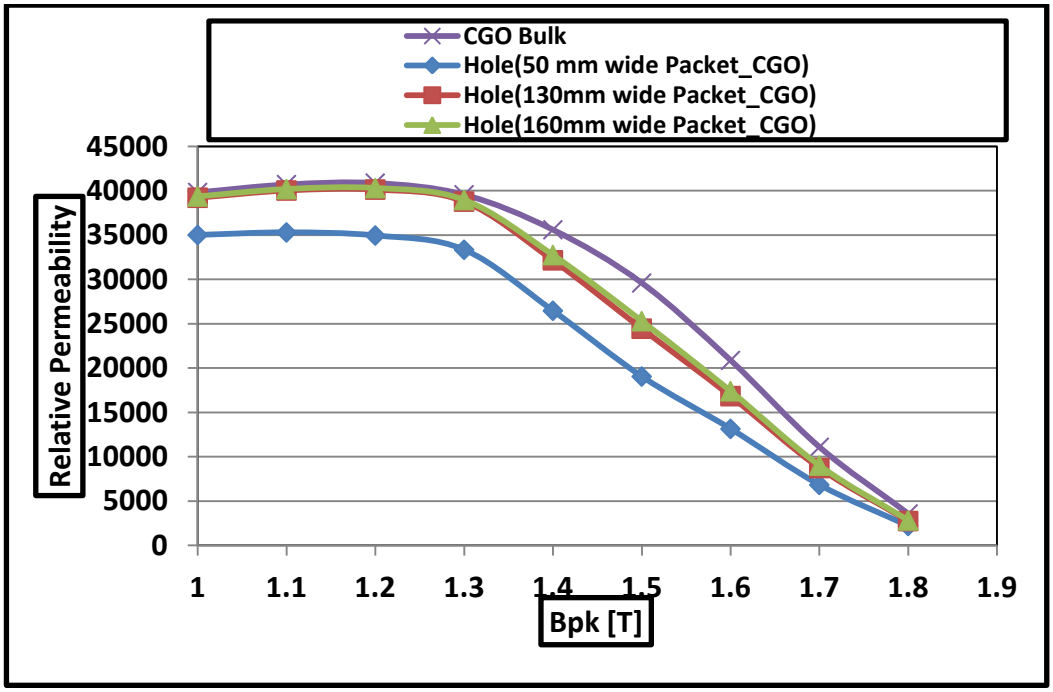

Fig. 4-42 Bulk permeability versus local relative permeability (due to 10mm diameter hole in 50mm, 130 mm and 160 mm wide CGO transformer packets).

The μ_r decreases as $\frac{d}{W}$ and B_{pk} increase for both HGO and CGO material because of increased B_{pk} distribution around the holes yielding in lower values of μ_r.

4.5.4 Local Relative Permeability around Slots in HGO and CGO material

The percentage decrease in μ_r around slots in electrical steel laminations is a function of $\frac{s_w}{W}$ and B_{pk} in the HGO and CGO material and is shown in Fig.4-29 and Fig.4-30 respectively. The μ_r decreases as $\frac{s_w}{W}$ and B_{pk} increase for both HGO and CGO material because of increased B_{pk} distribution around the slots yielding in lower values of μ_r.

The μ_r decrease in HGO and CGO material due to slots are higher as compared to μ_r decrease due to holes for similar $\frac{s_w}{W}$ and $\frac{d}{W}$ values as the length of the slot $(\sqrt{2}.s_w)$ is longer than the diameter of the hole (d). Regions of high H_{pk} around slots are longer as compared to holes and thus yield lower μ_r.

The local relative permeability was calculated using the derived data sets (Fig.4-29 and Fig.4-30). The calculated local relative permeability values for a 10 mm wide slot in 50mm, 130mm and 160 mm wide packets for HGO and CGO cores are shown in Fig. 4-43 and Fig. 4-44.

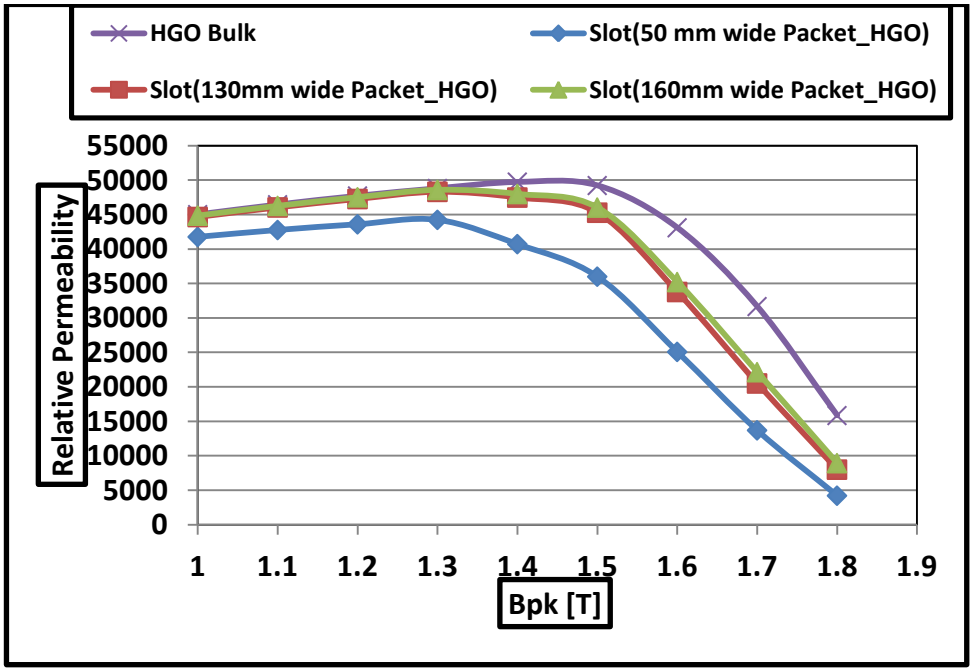

Fig. 4-43 Bulk permeability versus local relative permeability (due to 10mm wide slot in 50mm, 130 mm and 160 mm wide HGO transformer packets).

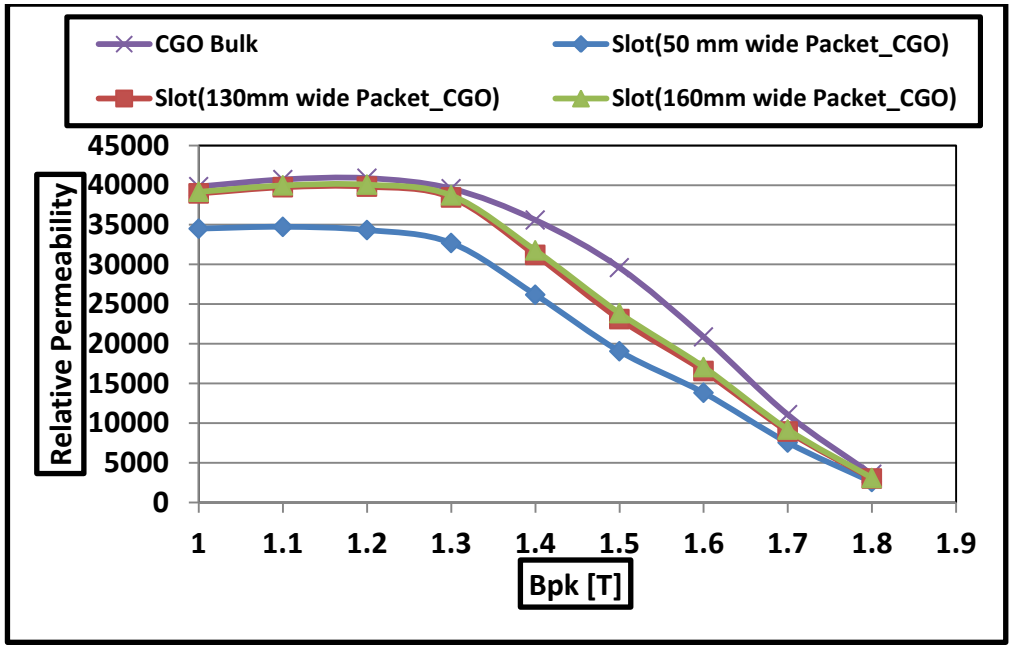

Fig. 4-44 Bulk permeability versus local relative permeability (due to 10mm wide slot in 50mm, 130 mm and 160 mm wide CGO transformer packets).

4.5.5 Other Factors affecting Predicted Results

The software package INFOLYTICA MAGNET was used to obtain the B_{pk} distribution around holes and slots. This software allows the user to input only the B-H characteristics along RD and TD. But in grain oriented electrical steel, the losses vary when magnetised at various angles to RD as shown in Fig.4-45 [72].

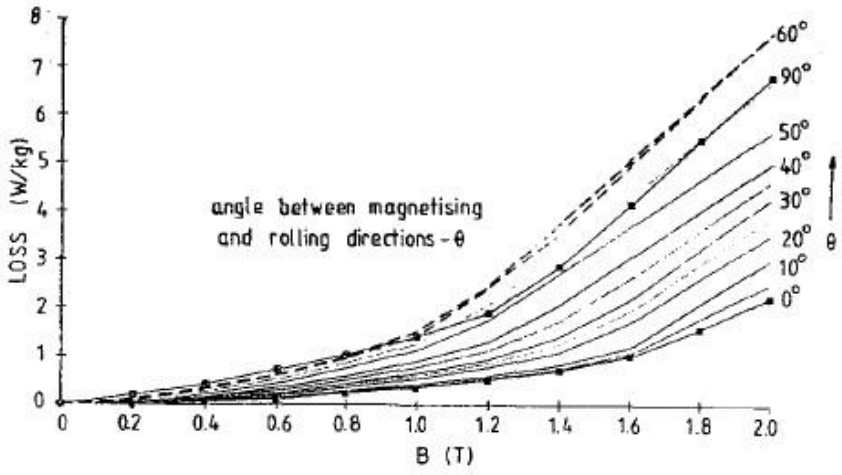

Fig. 4-45. The power loss variation when magnetised at various angles to the RD in grain oriented electrical steel [72].

The FE method also does not include factors like the effect of stresses on the power loss in electrical steel shown in Fig. 4-46 [73].

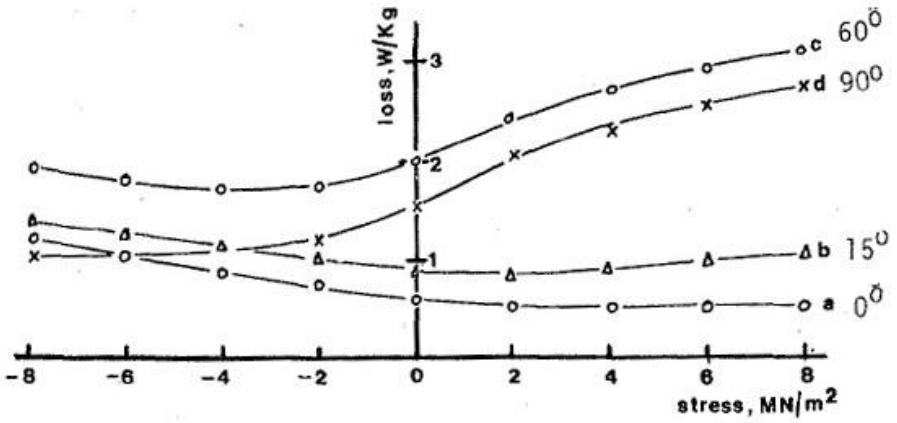

Fig. 4-46 The variation of power loss with stress in grain oriented electrical steel when magnetised at various angles to the RD [73].

4.6 Summary

The flux density distribution was simulated around 2mm, 4mm and 6mm diameter holes and 2mm, 4mm and 6mm wide slots for HGO and CGO at 1.3 T, 1.5 T and 1.7 T. The spatial data of flux density was used to generate data sets for power loss increase, permeability decrease and length of the uneven flux distribution for holes and slots in HGO and CGO material.

The estimated local building factor around the 10 mm diameter hole in the 50 mm HGO packet of the transformer core was 28 % higher than the 10 mm diameter holes in the HGO 160 mm packets at 1.7 T. For CGO, it was 12%. The estimated local building factor around the 10 mm wide slot in the 50 mm HGO packet of the transformer core was 28 % higher than the 10 mm wide slot in the HGO 160 mm packets at 1.7 T. For CGO, it was 17%. The estimated local building factor increases with increasing B_{pk}, $\frac{d}{W}$ and $\frac{s_w}{W}$ values.

The estimated local relative permeability around the 10 mm diameter hole in the 50 mm packet of the transformer core was 33 % lower than the 10 mm diameter holes in the 160 mm packet at 1.7 T. For CGO, it was 24%. The estimated local relative permeability around the 10 mm wide slot in the 50 mm packet of the

transformer core was 38 % lower than the 10 mm wide slot in the 160 mm packet at 1.7 T. For CGO, it was 17%. The estimated local relative permeability decreases with increasing B_{pk}, $\frac{d}{W}$ and $\frac{s_w}{W}$ values.

Chapter 5

Algorithm to Predict No-Load Specific Loss of Stacked HGO and CGO Three-Phase, Three-Limb Cores.

5.1 Introduction

An algorithm to predict losses in 3-phase, 3-limb HGO and CGO cores for B_{pk} =1.5 T – 1.8 T was built in NI LabVIEW 10 software considering the nominal loss, B-H characteristics, packet to packet variation of B_{pk}, localised loss data sets, affected regions and the overall geometry. The data on packet to packet variation in B_{pk} was obtained from the investigation in **Chapter 2**. Data sets for affected regions and losses of bolt holes and slots were obtained from the investigation in **Chapter 4**. Measurements were made to obtain the rotational loss for HGO and CGO material to generate rotational loss data sets. The affected regions for the rotational loss were sourced from literature. The corner joint affected regions were sourced from literature. The predicted losses were compared with the measured losses of 3-phase, 3-limb HGO and CGO multi packet and single packet cores. Losses were also predicted for multi-packet HGO and CGO cores without bolt holes and slots.

5.2 Algorithm Methodology

LabVIEW software was chosen because it has a graphical interface, allowing the user to visually identify and modify the errors in the program. A flow chart of the algorithm is shown in Fig. 5-1. The algorithm uses the user input and calculates the core mass and mass of the affected regions of the localised losses. Packet to packet variation of flux density data is used to establish the flux density in each packet corresponding to the hole diameter (slot width) lamination width ratio. The flux density in each packet is then interpolated for specific loss from the Epstein loss curve. The interpolated specific loss then serves as the reference for further calculations of the localised losses which are expressed in terms of percentage

increase in loss. The localised losses were optimised to obtain the specific loss of the HGO and CGO cores within 2% of the measured values.

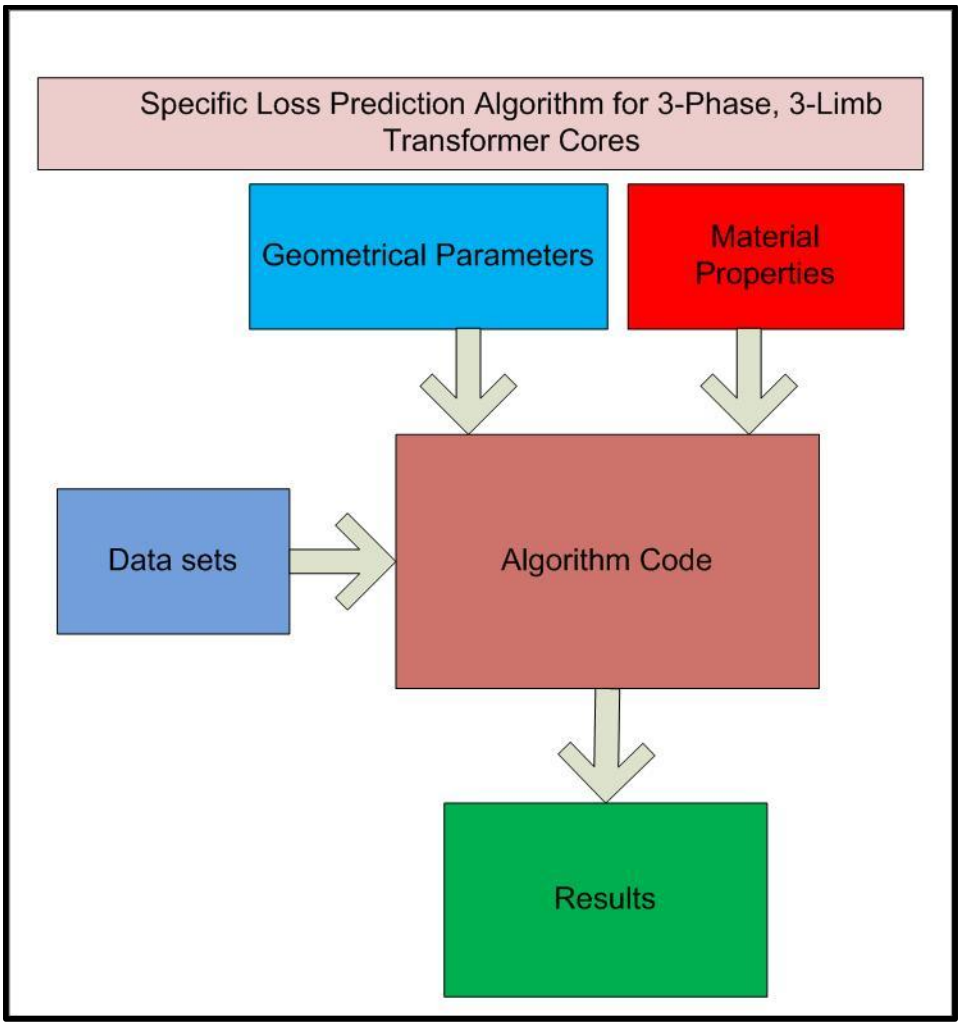

Fig.5-1 Flow chart of the specific loss prediction model.

The input parameters to the algorithm are:

- Core Width (C_W)
- Core Height (C_H)
- Packet Lamination Width (W)
- Packet Thickness (T_P)
- Stacking Factor (K)
- Number of step laps (N_S)
- Overlap length (l_o)
- Hole diameter (d)

- Number of holes (m)
- Number of packets in the core (N_p)
- Slot width (s_W)
- Number of slots (n)
- B-H curve for the material
- Nominal loss for the material

5.3 Mass calculations

5.3.1 Mass of the 3-Phase, 3-Limb Transformer Core

The geometrical parameters were used to calculate the volume of the packets which make up the core. The overall core geometry used for the calculations is shown in Fig.5-2. Then the mass of the packets was calculated by multiplying the volumes by the mass density (ρ) (7650 $\left[\frac{kg}{m^3}\right]$ [15] of the electrical steel and stacking factor (K)(0.97 [15]). The results were arithmetically added to obtain the total mass of the core.

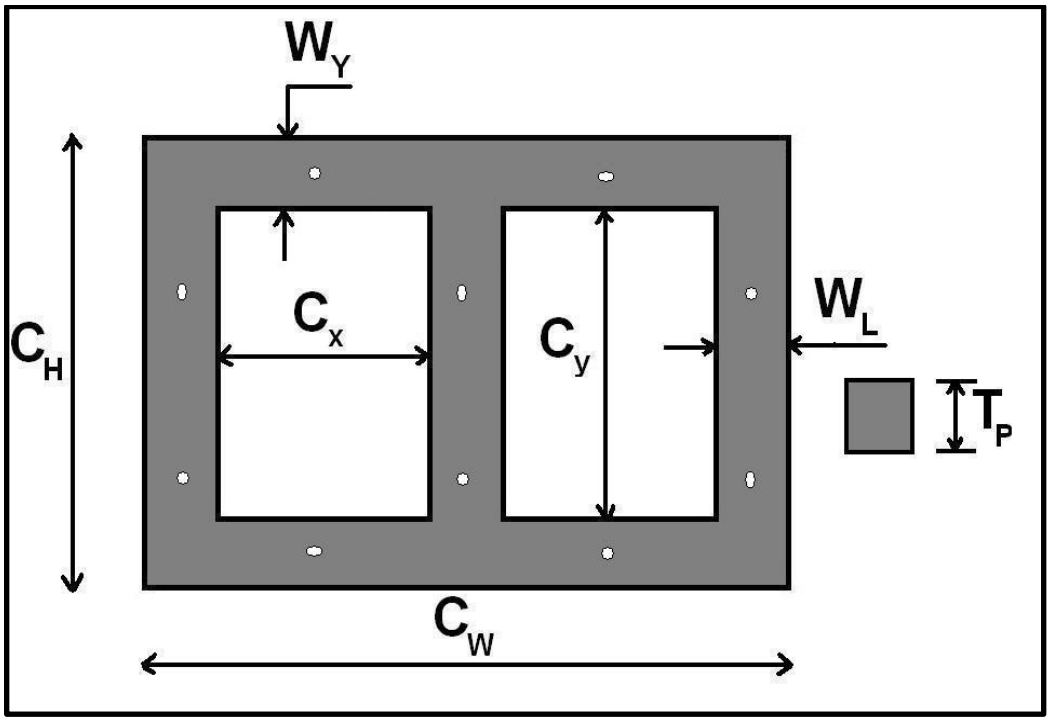

Fig.5-2 Schematic view of the geometry used to calculate the volume of the 3-phase, 3-limb transformer core.

Volume of the core window,

$$V_E = 2.\left(C_x.C_y.T_P\right) \quad [m^3] \tag{5.1}$$

$But\ 2C_x = C_W - (3W_L)$

&

$$C_y = (C_H - 2W_Y)$$

where C_x is the core window width and C_y is the core window height.

Substituting the values of $2C_x$ and C_y in equation (5.1),

$V_E = \left(C_W - (3W_L)\right).(C_H - 2W_Y).T_P$

For $W_L = W_Y = W$,

$$V_E = \left(C_W - (3W)\right) * (C_H - 2W).T_P \ [m^3] \tag{5.2}$$

Volume of holes,

$$V_h = \left[m.\left(\frac{\pi.d^2}{4}\right)\right].T_P \ [m^3] \tag{5.3}$$

Volume of slots,

$$V_s = \left[n.\left(\frac{\pi.s_w{}^2}{2} - \left(\frac{\pi.s_w{}^2}{4} - \frac{s_w{}^2}{4}\right)\right)\right].T_P \quad [m^3] \tag{5.4}$$

The area of slot is derived in **Appendix VI.**

Volume of core,

$$V_{core} = \left((C_W.C_H.T_P) - (V_E + V_h + V_s)\right).T_P \quad [m^3] \tag{5.5}$$

Total mass of core,

$$m_{core} = \sum_1^{N_p}\left(\left((C_W.C_H.T_P) - (V_E + V_h + V_s)\right).T_P\right).\rho.K\ \Big) \ [kg] \tag{5.6}$$

5.3.2 Mass of the Affected regions due to Holes and Slots

The affected region due to holes and slots is discussed in **Chapter 2**. The mass of the affected region is required to calculate the localised specific loss due to holes and the slots. The algorithm uses the following input parameters to calculate the mass of the affected regions due to holes and slots:

- Number of holes (m)
- Number of slots (n)
- Hole diameter (d)
- Slot width (s_w)
- Packet width (W)

The algorithm calculates the $\frac{d}{W}$ ratio and $\frac{s_w}{W}$ ratio and reads the corresponding $\frac{l_H}{d}$ ratio and $\frac{l_S}{s_l}$ ratio from the data sets (**Chapter 4**). The algorithm then calculates l_H from the equation (5.7) and l_S from the equation (5.8) respectively.

$$l_H = \left(\frac{l_H}{d}\right).d \quad [m] \tag{5.7}$$

$$l_S = \left(\frac{l_S}{s_l}\right).s_l = \left(\frac{l_S}{s_l}\right).\left(\sqrt{2}.s_w\right) \quad [m] \tag{5.8}$$

The total mass of the affected regions due to $'m'$ holes and $'n'$ slots is then calculated by subtracting the hole and slot volumes from the affected region volumes using equations (5.9) and (5.10) respectively.

$$m_{hole} = \sum_1^{N_p}\left(\left((m.l_H.W) - \left(m.\left(\frac{\pi.d^2}{4}\right)\right)\right).T_P.\rho.K\right)[kg] \tag{5.9}$$

$$m_{slot} = \sum_1^{N_p}\left(\left((n.l_S.W) - \left(n.\left(\frac{\pi.s_w{}^2}{2} - \left(\frac{\pi.s_w{}^2}{4} - \frac{s_w{}^2}{4}\right)\right)\right)\right).T_P.\rho.K\right)[kg] \tag{5.10}$$

5.3.3 Mass of the Affected region due to Rotational Loss

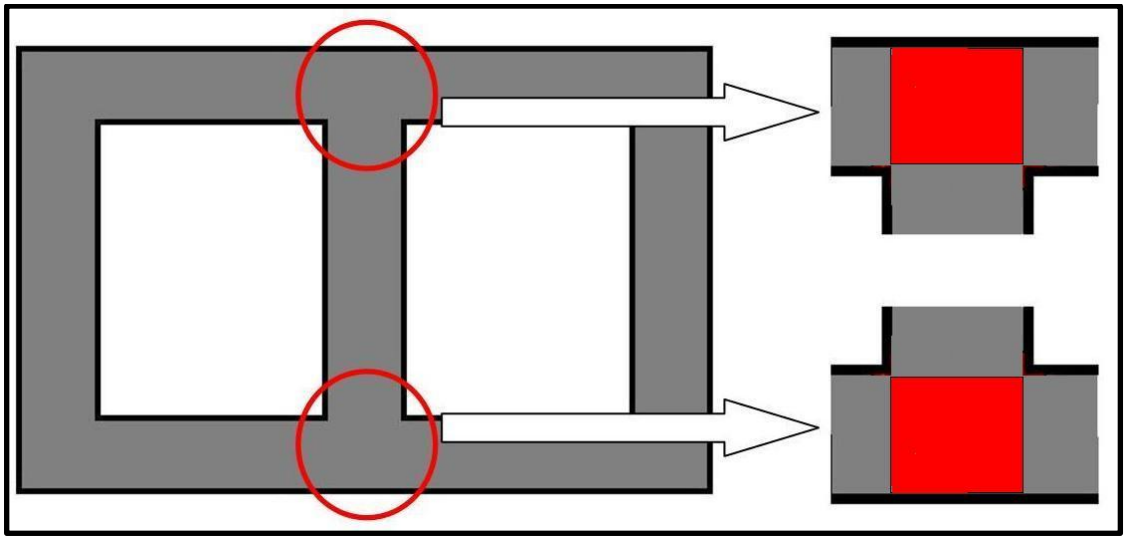

Fig.5-3 Schematic view of the geometry used to calculate the volume of the affected region due to rotational loss in a 3-phase, 3-limb transformer core T- joint.

Mass of the affected region due to rotational loss from Fig. 5-3,

$m_{rot} = 2.(W_L.W_Y.T_P.K)$

For $W_L = W_Y = W$,

$$m_{rot} = \sum_1^{N_p}\left(2.(W^2.T_P.K)\right)\ [kg] \tag{5.11}$$

Mass of the Affected region due to Corner Joint Losses

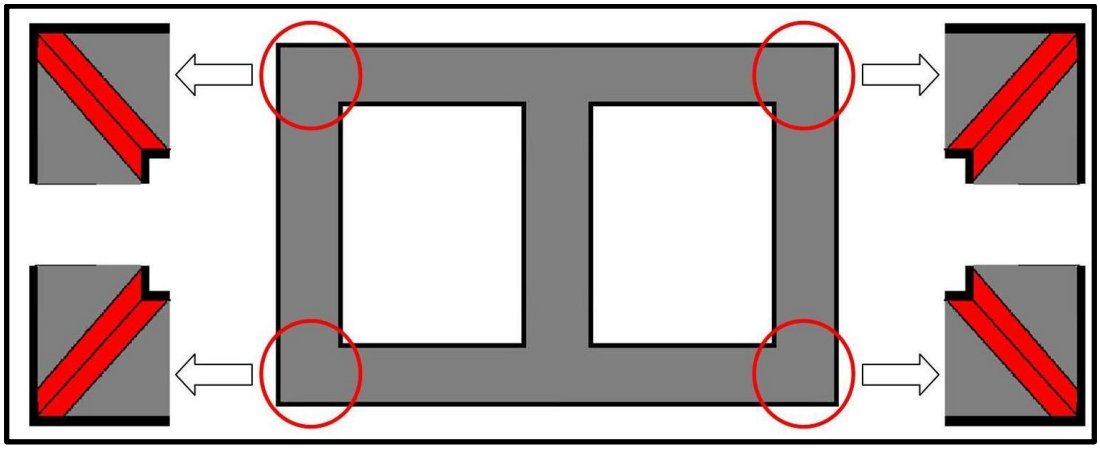

Fig.5-4 Schematic view of the geometry used to calculate the volume of the affected region due to joint loss in a 3-phase, 3-limb transformer core corner joint.

Mass of the affected region due to corner joint losses from Fig. 5-4,

$$m_{cj} = \sum_{1}^{N_p} \left(4.\left(\sqrt{2}.W.N_s.(l_o + 0.005).T_P.\rho.K\ \right)\right)\ [kg] \quad (5.12)$$

The assumed affected length (0.005) in m is from [74].

5.3.4 Mass of the regions with Flux in RD (Bulk regions)

Mass of the regions with flux in the RD,

$$m_{RD} = \sum_{1}^{N_p} \Bigg(\Bigg(\Bigg(\Big((C_W.C_H.T_P) - (V_E + V_h\ + V_s\ )).T_P\Big)\ .\rho.K\ \Bigg) - \Big(\big((m.l_H.W.T_P)\ .\rho.K\big) + \big((n.l_S.W.T_P)\ .\rho.K\big) + \big(2.(W^2.T_P.K)\big) + \Big(4.\left(\sqrt{2}.N_s.(l_o + 0.005).T_P.\rho.K\ \right)\Big)\Big)\Bigg)\ [kg] \quad (5.13)$$

5.3.5 Material Properties

The algorithm requires the measured B-H characteristics and nominal specific loss to compute the results. The B-H characteristics and nominal specific loss of HGO and CGO material were obtained by Epstein measurements described in **Chapter 3**. The B-H characteristics of HGO and CGO material used in the algorithm are shown in Fig.5-5. Nominal specific loss of HGO and CGO material used in the algorithm are shown in Fig. 5-6.

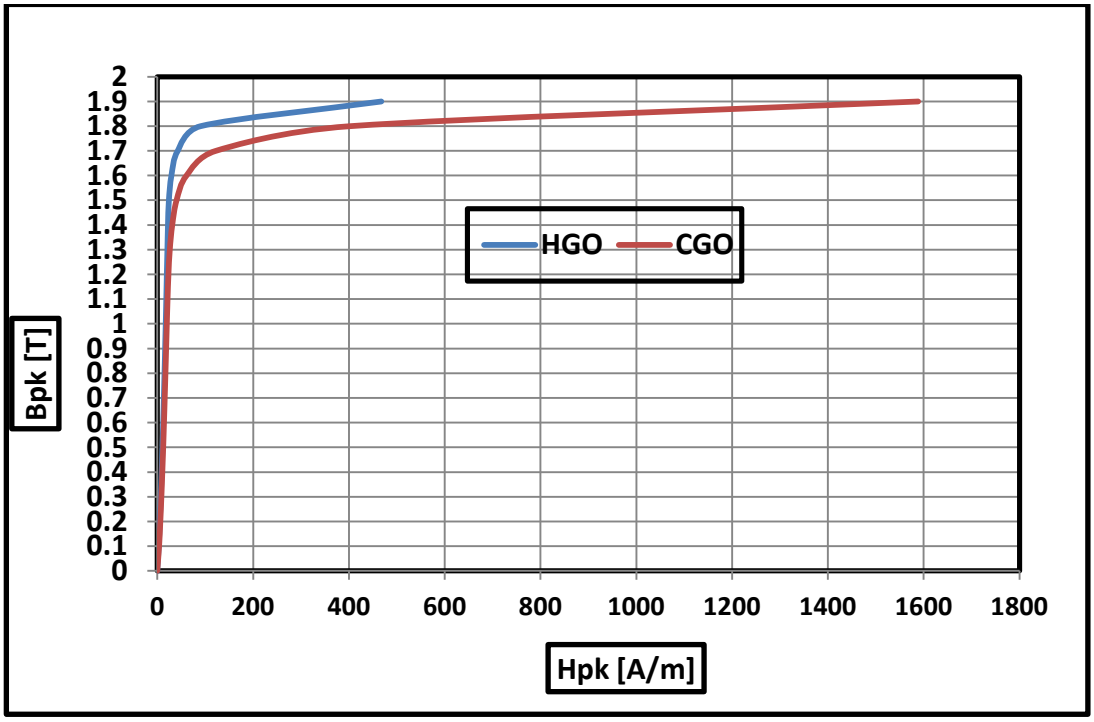

Fig.5-5 B-H characteristics of HGO and CGO material used as an input for the algorithm.

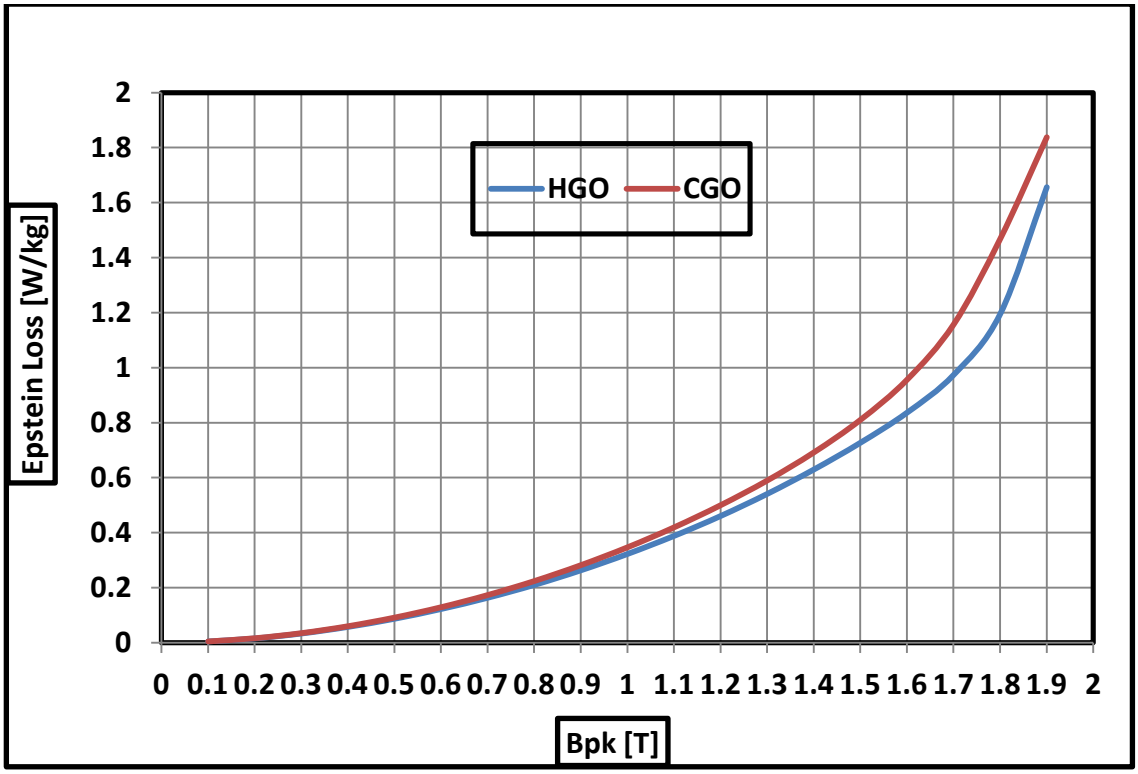

Fig.5-6 Epstein Loss of HGO and CGO material used as an input for the algorithm.

5.4 Data Sets for Algorithm

5.4.1 Packet to Packet Variation of Flux Density

The results of the H_{pk} variation in HGO and CGO two limb single phase cores (**Chapter 2)** and the HGO and CGO material B-H curve (**Chapter 3**) were used to generate data sets. The data sets for percentage increase in H_{pk} in HGO and CGO material for varying $\frac{d}{W}$ and $\frac{s_w}{W}$ ratios is shown in Fig.5-7 and Fig.5-8 respectively. The percentage increase in H_{pk} is a function of the B_{pk} and bolt hole (slot width) / lamination width ratio. As the user inputs the bolt hole diameter (or slot width), lamination width and the B-H curve, the algorithm calculates the ratio of bole hole diameter (or slot width) and lamination width. It then selects the corresponding values of percentage increase in H_{pk} for B_{pk} values from the data set. The algorithm then calculates the value of the new H'_{pk}, knowing the H_{pk} from the B-H curve and the percentage increase in H_{pk} from the data set. This new H'_{pk} is then interpolated for the corresponding B'_{pk} values from the B-H curve. Thus, for different packets,

the algorithm calculates different B'_{pk} with the largest packet width as reference. The new nominal power loss P in each packet is then obtained by interpolating the packet to packet variation of B'_{pk} from the Epstein loss curves (Fig.5-6) and was used for further calculations.

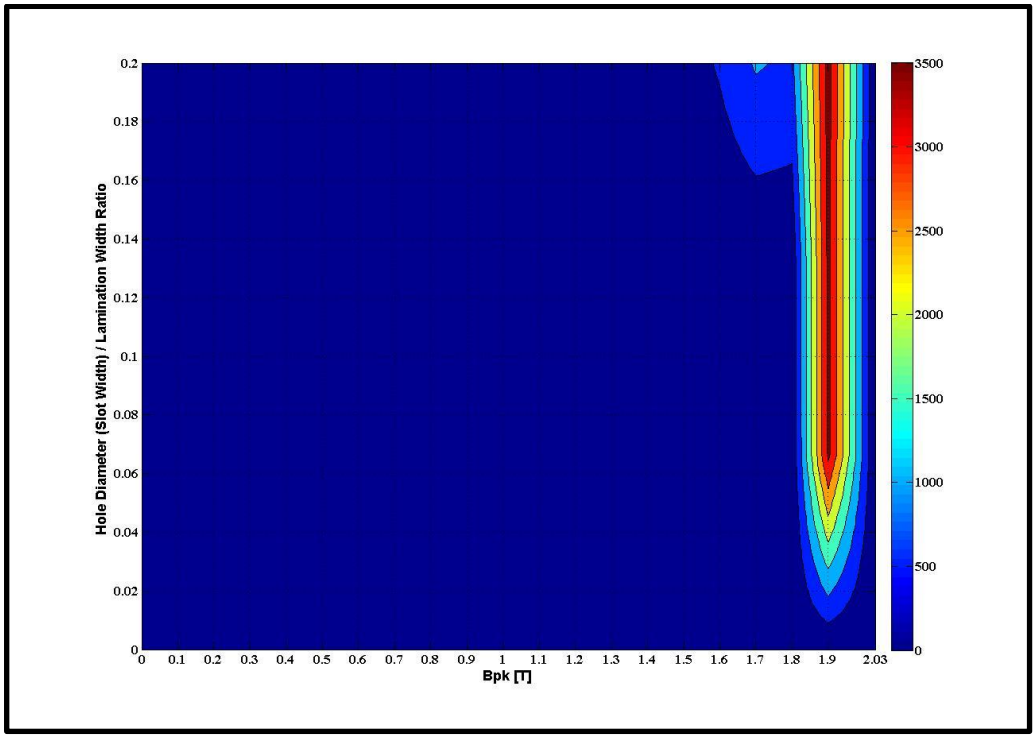

Fig.5-7 Percentage increase in H_{pk} for varying $\frac{d}{W}$ & $\frac{s_w}{W}$ for packet to packet variation of B_{pk} in HGO three-phase, three-limb transformer cores.

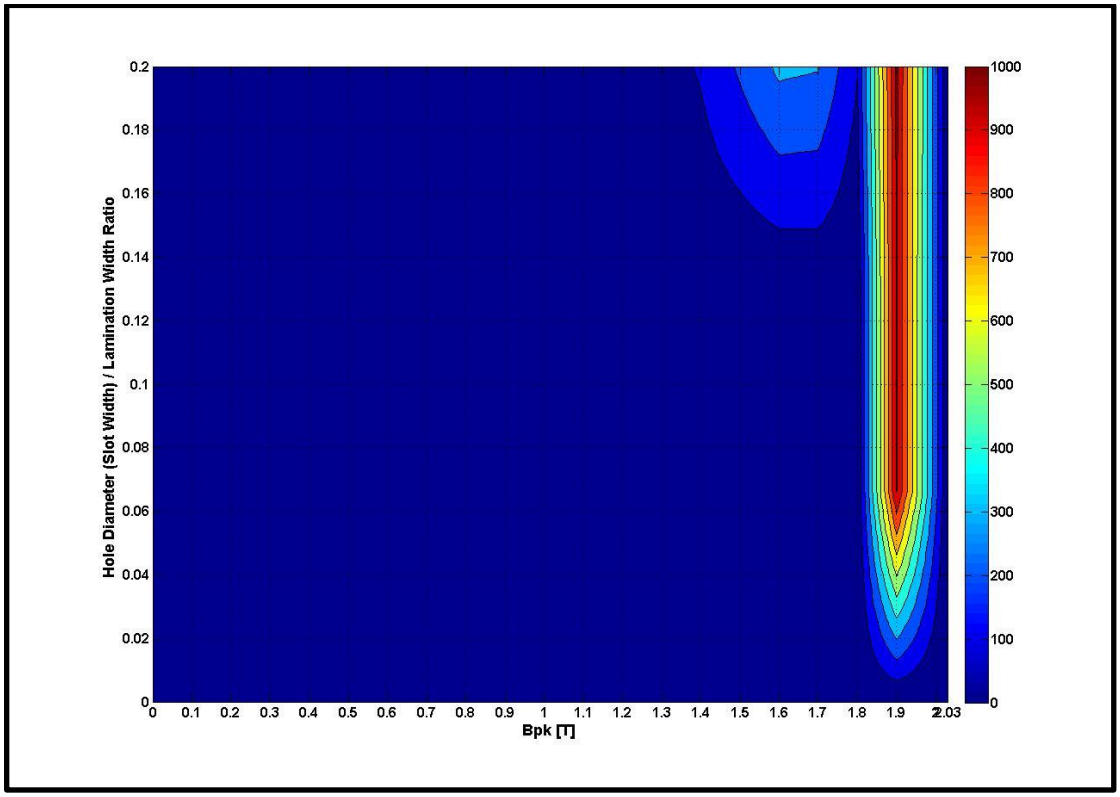

Fig.5-8 Percentage increase in H_{pk} for varying $\frac{d}{W}$ & $\frac{s_w}{W}$ for packet to packet variation of B_{pk} in CGO three-phase, three-limb transformer cores.

5.4.2 Bolt Holes and Slots

The data sets for bolt holes and slots are discussed in **Chapter 4**. The algorithm uses the data sets to obtain the affected length and percentage increase in specific loss. The localised loss due to holes and slots are calculated by equations (5.14) and (5.15) respectively.

$$P_H = \sum_{1}^{N_p} \left(\left(\left(\frac{\%\ increase\ in\ Sp.loss\ \ due\ to\ Holes}{100} \right) * P \right) + P \right) * m_{hole} \ \ [W] \tag{5.14}$$

$$P_S = \sum_{1}^{N_p} \left(\left(\left(\frac{\%\ increase\ in\ Sp.loss\ \ due\ to\ Slots}{100} \right) * P \right) + P \right) * \ m_{slot} \ \ [W] \tag{5.15}$$

5.4.3 Rotational Loss

A 2D magnetisation system [75] for measurement of rotational loss was used to measure the rotational loss for HGO and CGO electrical steels. The measurements were carried out at B_{pk} range 1.0 T to 1.6 T for axis ratios ($\frac{B_x}{B_y}$) 0.25, 0.5, 0.6, 0.65, 0.75, 0.9 and 1 in clockwise (CW) anticlockwise (ACW) directions (Fig.5-9). Measurements at B_{pk} = 1.7 T was carried out for axis ratios ($\frac{B_x}{B_y}$) 0.25, 0.5, 0.6, 0.65 and 0.75 in clockwise (CW) and anticlockwise (ACW) directions due to limitations in the power amplifiers.

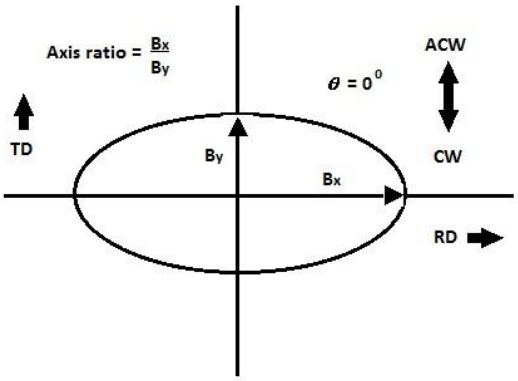

Fig.5-9 Loci of the flux density used for the measurements.

Annealed HGO and CGO circular samples of thickness 0.3 mm and 80 mm diameter were used for the measurements (Fig.5-10). Four holes of 0.5 mm diameter were slowly drilled for the search coils to detect instantaneous flux densities in the RD and TD, b_x and b_y respectively. The holes were separated by a length of 20mm. The effective length of the search coils was equal to the length between two edges of the 0.5 mm diameter holes. Therefore the effective length (l_b) of the search coils was equal to 19.5 mm.

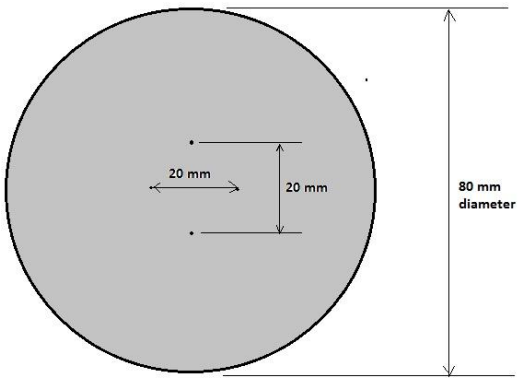

Fig.5-10 Circular sample for rotational measurements.

The measurement system yoke is shown in Fig. 5-11 and the measurement circuit is shown in Fig.5-12.

Fig.5-11 Rotational loss measurement yoke (a) Top view (b) Front view [75].

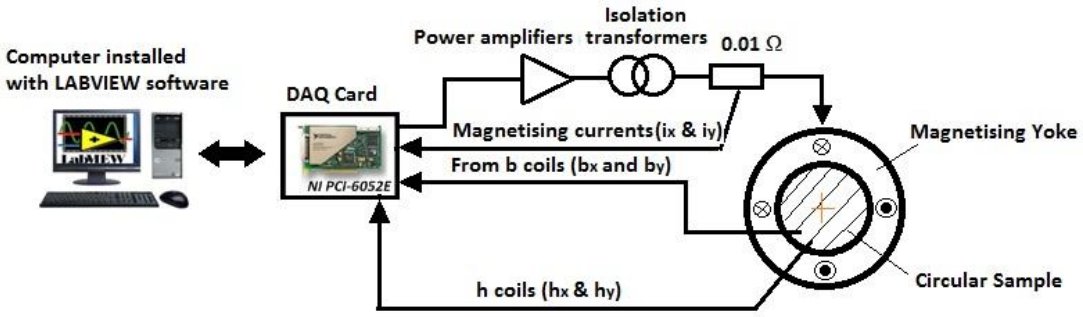

Fig.5-12 Rotational loss measurement circuit.

The tangential components of magnetic field in the RD and TD, h_x and h_y were measured using previously calibrated [3] orthogonal H coils sourced from Okayama University, Japan. A 0.5 mm thick plastic former was wound with 0.05 mm thick

enamelled copper wires to obtain h_y coil. The h_x coil was wound orthogonally on the h_y coil with the same copper wires.

The voltages induced in the orthogonal search coils (e_x and e_y) were used to calculate the instantaneous b_x and b_y by equations (5.16) and (5.17) respectively.

$$b_x = -\frac{1}{(t_s.l_b)} \int e_x \, dt \tag{5.16}$$

$$b_y = -\frac{1}{(t_s.l_b)} \int e_y \, dt \tag{5.17}$$

where t_s is the sample thickness (0.3mm) and l_b is the effective length of the search coils.

The voltages induced in the H-coils (e_{h_x} & e_{h_y}) were used to calculate the instantaneous h_x and h_y by equations (5.18) and (5.19) respectively.

$$h_x = -\frac{1}{(\mu_0.K_{h_x})} \int e_{h_x} \, dt \tag{5.18}$$

$$h_y = -\frac{1}{(\mu_0.K_{h_y})} \int e_{h_y} \, dt \tag{5.19}$$

where K_{h_x} is the area turn constant of the h_x coil (0.003119 m^2 [3]) and K_{h_y} is the area turn constant of the h_y coil (0.001989 m^2 [3]).

The measured rotational loss (P_r) was then calculated by equation (5.20),

$$P_r = \frac{1}{(T.\rho)} \int_0^T \left(h_x.\frac{db_x}{dt} + h_y.\frac{db_y}{dt} \right) dt \qquad \left[\frac{W}{kg} \right] \tag{5.20}$$

Three trials of measurements were carried out on each of the three samples of HGO and three samples of CGO.

The rotational loss measured in CW and ACW directions were averaged [75] to obtain the final rotational loss. The resulting rotational loss for HGO at varying axis ratios is shown in Fig.5-13. The rotational loss for CGO at varying axis ratios is shown in Fig. 5-14.

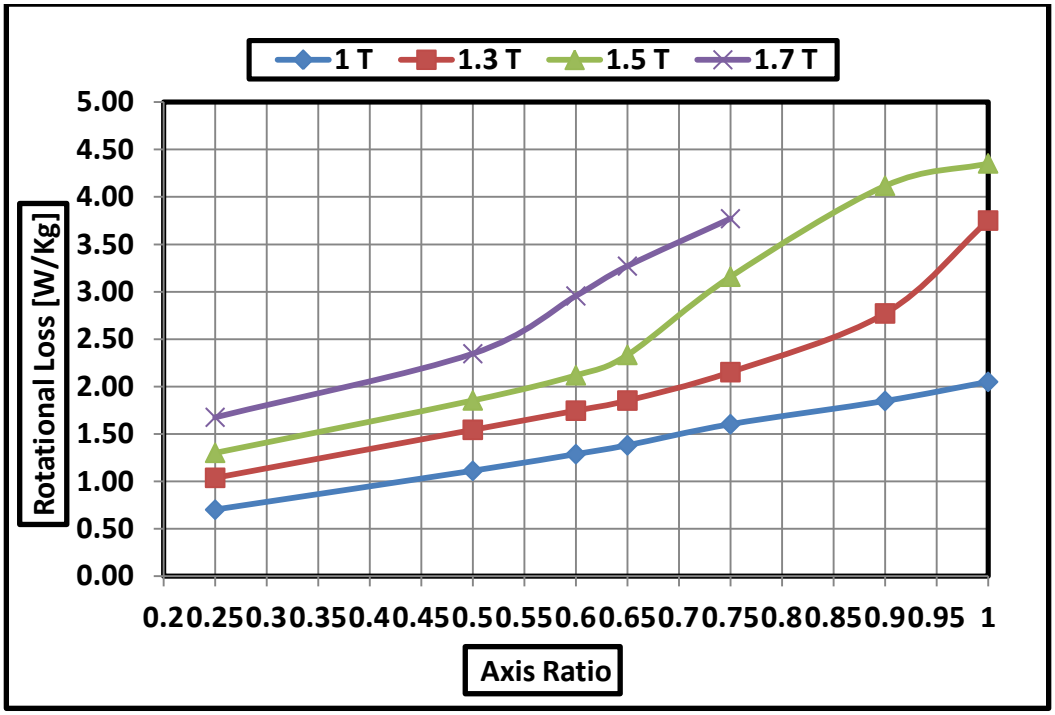

Fig.5-13 Rotational loss versus axis ratios for HGO samples.

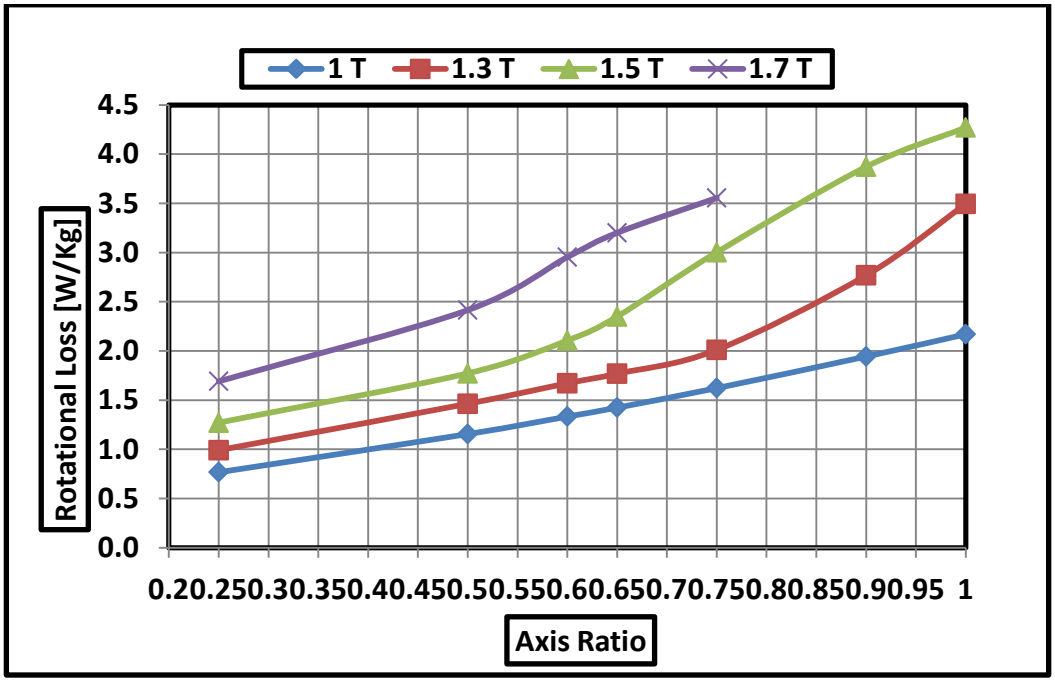

Fig.5-14 Rotational loss versus axis ratios for CGO samples.

All the results for HGO material were then divided by the nominal loss of the steel measured in RD (Fig.5-6) to obtain the percentage increase in rotational loss using equation (5.21).

$$\%\ increase\ in\ P_r = \left(\frac{P_r - P}{P}\right) * 100 \tag{5.21}$$

Similar calculations were carried out to obtain the percentage increase in rotational loss for CGO material.

The percentage increase in rotational loss results for B_{pk} of 1.7 T were extrapolated up to the axis ratio of 1. All the results were then extrapolated to saturation magnetisation (2.03T) and interpolated for B_{pk} values from 0.01 T to 2.03 T in steps of 0.01 T. The resulting data set for HGO and CGO can be visualised in Fig. 5-15 and Fig. 5-16 respectively.

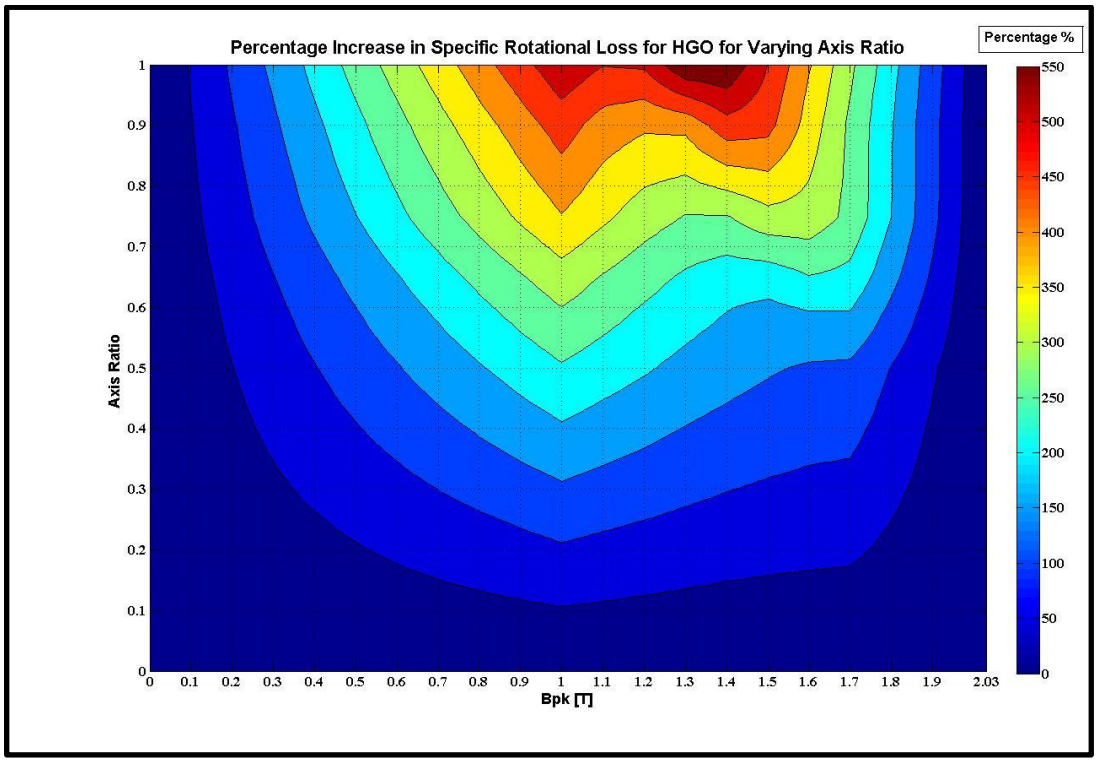

Fig.5-15 Contour graph of percentage increase in rotational loss for varying rotational flux axis ratio for B_{pk} range 0.0 T to 2.03 T in HGO.

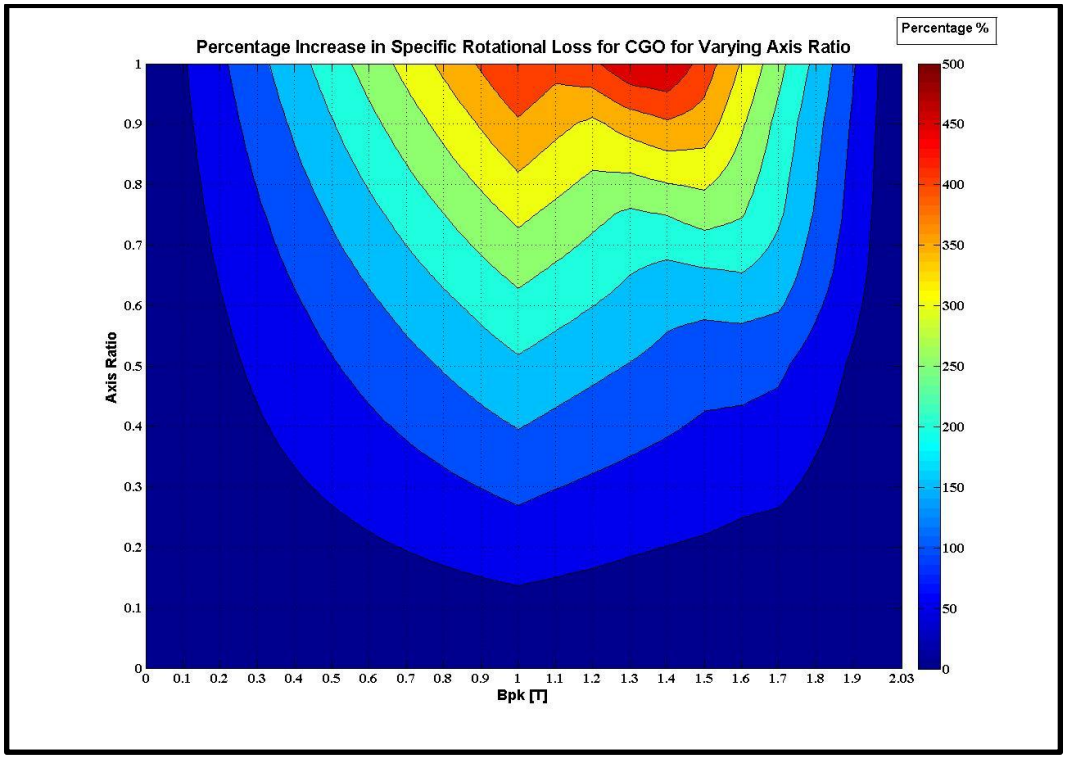

Fig.5-16 Contour graph of percentage increase in rotational loss for varying rotational flux axis ratio for B_{pk} range 0.0 T to 2.03 T in CGO.

The algorithm reads the rotational flux axis ratio required for a particular flux density from an optimised data set shown in Fig. 5-17.

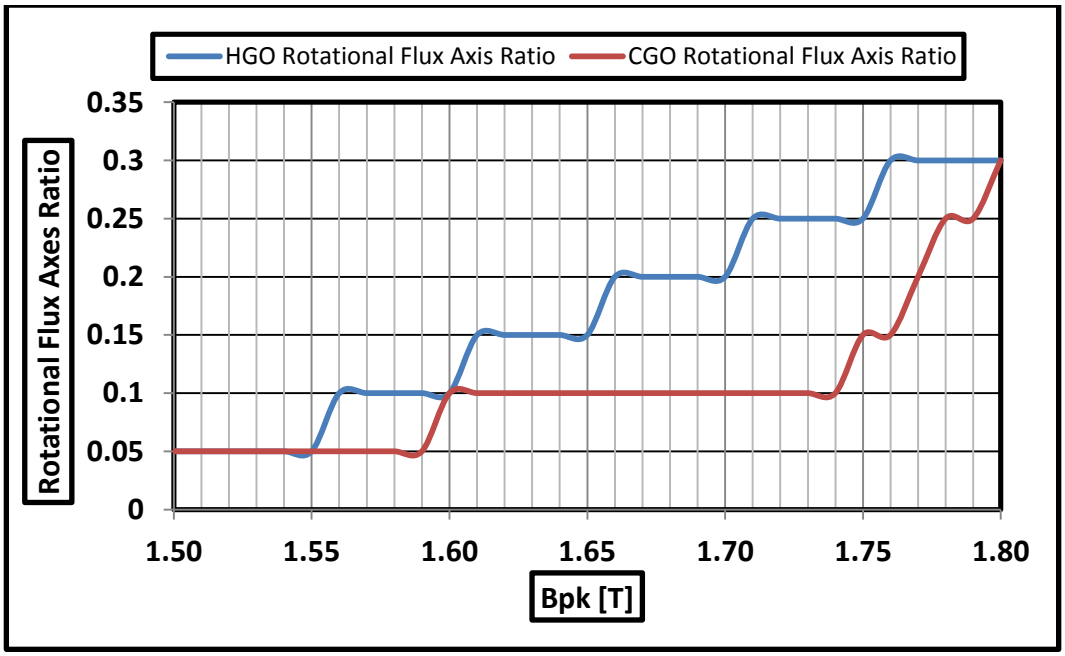

Fig.5-17 Optimised rotational flux axis ratio versus B_{pk} for HGO and CGO cores.

The algorithm then reads the percentage increase in rotational loss from nominal loss at the optimised axis ratios. The rotational loss in the core is then calculated using the equation (5.22).

$$P_{rot} = \sum_{1}^{N_p} \left(\left(\left(\frac{\%\ increase\ in\ P_r}{100} \right) * P \right) + P \right) * m_{rot} \quad [W] \tag{5.22}$$

5.4.4 Loss due to Corner joints, Stress and Harmonics

The additional losses in HGO core may be thought to be affected by the corner joints, flux deviating from the rolling direction under complex stress distribution in the core and harmonics. The additional losses were combined together as a single entity and optimised to be read by the algorithm as there is no data available on their affected regions. Fig.5-18 shows the additional losses in percentage for HGO and CGO cores. The additional losses for HGO core are higher than CGO as HGO material is more stress sensitive [76].

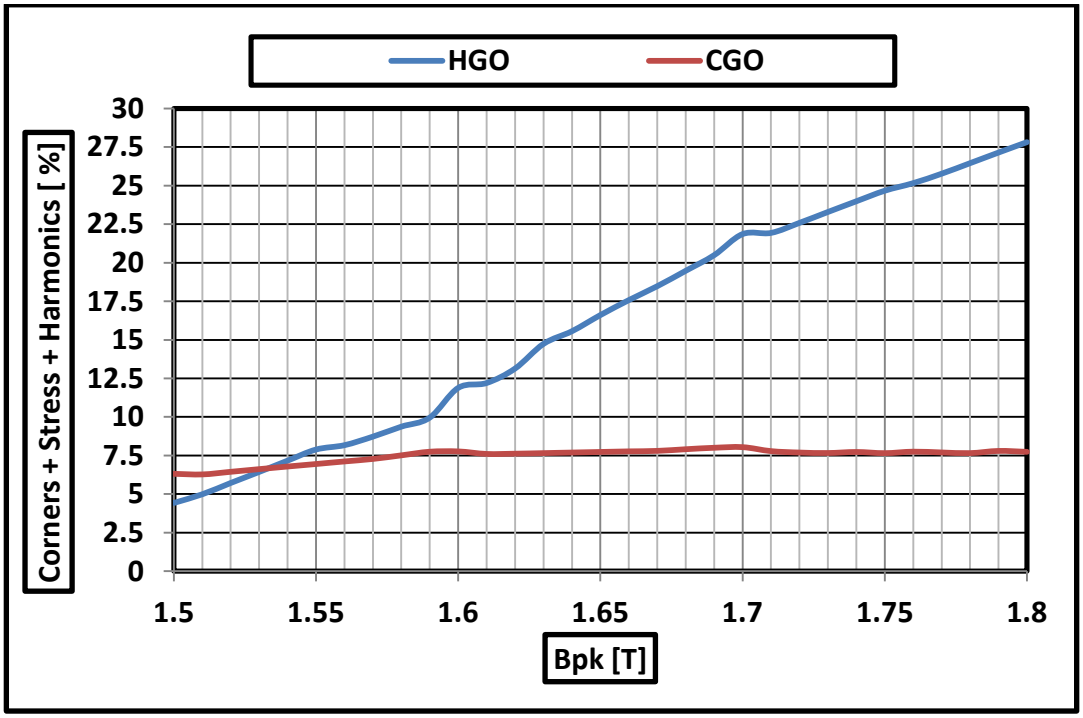

Fig.5-18 Optimised losses due to corners, stress and harmonics in percentage versus B_{pk} for HGO and CGO cores.

The algorithm reads the percentage increase in additional losses from the data in Fig.5-18. The additional losses are calculated using the equation (5.23).

$$P_{ad} = \left(\sum_{1}^{N_p}(P_{RD} + P_H + P_S + P_{rot})\right) * (additional\ losses\ in\ \%)\ [W] \quad (5.23)$$

where $P_{RD}$is loss in the rolling direction obtained by multiplying nominal loss and m_{RD}.

5.5 Predicted Results

5.5.1 Input Parameters

The geometrical parameters of the multi-packet and single packet HGO and CGO 3-phase, 3-limb transformer cores (**Chapter 2 & 3**) were used to predict the specific losses. The parameters are listed in **Appendix VI**.

5.5.2 Packet to Packet variation of Peak Flux Density

The measured and predicted packet to packet variation for multi-packet HGO and CGO 3-phase, 3-limb transformer cores are shown in Fig. 5-19 and Fig.5-20 respectively.

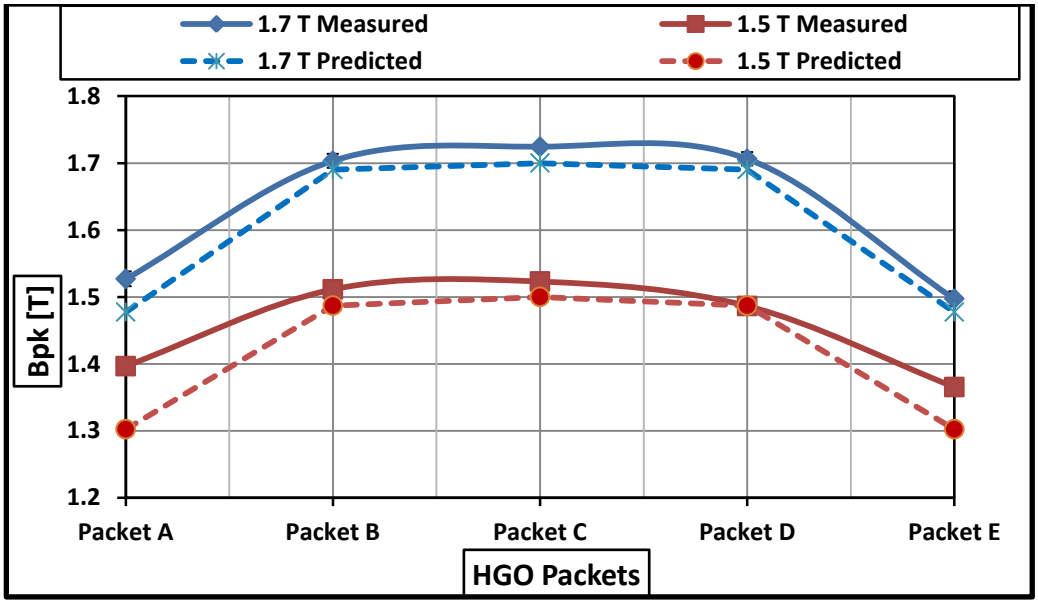

Fig.5-19 Measured and predicted packet to packet variation of peak flux density for multi-packet HGO Core at B_{pk}=1.5 T & 1.7 T.

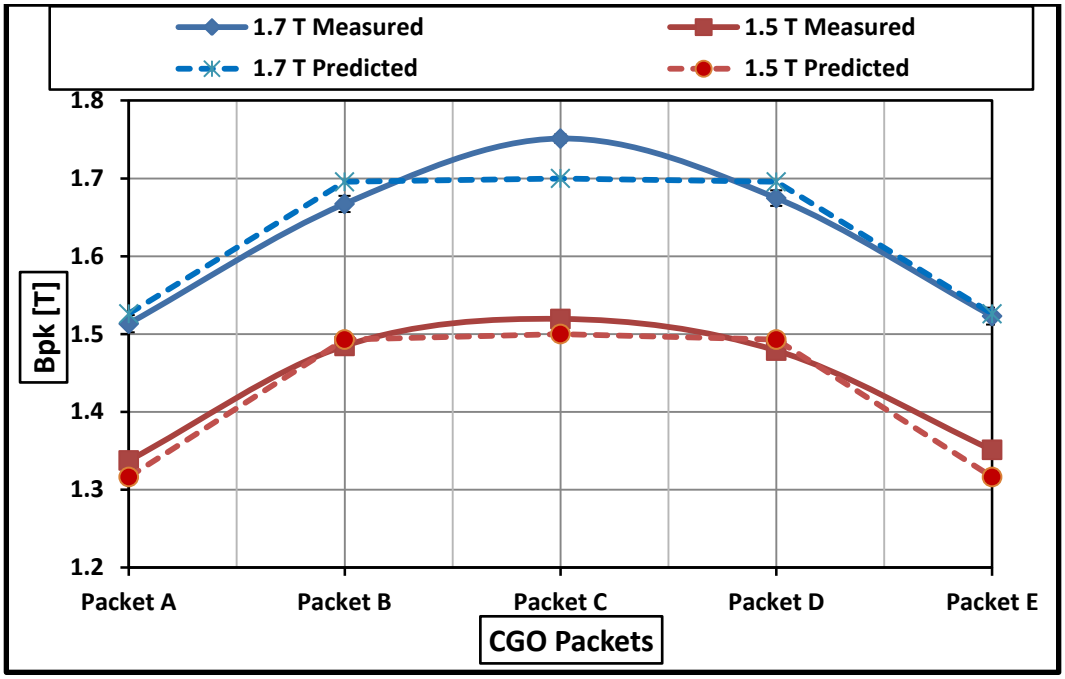

Fig.5-20 Measured and predicted packet to packet variation of peak flux density for multi-packet CGO Core at B_{pk}=1.5 T & 1.7 T.

The difference in the predicted results was high as 4-6% in packet A and E (50 mm width) at B_{pk} =1.5 T and 3% at B_{pk} =1.7 T in HGO core. For CGO core, the difference in the predicted results was around 3% at B_{pk} =1.5 T and around 1% at B_{pk} =1.7 T. The difference in packets B and D (130mm width) for HGO and CGO core was less than 2% at B_{pk} =1.5 T and 1.7 T. The difference in the results for packet C (160 mm width) for HGO and CGO core was 2% and 3% at 1.7 T.

5.5.3 Specific Power Loss of Three Phase, Three Limb Transformer Cores

The predicted losses are computed using equation (5.24).

$$P_{core} = \frac{P_{RD}+P_H+P_S+P_{rot}+P_{ad}}{m_{core}} \left[\frac{W}{kg}\right] \quad (5.24)$$

The measured and predicted specific power loss for multi-packet HGO and CGO 3-phase, 3-limb transformer cores are shown in Fig. 5-21. The difference in predicted and measured specific loss for multi-packet HGO and CGO 3-phase, 3-limb transformer cores was less than 1% and is shown in Fig. 5-22.

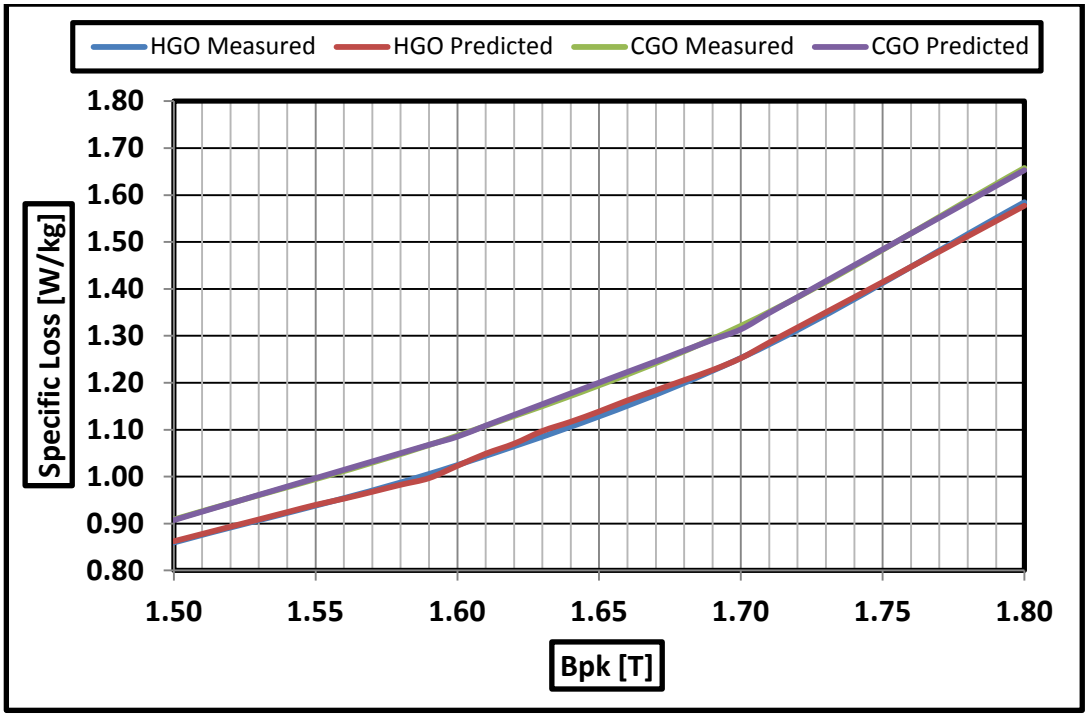

Fig.5-21 Measured and predicted specific loss for HGO and CGO cores.

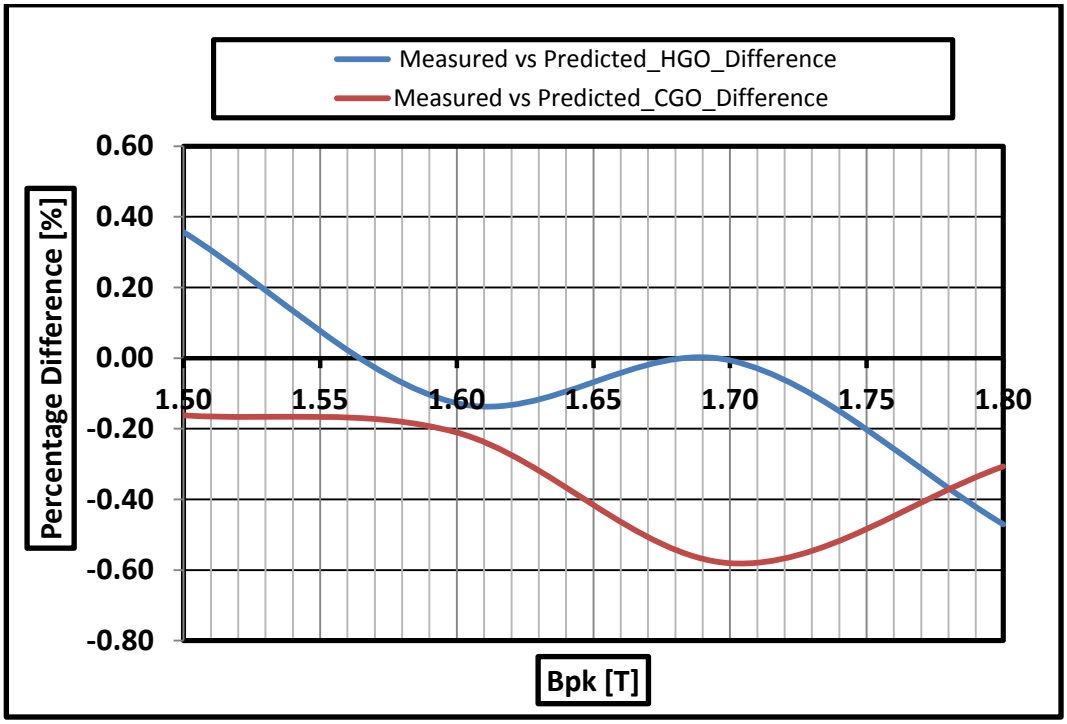

Fig.5-22 Difference in predicted and measured specific loss for multi-packet, 3-phase, 3-limb HGO and CGO cores.

5.5.4 Localised Losses of Multi-packet Three Phase, Three Limb Transformer Cores

The breakdown of localised losses in multi-packet HGO and CGO cores is shown in Fig. 5-23 and Fig. 5-24 respectively.

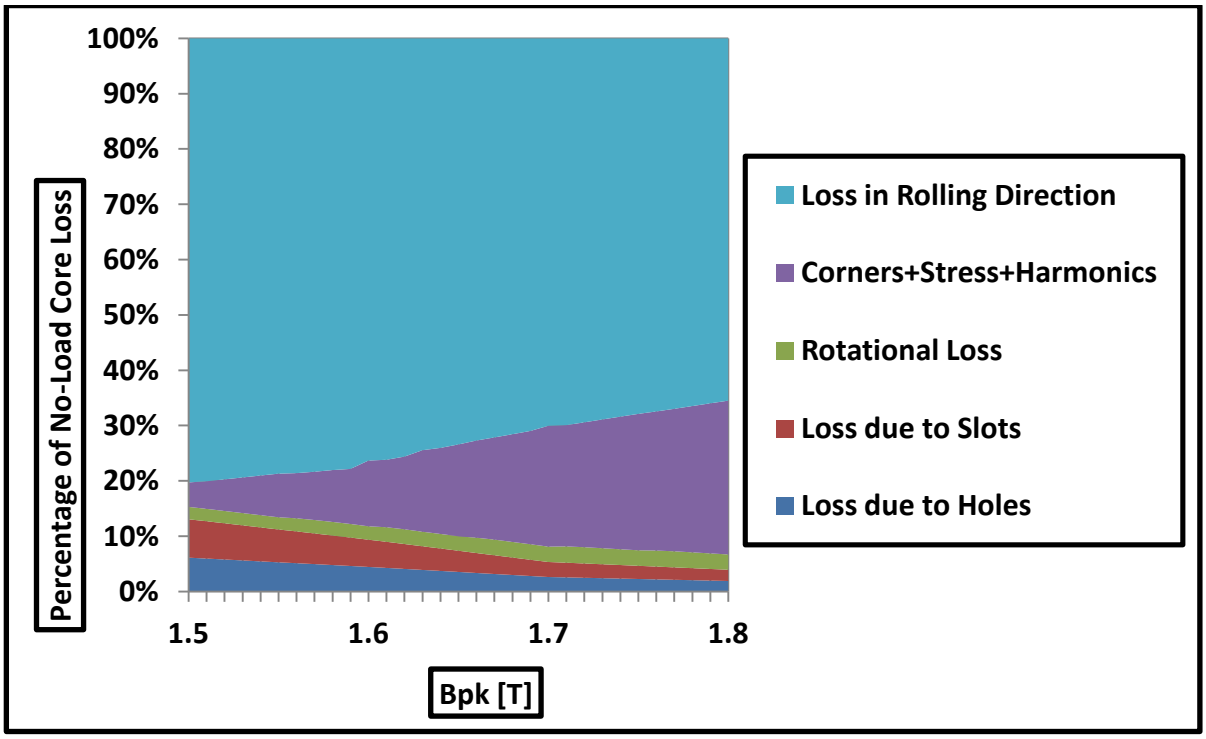

Fig.5-23 Breakdown of the contributors of HGO core loss.

For a transformer core to be more efficient, the flux must traverse paths which are parallel to the RD. If the flux deviates from the RD in the corner regions, additional losses occur due to stress and harmonics and increase with increasing flux density. The loss in the rolling direction (P_{RD}) forms a major part of HGO and CGO core losses. In the CGO core, P_{RD} is greater than that of the HGO core. This is because the building factor of CGO cores is lower than the building factor of HGO cores.[59]

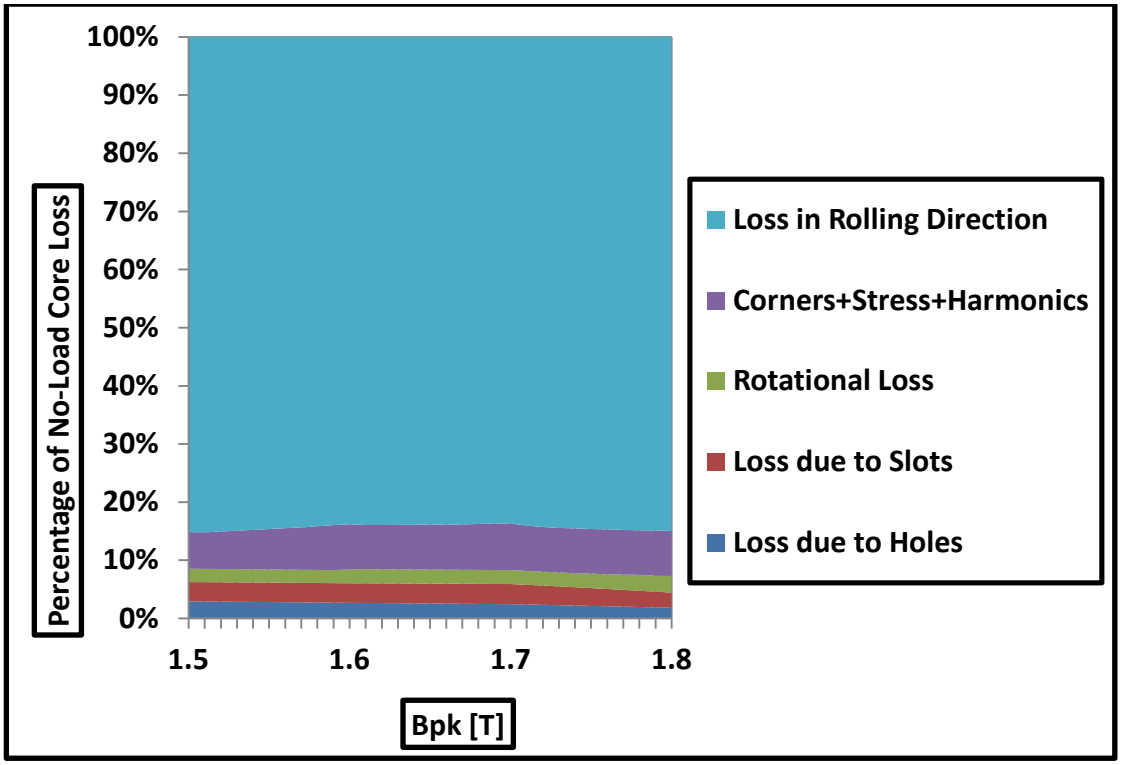

Fig.5-24 Breakdown of the contributors of CGO core loss.

A pie chart showing the contributors of HGO core loss at B_{pk} = 1.7 T is shown in Fig.5-25. A Pie chart showing the contributors of CGO core loss at B_{pk} = 1.7 T is shown in Fig.5-26.

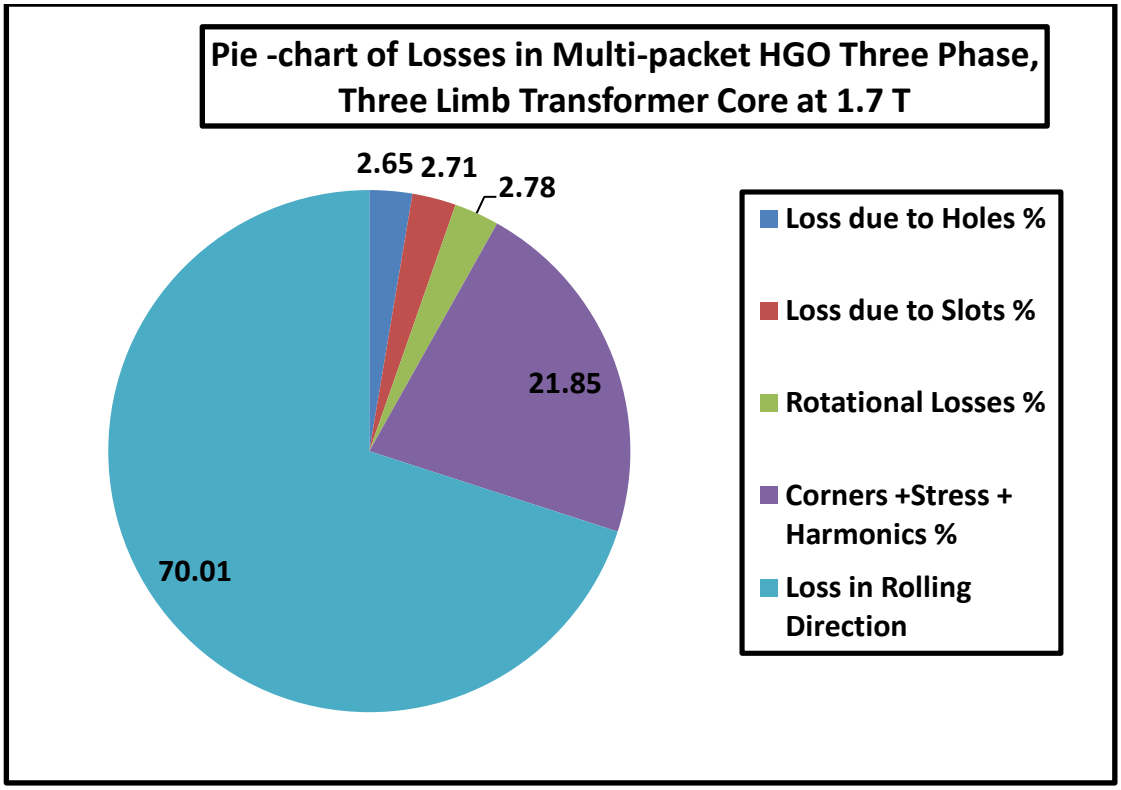

Fig.5-25 Pie chart of the of the contributors of HGO core loss at B_{pk}= 1.7 T.

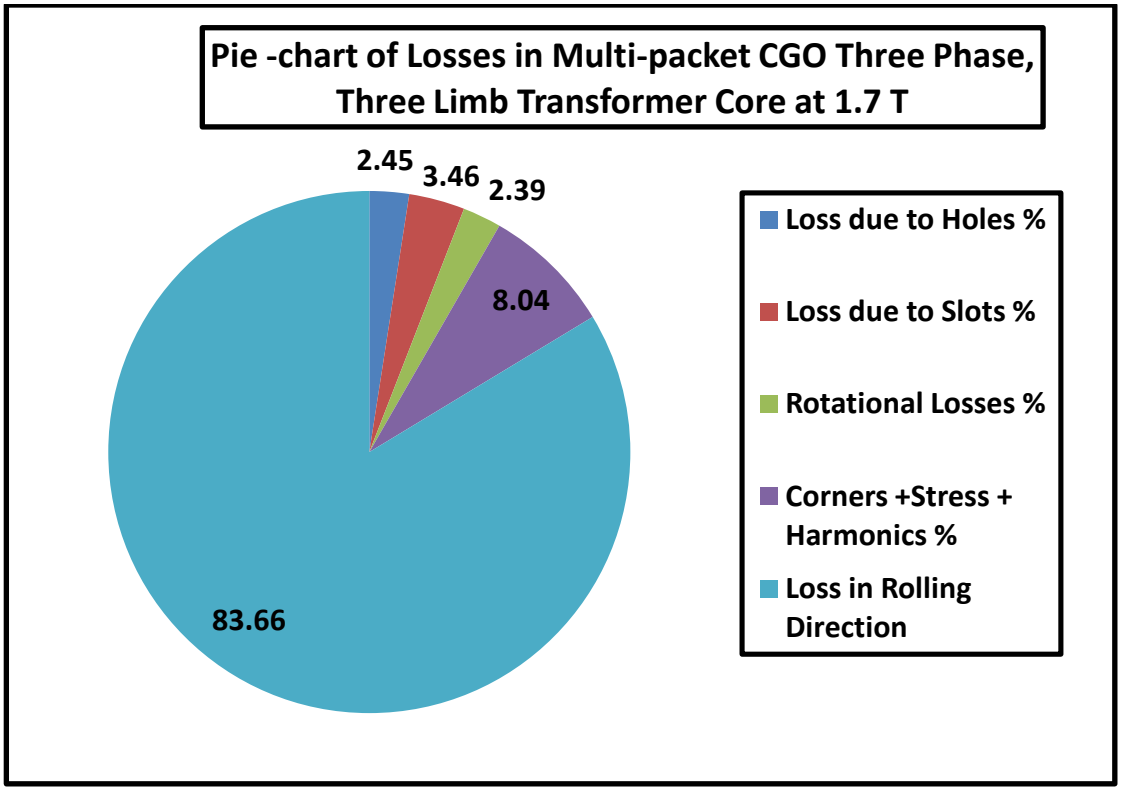

Fig.5-26 Pie chart of the of the contributors of CGO core loss at B_{pk}=1.7 T.

5.5.5 Prediction for Multi-Packet 3-Phase, 3-Limb Transformer Cores without Bolt Holes and Slots

The specific loss results for the boltless HGO and CGO cores are shown in Fig.5-27 and Fig.5-28 respectively.

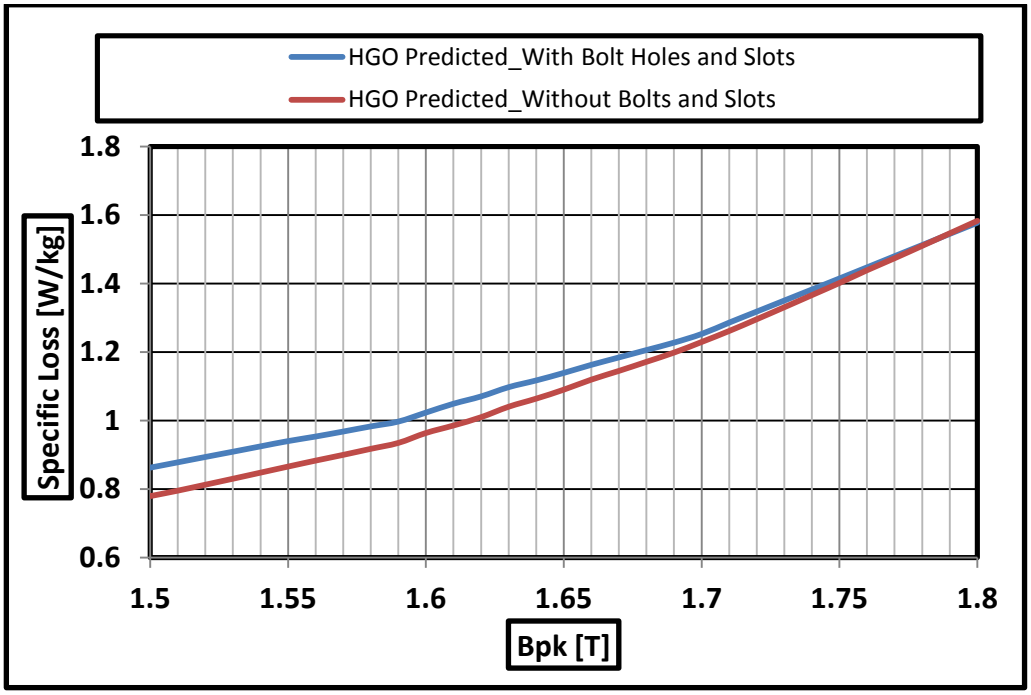

Fig.5-27 Comparison of the predicted core loss for HGO cores with and without bolt holes and slots.

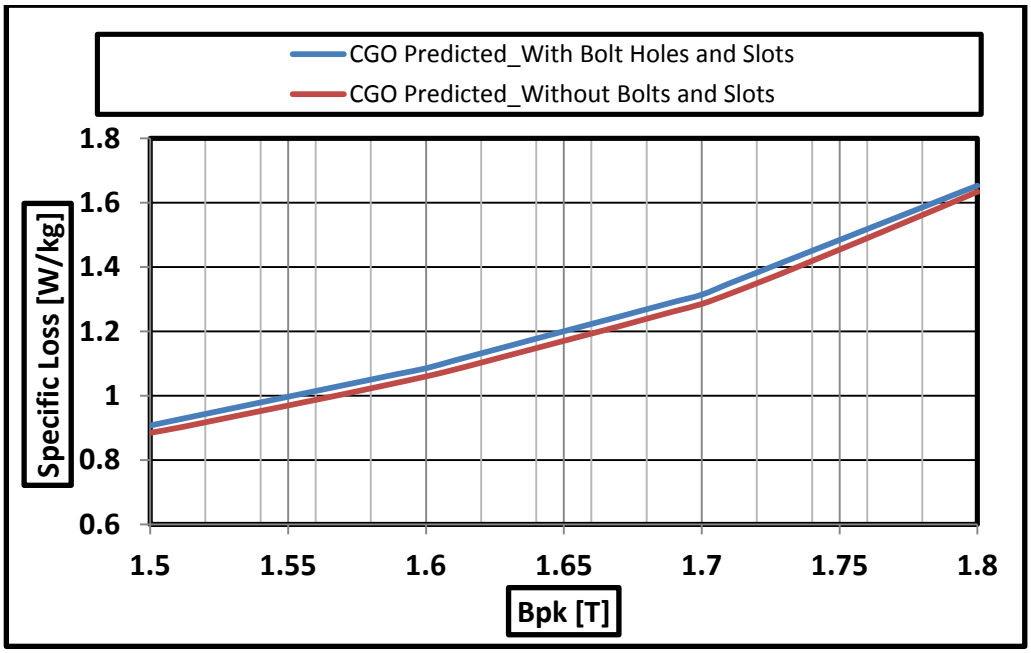

Fig.5-28 Comparison of the predicted core loss for CGO cores with and without bolt holes and slots.

The percentage difference in specific losses in HGO and CGO cores for with and without bolt holes and slots is shown in Fig. 5-29.

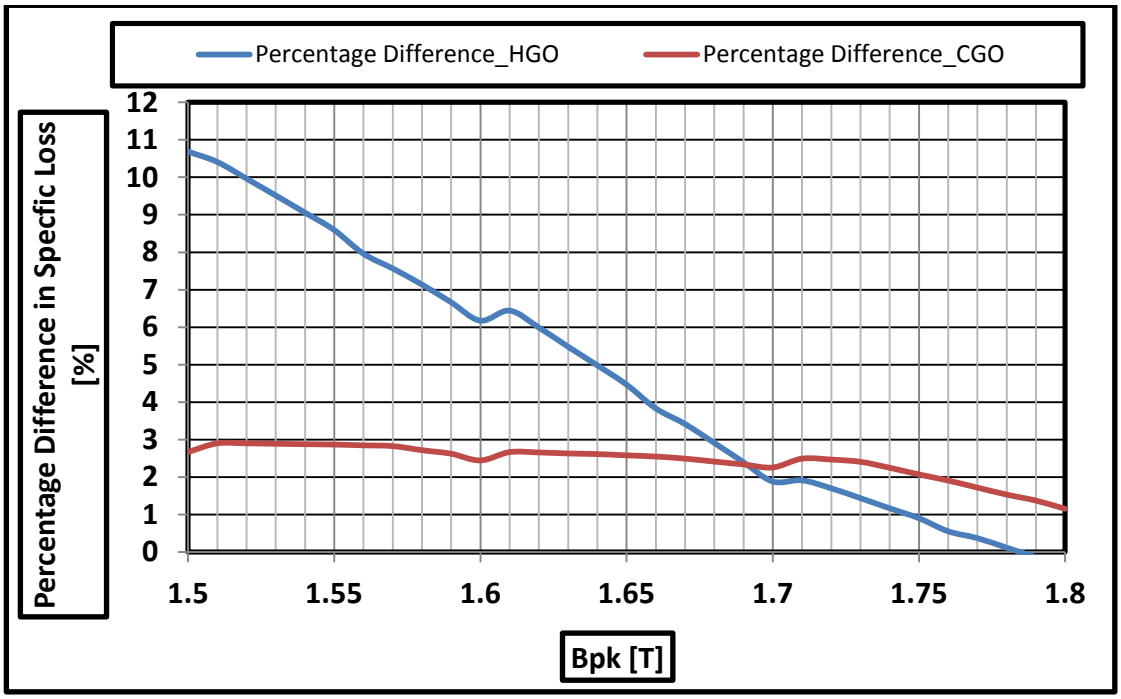

Fig.5-29 Percentage difference in specific core loss for multi-packet 3-phase, 3-limb HGO and CGO cores with and without bolt holes and slots.

The predictions for without bolt holes and slots assumed the same additional losses in HGO cores. The difference was between 11 % for B_{pk} = 1.5 T and 2% for B_{pk} = 1.7 T, the two common operating flux densities of the transformer cores.

For CGO cores, the difference was about 3% at B_{pk} = 1.5 T and 2% for B_{pk} = 1.7 T.

Considering the fact that there are thousands of transformer cores in the electrical distribution system operating continuously for years, even a 2% reduction in core losses would be beneficial in economic terms. Thus boltless cores can be economically beneficial over the cores with bolt holes and slots.

Glass fibre band technology [36] or adhesive technology [77] can be used along with an associated clamping system to obtain a boltless core. The advantages of a boltless core are that it can be lighter with lower loss and effective use of magnetic material [77]. A boltless core built with adhesive technology is shown in Fig.5-30. Because of the absence of bolts, the size of the clamping system in a boltless core is smaller

than that of the conventional core with bolts. In adhesive technology, the laminations are glued together by a special adhesive coating [77].

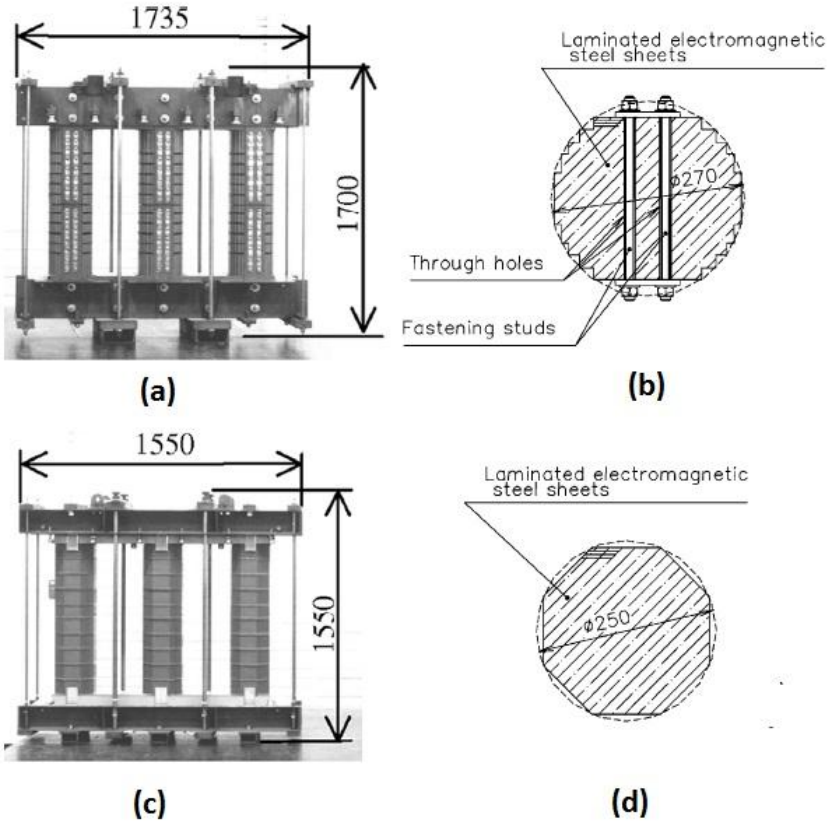

Fig.5-30 Transformer core and cross section (a) Conventional core with bolts (b) Conventional core cross section showing bolts (c) Boltless core (d) Boltless core cross section [77].

A Pie chart showing the contributors of HGO core loss without bolt holes and slots at B_{pk} = 1.7 T is shown in Fig.5-31. A Pie chart showing the contributors of CGO core loss without bolt holes and slots at B_{pk} = 1.7 T is shown in Fig.5-32.

The percentage of losses in the RD in the boltless HGO and CGO cores increased as compared to cores with bolt holes and slots, thus reducing the total specific loss. The loss reduction could be higher, as the percentage of additional losses can be much lower. The additional losses for boltless cores could not be optimised because of the absence of measurements results.

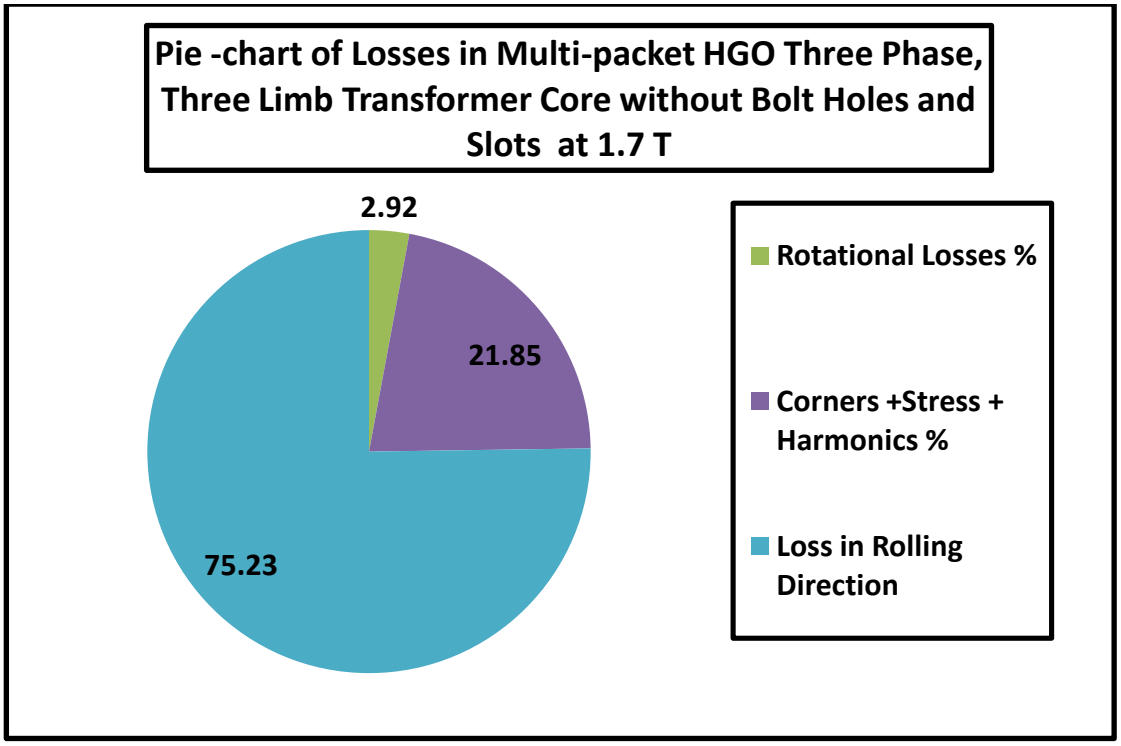

Fig.5-31 Pie chart of the contributors of core loss at B_{pk}=1.7 T for HGO core without bolt holes and slots.

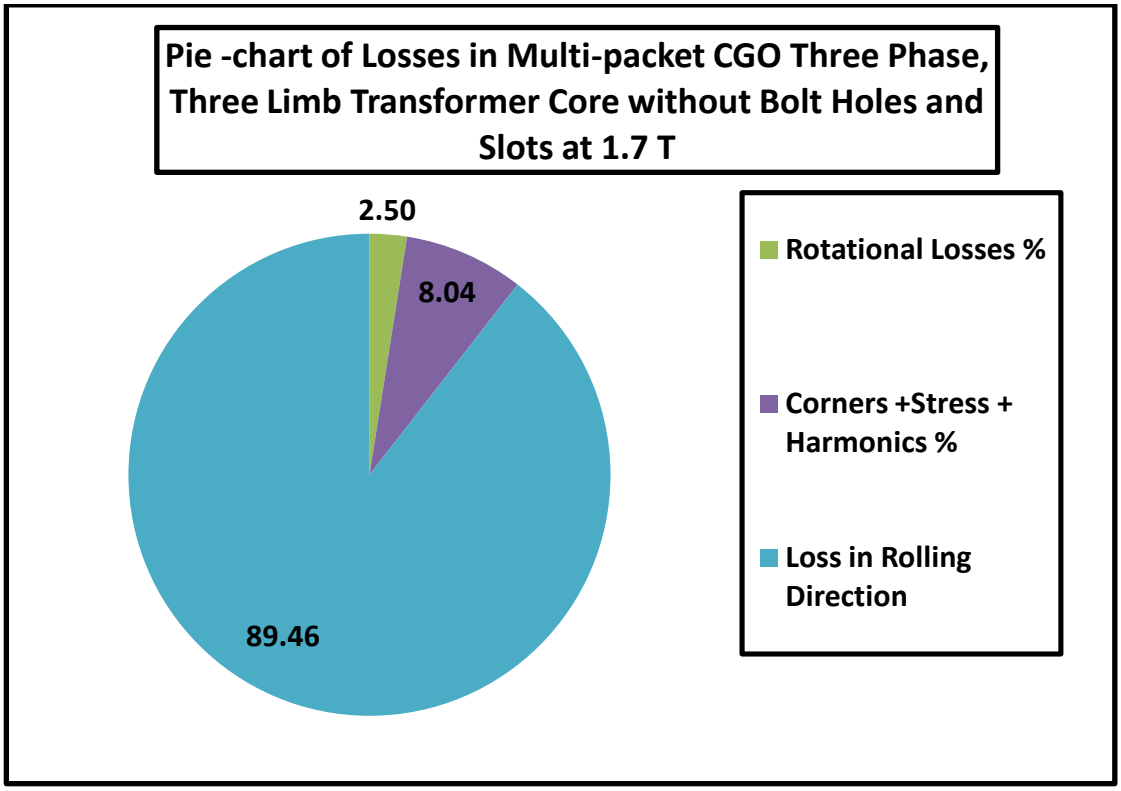

Fig.5-32 Pie chart of the contributors of core loss at B_{pk}=1.7 T for CGO core without bolt holes and slots.

5.5.6 Prediction for Single Packet 3-Phase, 3-Limb Transformer Cores

Predictions were made for single packet, 3-phase, 3-limb HGO and CGO cores discussed in **chapters 3 & 4**. The measured and predicted losses for 160 mm lamination width single packet HGO and CGO cores are shown in Fig. 5-33.

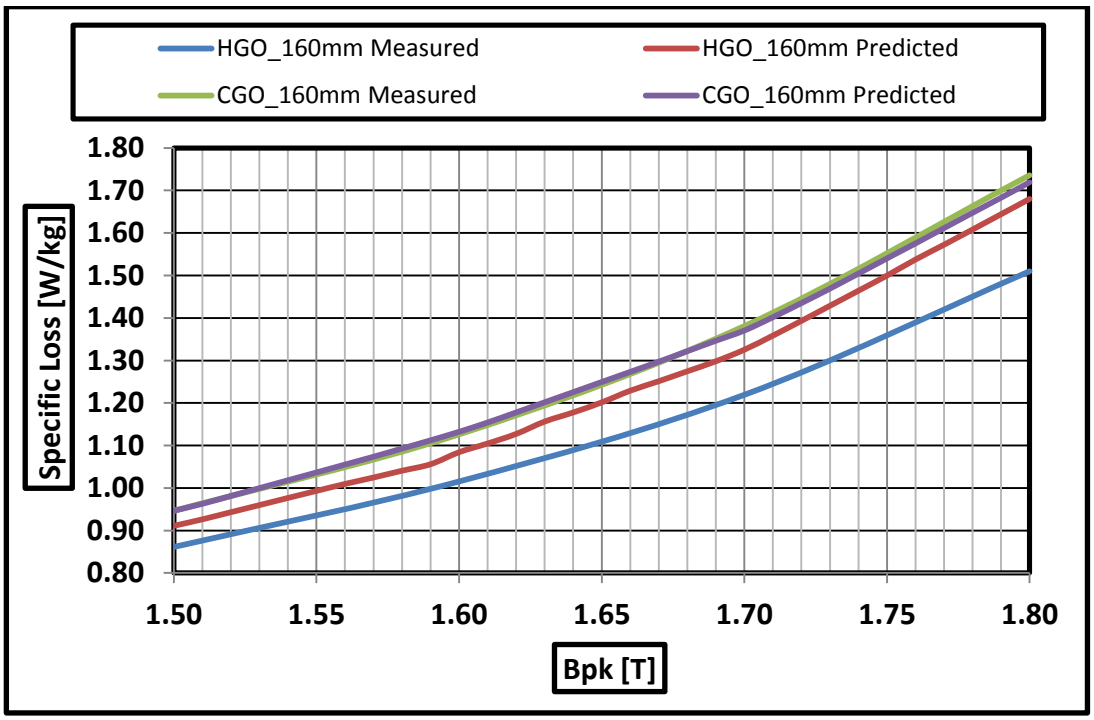

Fig.5-33 Measured and predicted specific loss for 160mm lamination width, single packet 3-phase, 3-limb HGO and CGO cores.

A good agreement is observed between the measured and predicted specific losses for CGO cores with the difference being around 2% at B_{pk} = 1.7 T.

As the specific loss measurements were carried out on HGO and CGO multi-packet cores, the additional losses of HGO and CGO multi-packet cores were used to predict losses of other cores.

Since the algorithm considered the same additional losses used to predict the specific losses for multi-packet HGO cores, the predicted specific losses for single packet 160 mm lamination width HGO core is higher than the measured specific losses. The difference in predicted and measured specific loss at B_{pk} = 1.7 T is 9%.

The results show that the additional losses in CGO cores do not vary as much as that of HGO cores with geometry.

Similar observation is made for the predicted and measured specific losses for single packet, 130 mm lamination width HGO and CGO cores shown in Fig.5-34.

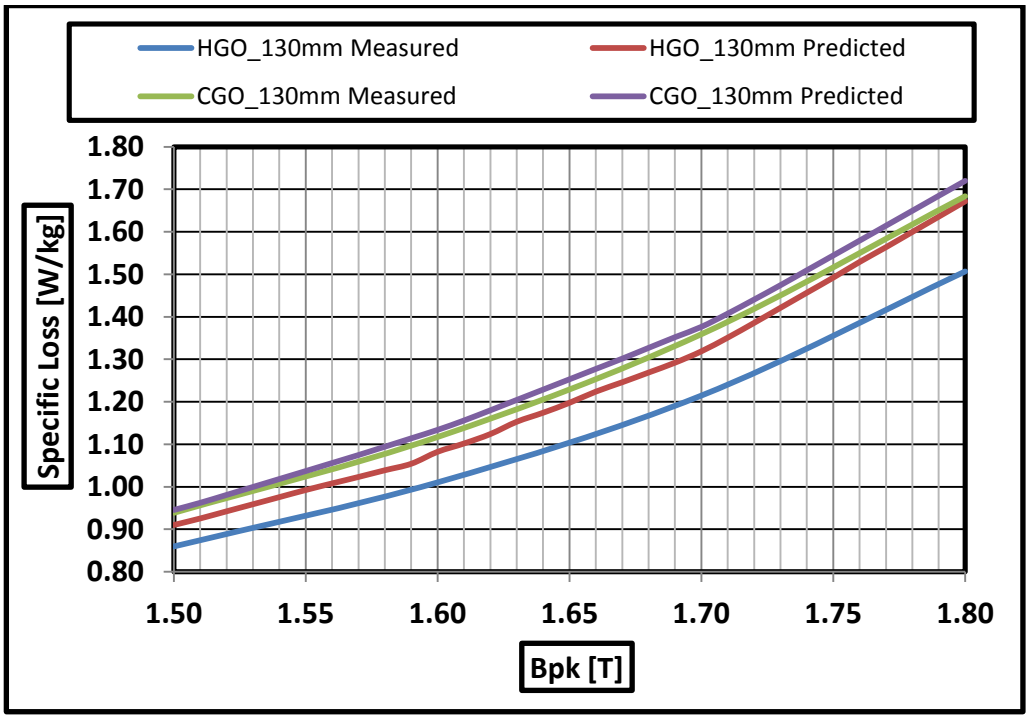

Fig.5-34 Measured and predicted specific loss for 130mm lamination width, single packet 3-phase, 3-limb HGO and CGO cores.

The measured and predicted losses for 50 mm lamination width single packet HGO and CGO cores are shown in Fig. 5-35.

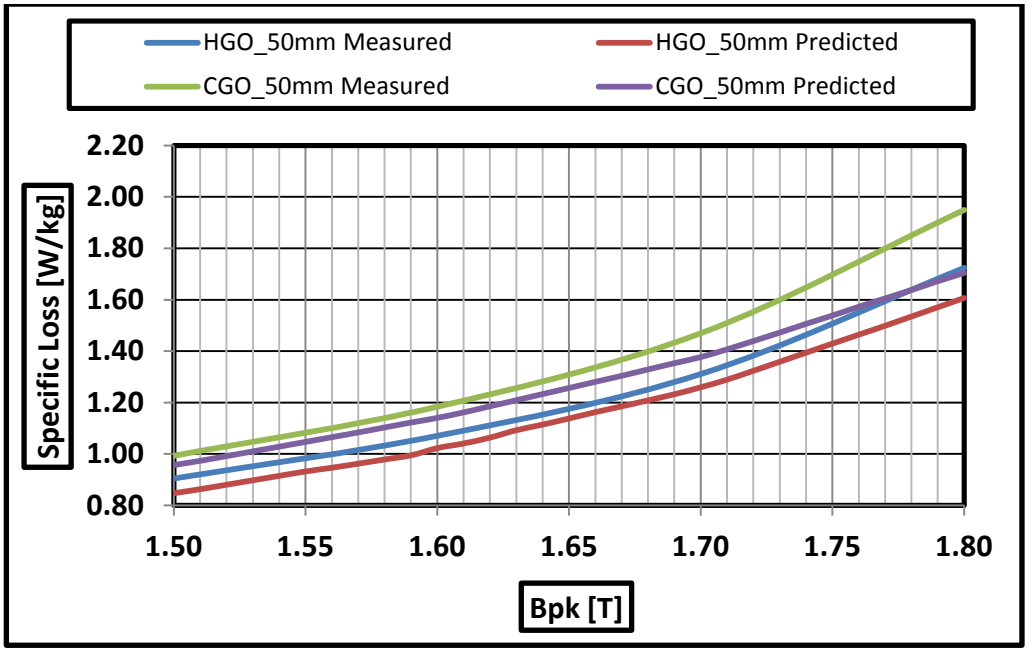

Fig.5-35 Measured and predicted specific loss for 50mm lamination width, single packet 3-phase, 3-limb HGO and CGO cores.

The predicted specific losses for single packet 50 mm lamination width HGO and CGO cores are lower than the measured specific losses.

The single packet, 50mm lamination width HGO and CGO cores have a higher $\frac{d}{W}$ & $\frac{s_w}{W}$ ratio (0.2) which increases losses in the corner joints. The additional losses assumed for the multi-packet cores are lower when applied to cores which have a higher $\frac{d}{W}$ & $\frac{s_w}{W}$ ratio (0.2).

The percentage difference in predicted and measured specific losses for full size multi-packet and single packet HGO cores is shown in Fig. 5-36.

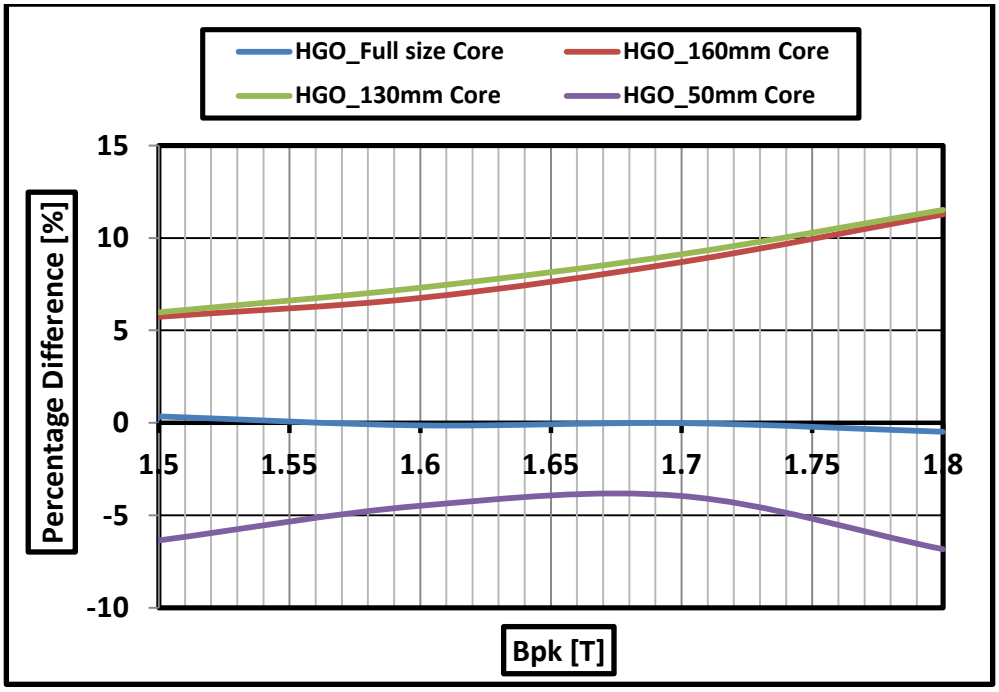

Fig.5-36 Percentage difference in predicted and measured specific loss for full size multi-packet and single packet HGO 3-phase, 3-limb cores.

The percentage difference in predicted and measured specific losses for full size multi-packet and single packet CGO cores is shown in Fig. 5-37.

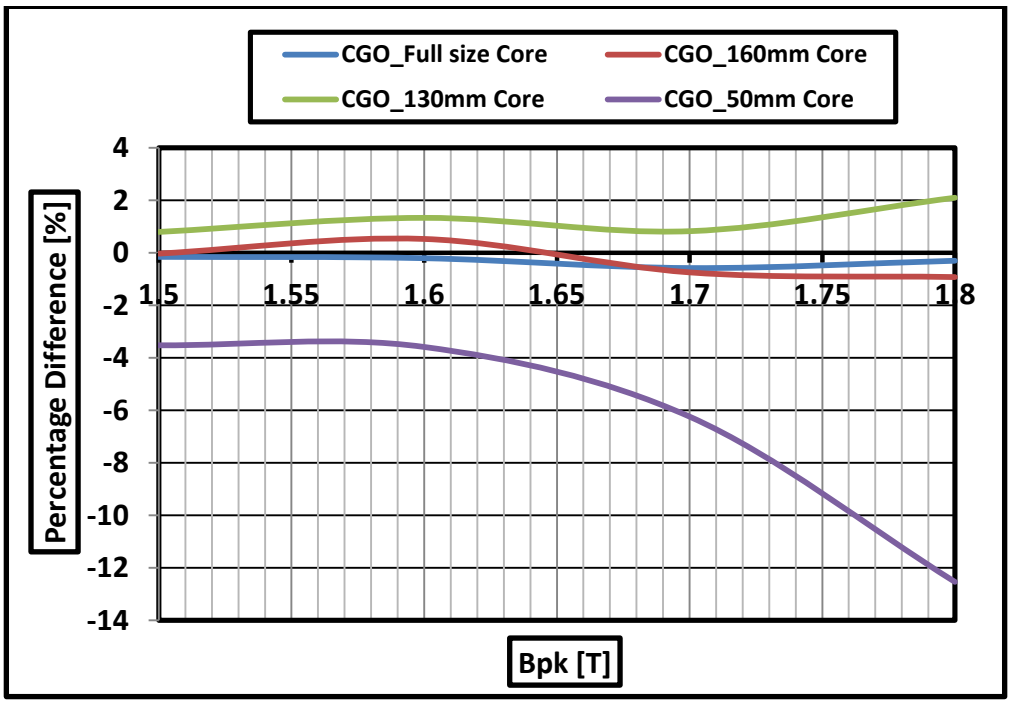

Fig.5-37 Percentage difference in predicted and measured specific loss for multi-packet full size and single packet CGO 3-phase, 3-limb cores.

The percentage difference in measured and predicted specific losses shown in Fig. 5-36 and Fig.5-37 could be used as correction factors when predicting for different single packet geometries. For example, the percentage difference between the measured and predicted losses of CGO 50 mm wide packet is - 6% at B_{pk} = 1.7 T at (Fig.5-37). This 6 % can be added as a correction factor to the predicted results of CGO 50 mm wide packet for error to be negligible.

5.5.7 Differences in the Predicted and Measured Results

The differences arising in the predictions are due to packet to packet variation of flux density, localised loss data sheets and affected regions. Also the results do not take into account the effects of magnetic path length which varies across the sheet width [78]. Also, the algorithm does not include the dependence of power loss on the location of the bolt holes and slots in the core geometry. The predicted results are indicative of the amount of localised losses and total losses occurring in the actual cores. This method can serve transformer core and electrical steel manufacturers to quickly predict losses for commercial multi-packet and single packet designs using the geometry and material properties rather than the time consuming data sheets.

5.5.8 Suggested Design Changes

Changes in design can be made based on the indicative results. For the multi-packet HGO and CGO cores investigated, the packet (50mm wide) with the highest $\frac{d}{W}$ & $\frac{s_w}{W}$ of 0.2 must be replaced with a packet with much lower $\frac{d}{W}$ & $\frac{s_w}{W}$ value closer to that of the two wider packets (130mm and 160mm) in order to obtain a better flux distribution and lower losses in the cores. Boltless cores can also serve as an option.

5.6 Summary

An algorithm to predict the total specific losses and local losses of HGO and CGO 3-phase, 3-limb transformer cores was presented and its accuracy and applications are demonstrated and discussed. The difference between the measured and predicted results was within 1% for multi-packet 3-phase, 3-limb transformer cores. The predicted losses for boltless cores indicate that a 2% loss reduction is possible in

HGO and CGO cores at B_{pk} = 1.7 T. The difference between the measured and predicted results was within 9% for HGO single packet 3-phase, 3-limb transformer cores at B_{pk} = 1.7 T. The difference between the measured and predicted results is within 2% for CGO single packet 3-phase, 3-limb transformer cores at B_{pk} = 1.7 T. Correction factors for single packet HGO and CGO 3-phase, 3-limb cores are shown.

Chapter 6

Conclusion and Future Work

6.1 Conclusions

An algorithm was built in NI LabVIEW which can be used to predict specific losses for any multi-packet and single packet stacked HGO and CGO 3-phase, 3-limb transformer cores. The algorithm considered geometrical parameters and material properties as input. The difference in predicted and measured values was found to be within 1% for multi-packet HGO and CGO cores. The difference in predicted and measured values was within 9% for single packet HGO cores and within 2% for single packet CGO cores. The differences in predicted and measured specific losses for HGO and CGO single packet cores can be corrected by applying correction factors to the predicted results. A 2% specific loss reduction is predicted by the algorithm for the multi-packet 3-phase, 3-limb design if the bolt holes and slots are eliminated. This algorithm can be used by electrical steel manufacturers and transformer designers.

The packet to packet variation of flux density in stacked, multi-packet, HGO and CGO, 3-phase, 3-limb transformer cores built with multi-step lap (MSL) joints has been found to be affected by the bolt hole diameter and lamination width ratio $\left(\frac{d}{W}\right)$ and slot width and lamination width ratio $\left(\frac{s_w}{W}\right)$ ratio in the packets. The higher the ratio, the lower is the effective permeability of the packets and vice versa. This result must be considered by transformer designers in order to design transformers with better flux distribution.

The variation of no load apparent power of mixed single phase Epstein size cores built with HGO with CGO is linear. The variation of no load power loss and apparent power with CGO material content in a multi-packet 3-phase, 3-limb transformer core design predominantly built with HGO material is non-linear. This is because the losses and apparent power are affected by the packet to packet variation of flux density. This result must be considered by transformer designers to design multi packet mixed cores.

Data sets for percentage increase in specific loss and percentage decrease in relative permeability around different sizes of bolt holes and slots for varying flux density were processed from FE simulations. The Data sets for affected region length and percentage increase in specific loss were used in the loss prediction algorithm. The Data sets for affected region length, percentage increase in flux density and percentage decrease in relative permeability were used in calculating the effective permeability of transformer packets. The processed data sets can be used by transformer designers to estimate the localised magnetic properties around holes and slots.

6.2 Future Work

Specific loss measurements for HGO and CGO 3-phase, 3-limb transformer cores of various shapes and sizes are necessary to optimise the factors affecting the predicted specific losses and improve the overall accuracy of the presented algorithm. A data bank can be created to train the algorithm to convert it into a full-fledged neural network algorithm considering the position dependence of localised losses. The algorithm can be modified to predict specific losses of single phase cores.

Mixing Materials for various core designs with different aspect ratios (ratio of length of yoke and length of limb) for boltless multi-packet cores will negate the effect of $\left(\frac{d}{W}\right)$ and $\left(\frac{s_w}{W}\right)$ ratios on the increase in specific loss of the cores. The results of such an investigation could be useful in the design of various sizes of boltless commercial mixed cores which can be installed in the power network.

The simulation results of affected region length and increase in specific power loss around holes and slots in electrical steel can be verified by thermography.

A multi-physics model simulating the mechanical stress distribution and magnetic flux distribution is necessary to estimate the effect of stress on the flux waveform. Knowing the material characteristics, specific losses can be estimated from the flux waveforms.

Appendix I (References)

[1] D. C. Jiles, “Introduction to Magnetism and Magnetic Materials,” Second edition, Chapman & Hall/CRC, London, 1998.

[2] B. D. Cullity, “Introduction to Magnetic Materials,” Addison-Wesley, Reading, Massachusetts, 1972.

[3] S. Somkun, “Magnetostriction and Magnetic Anisotropy in Non-oriented Electrical Steels and Stator Core Laminations,” Doctoral Thesis, Cardiff University, 2010.

[4] R. A. Hadfield, “Magnetic composition and method of making the same,” *United States Patent Office*, Patent No. 745829, December 1, 1903.

[5] K. Beck, “The magnetic properties of Fe crystals at ordinary temperature,” *Zurich Naturforsch Ges.*, 63, pp. 116186, 1918.

[6] W. E. Ruder, “Magnetisation and crystal orientation,” *Trans. Am. Soc. Steel Treating*, pp. 23-29, 1920.

[7] N. P. Goss, “Electrical sheet and method and apparatus for its manufacture and test,” *United States Patent Office*, Patent No. 1965559, July 3, 1934.

[8] A. J. Moses, “Electrical Steels: Past, Present and Future Developments,” *IEE Proceedings*, vol. 137, Pt. A, No. 5, pp. 233-245, 1990.

[9] P. Beckley, “Electrical Steels: A Handbook for Producers and Users,” First edition, European Electrical Steels, Newport, South Wales, 2000.

[10] G. E. Fish, “Soft magnetic materials,” *Proceedings of the IEEE*, vol. 78, pp. 947-972, 1990.

[11] T. Suzuki, H. Nakayama, T. Yamamoto and S. Taguchi, “Transformer Characteristics of Orientcore-Hi-B,” *IEEE Transactions on Magnetics*, vol. 8, pp. 321-323, 1972.

[12] T. Yamamoto, S. Taguchi, A. Sakakura and T. Nozawa, “Magnetic Properties of Grain-Oriented Silicon Steel with High Permeability Orientcore Hi-B,” *IEEE Transactions on Magnetics,* vol. 8, pp. 677-681, 1972.

[13] S. Taguchi, S. Yamamoto and A. Sakakura, “New Grain-Oriented Silicon Steel with High Permeability Orientcore Hi-B,” *IEEE Transactions on Magnetics*, vol. 10, pp. 123-127, 1974.

[14] T. Nozawa, T. Yamamoto, Y. Matsuo and Y. Ohyo, “Effects on Scratching on Losses in 3-percent Si-Fe Single Crystals with Orientation near (110) [001],” *IEEE Transactions on Magnetics*, vol. 2, pp. 972-981, 1979.

[15] ThyssenKrupp Electrical Steel, www.tkes.com, retrieved Feb 12 2012.

[16] BS EN 60404-2:1998 + A1:2008, “*Magnetic Materials-Part 2: Method of Measurement of the Magnetic Properties of Electrical Steel Sheet and Strip by Means of an Epstein Frame*,” British Standard*, 2009.*

[17] BS EN 10280:2001 + A1:2007, “*Magnetic Materials - Methods of measurement of the magnetic properties of electrical sheet and strip by means of a single sheet tester*,” British Standard, 2008.

[18] P. Marketos, S. Zurek and A. J. Moses, “A method for defining the mean path length of the Epstein frame,” *IEEE Transactions on Magnetics*, vol. 43, pp. 2755-2757, Jun 2007.

[19] J. Sievert, “The measurement of magnetic properties of electrical steel sheet survey on methods and situation of standards,” *Journal of Magnetism and Magnetic Materials*, vol. 215-216, pp. 647-651, 2000.

[20] G. Bertotti, “General-Properties of Power Losses in Soft Ferromagnetic Materials,” *IEEE Transactions on Magnetics*, vol. 24, pp. 621-630, Jan 1988.

[21] A. J. Moses, “Energy efficient electrical steels: Magnetic performance prediction and optimization,” *Scripta Materialia*, vol. 67, pp. 560-565, Sep 2012.

[22] S.E. Zirka, Y. I. Moroz, P. Marketos and A. J. Moses, “Novel approach to modelling losses in electrical steel laminations,” *Proceedings of the Fourth International Conference on Computation in Electromagnetics*, 8-11 April 2002.

[23] S. E. Zirka, Y. I. Moroz, P. Marketos and A. J. Moses, “Modelling losses in electrical steel laminations,” *IEE Proc. – Sci. Meas. Technol.*, vol. 149, no. 5, pp. 218-221, September 2002.

[24] S. E. Zirka, I. Moroz, P. Marketos and A. J. Moses, “A viscous-type dynamic hysteresis model as a tool for loss separation in conducting ferromagnetic laminations,” *IEEE Transactions on Magnetics*, vol. 41, no. 3, pp. 1109-1111, March 2005.

[25] S. E. Zirka, I. Moroz, P. Marketos and A. J. Moses, “Viscosity-based magnetodynamic model of soft magnetic materials,” *IEEE Transactions on Magnetics*, vol. 42, pp. 2121-2132, Sep 2006.

[26] A. J. Moses, “Loss prediction in electrical steel laminations and motor cores,” *Steel Research International Journal*, 76 (6), 455-460, 2005.

[27] L. R. Dupre, R. VanKeer and J. A. A. Melkebeek, “Modelling and identification of iron losses in non-oriented steel laminations using Preisach theory,” *IEE Proc. – Electr. Power Appl.*, vol. 144, no. 4, pp. 227-234, 1997.

[28] L. R. Dupre, G. Bertotti and J. A. A. Melkebeek, “Dynamic Preisach model and energy dissipation in soft magnetic materials,” *IEEE Transactions on Magnetics*, vol. 34, no. 4, pp. 1168-1170, July 1998.

[29] L. R. Dupre, O. Bottauscio, M. Chiampi and F. Fiorillo, “Dynamic Preisach modelling of ferromagnetic laminations under distorted flux excitations,” *IEEE Transactions on Magnetics*, vol. 34, no. 4, pp. 1231-1233, July 1998.

[30] A. J. Moses and B. Thomas, “Measurement of rotating flux in silicon iron laminations,” *IEEE Transactions on Magnetics*, vol. 9, pp. 651-654, 1973.

[31] R. M. Bozorth, “Ferromagnetism,” D. Van Nostrand Company, Inc., Princeton, New Jersey, USA, 1951.

[32] William Stanley Jr., “Induction Coil,” United States Patent Office, Patent No. 349611, September 21, 1886.

[33] J. W. Coltman, “The transformer,” *IEEE Industry Applications Magazine*, vol. 8, pp. 8-15, Jan-Feb 2002.

[34] S. S. Mulukutla, “Electric machines: - steady-state theory and dynamic performance,” West Publ. Co., New York, 1986.

[35] “IEEE Guide for Transformer Loss Measurement,” *IEEE Std C57.123-2002*, pp.0_1-36, 2002.

[36] M. Heathcote, “J & P Transformer Book,” Twelfth edition, 1998.

[37] F. Brailsford and V. R. Mazza, “The alternating flux distribution in right angled corners of transformer laminations,” *IEE*, no. 3870s, pp. 173-180, April 1962.

[38] A. J. Moses, B. Thomas and J. Thompson, “Power Loss and Flux Density Distributions in T-Joint of a 3 Phase Transformer Core,” *IEEE Transactions on Magnetics*, vol. 8, pp. 785-790, 1972.

[39] A. J. Moses and B. Thomas, “Spatial Variation of Localized Power Loss in 2 Practical Transformer T-Joints,” *IEEE Transactions on Magnetics*, vol. 9, pp. 655-659, 1973.

[40] M. A. Jones and A. J. Moses, “Comparison of Localized Power Loss and Flux Distribution in Butt and Lap and Mitered Overlap Corner Configurations,” *IEEE Transactions on Magnetics*, vol. 10, pp. 321-326, 1974.

[41] A. J. Moses, “Problems in the Use of High Permeability Silicon-Iron in Transformer Cores,” *Journal of Magnetism and Magnetic Materials*, vol. 19, pp. 36-38, 1980.

[42] Z. Valkovic and A. Rezic, “Improvement of Transformer Core Magnetic-Properties Using the Step-Lap Design,” *Journal of Magnetism and Magnetic Materials*, vol. 112, pp. 413-415, Jul 1992.

[43] F. Loffler, T. Booth, H. Pfutzner, C. Bengtsson and K. Gramm, “Relevance of Step-Lap Joints for Magnetic Characteristics of Transformer Cores,” *IEE Proceedings-Electric Power Applications*, vol. 142, pp. 371-378, Nov 1995.

[44] A. J. Moses and B. Thomas, “Problems in Design of Power Transformers,” *IEEE Transactions on Magnetics*, vol. 10, pp. 148-150, 1974.

[45] A. Basak and A. J. Moses, “Harmonic Losses in a 3 Phase Transformer Core,” *IEEE Transactions on Magnetics*, vol. 14, pp. 990-992, 1978.

[46] A. J. Moses and A. Sakaida, “Effect of Distorted Flux-Density on 3-Phase Transformer Cores Assembled from High-Quality Electrical Steels,” *IEEE Transactions on Magnetics*, vol. 22, pp. 532-534, Sep 1986.

[47] A. Basak, A. J. Moses and R. Al-Bir, “Effect of Clamping Stress on Power Loss in Powercore Strip and Si-Fe Transformer Cores,” *IEEE Transactions on Magnetics*, vol. 26, pp. 1999-2001, Sep 1990.

[48] R. S. Girgis, E. G. teNijenhuis, K. Gramm and J. E. Wrethag, “Experimental investigations on effect of core production attributes on transformer core loss performance,” *IEEE Transactions on Power Delivery*, vol. 13, pp. 526-531, Apr 1998.

[49] E. teNyenhuis and R. Girgis, “Effect of slitting electrical core steel on measured iron loss,” *Journal of Magnetism and Magnetic Materials*, vol. 215, pp. 110-111, Jun 2000.

[50] A. Basak and A. A. A. Qader, “Fundamental and Harmonic Flux Behavior in a 100 Kva Distribution Transformer Core,” *IEEE Transactions on Magnetics*, vol. 19, pp. 2100-2102, 1983.

[51] B. Thomas, “Flux Paths and Flux Transfer Mechanism in T-Joints of 3-Phase Transformer Cores,” *IEEE Transactions on Magnetics*, vol. 11, pp. 65-71, 1975.

[52] H. Pfutzner, C. Bengtsson, T. Booth, F. Loffler and K. Gramm, “3-Dimensional Flux Distributions in Transformer Cores as a Function of Package Design,” *IEEE Transactions on Magnetics*, vol. 30, pp. 2713-2727, Sep 1994.

[53] Z. Valkovic, “Additional Losses in 3-Phase Transformer Cores,” *Journal of Magnetism and Magnetic Materials*, vol. 41, pp. 424-426, 1984.

[54] E. G. teNyenhuis, R. S. Girgis and G. F. Mechler, “Other factors contributing to the core loss performance of power and distribution transformers,” *IEEE Transactions on Power Delivery*, vol. 16, pp. 648-653, Oct 2001.

[55] P. C. Joslin, A. J. Moses and J. E. Thompson, “Some Aspects of Effects of Longitudinal and Normal Stress on Power Loss and Flux Distribution within a Transformer Core,” *Proceedings of the Institution of Electrical Engineers-London*, vol. 119, pp. 709-716, 1972.

[56] B. Fukuda, K. Satoh, Y. Shimizu and Y. Ito, “Effect of Crystalline Texture in Grain Oriented Si-Fe Sheets on the Building Factor of Transformers,” *Journal of Applied Physics*, vol. 55, pp. 2130-2132, 1984.

[57] A. J. Moses, “Prediction of core losses of three phase transformers from estimation of the components contributing to the building factor,” *Journal of Magnetism and Magnetic Materials*, vol. 254, pp. 615-617, Jan 2003.

[58] Z. Valkovic, “Recent Problems of Transformer Core Design,” *Physica Scripta*, vol. T24, pp. 71-74, 1988.

[59] A. J. Moses and S. Hamadeh, “Effects of Mixing Materials on Losses and Cost of Operation of 3-Phase Transformer Cores,” *Journal of Applied Physics*, vol. 64, pp. 5379-5381, Nov 15 1988.

[60] M. L. Megherbi and A. Basak, “Magnetic Characteristics of Sandwich-Transformer Cores Built with Si-Fe and Amorphous Materials,” *IEEE Transactions on Magnetics*, vol. 25, pp. 3336-3338, Sep 1989.

[61] D. Snell and A. Coombs, “The influence of core materials and mix on the performance of a 100 kVA three phase transformer core,” *Journal of Magnetism and Magnetic Materials*, vol. 254, pp. 349-351, Jan 2003.

[62] T. D. Kefalas, P. S. Georgilakis, A. G. Kladas, A. T. Souflaris and D. G. Paparigas, “Multiple grade lamination wound core: A novel technique for transformer iron loss minimization using simulated annealing with restarts and an anisotropy model,” *IEEE Transactions on Magnetics*, vol. 44, pp. 1082-1085, Jun 2008.

[63] T. D. Kefalas and A. G. Kladas, “Mixed Si-Fe Wound Cores Five Legged Transformer: Losses and Flux Distribution Analysis,” *IEEE Transactions on Magnetics*, vol. 48, pp. 1609-1612, Apr 2012.

[64] T. D. Kefalas and A. G. Kladas, “Development of Distribution Transformers Assembled of Composite Wound Cores,” *IEEE Transactions on Magnetics*, vol. 48, pp. 775-778, Feb 2012.

[65] E. E. Lesniewska and R. Rajchert, “Application of the Field-Circuit Method for the Computation of Measurement Properties of Current Transformers With Cores Consisting of Different Magnetic Materials,” *IEEE Transactions on Magnetics*, vol. 46, pp. 3778-3782, Oct 2010.

[66] R. Pytlech, “Mixed D-Core With a Distributed Air Gap as an Alternative for Medium Voltage Instrument Transformers,” *IEEE Transactions on Magnetics*, vol. 46, pp. 3816-3825, Oct 2010.

[67] BS EN 600761-1:1997, “*Power Transformers-Part 1: General*,” *2004.*

[68] A. Ilo, H. Pfutzner, T. Nakata, “Critical induction - a key quantity for the optimisation of transformer core operation,” *Journal of Magnetism and Magnetic Materials*, vol. 215, pp. 637-640, Jun 2000.

[69] National Instruments, “*DAQ NI 6115/6120 User Manual - Multifunctions devices for PCI/PXI/CompactPCI bus computers,”* 2002.

[70] UKAS M3003, “*The Expression of Uncertainty and Confidence in Measurement,”* 1997.

[71] H. Shimoji, B. E. Borkowski, T. Todaka and M. Enokizono, “Measurement of Core-Loss Distribution Using Thermography,” *IEEE Transactions on Magnetics*, vol. 47, No. 10, pp. 4372-4375, Oct 2011.

[72] A. Basak and G. Lloyd, “Efficient Transformer Design by Computing Core Loss Using a Novel-Approach,” *IEEE Transactions on Magnetics*, vol. 30, pp. 3725-3728, Sep 1994.

[73] A. J. Moses, “Effects of Stress on the Magnetic-Properties of Grain-Oriented Silicon-Iron Magnetized in Various Directions,” *IEEE Transactions on Magnetics*, vol. 17, pp. 2872-2874, 1981.

[74] B. Weiser, H. Pfutzner and J. Anger, "Relevance of Magnetostriction and Forces for the Generation of Audible Noise of Transformer Cores," *IEEE Transactions on Magnetics,* vol. 36, pp. 37559-3777, Sep 2000.

[75] S. Zurek, “Two-dimensional Magnetisation Problems in Electrical Steels,” Doctoral Thesis, Cardiff University, United Kingdom, 2005.

[76] A. Moses,”Prediction of Building Factors in Transformers,” *Developments in Distribution and Power Transformers- UK Magnetic Society Seminar”*, 20 October 2011.

[77] M. Kuwata, S. Nogawa, N. Takahashi, D. Miyagi and K. Takeda, “Development of molded-core-type gapped iron-core reactor,” *IEEE Transactions on Magnetics*, vol. 41, pp. 4066-4068, Oct 2005.

[78] A. Basak, “The Spatial-Distribution of Flux Waveform across the Limbs in a 3-Phase Transformer Core,” *IEEE Transactions on Magnetics*, vol. 16, pp. 540-544, 1980.

Appendix II (List of Publications and Conference Presentations)

International Journals

1. **M. B. BALEHOSUR,** P. Marketos, A. J. Moses and J. N. Vincent, "*Packet to packet variation of flux density in a 3 phase, 3 limb power transformer core*", **IEEE Transactions on Magnetics,** Vol. 46, No. 2, 642-645, February 2010.

2. **M. B. BALEHOSUR**, P. Marketos and A. J. Moses, "*Effect of Excitation Voltage Harmonics on the No-load Loss and Apparent Power of a 3 Phase 3 Limb Transformer Core*", **Przegląd Elektrotechniczny** (Electrical Review), Vol. 85, No.1, 108-110, January 2009.

International Conferences

1. **M. B. BALEHOSUR**, A. J. Moses, J. P. Hall and T. Belgrand, "Effect of mixing HGO and CGO grain oriented steel laminations on the no load performance of 3 phase, 3 limb, power transformer cores", **20th Soft Magnetic Materials Conference**, **Kos Islands, Greece, 18-22 September, 2011**–Page 71, Book of abstracts / Poster presentation.

2. **M. B. BALEHOSUR,** A. J. Moses and T. Belgrand, "Effect of mixing HGO and CGO grain oriented steel laminations on the no load specific losses and building factor of 3 phase, 3 limb, power transformer cores", **IEEE International Magnetics Conference (INTERMAG) 2011 Conference, Taipei, Taiwan, 25-29 April, 2011** –Digest USB / Poster presentation.

3. **M. B. BALEHOSUR,** P. Marketos, A. J. Moses and J. N. Vincent, "*Packet to packet variation of flux density in a 3 phase, 3 limb power transformer core*", **19th Soft Magnetic Materials Conference, Torino, Italy, 6-9 September, 2009** – Book of abstracts (H2-21) / Poster presentation.

4. **M. B. BALEHOSUR,** P. Marketos and A. J. Moses, "*Assessment of the effect of building factor and material defects on transformer core losses***", IEEE Magnetics Society UKRI Chapter Postgraduate Conference 2009, Cardiff, United Kingdom, 9 July, 2009** – Oral presentation.

5. **M. B. BALEHOSUR**, P. Marketos and A. J. Moses, "*Effect of Excitation Voltage Harmonics on the No-load Loss and Apparent Power of a 3 Phase 3 Limb Transformer Core*", **10th International Workshop on 1&2 Dimensional Magnetic Measurement and Testing (1&2DM), Cardiff, United Kingdom, 1-3 September, 2008** – Book of abstracts (P-15) / Poster presentation.

Appendix III (Chapter 2)

A. Input Current Calculation for 3-phase, 3-limb cores under no-load

I. Procedure

The input current for the LTC cores under investigation is calculated by the following steps:

1) Calculation of cross-sectional area.
2) Calculation of the number of winding turns required.
3) Calculation of input current.

1) Calculation of cross-sectional area.

Fig.A-1) shows the cross-sectional area of the multi-packet core. (All dimensions are in mm)

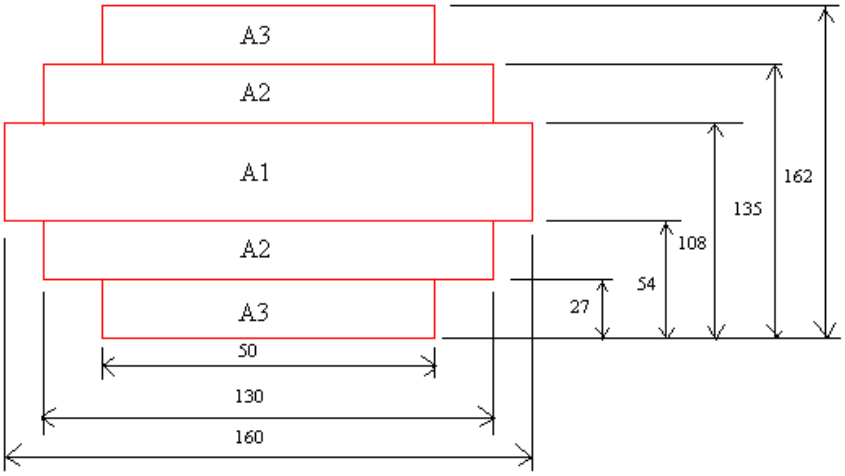

Fig. A-1 The multi-packet core cross-section.

The cross-sectional area 'A' = A1 + 2 A2 + 2A3

= (54 x 160) + 2(27 x 130) + 2(27 x 50)

= 8640 + (3510x2) + (1350x2)

= 18360 mm^2

= 0.01836 m^2

Considering stacking factor = 97 %,

The cross-sectional area 'A' = 0.01836 x 0.97 = 0.0178 m^2

2) Calculation of the number of winding turns required.

We have,

$V_{rms} = 4.44 \times B_{pk} \times N \times A \times f$.

Where V_{rms} = Induced voltage in volts.

B_{pk} = Maximum flux density in the core in Tesla.

N = number of turns

A = area of cross section in m^2

f = frequency in Hz

For B_{pk} = 1.9 T, f = 50 Hz and assumed induced voltage = 240 V,

N = 240 / (4.44x1.9x50x0.0178) = 31.96

For an induced voltage of less than 240 V,

The number of turns is reduced to **30**.

The corresponding induced voltage will be,

V_{rms} = 4.44x1.9x30x0.0178x50 = **225.24 Volts.**

3) Calculation of input current.

Using the equation $V_{rms} = 4.44 \times B_{pk} \times N \times A \times f$,

For B_{pk} = 1.9 T, f = 50 Hz , A = 0.0178 m^2 and N = 12,

V_{rms} = 90.09 Volts.

We know that primary current I = 50 Amps for 12 turns (Data sourced from the transformer manufacturer – LTC, Italy)

Therefore VA = 90.09 x 50 = 4504.5 volt-amperes.

Now knowing VA at 1.9 T = 4504.5 volt-amperes, we can calculate input current I for induced voltage V_{rms} = 225.24 Volts.

I = VA / V = 4504.5 / 225.24 = **20 Amps**.

Therefore primary current required to magnetise the core to 1.9 T = 20 Amperes.

II. Summary

The results for B_{pk} = 1.9 T and f = 50 Hz are summarised in Table A1

Table A1

Number of turns N	Induced Voltage 'V_{rms}' in volts	Input Current / Magnetizing current in Amperes
30	**225.24**	**20**

.

B. Variables obtained from FE Investigations to Calculate Effective Permeability

Table A2 Variables used to calculate the Effective Permeability of 50mm HGO Packet

B_{pk} [T]	l_H [m]	l_S [m]	B_H [T]	B_S [T]	B_g [T]	μ_{rH}	μ_{rS}
1.0	0.121	0.132	1.01	1.01	0.001	42228	41777
1.1	0.133	0.145	1.11	1.12	0.005	43286	42775
1.2	0.145	0.159	1.22	1.22	0.012	44178	43605
1.3	0.157	0.172	1.32	1.32	0.017	44885	44250
1.4	0.147	0.157	1.42	1.43	0.031	42033	40728
1.5	0.137	0.141	1.52	1.54	0.084	37951	36008
1.6	0.095	0.099	1.65	1.66	0.245	27317	25092
1.7	0.053	0.057	1.79	1.78	0.658	15729	13710
1.8	0.040	0.044	1.91	1.90	1.188	5919	4225

Table A3 Variables used to calculate the Effective Permeability of 130mm HGO Packet

B_{pk} [T]	l_H [m]	l_S [m]	B_H [T]	B_S [T]	B_g [T]	μ_{rH}	μ_{rS}
1.0	0.192	0.249	1.00	1.00	0.001	44708	44662
1.1	0.212	0.274	1.10	1.10	0.001	46102	46049
1.2	0.231	0.299	1.20	1.20	0.001	47333	47274
1.3	0.250	0.324	1.30	1.30	0.002	48382	48316
1.4	0.236	0.287	1.41	1.41	0.008	47757	47487
1.5	0.222	0.251	1.51	1.51	0.015	45758	45289
1.6	0.159	0.174	1.61	1.61	0.027	35146	33784
1.7	0.095	0.096	1.72	1.72	0.076	22212	20511
1.8	0.069	0.072	1.82	1.82	0.212	9046	8007

Table A4 Variables used to calculate the Effective Permeability of 160mm HGO Packet

B_{pk} [T]	l_H [m]	l_S [m]	B_H [T]	B_S [T]	B_g [T]	μ_{rH}	μ_{rS}
1.0	0.190	0.251	1.00	1.00	0.001	44873	44859
1.1	0.209	0.276	1.10	1.10	0.001	46288	46273
1.2	0.228	0.301	1.20	1.20	0.001	47543	47525
1.3	0.247	0.327	1.30	1.30	0.002	48614	48595
1.4	0.233	0.288	1.41	1.40	0.007	48181	48005
1.5	0.219	0.250	1.51	1.51	0.014	46362	46034
1.6	0.157	0.173	1.61	1.61	0.023	36449	35224
1.7	0.095	0.096	1.71	1.71	0.061	23737	22148
1.8	0.069	0.071	1.82	1.81	0.170	10100	8949

Table A5 Variables used to calculate the Effective Permeability of 50mm CGO Packet

B_{pk} [T]	l_H [m]	l_S [m]	B_H [T]	B_S [T]	B_g [T]	μ_{rH}	μ_{rS}
1.0	0.082	0.098	1.01	1.01	0.004	35010	34513
1.1	0.090	0.108	1.11	1.12	0.009	35301	34742
1.2	0.098	0.118	1.22	1.22	0.015	34953	34340
1.3	0.107	0.128	1.32	1.32	0.027	33349	32707
1.4	0.113	0.130	1.42	1.43	0.057	26469	26186
1.5	0.120	0.131	1.52	1.54	0.136	19054	19063
1.6	0.107	0.130	1.65	1.66	0.299	13151	13833
1.7	0.093	0.128	1.79	1.78	0.581	6834	7555
1.8	0.068	0.093	1.91	1.90	0.800	2203	2586

Table A6 Variables used to calculate the Effective Permeability of 130mm CGO Packet

B_{pk} [T]	l_H [m]	l_S [m]	B_H [T]	B_S [T]	B_g [T]	μ_{rH}	μ_{rS}
1.0	0.126	0.136	1.00	1.00	0.001	39218	38958
1.1	0.139	0.149	1.10	1.10	0.000	40033	39741
1.2	0.151	0.163	1.20	1.20	0.003	40136	39816
1.3	0.164	0.176	1.30	1.31	0.006	38784	38448
1.4	0.126	0.139	1.41	1.41	0.014	32161	31207
1.5	0.088	0.101	1.51	1.52	0.025	24450	23116
1.6	0.083	0.104	1.61	1.62	0.053	16846	16572
1.7	0.078	0.107	1.72	1.72	0.119	8738	8947
1.8	0.057	0.079	1.83	1.81	0.212	2756	3020

Table A7 Variables used to calculate the Effective Permeability of 130mm CGO Packet

B_{pk} [T]	l_H [m]	l_S [m]	B_H [T]	B_S [T]	B_g [T]	μ_{rH}	μ_{rS}
1.0	0.124	0.133	1.00	1.00	0.001	39353	39167
1.1	0.137	0.146	1.10	1.10	0.001	40185	39976
1.2	0.149	0.160	1.20	1.20	0.004	40303	40073
1.3	0.162	0.173	1.30	1.30	0.008	38958	38718
1.4	0.124	0.134	1.40	1.41	0.014	32748	31782
1.5	0.086	0.096	1.51	1.52	0.022	25296	23870
1.6	0.076	0.096	1.61	1.62	0.045	17399	17071
1.7	0.067	0.096	1.72	1.71	0.109	9009	9194
1.8	0.049	0.071	1.83	1.81	0.302	2823	3090

Appendix III (Chapter 3)

A. Mixed Epstein Combinations

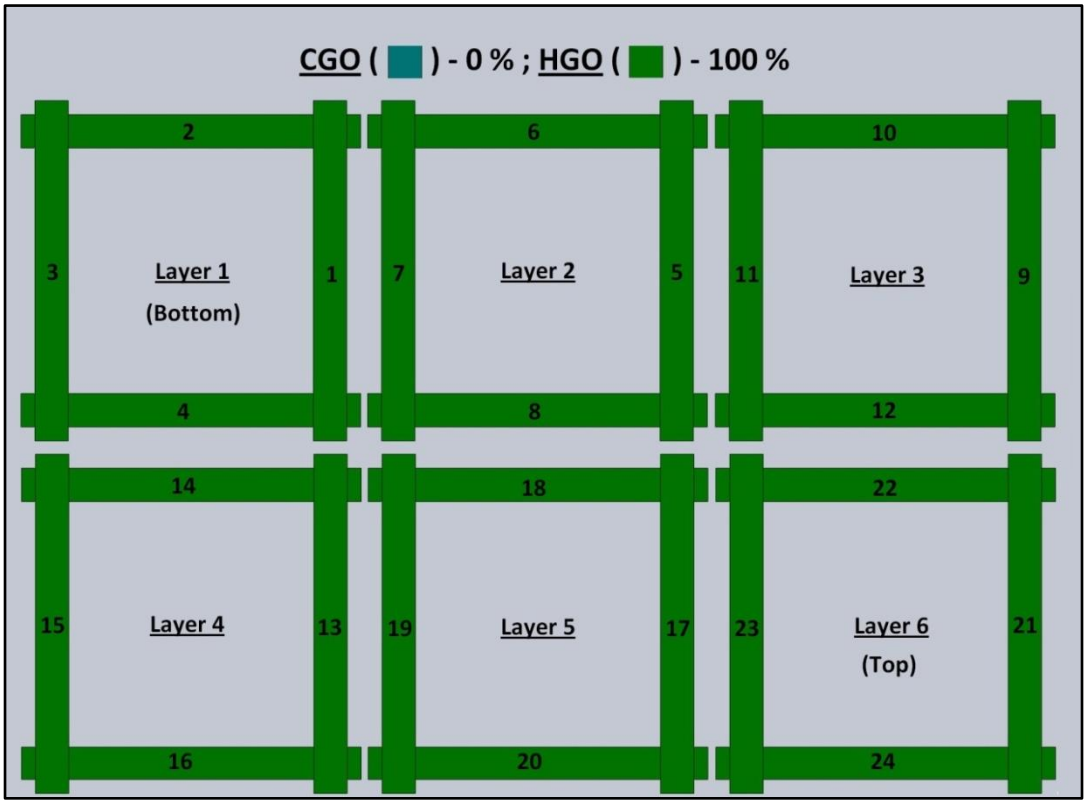

Fig. A-2 Mixed assembly of Epstein Strips for Combination 1 (CGO-0%, HGO -100%).

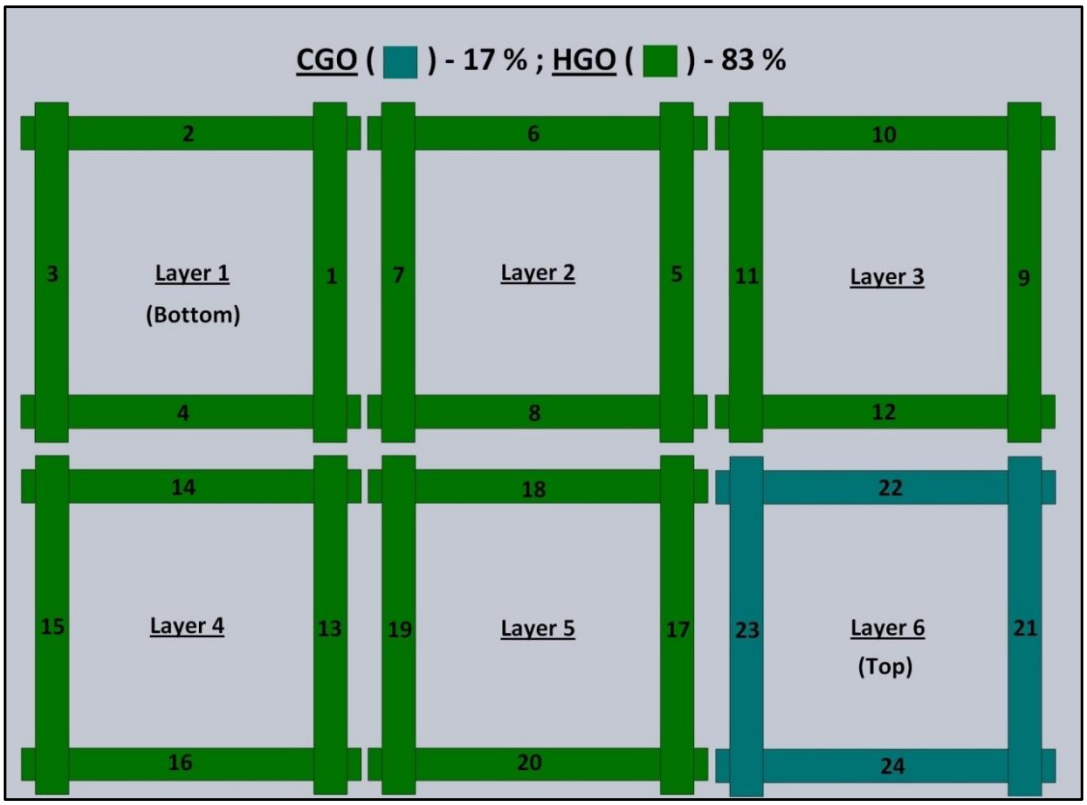

Fig. A-3 Mixed assembly of Epstein Strips for Combination 1 (CGO-17%, HGO -83%).

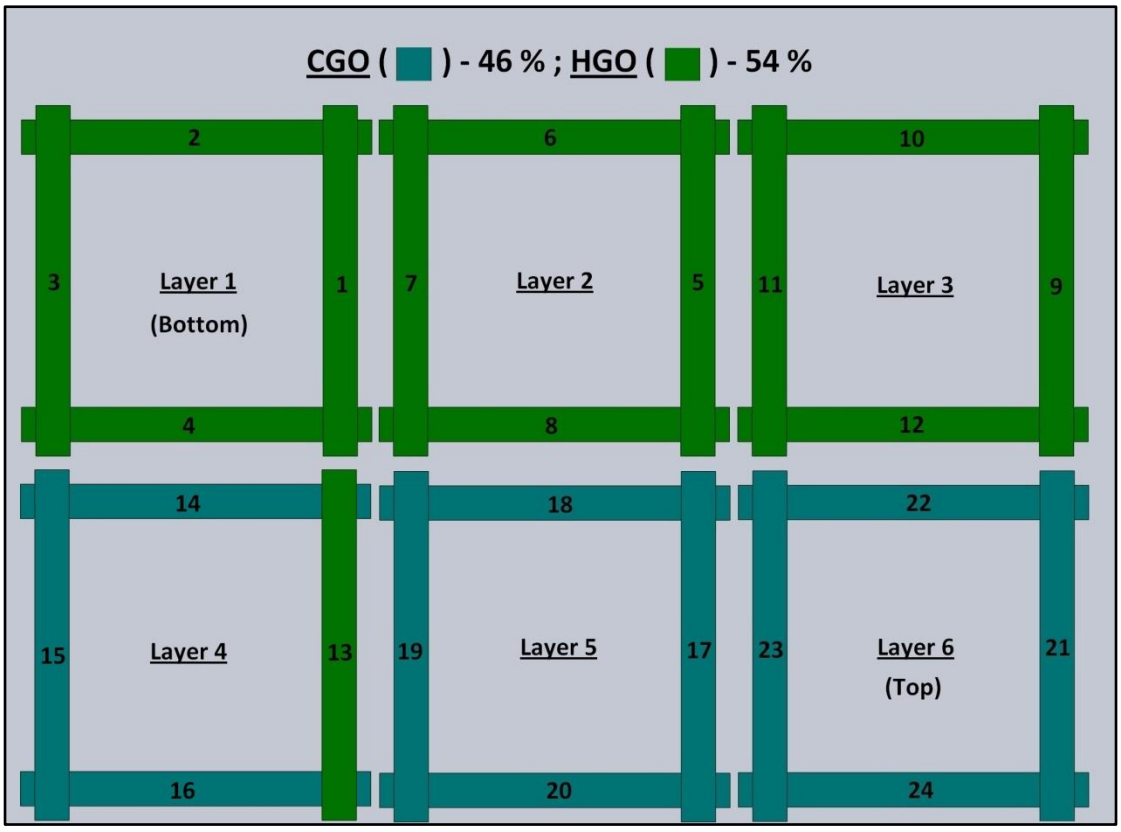

Fig. A-4 Mixed assembly of Epstein Strips for Combination 1 (CGO-46%, HGO -54%).

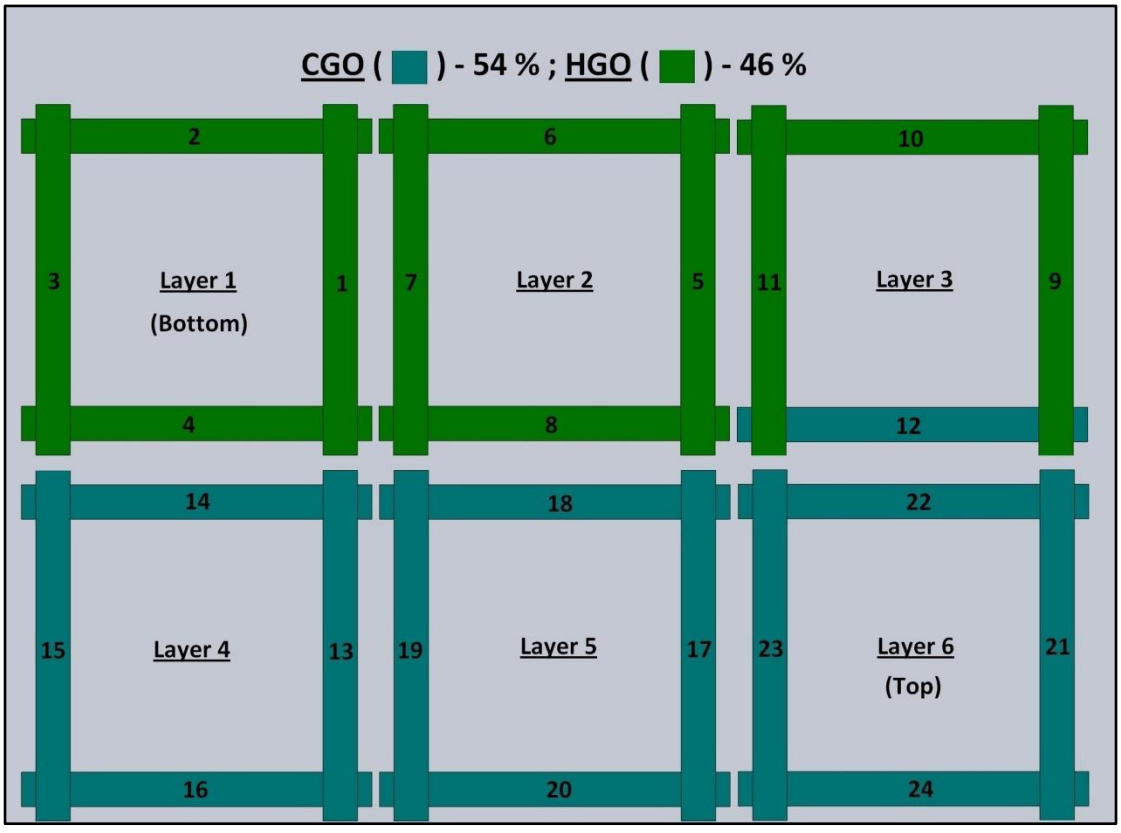

Fig. A-5 Mixed assembly of Epstein Strips for Combination 1 (CGO-54%, HGO -46%).

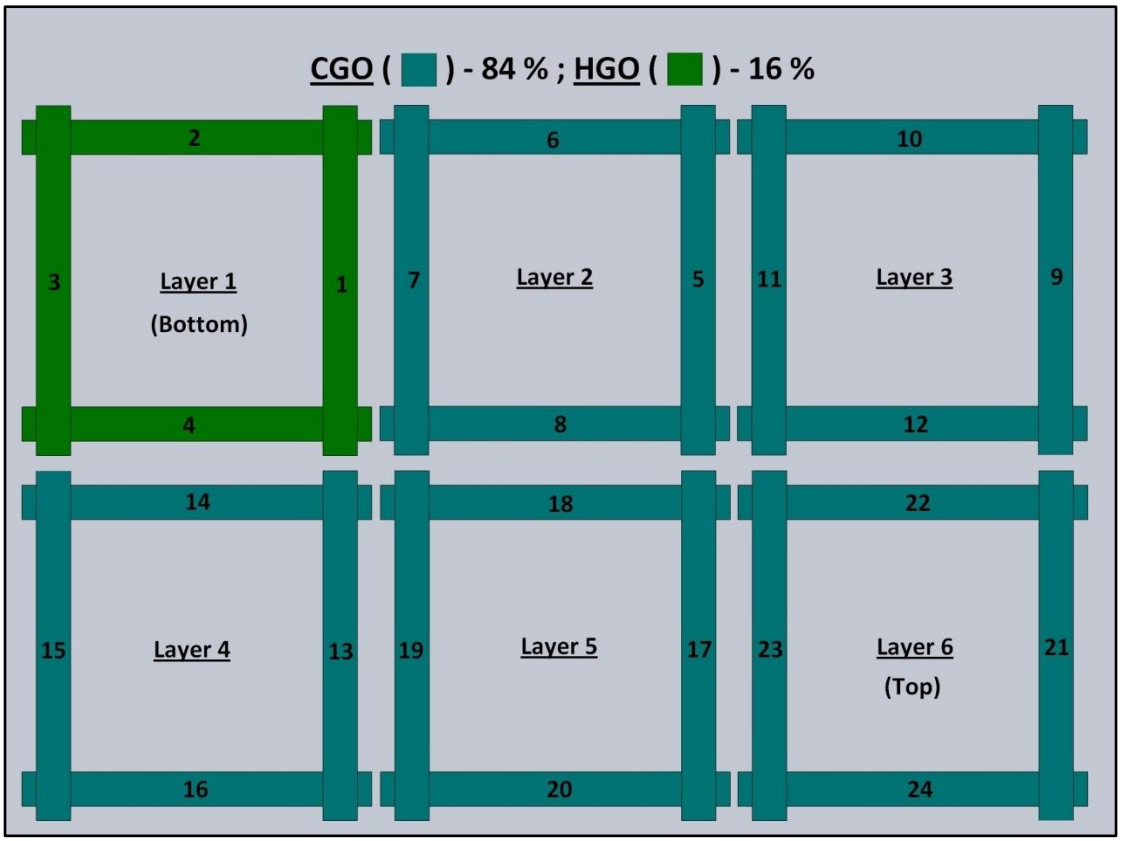

Fig. A-6 Mixed assembly of Epstein Strips for Combination 1 (CGO-84%, HGO -16%).

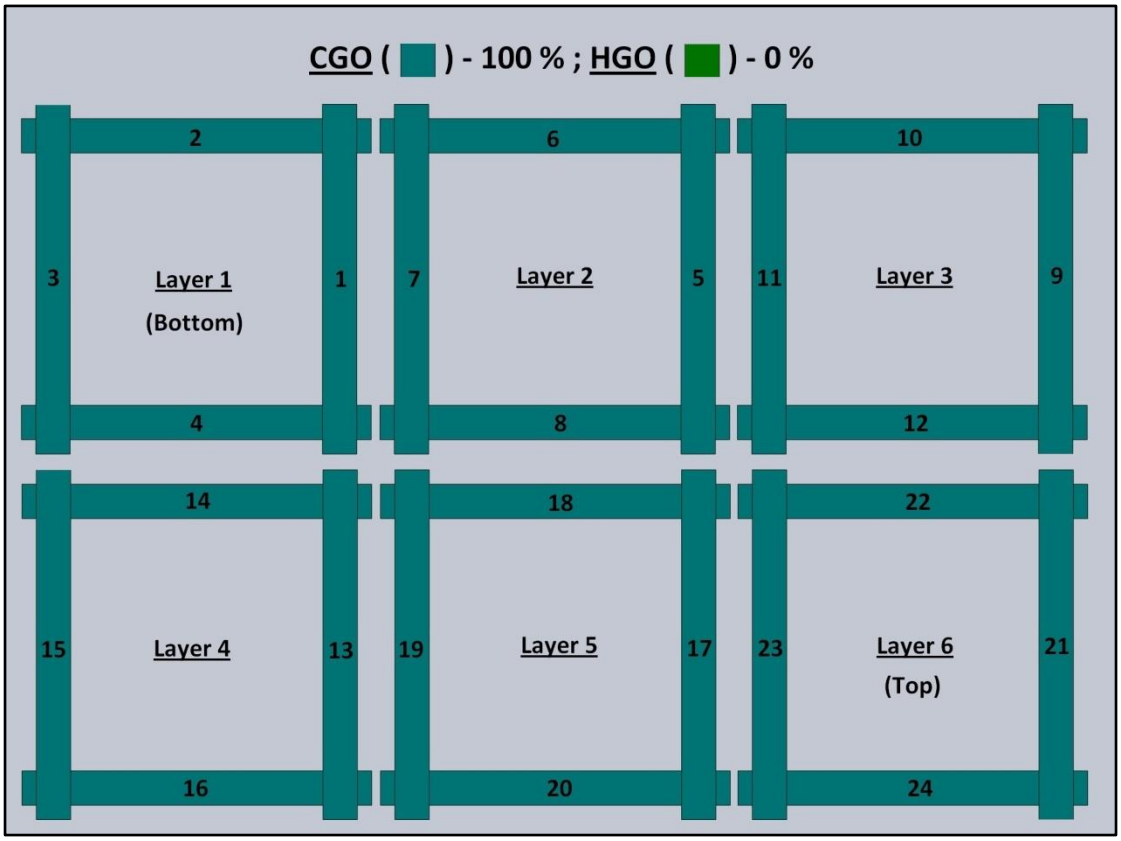

Fig. A-7 Mixed assembly of Epstein Strips for Combination 1 (CGO-100%, HGO -0%).

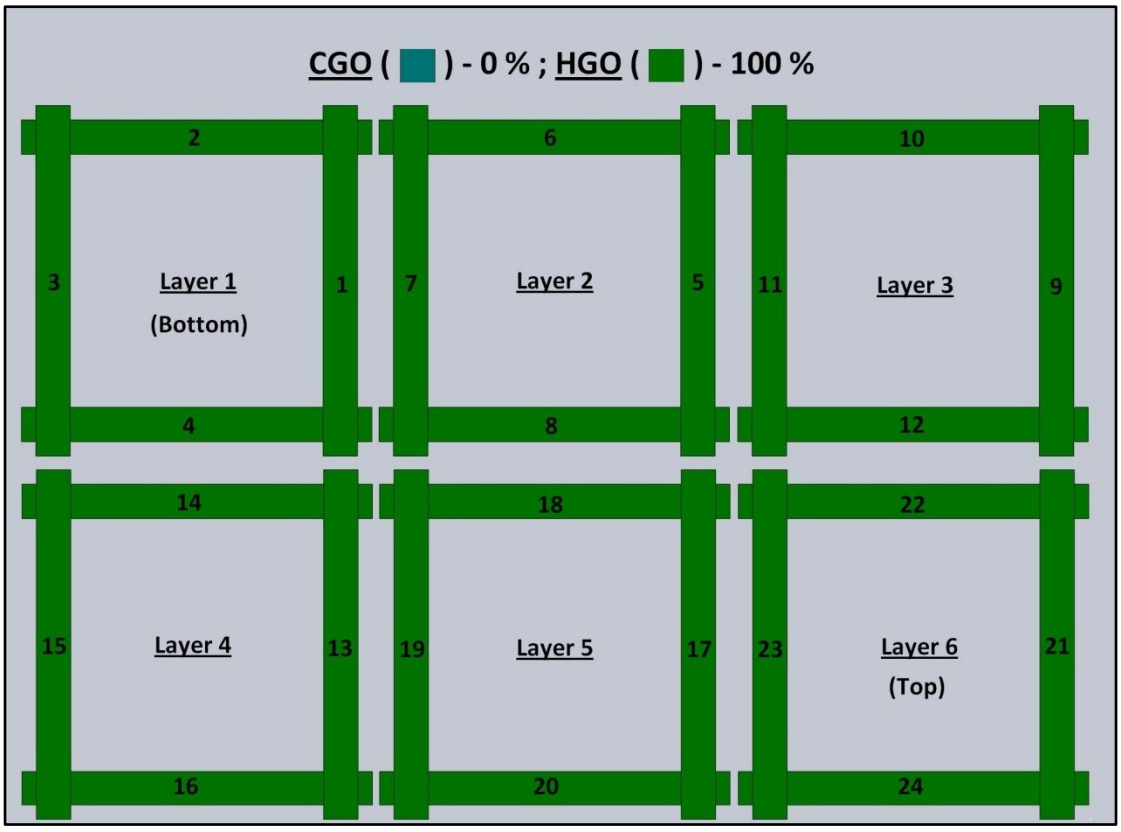

Fig. A-8 Mixed assembly of Epstein Strips for Combination 2 (CGO-0%, HGO -100%).

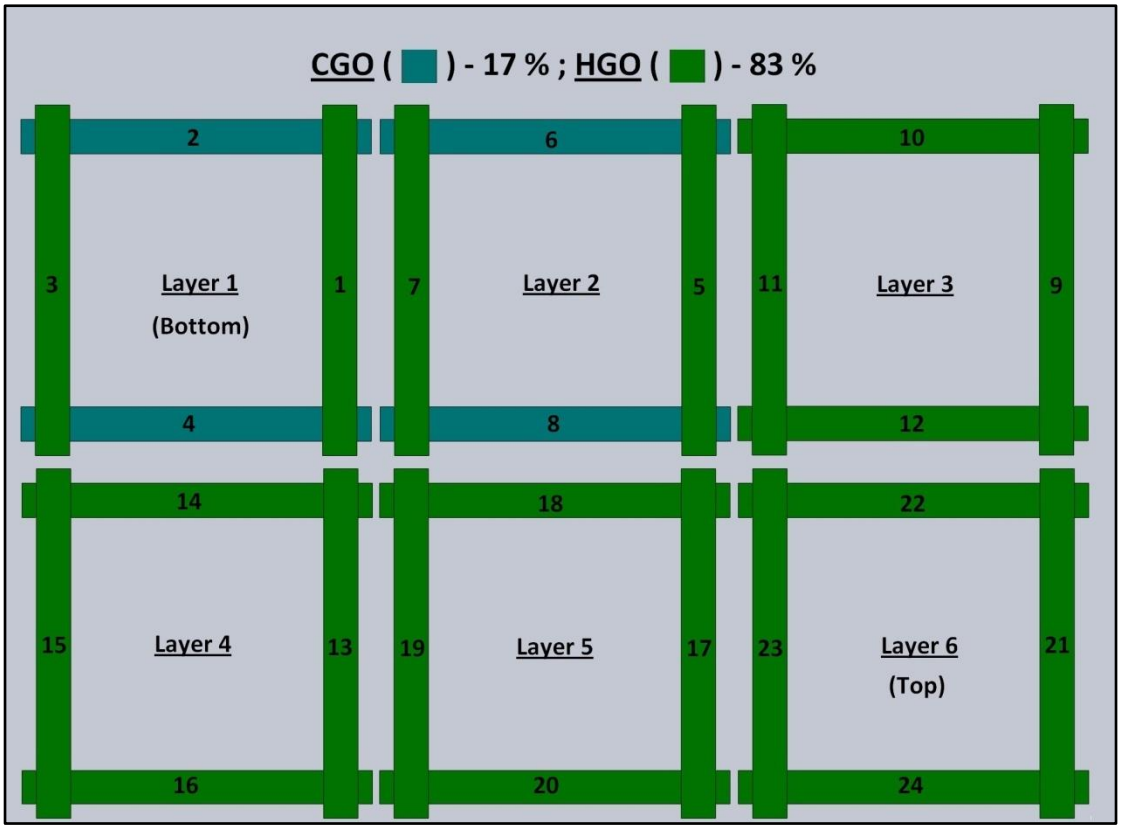

Fig. A-9 Mixed assembly of Epstein Strips for Combination 2 (CGO-17%, HGO -83%).

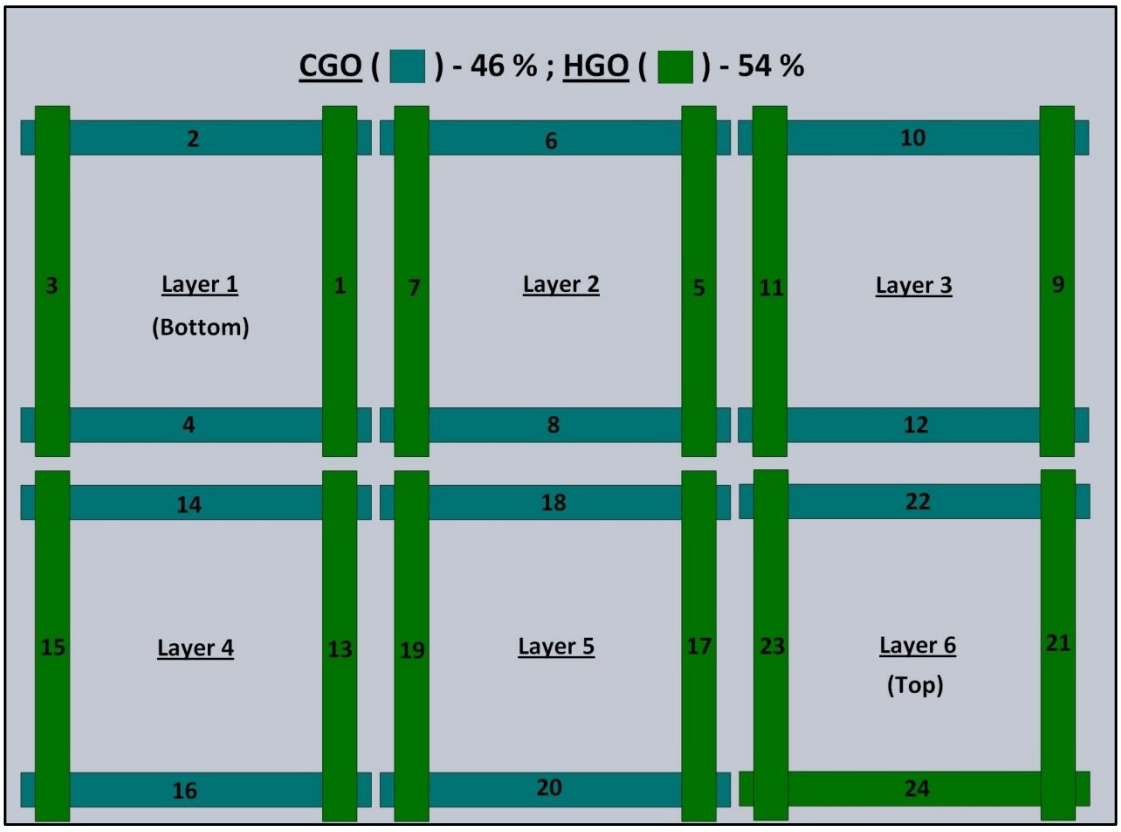

Fig. A-10 Mixed assembly of Epstein Strips for Combination 2 (CGO-46%, HGO -54%).

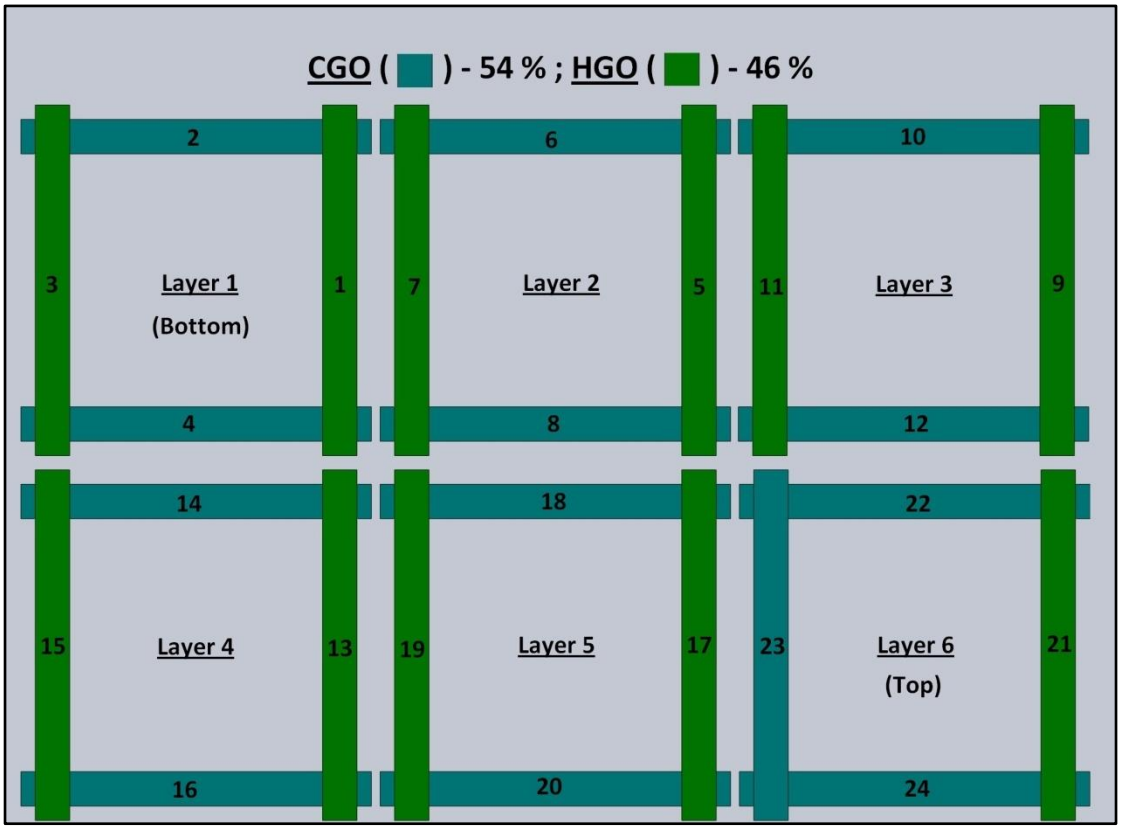

Fig. A-11 Mixed assembly of Epstein Strips for Combination 2 (CGO-54%, HGO -46%).

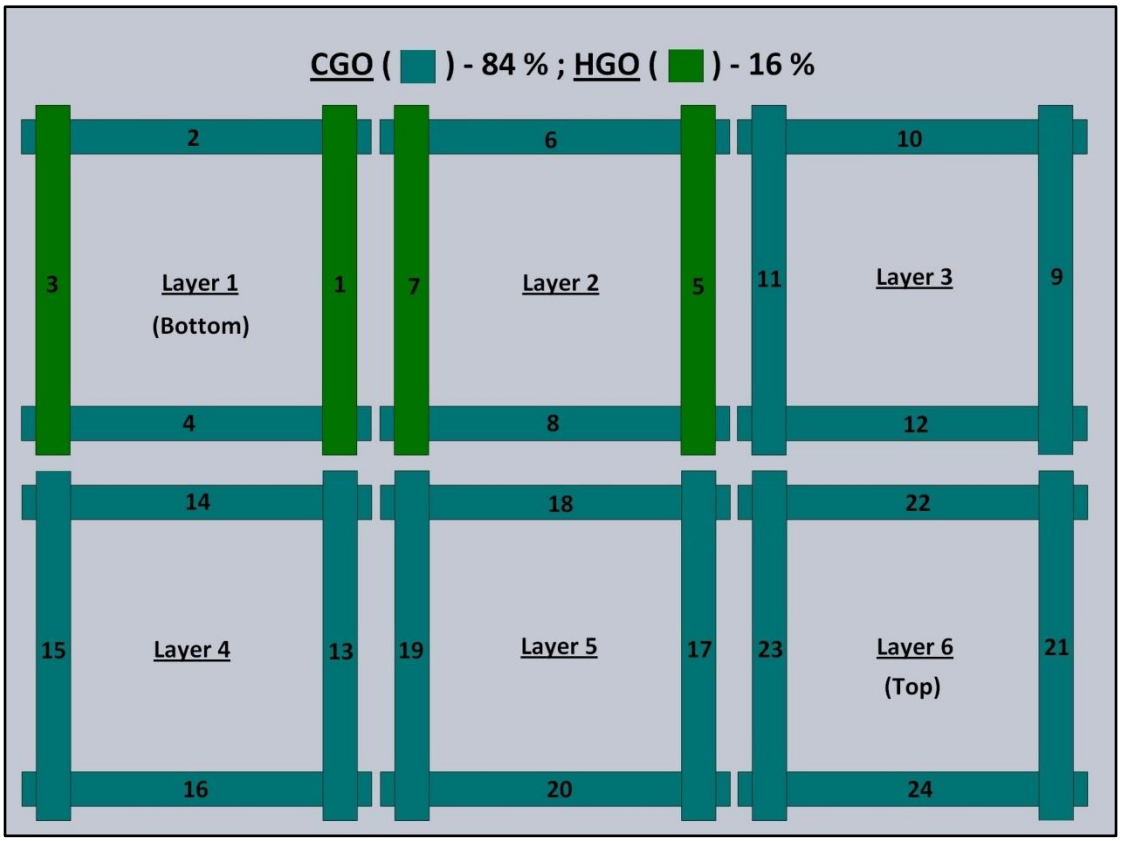

Fig. A-12 Mixed assembly of Epstein Strips for Combination 2 (CGO-84%, HGO -16%).

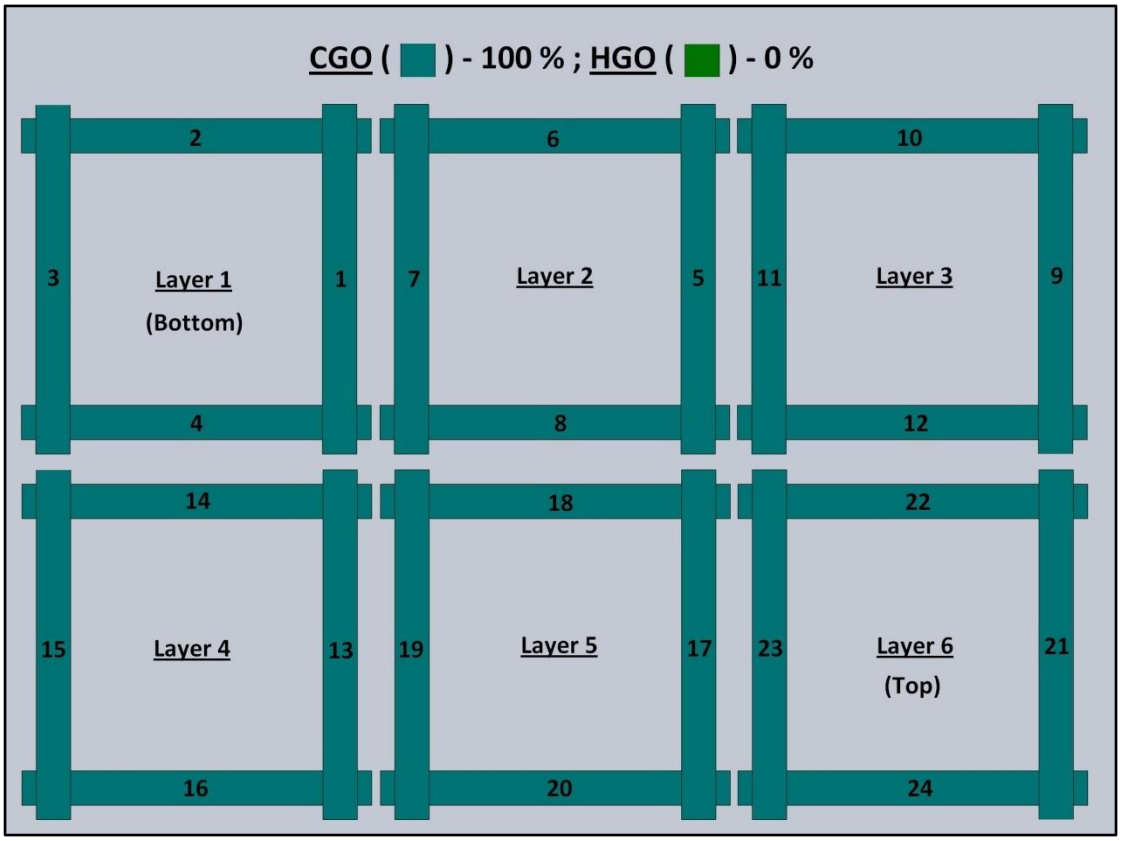

Fig. A-13 Mixed assembly of Epstein Strips for Combination 2 (CGO-100%, HGO -0%).

Appendix IV (Chapter 4)

A. Peak Flux Density Distribution around Holes and Slots

I. Notes

- The flux distribution shown is in the RD.
- All the figures are not to scale as Infolytica MAGNET does not have an option like computer aided software (CAD) to show the dimensions. The width of the strips shown is 30 mm.
- The flux distribution is not symmetrical because of the differences in the mean path length.

II. HGO_Holes

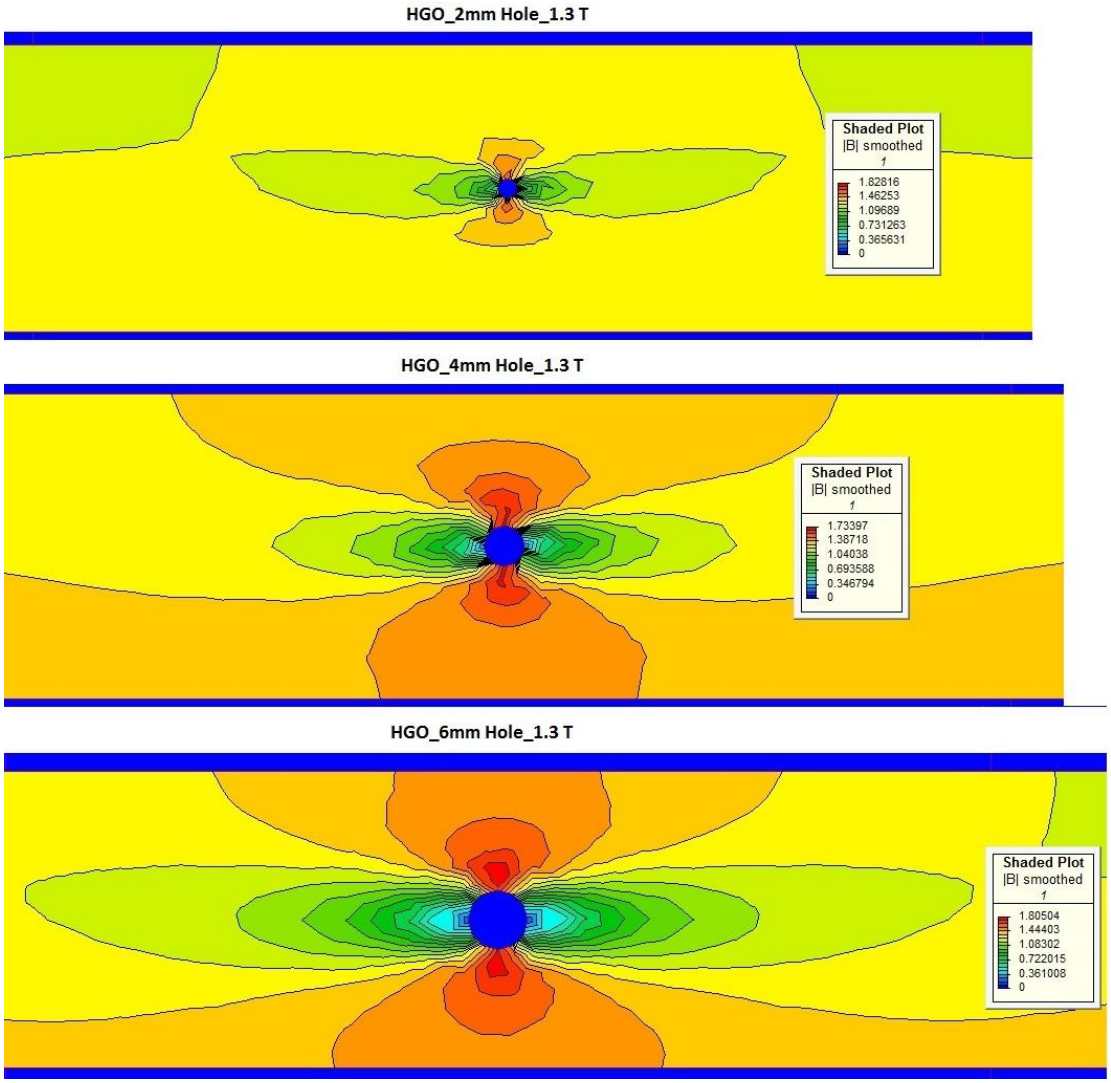

Fig. A-14 Flux density distribution around 2mm, 4mm and 6mm diameter holes in 30mm wide HGO strip at B_{pk}=1.3 T (Not to scale).

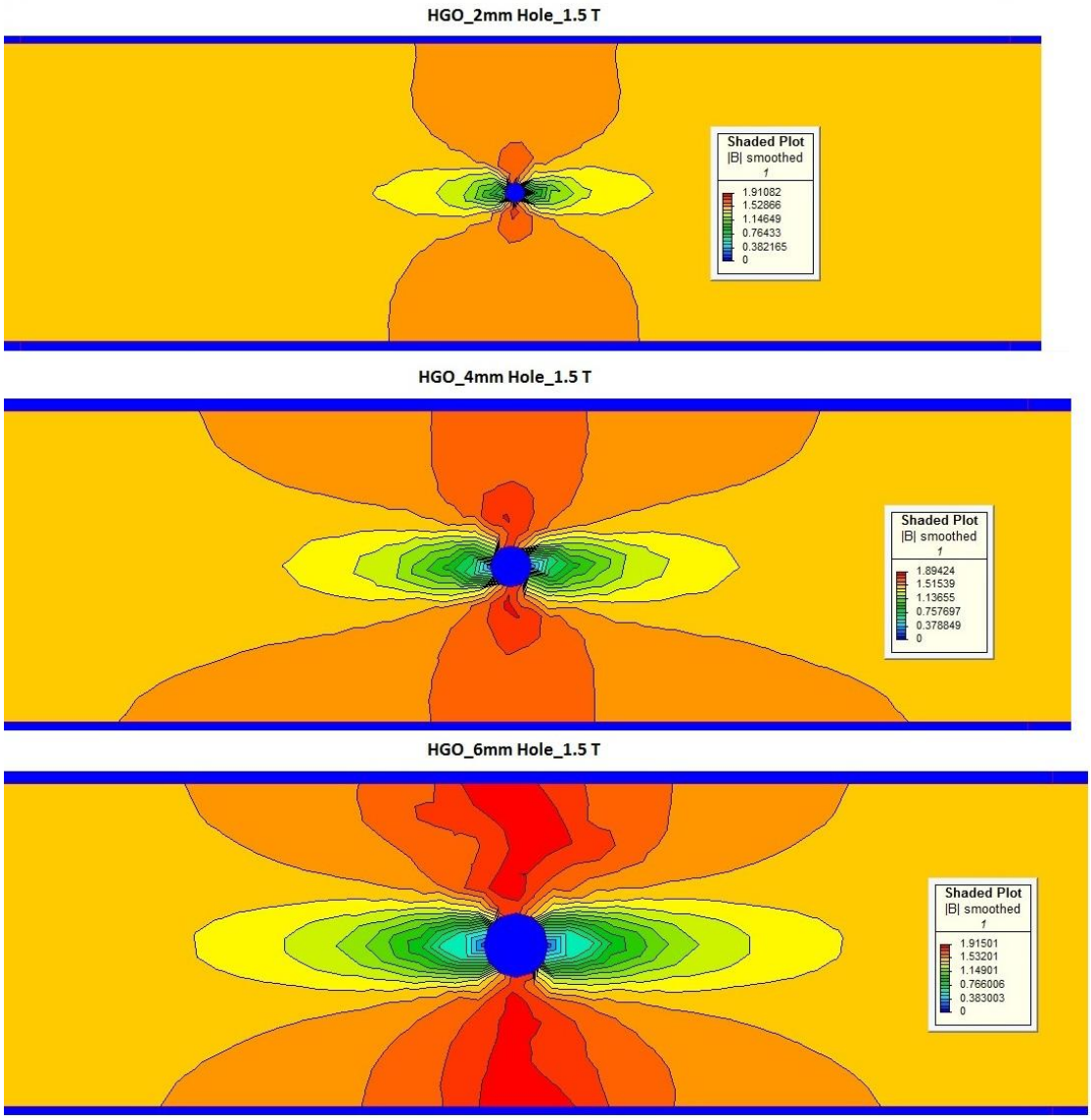

Fig. A-15 Flux density distribution around 2mm, 4mm and 6mm diameter holes in 30mm wide HGO strip at B_{pk}=1.5 T (Not to scale).

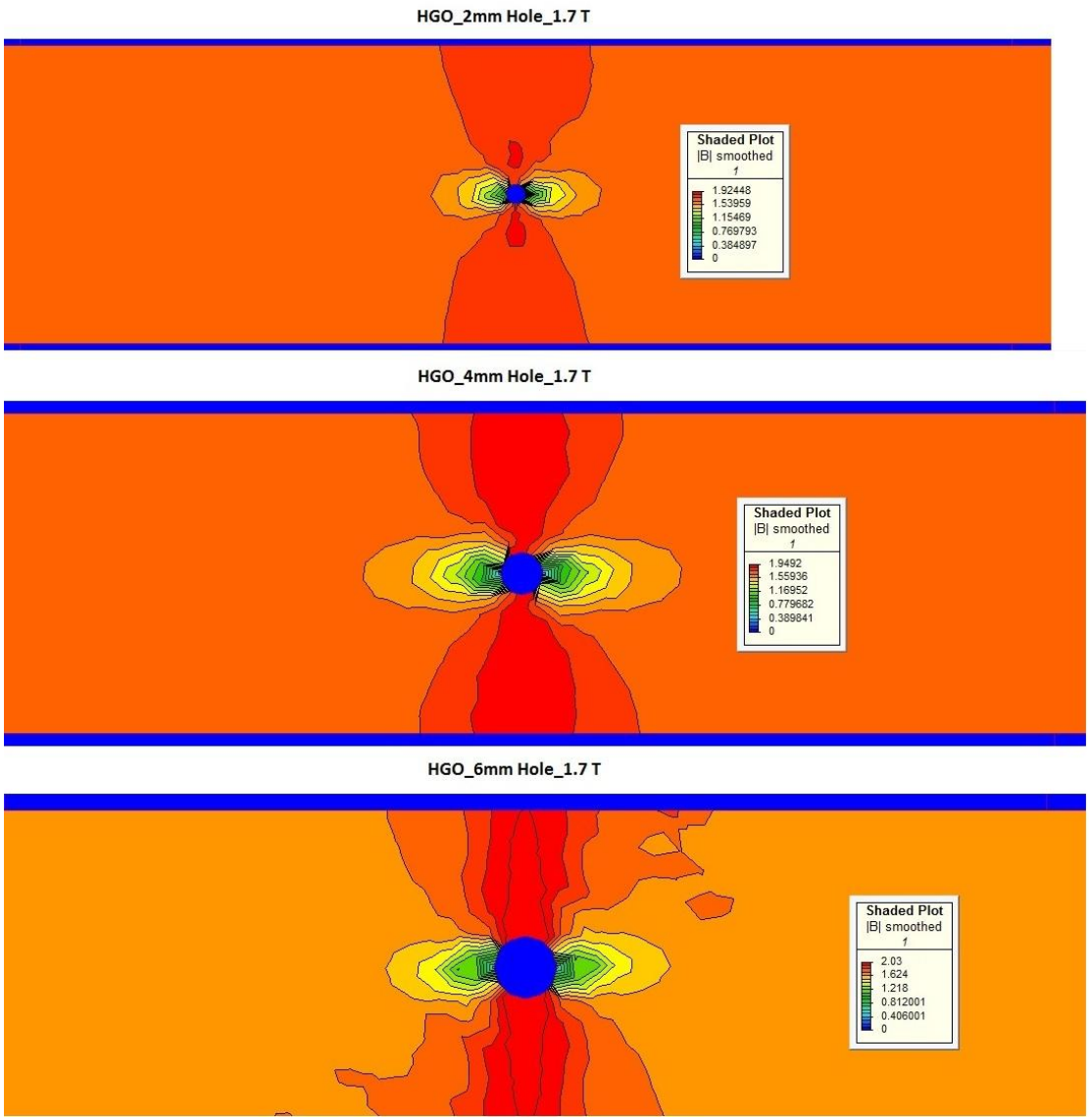

Fig. A-16 Flux density distribution around 2mm, 4mm and 6mm diameter holes in 30mm wide HGO strip at B_{pk}=1.7 T (Not to scale).

III. HGO_Slots

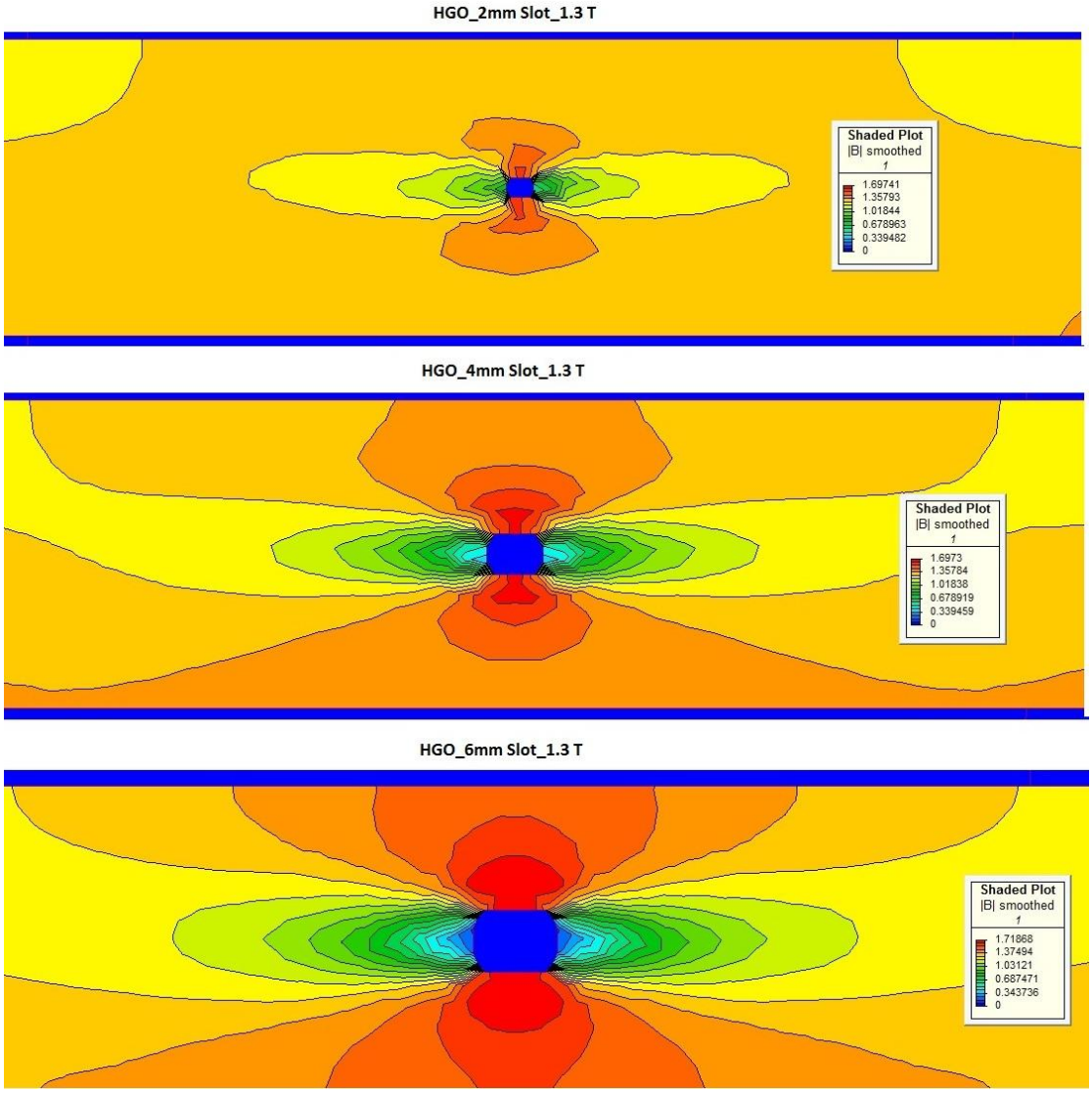

Fig. A-17 Flux density distribution around 2mm, 4mm and 6mm wide slots in 30mm wide HGO strip at B_{pk}=1.3 T (Not to scale).

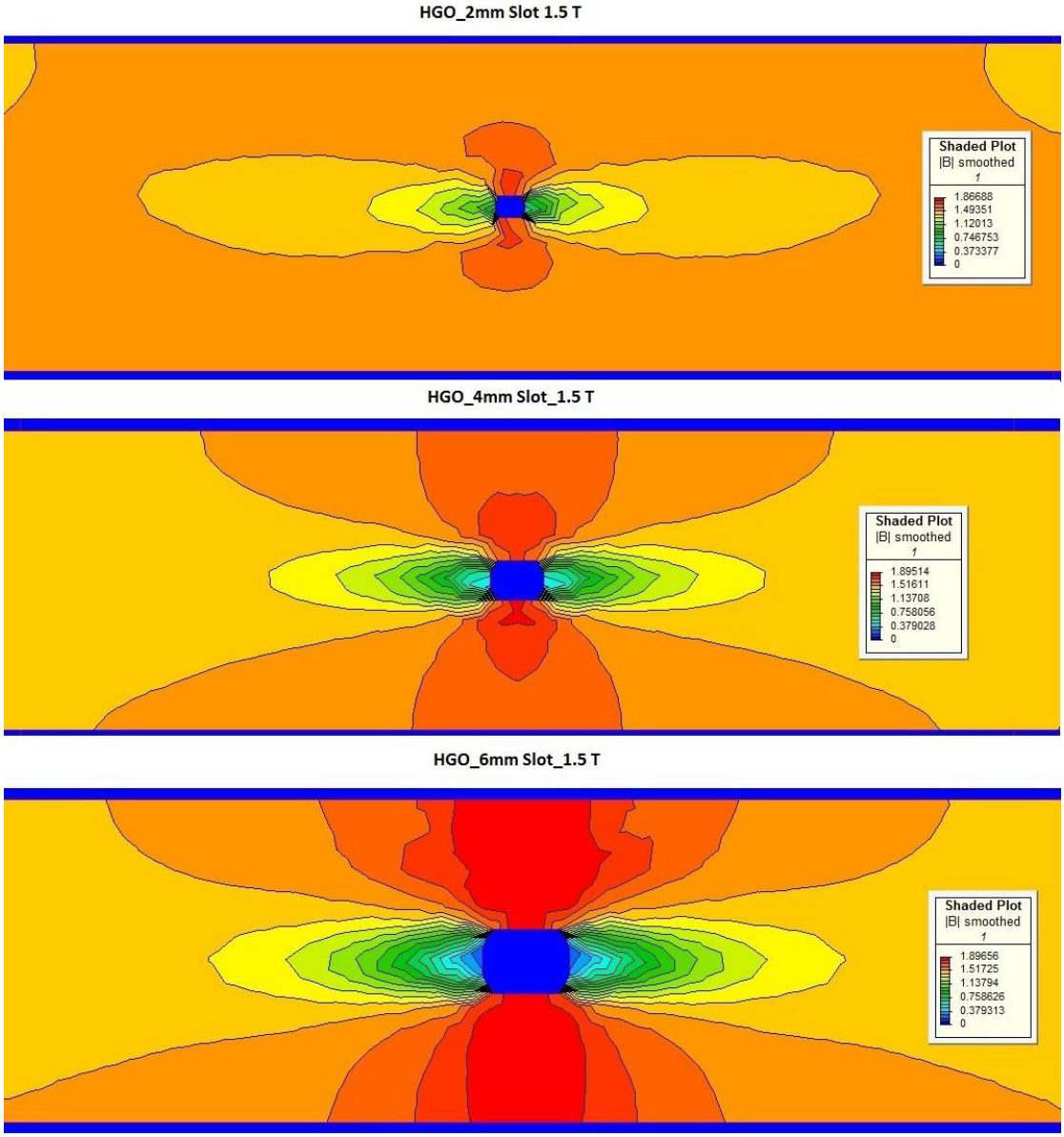

Fig. A-18 Flux density distribution around 2mm, 4mm and 6mm wide slots in 30mm wide HGO strip at B_{pk}=1.5 T (Not to scale).

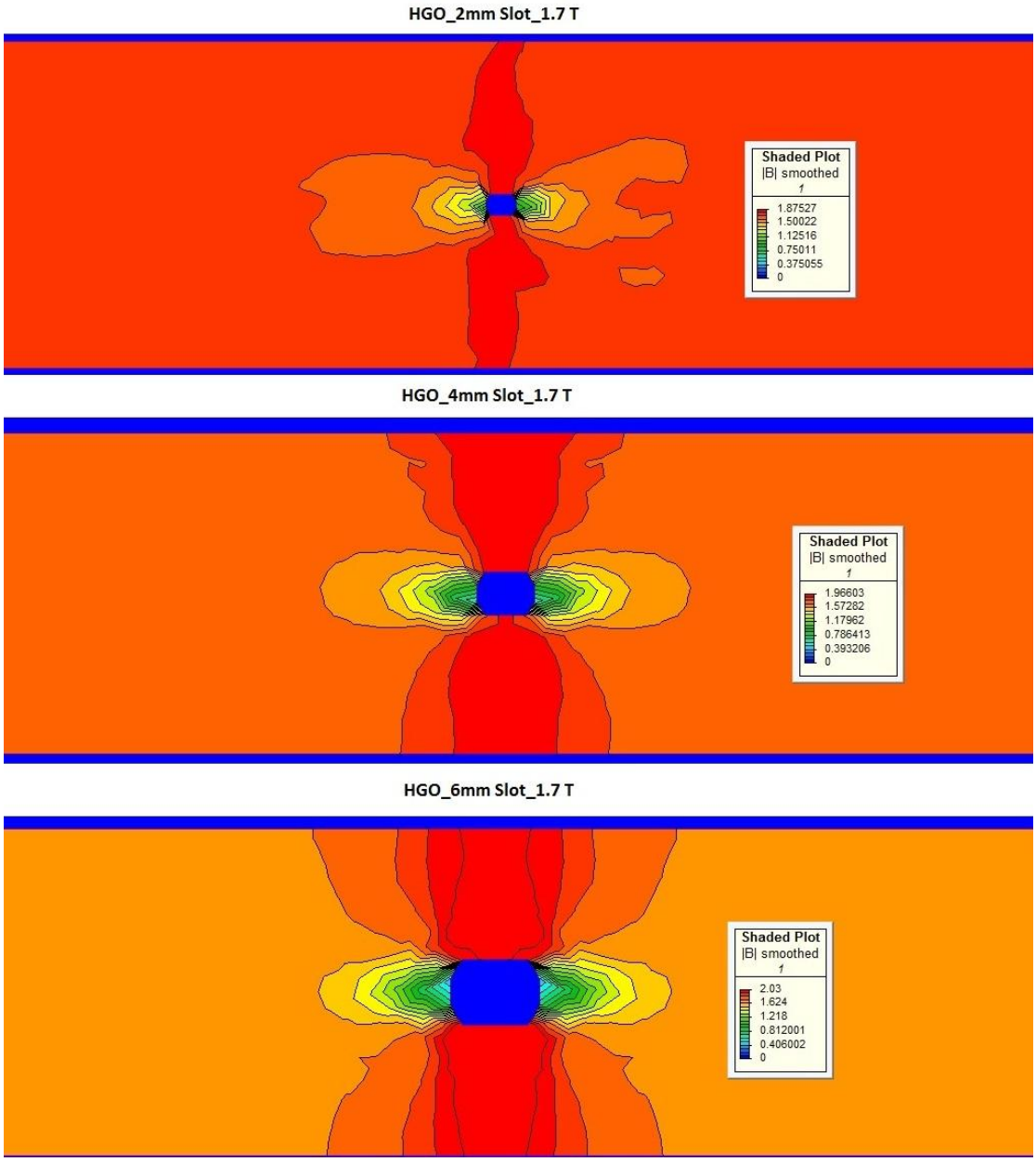

Fig. A-19 Flux density distribution around 2mm, 4mm and 6mm wide slots in 30mm wide HGO strip at B_{pk}=1.7 T (Not to scale).

IV. CGO_Holes

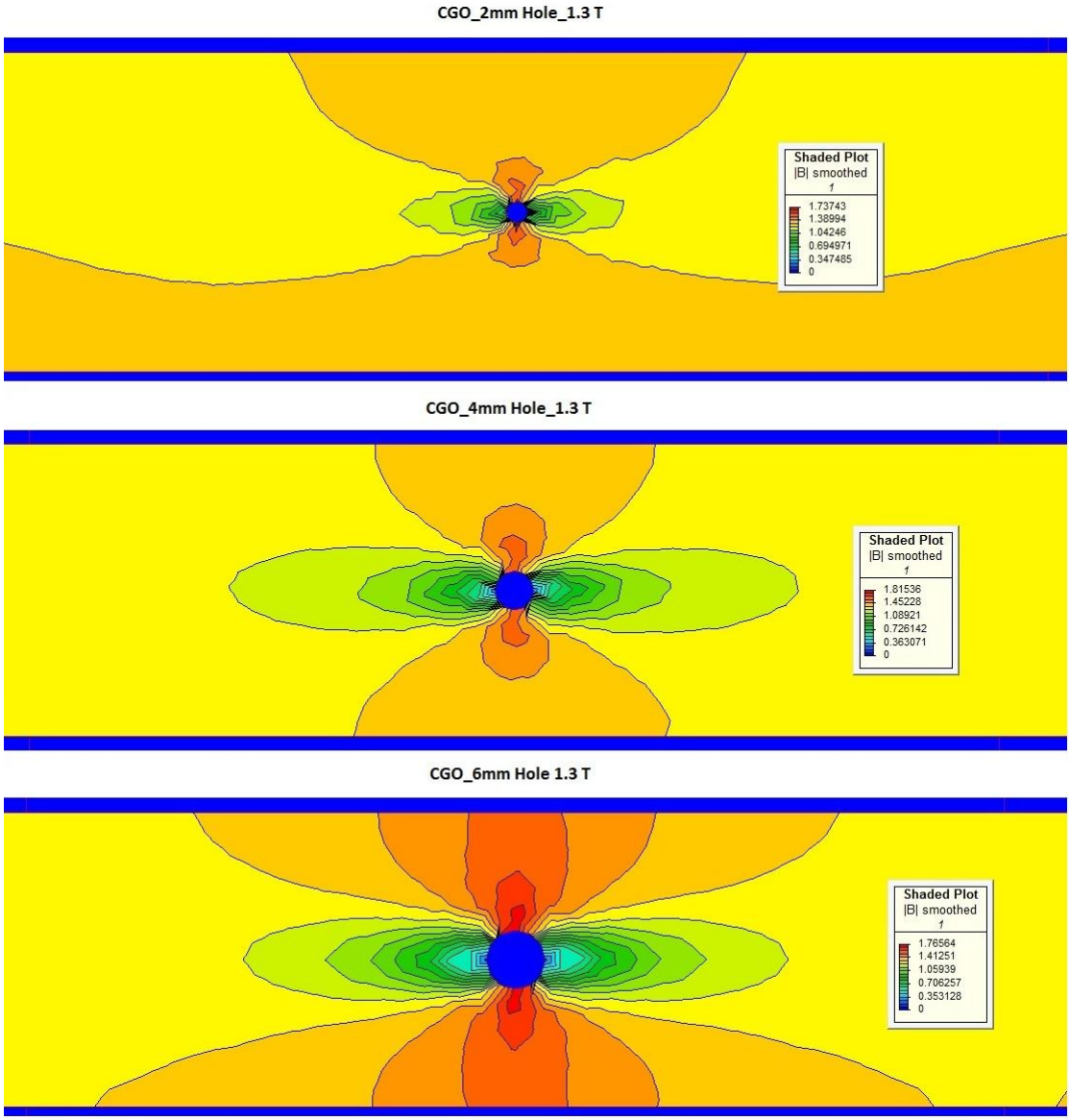

Fig. A-20 Flux density distribution around 2mm, 4mm and 6mm diameter holes in 30mm wide CGO strip at B_{pk}=1.3 T (Not to scale).

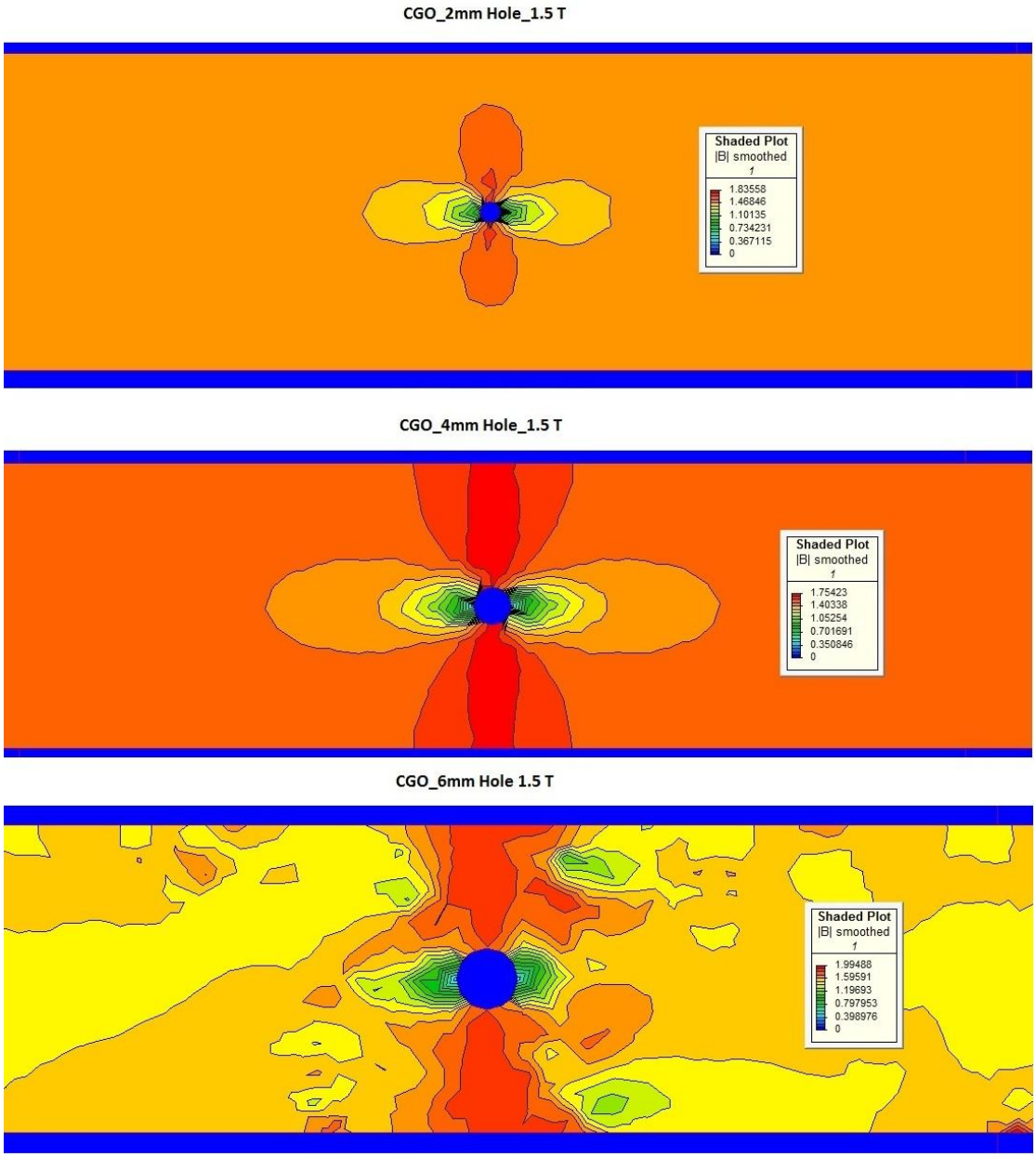

Fig. A-21 Flux density distribution around 2mm, 4mm and 6mm diameter holes in 30mm wide CGO strip at B_{pk}=1.5 T (Not to scale).

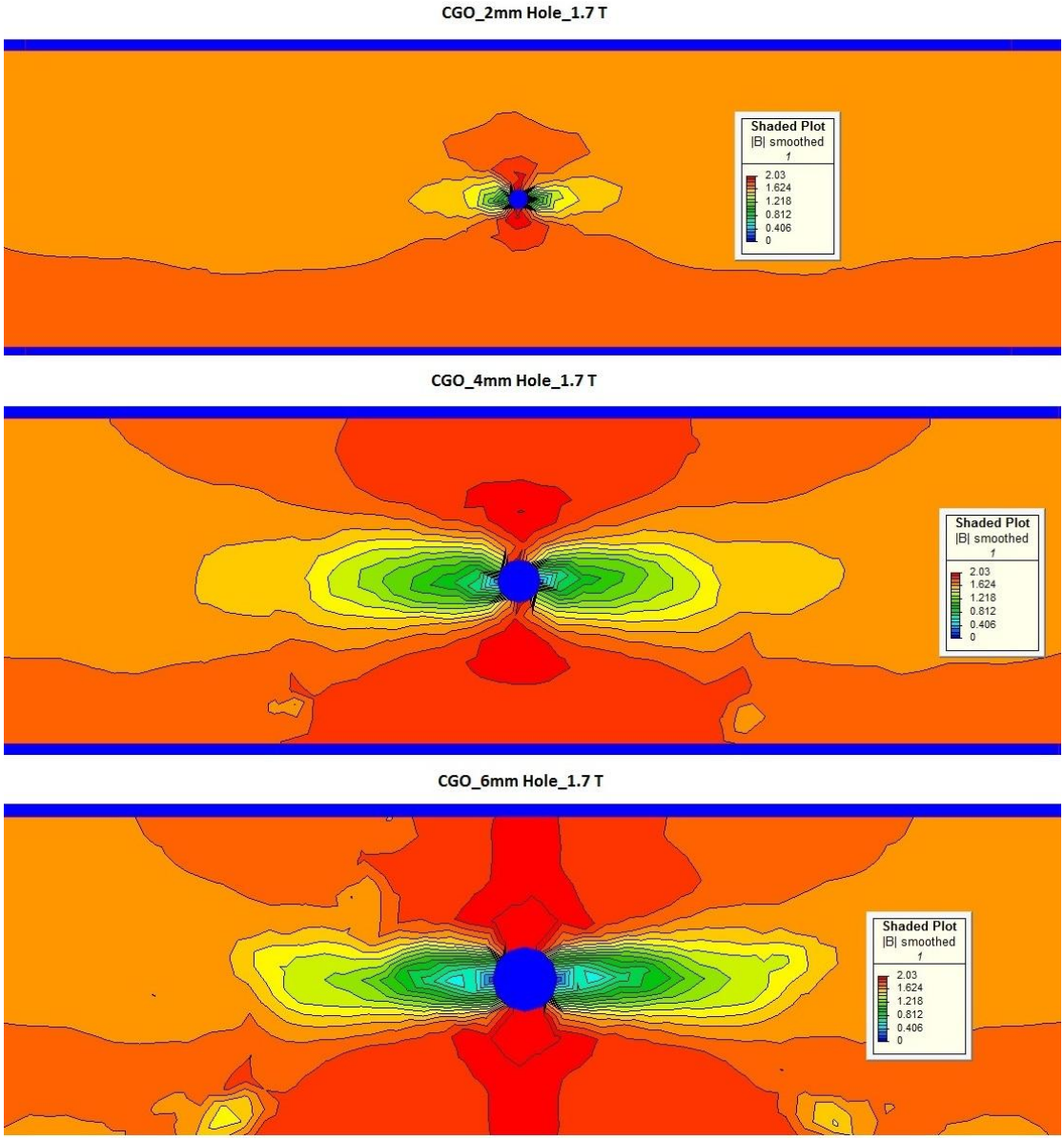

Fig. A-22 Flux density distribution around 2mm, 4mm and 6mm diameter holes in 30mm wide CGO strip at B_{pk}=1.7 T (Not to scale).

V. CGO_Slots

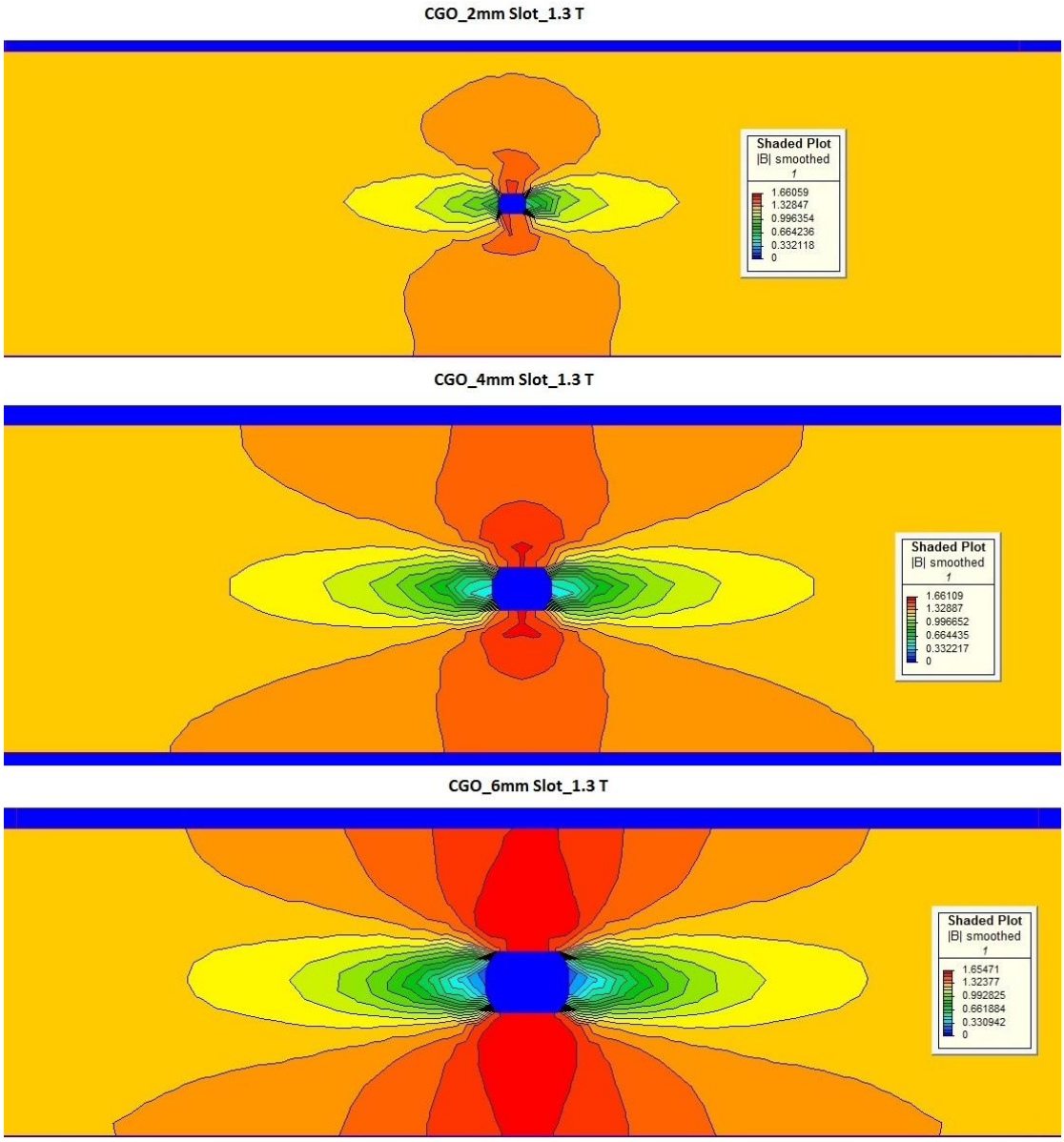

Fig. A-23 Flux density distribution around 2mm, 4mm and 6mm wide slots in 30mm wide CGO strip at B_{pk}=1.3 T (Not to scale).

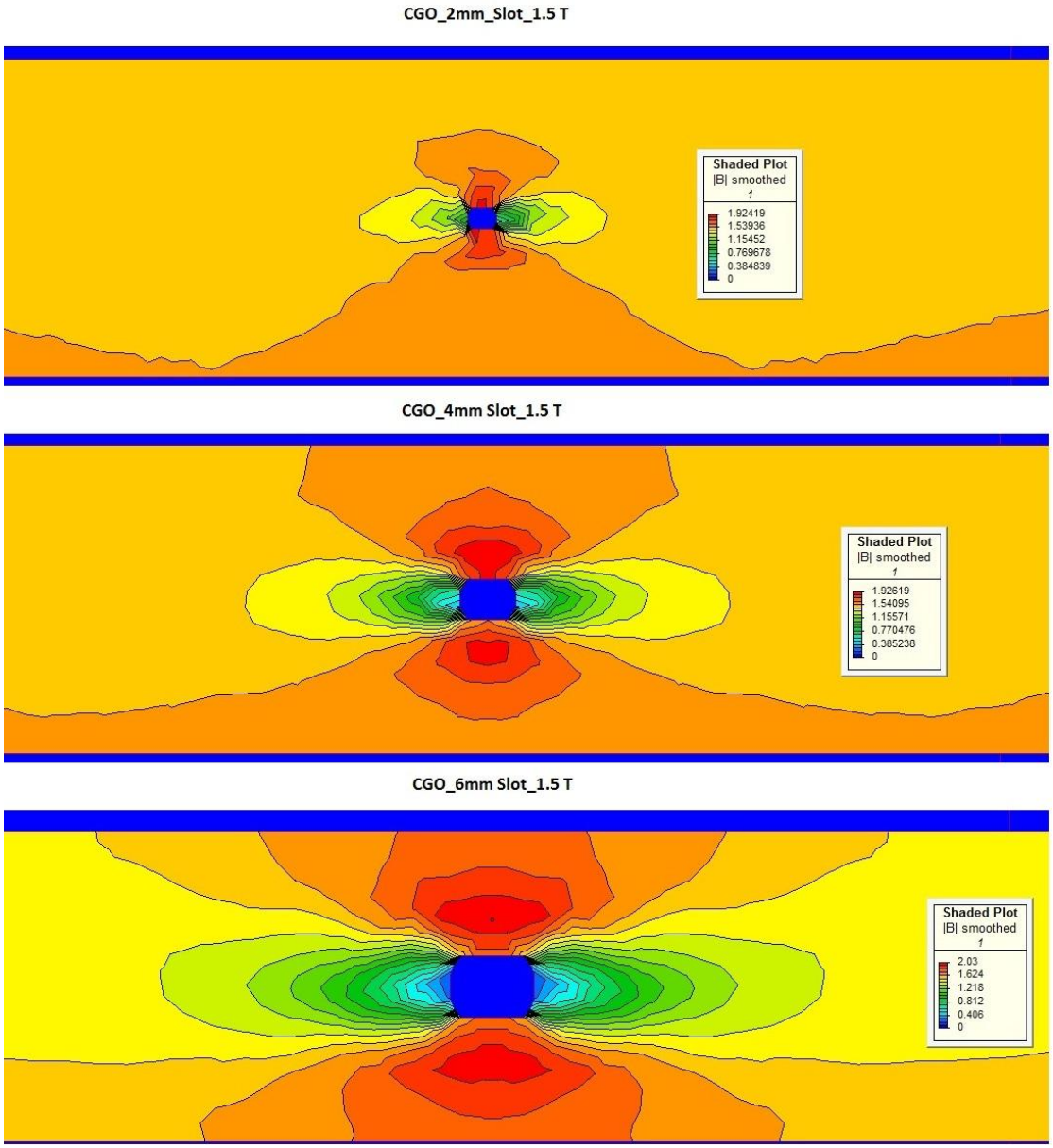

Fig. A-24 Flux density distribution around 2mm, 4mm and 6mm wide slots in 30mm wide CGO strip at B_{pk}=1.5 T (Not to scale).

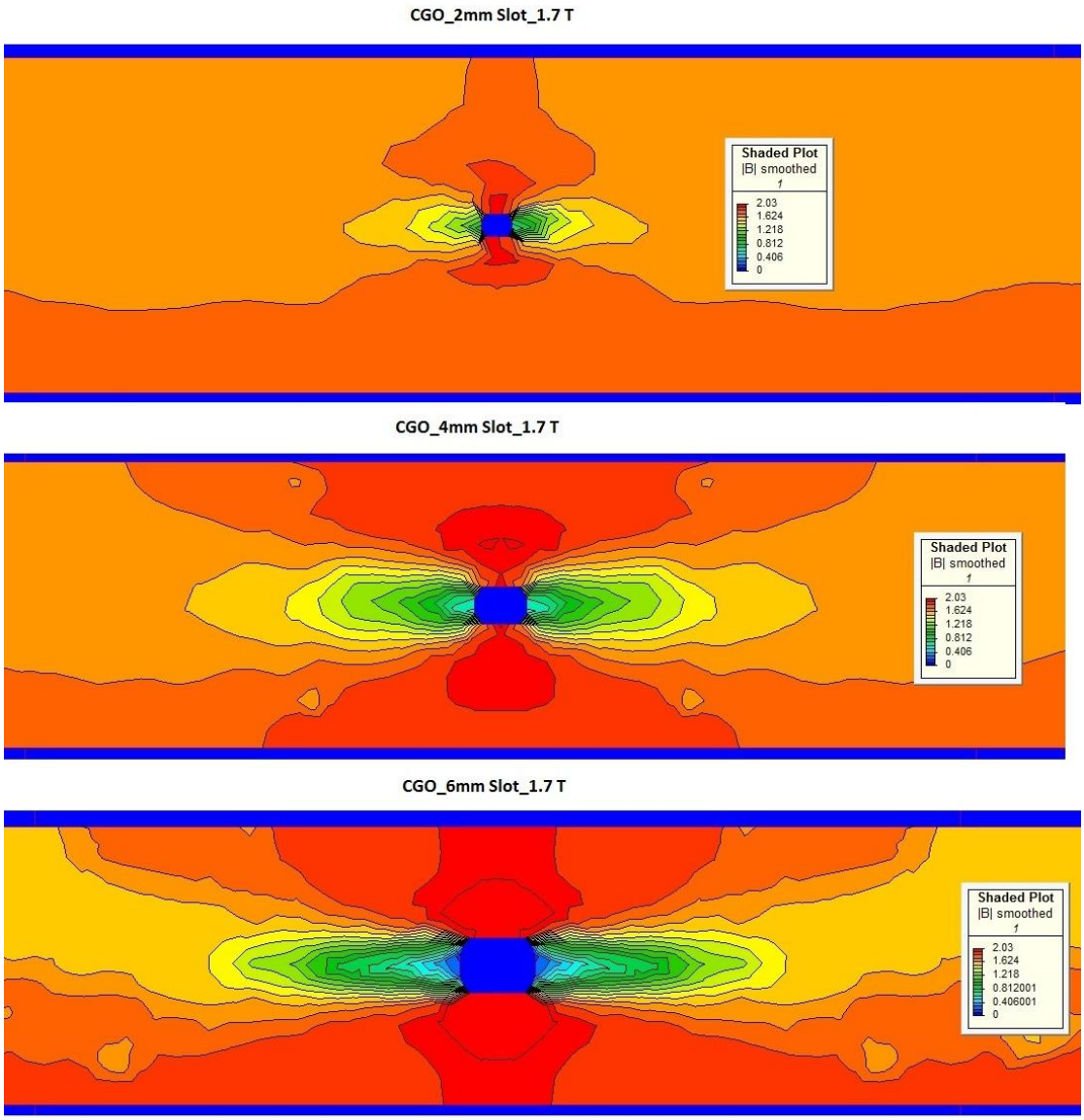

Fig. A-25 Flux density distribution around 2mm, 4mm and 6mm wide slots in 30mm wide CGO strip at B_{pk}=1.7 T (Not to scale).

B. Data Processing

I. Affected Length – Hole Diameter Ratio for Varying Hole diameter - Lamination Width Ratio

The Affected Length – Hole Diameter Ratio for Varying Hole diameter - Lamination Width Ratio values are tabulated in Table A8.

Table A8 Affected Length – Hole Diameter Ratio $\left(\frac{l_H}{d}\right)$ for Varying Hole diameter - Lamination Width Ratio $\left(\frac{d}{W}\right)$ computed for a fixed Lamination Width (W) = 0.03 m

Material	Hole Diameter (d) [m]	Peak Flux Density (B_{pk}) [T]	Hole Diameter – Lamination Width Ratio $\left(\frac{d}{W}\right)$	Affected Length (l_H) [m]	Affected Length – Hole Diameter Ratio $\left(\frac{l_H}{d}\right)$
HGO	0.002	1.3	0.067	0.052	26.00
		1.5	0.067	0.046	23.00
		1.7	0.067	0.020	10.00
	0.004	1.3	0.133	0.078	19.50
		1.5	0.133	0.072	18.00
		1.7	0.133	0.026	6.50
	0.006	1.3	0.200	0.094	15.67
		1.5	0.200	0.082	13.67
		1.7	0.200	0.032	5.33
CGO	0.002	1.3	0.067	0.034	17.00
		1.5	0.067	0.018	9.00
		1.7	0.067	0.014	7.00
	0.004	1.3	0.133	0.052	13.00
		1.5	0.133	0.030	7.50
		1.7	0.133	0.048	12.00
	0.006	1.3	0.200	0.064	10.67
		1.5	0.200	0.072	12.00
		1.7	0.200	0.056	9.33

II. Affected Length – Slot Length Ratio for Varying Slot Width - Lamination Width Ratio

The Affected Length – Slot Length Ratio for Varying Slot Width - Lamination Width Ratio values are tabulated in Table A9.

Table A9 Affected Length – Slot Length Ratio $\left(\frac{l_S}{s_L}\right)$ for Varying Slot Width - Lamination Width Ratio $\left(\frac{s_w}{W}\right)$ computed for a fixed Lamination Width (W) = 0.03 m

Material	Slot Width (s_w) [m]	Slot Length $s_l = \sqrt{2}.s_w$ [m]	Peak Flux Density (B_{pk}) [T]	Slot Width – Lamination Width Ratio $\left(\frac{s_w}{W}\right)$	Affected Length (l_S) [m]	Affected Length – Slot Length Ratio $\left(\frac{l_S}{s_l}\right)$
HGO	0.002	0.0028	1.3	0.067	0.068	24.29
			1.5	0.067	0.052	18.57
			1.7	0.067	0.02	7.14
	0.004	0.0056	1.3	0.133	0.084	15.00
			1.5	0.133	0.074	13.21
			1.7	0.133	0.028	5.00
	0.006	0.0084	1.3	0.200	0.102	12.14
			1.5	0.200	0.084	10.00
			1.7	0.200	0.034	4.05
CGO	0.002	0.002	1.3	0.067	0.036	12.86
			1.5	0.067	0.020	7.14
			1.7	0.067	0.020	7.14
	0.004	0.004	1.3	0.133	0.058	10.36
			1.5	0.133	0.040	7.14
			1.7	0.133	0.056	10.00
	0.006	0.006	1.3	0.200	0.076	9.05
			1.5	0.200	0.078	9.29
			1.7	0.200	0.076	9.05

III. Percentage Increase in Peak Flux Density

Hole

Percentage increase in $\boldsymbol{B_{pk}}$ around holes over an area $\boldsymbol{l_H.W}$ is tabulated in table A10

Table A10 HOLE: Percentage Increase in Peak Flux Density computed for a fixed Lamination Width $(\boldsymbol{W})$ = 0.03 m

Material	Hole Diameter $(\boldsymbol{d})$ [m]	Peak Flux Density $(\boldsymbol{B_{pk}})$ [T]	Affected Length $(\boldsymbol{l_H})$ [m]	% Increase in Peak Flux Density around the Hole
HGO	0.002	1.3	0.052	0.27
		1.5	0.046	0.49
		1.7	0.020	0.77
	0.004	1.3	0.078	0.76
		1.5	0.072	0.69
		1.7	0.026	2.14
	0.006	1.3	0.094	1.52
		1.5	0.082	1.47
		1.7	0.032	5.13
CGO	0.002	1.3	0.034	0.20
		1.5	0.018	0.36
		1.7	0.014	1.22
	0.004	1.3	0.052	1.34
		1.5	0.030	2.05
		1.7	0.048	1.44
	0.006	1.3	0.064	2.00
		1.5	0.072	2.43
		1.7	0.056	0.96

Slot

Percentage increase in $\boldsymbol{B_{pk}}$ around slots over an area $\boldsymbol{l_S.W}$ is tabulated in table A11

Table A11 SLOT: Percentage Increase in Peak Flux Density for Lamination Width $(\boldsymbol{W})$ = 0.03 m

Material	Hole Diameter $(\boldsymbol{d})$ [m]	Peak Flux Density $(\boldsymbol{B_{pk}})$ [T]	Affected Length $(\boldsymbol{l_S})$ [m]	% Increase in Peak Flux Density around the Slot
HGO	0.002	1.3	0.068	0.20
		1.5	0.052	0.44
		1.7	0.02	0.63
	0.004	1.3	0.084	0.99
		1.5	0.074	1.15
		1.7	0.028	3.15
	0.006	1.3	0.102	1.92
		1.5	0.084	2.48
		1.7	0.034	4.85
CGO	0.002	1.3	0.036	0.17
		1.5	0.020	1.08
		1.7	0.020	0.90
	0.004	1.3	0.058	1.60
		1.5	0.040	2.54
		1.7	0.056	1.20
	0.006	1.3	0.076	2.11
		1.5	0.078	2.69
		1.7	0.076	1.26

IV. Percentage Increase in Specific Loss

Hole

Percentage increase in specific power loss around holes over an area $\boldsymbol{l_H.W}$ is tabulated in table A12

Table A12 HOLE: Percentage Increase in Specific Power Loss for Lamination Width $(\boldsymbol{W})$ = 0.03 m

Material	Hole Diameter $(\boldsymbol{d})$ [m]	Peak Flux Density $(\boldsymbol{B_{pk}})$ [T]	Affected Length $(\boldsymbol{l_H})$ [m]	% Increase in Specific Power Loss around the Hole
HGO	0.002	1.3	0.052	2.59
		1.5	0.046	4.44
		1.7	0.020	13.16
	0.004	1.3	0.078	6.99
		1.5	0.072	8.50
		1.7	0.026	32.89
	0.006	1.3	0.094	12.33
		1.5	0.082	16.48
		1.7	0.032	44.29
CGO	0.002	1.3	0.034	4.46
		1.5	0.018	10.43
		1.7	0.014	15.58
	0.004	1.3	0.052	12.21
		1.5	0.030	23.47
		1.7	0.048	27.62
	0.006	1.3	0.064	18.76
		1.5	0.072	23.60
		1.7	0.056	28.83

Slot

Percentage increase in specific power loss around slots over an area $\boldsymbol{l_S.W}$ is tabulated in table A13

Table A13 SLOT: Percentage Increase in Specific Power Loss for Lamination Width $(\boldsymbol{W})$ = 0.03 m

Material	Slot Width $(\boldsymbol{s_w})$ [m]	Peak Flux Density $(\boldsymbol{B_{pk}})$ [T]	Affected Length $(\boldsymbol{l_S})$ [m]	% Increase in Specific Power Loss around the Slot
HGO	0.002	1.3	0.068	3.78
		1.5	0.052	4.45
		1.7	0.02	14.03
	0.004	1.3	0.084	7.94
		1.5	0.074	10.28
		1.7	0.028	39.20
	0.006	1.3	0.102	14.27
		1.5	0.084	22.10
		1.7	0.034	59.74
CGO	0.002	1.3	0.036	5.07
		1.5	0.020	9.64
		1.7	0.020	15.14
	0.004	1.3	0.058	13.32
		1.5	0.040	24.28
		1.7	0.056	27.89
	0.006	1.3	0.076	19.63
		1.5	0.078	31.12
		1.7	0.076	32.99

V. Percentage Decrease in Relative Permeability

Hole

Percentage decrease in relative permeability around holes over an area $\boldsymbol{l_H.W}$ is tabulated in table A14.

Table A14 HOLE: Percentage Decrease in Relative Permeability for Lamination Width $(\boldsymbol{W})$ = 0.03 m

Material	Hole Diameter $(\boldsymbol{d})$ [m]	Peak Flux Density $(\boldsymbol{B_{pk}})$ [T]	Affected Length $(\boldsymbol{l_H})$ [m]	% Decrease in Relative Permeability around the Hole
HGO	0.002	1.3	0.052	0.42
		1.5	0.046	6.13
		1.7	0.020	26.34
	0.004	1.3	0.078	3.44
		1.5	0.072	12.27
		1.7	0.026	49.68
	0.006	1.3	0.094	8.04
		1.5	0.082	22.91
		1.7	0.032	50.34
CGO	0.002	1.3	0.034	1.59
		1.5	0.018	15.29
		1.7	0.014	19.70
	0.004	1.3	0.052	4.00
		1.5	0.030	29.26
		1.7	0.048	29.46
	0.006	1.3	0.064	15.70
		1.5	0.072	35.63
		1.7	0.056	38.35

Slot

Percentage decrease in relative permeability around slots over an area $\boldsymbol{l_S.W}$ is tabulated in table A15.

Table A15 SLOT: Percentage Decrease in Relative Permeability for Lamination Width $(\boldsymbol{W})$ = 0.03 m

Material	Slot Width $(\boldsymbol{s_w})$ [m]	Peak Flux Density $(\boldsymbol{B_{pk}})$ [T]	Affected Length $(\boldsymbol{l_S})$ [m]	% Decrease in Relative Permeability around the Slot
HGO	0.002	1.3	0.068	0.47
		1.5	0.052	6.83
		1.7	0.02	31.62
	0.004	1.3	0.084	4.09
		1.5	0.074	14.63
		1.7	0.028	55.58
	0.006	1.3	0.102	9.34
		1.5	0.084	26.86
		1.7	0.034	56.71
CGO	0.002	1.3	0.036	2.24
		1.5	0.020	20.36
		1.7	0.020	17.94
	0.004	1.3	0.058	6.02
		1.5	0.040	30.62
		1.7	0.056	26.89
	0.006	1.3	0.076	17.32
		1.5	0.078	35.60
		1.7	0.076	31.85

Appendix V (Chapter 5)

A. Derivation for Area of Slot

The area of a slot is derived in this section.

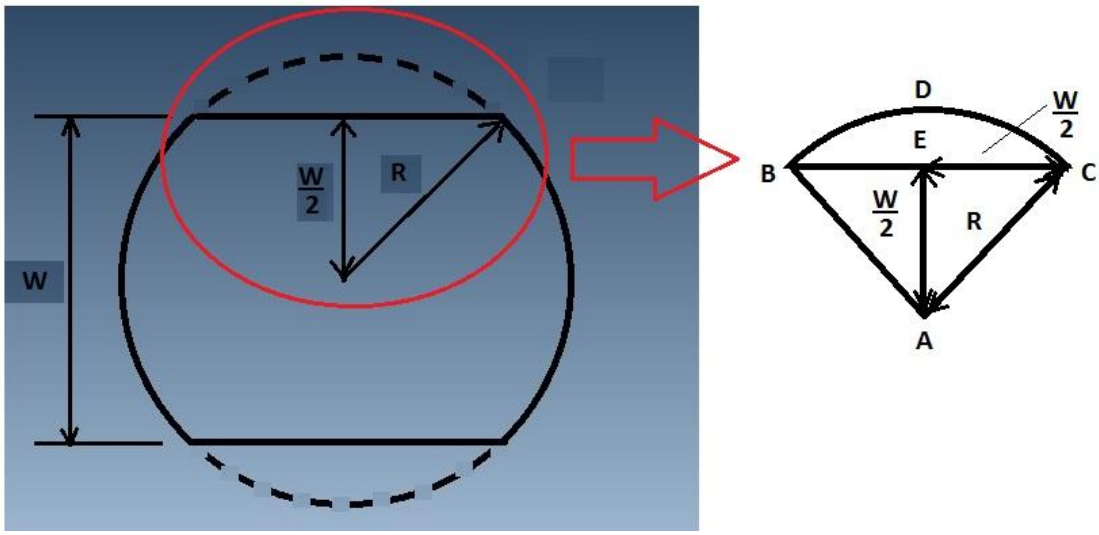

Fig. A-26 Slot geometry.

From Fig. A-26,

$$\text{Area of BDCE} = (\text{Area of sector ABDCA} - \text{Area of triangle ABC}) \quad (1)$$

$$\text{Area of sector ABDCA} = \left(\frac{\text{Angle BAC}}{360^0}\right).\text{R}^2$$

$$\text{Area of sector ABDCA} = \frac{\pi}{4}.\text{R}^2 \quad (2)$$

$$\text{Area of triangle ABC} = \frac{1}{2}.\text{EC}.\text{EA}$$

$$\text{Area of triangle ABC} = \frac{1}{2}.\frac{1}{2}.\text{W}.\frac{1}{2}.\text{W} = \frac{\text{W}^2}{8} \quad (3)$$

Substituting equation (2) and (3) in equation (1),

$$\text{Area of BDCE} = (\frac{\pi}{4}.\text{R}^2 - \frac{\text{W}^2}{8}) \quad (4)$$

$$\text{Area of slot of width 'W'} = (\text{Area of circle with radius 'R'} - 2(\text{Area of BDCE})$$

$$\text{Area of slot of width 'W'} = (\pi.\text{R}^2 - 2(\frac{\pi}{4}.\text{R}^2 - \frac{\text{W}^2}{8}) \quad (5)$$

$$\text{R}^2 = \left(\frac{1}{2}.\text{W}\right)^2 + \left(\frac{1}{2}.\text{W}\right)^2 = \frac{\text{W}^2}{2} \quad (6)$$

$$R = \frac{W}{\sqrt{2}} \tag{7}$$

Substituting equation (7) in equation (5),

$$\text{Area of slot of width 'W'} = \left(\frac{\pi.W^2}{2} - \left(\frac{\pi.W^2}{4} - \frac{W^2}{4}\right)\right) \tag{8}$$

For a slot with width $\mathbf{s_w}$,

$$\text{Area of slot } = \left(\frac{\pi.{s_w}^2}{2} - \left(\frac{\pi.{s_w}^2}{4} - \frac{{s_w}^2}{4}\right)\right) \tag{8}$$

B. Input Parameters for the No-Load Specific Loss Prediction Algorithm for Multi-packet HGO and CGO 3-Phase, 3-Limb Transformer Cores

Table A16 160mm Packet Width

Parameter	Value	Unit
Core Width (C_W)	0.8	m
Core Height (C_H)	0.72	m
Packet Lamination Width (Limbs & Yokes)(W)	0.16	m
Packet Thickness (T_P)	0.054	m
Stacking Factor (K)	0.97	-
Number of step laps (N_S)	7	-
Overlap length (l_o)	0.003	m
Hole diameter (d)	0.01	m
Total number of holes (m)	5	-
Slot width (s_W)	0.01	m
Total number of slots (n)	5	-

Table A17 130mm Packet Width

Parameter	Value	Unit
Core Width (C_W)	0.77	m
Core Height (C_H)	0.69	m
Packet Lamination Width (Limbs & Yokes)(W)	0.13	m
Packet Thickness (T_P)	0.027	m
Stacking Factor (K)	0.97	-
Number of step laps (N_S)	7	-
Overlap length (l_o)	0.003	m
Hole diameter (d)	0.01	m
Total number of holes (m)	5	-
Slot width (s_W)	0.01	m
Total number of slots (n)	5	-

Note: There are two 130 mm lamination width packets in the core. So this data has to be inserted twice in the algorithm.

Table A18 50mm Packet Width

Parameter	Value	Unit
Core Width (C_W)	0.69	m
Core Height (C_H)	0.61	m
Packet Lamination Width (Limbs & Yokes)(W)	0.05	m
Packet Thickness (T_P)	0.027	m
Stacking Factor (K)	0.97	-
Number of step laps (N_S)	7	-
Overlap length (l_o)	0.003	m
Hole diameter (d)	0.01	m
Total number of holes (m)	5	-
Slot width (s_W)	0.01	m
Total number of slots (n)	5	-

Note: There are two 50 mm lamination width packets in the core. So this data has to be inserted twice in the algorithm.

C. Input Parameters for the N-Load Specific Loss Prediction Algorithm for 160mm Lamination width HGO and CGO Single Packet 3-Phase, 3-Limb Transformer Cores

Table A19 160mm Packet Width (Single Packet Core)

Parameter	Value	Unit
Core Width (C_W)	0.8	m
Core Height (C_H)	0.72	m
Packet Lamination Width (Limbs & Yokes)(W)	0.16	m
Packet Thickness (T_P)	0.054	m
Stacking Factor (K)	0.97	-
Number of step laps (N_S)	7	-
Overlap length (l_o)	0.003	m
Hole diameter (d)	0.01	m
Total number of holes (m)	5	-
Slot width (s_W)	0.01	m
Total number of slots (n)	5	-

D. Input Parameters for the N-Load Specific Loss Prediction Algorithm for 130mm Lamination width HGO and CGO Single Packet 3-Phase, 3-Limb Transformer Cores

Table A20 130mm Packet Width (Single Packet Core)

Parameter	Value	Unit
Core Width (C_W)	0.77	m
Core Height (C_H)	0.69	m
Packet Lamination Width (Limbs & Yokes)(W)	0.13	m
Packet Thickness (T_P)	0.027	m
Stacking Factor (K)	0.97	-
Number of step laps (N_S)	7	-
Overlap length (l_o)	0.003	m
Hole diameter (d)	0.01	m
Total number of holes (m)	5	-
Slot width (s_W)	0.01	m
Total number of slots (n)	5	-

E. Input Parameters for the N-Load Specific Loss Prediction Algorithm for 50mm Lamination width HGO and CGO Single Packet 3-Phase, 3-Limb Transformer Cores

Table A21 50mm Packet Width (Single Packet Core)

Parameter	Value	Unit
Core Width (C_W)	0.69	m
Core Height (C_H)	0.61	m
Packet Lamination Width (Limbs & Yokes)(W)	0.05	m
Packet Thickness (T_P)	0.027	m
Stacking Factor (K)	0.97	-
Number of step laps (N_S)	7	-
Overlap length (l_o)	0.003	m
Hole diameter (d)	0.01	m
Total number of holes (m)	5	-
Slot width (s_W)	0.01	m
Total number of slots (n)	5	-

Appendix VI (Uncertainty Budgets)

A. Uncertainty Budgets for Measurements

I. Uncertainty of Measurements

The uncertainty calculations in this chapter are based on the recommendations of UKAS M3003, *The Expression of Uncertainty and Confidence in Measurement*, 1997.

The calculation procedure is shown in the following sections.

Type-A Uncertainty (Repeatability)

The measurement quantity (y) can be expressed as a function of the input quantities $x_1, x_2, x_3, \dots x_N$ as,

$$y = f(x_1, x_2, x_3, \dots x_N) \tag{1}$$

For n repeated measurements, the Type-A uncertainty of y $\left(u_A(y)\right)$is calculated from equation (2)

$$u_A(y) = \frac{S_D}{\sqrt{n}} \tag{2}$$

where S_D is the standard deviation.

Standard deviation is calculated from equation (3),

$$S_D = \sqrt{\frac{\sum_{i=1}^{n}(q_i - \overline{q})^2}{n-1}} \tag{3}$$

where q_i is the measured value of y and $\overline{q}$ is the average value of y over n repeated measurements and is calculated using equation (4),

$$\overline{q} = \frac{1}{n}\sum_{i}^{n} q_i \tag{4}$$

Type-B Uncertainty

The standard uncertainties $\left(u(x_1)\right)$ of the measurement inputs (x_1) contribute to the Type-B uncertainty which is mathematically expressed as,

$$u^2{}_B(\mathrm{y}) = {c_1}^2.u^2(x_1) + {c_2}^2.u^2(x_2) + {c_3}^2.u^2(x_3) \dots + {c_N}^2.u^2(x_N). \tag{5}$$

where c_i is the sensitivity co-efficient and is the partial derivative $\frac{\partial y}{\partial x_i}$

The sensitivity co-efficient c_i is determined experimentally from $\frac{\Delta y}{\Delta x}$ by varying the values of x_i.

Combined Uncertainty

The combined uncertainty of the measurement quantity (y) is calculated using equation (6),

$$u(y) = \sqrt{\left(u^2{}_A(y) + u^2{}_B(y)\right)} \tag{6}$$

The calculated $u(y)$ is then multiplied by a coverage factor k_{95} to obtain the expanded uncertainty $U(y)$ from equation (7). A confidence level of 95 % of the normal distribution is provided by k_{95}.

$$U(y) = k_{95}.u(y) \tag{7}$$

The measured quantity $y(Y)$ is then reported as,

$$y = Y + U(y) \tag{8}$$

II. Three Phase, Three Limb Transformer Cores

Table A22 Uncertainty Budget for B_{pk} in Multi-packet 3-phase, 3-Limb HGO core

Sources of Uncertainty	Value +/- %	Probability Distribution	Divisor	Ci	U(xi) +/- %	Vi or Veff
Voltmeter	0.1	Normal	2	1	0.05000	∞
Packet Thickness	0.926	Rectangular	1.73	1	0.53458	∞
Packet Lamination Width	0.500	Rectangular	1.73	1	0.28868	∞
Frequency	0.025	Normal	2	1	0.01250	∞
Voltage Type B uncertainty					0.60973	∞
Voltage Type A uncertainty	0.100	Normal	1	1	0.10000	2
Combined Uncertainty					0.61787	∞
Expanded Uncertainty, k =2					1.24	
Declared uncertainty in B_{pk} at a confidence level of 95 %					1.24	

The uncertainties of the B_{pk} in the multi-packet 3-phase, 3-limb HGO core detailed in table A-21 have been estimated based on the following calculations:

1) Accuracy of the voltmeter – The accuracy of the voltage measurements obtained from NORMA600O wide band power analyser was 0.1% of the measured value.

2)Packet Thickness – The least packet thickness measured was 27 mm of the 50mm and 130 mm lamination width packets. It was measured using a metal ruler with a resolution of 0.5 mm. Its uncertainty was assumed as a half of the resolution resulting in 0.926 % of the packet thickness of 27 mm.

3)Packet Lamination Width – The least packet lamination width measured was 50 mm of the 50mm lamination width packets. It was measured using a metal

ruler with a resolution of 0.5 mm. Its uncertainty was assumed as a half of the resolution resulting in 0.5 % of the measured value.

4)Voltage –Type A- The type A uncertainty of the induced secondary voltage was less than 0.1% for 3 trials. It was assumed to be 0.1%.

The declared uncertainty in B_{pk} in the multi-packet 3-phase, 3-limb HGO at 1.7 T is $\pm$ 1.24%. The uncertainties of all the multi-packet and single packet 3-phase, 3-limb cores is estimated in the same manner as described above.

Table A23 Uncertainty Budget for I_{rms}in Multi-packet 3-phase, 3-Limb HGO core

Sources of Uncertainty	Value +/- %	Probability Distribution	Divisor	Ci	U(xi) +/- %	Vi or Veff
Resistor Phase A	**0.03**	**Normal**	**2**	**1**	**0.02**	∞
Resistor Phase B	**0.03**	**Normal**	**2**	**1**	**0.02**	∞
Resistor Phase C	**0.03**	**Normal**	**2**	**1**	**0.02**	∞
Current Type B uncertainty					**0.03**	∞
Current Type A uncertainty	**0.27**	**Normal**	**1**	**1**	**0.27**	**2**
Combined Uncertainty					**0.27**	∞
Expanded Uncertainty, k =2					**0.54**	
Declared uncertainty in I_{rms} at a confidence level of 95 %					**0.54**	

The uncertainties of the I_{rms} of the multi-packet 3-phase, 3-limb HGO core detailed in table A-23 have been estimated based on the following calculations:

1)Accuracy of the three resistors – The accuracy of the resistors of NORMA600O wide band power analyser was 0.03%.

2)Current –Type A- The relative type A uncertainty of the measured rms value of primary current was 0.27%

The declared uncertainty in I_{rms} in the multi-packet 3-phase, 3-limb HGO at 1.7 T is $\pm$ 0.54 %. The uncertainties of all the multi-packet and single packet 3-phase, 3-limb cores is estimated in the same manner as described above.

Table A24 Uncertainty Budget for No-Load Loss in Multi-packet 3-phase, 3-Limb HGO core

Sources of Uncertainty	Value +/- %	Probability Distribution	Divisor	Ci	U(xi) +/- %	Vi or Veff
Mass	**0.01**	**Normal**	**2**	**1**	**0.005**	**∞**
Power meter	**0.10**	**Normal**	**2**	**1**	**0.05**	**∞**
Dependence of No-load Loss on Bpk	**1.24**	**Normal**	**2**	**4.6**	**2.83**	**∞**
Current	**0.54**	**Normal**	**2**	**1**	**0.27**	
No Load Loss type B uncertainty					**2.84**	**∞**
No Load Loss type A uncertainty	**0.29**	**Normal**	**1**	**1**	**0.29**	**2**
Combined Uncertainty					**2.86**	**∞**
Expanded Uncertainty, k =2					**5.72**	
Declared uncertainty in No-load Loss at a confidence level of 95 %					**5.72**	

The uncertainties of no-load specific loss of the multi-packet 3-phase, 3-limb HGO core detailed in table A-24 have been estimated based on the following calculations:

1)Mass measurement – The mass of the samples was measured using an Avery Berkel FB31 scale with a resolution of 0.01 g and accuracy of ±0.0002 g. Each sample was weighed three times and the expanded uncertainty of all samples was within ± 0.01 %.

2)Accuracy of the powermeter – The accuracy of the power loss measurements obtained from NORMA600O wide band power analyser was 0.1% of the measured value.

3) The B_{pk} and I_{rms} measurement uncertainties were obtained from tables A22 and A23.

4)Dependence of no-load loss on B_{pk} - The sensitivity coefficient (Ci) was calculated to be equal to 4.6 from the measured no-load loss versus B_{pk} curves. At 1.7 T, the Ci is the ratio of the difference in no-load loss (measured at 1.8 T and 1.7 T) and the difference in B_{pk} (1.8 T -1.7 T =0.1T).

5)No-load loss –Type A- The relative type A uncertainty of the measured no-load loss was 0.29%.

The declared uncertainty in no-load loss in the multi-packet 3-phase, 3-limb HGO at 1.7 T is $\pm$ 6%. The uncertainties of all the multi-packet and single packet 3-phase, 3-limb cores is estimated in the same manner as described above.

Table A25 Uncertainty Budget for No-Load Apparent Power in Multi-packet 3-phase, 3-Limb HGO core

Sources of Uncertainty	Value +/- %	Probability Distribution	Divisor	Ci	U(xi) +/- %	Vi or Veff
Mass	**0.01**	**Normal**	**2**	**1**	**0.005**	**∞**
Power meter	**0.1**	**Normal**	**2**	**1**	**0.05**	**∞**
Dependence of No-Load Apparent Power on Bpk	**1.24**	**Normal**	**2**	**30**	**18.28**	**∞**
Current	**0.54**	**Normal**	**2**	**1**	**0.27**	
Apparent Power type B uncertainty					**18.28**	**∞**
Apparent Power type A uncertainty	**0.27**	**Normal**	**1**	**1**	**0.27**	**2**
Combined Uncertainty					**18.28**	**∞**
Expanded Uncertainty, k =2					**36.56**	
Declared uncertainty in No-load apparent power at a confidence level of 95 %					**36.56**	

The uncertainties of no-load apparent power of the multi-packet 3-phase, 3-limb HGO core detailed in table A-25 have been estimated based on the following calculations:

1)Mass measurement – The mass of the samples was measured using an Avery Berkel FB31 scale with a resolution of 0.01 g and accuracy of ±0.0002 g. Each sample was weighed three times and the expanded uncertainty of all samples was within ± 0.01 %.

2)Accuracy of the powermeter – The accuracy of the power loss measurements obtained from NORMA600O wide band power analyser was 0.1% of the measured value.

3) The B_{pk} and I_{rms} measurement uncertainties were obtained from tables A22 and A23.

4)Dependence of no-load apparent power on B_{pk} - The sensitivity coefficient (Ci) was calculated to be equal to 30 from the measured no-load apparent power versus B_{pk} curves. At 1.7 T, the Ci is the ratio of the difference in no-load apparent power (measured at 1.8 T and 1.7 T) and the difference in B_{pk} (1.8 T -1.7 T =0.1T).

5)No-load apparent power –Type A- The relative type A uncertainty of the measured no-load apparent power was 0.27%.

The declared uncertainty in no-load apparent power in the multi-packet 3-phase, 3-limb HGO at 1.7 T is $\pm$ 37%. The uncertainties of all the multi-packet and single packet 3-phase, 3-limb cores is estimated in the same manner as described above.

III. Single Phase, Two Limb Transformer Cores

Table A26 Uncertainty Budget for B_{pk} in Single Phase, Two Limb HGO Core built with 160 mm wide laminations

Sources of Uncertainty	Value +/- %	Probability Distribution	Divisor	Ci	U(xi) +/- %	Vi or Veff
Voltmeter	0.1	Normal	2	1	0.05000	∞
Packet Thickness	0.463	Rectangular	1.73	1	0.26729	∞
Packet Width	0.156	Rectangular	1.73	1	0.09021	∞
Frequency	0.025	Normal	2	1	0.01250	∞
Voltage Type B uncertainty					0.28677	∞
Voltage -Type A uncertainty	0.100	Normal	1	1	0.10000	2
Combined Uncertainty					0.30371	∞
Expanded Uncertainty, k =2					0.61	
Declared uncertainty in B_{pk} at a confidence level of 95 %					0.607	

The uncertainties of the B_{pk} of the 160mm lamination width single phase, two limb core detailed in table A-26 have been estimated based on the following calculations:

1) Accuracy of the voltmeter – The accuracy of the voltage measurements obtained from NORMA600O wide band power analyser was 0.1% of the measured value.

2) Packet Thickness – The least packet thickness measured was 54 mm of the 160 mm lamination width packets. It was measured using a metal ruler with a resolution of 0.5 mm. Its uncertainty was assumed as a half of the resolution resulting in 0.463 % of the packet thickness of 27 mm.

3)Packet Lamination Width – The least packet lamination width measured was 160 mm of the 160mm lamination width packets. It was measured using a metal ruler with a resolution of 0.5 mm. Its uncertainty was assumed as a half of the resolution resulting in 0.156 % of the measured value.

4)Voltage –Type A- The type A uncertainty of the induced secondary voltage was less than 0.1% for 3 trials. It was assumed to be 0.1%.

The declared uncertainty in B_{pk} in the 160mm lamination width single phase, two limb core at 1.7 T is less than $\pm$ 1%. The uncertainties of the entire single packet, two limb cores are estimated in the same manner as described above.

Table A27 Uncertainty Budget for I_{rms} in Single Phase, Two Limb HGO Core built with 160 mm wide laminations

Sources of Uncertainty	Value +/- %	Probability Distribution	Divisor	Ci	U(xi) +/- %	Vi or Veff
Resistor	**0.030**	**Normal**	**2**	**1**	**0.01500**	**∞**
Current Type B uncertainty					**0.01500**	**∞**
Current Phase Type A uncertainty	**0.467**	**Normal**	**1**	**1**	**0.46668**	**2**
Combined Uncertainty					**0.46693**	**∞**
Expanded Uncertainty, k =2					**0.93**	
Declared uncertainty in I_{rms} at a confidence level of 95 %					**0.93**	

The uncertainties of the I_{rms} of the 160mm lamination width single phase, two limb core detailed in table A-27 have been estimated based on the following calculations:

5)Accuracy of resistor – The accuracy of the resistor of NORMA600O wide band power analyser was 0.03%.

6)Current –Type A- The relative type A uncertainty of the measured rms value of primary current was 0.467%.

The declared uncertainty in I_{rms} in the 160mm lamination width single phase, two limb core at 1.7 T is less than $\pm$ 1%. The uncertainties of the entire single packet, two limb cores are estimated in the same manner as described above.

Table A28 Uncertainty Budget for No-load Loss in Single Phase, Two Limb HGO Core built with 160 mm wide laminations

Sources of Uncertainty	Value +/- %	Probability Distribution	Divisor	Ci	U(xi) +/- %	Vi or Veff
Mass	**0.010**	**Normal**	**2**	**1.00**	**0.01**	∞
Power meter	**0.100**	**Normal**	**2**	**1.00**	**0.05**	∞
Dependence of No-load Loss on Bpk	**0.61**	**Normal**	**2**	**4.06**	**1.23**	∞
RMS Current	**0.93**	**Normal**	**2**	**1.00**	**0.47**	
No Load Loss type B uncertainty					**1.32**	∞
No Load Loss type A uncertainty	**0.174**	**Normal**	**1**	**1.00**	**0.17**	2
Combined Uncertainty					**1.33**	∞
Expanded Uncertainty, k =2					**2.66**	
Declared uncertainty in No-load Loss at a confidence level of 95 %					**2.66**	

The uncertainties of no-load loss of the 160mm lamination width single phase, two limb core detailed in table A-28 have been estimated based on the following calculations:

1) Mass measurement – The mass of the samples was measured using an Avery Berkel FB31 scale with a resolution of 0.01 g and accuracy of ±0.0002 g. Each sample was weighed three times and the expanded uncertainty of all samples was within ± 0.01 %.

2) Accuracy of the power meter – The accuracy of the power loss measurements obtained from NORMA600O wide band power analyser was 0.1% of the measured value.

3) The B_{pk} and I_{rms} measurement uncertainties were obtained from tables A26 and A27.

4)Dependence of no-load loss on B_{pk} - The sensitivity coefficient (Ci) was calculated to be equal to 4.06 from the measured no-load loss versus B_{pk} curves. At 1.7 T, the Ci is the ratio of the difference in no-load loss (measured at 1.8 T and 1.7 T) and the difference in B_{pk} (1.8 T -1.7 T =0.1T).

5)No-load loss –Type A- The relative type A uncertainty of the measured no-load loss was 0.174%.

The declared uncertainty in no-load loss in the 160mm lamination width single phase, two limb core at 1.7 T is $\pm$ 3%. The uncertainties of the entire single packet, two limb cores are estimated in the same manner as described above.

Table A29 Uncertainty Budget for No-load Apparent Power in Single Phase, Two Limb HGO Core built with 160 mm wide laminations

Sources of Uncertainty	Value +/- %	Probability Distribution	Divisor	Ci	U(xi) +/- %	Vi or Veff
Mass	**0.010**	**Normal**	**2**	**1**	**0.005**	∞
Power meter	**0.100**	**Normal**	**2**	**1**	**0.05**	∞
Dependence of No-Load Apparent Power on Bpk	**0.61**	**Normal**	**2**	**20.78**	**6.31**	∞
Current	**0.64**	**Normal**	**2**	**1**	**0.32**	
Apparent Power type B uncertainty					**6.32**	∞
Apparent Power type A uncertainty	**0.470**	**Normal**	**1**	**1**	**0.47**	2
Combined Uncertainty					**6.34**	∞
Expanded Uncertainty, k =2					**12.67**	
Declared uncertainty in No-load apparent power at a confidence level of 95 %					**12.67**	

The uncertainties of no-load apparent power of the 160mm lamination width single phase, two limb HGO core detailed in table A-29 have been estimated based on the following calculations:

1)Mass measurement – The mass of the samples was measured using an Avery Berkel FB31 scale with a resolution of 0.01 g and accuracy of ±0.0002 g. Accuracy of the power meter – The accuracy of the power loss measurements obtained from NORMA600O wide band power analyser was 0.1% of the measured value.

2)The B_{pk} and I_{rms} measurement uncertainties were obtained from tables A26 and A27.

3)Dependence of no-load apparent power on B_{pk} - The sensitivity coefficient (Ci) was calculated to be equal to 20.78 from the measured no-load apparent power versus B_{pk} curves. At 1.7 T, the Ci is the ratio of the difference in no-load apparent power (measured at 1.8 T and 1.7 T) and the difference in B_{pk} (1.8 T -1.7 T =0.1T).

4)No-load apparent power –Type A- The relative type A uncertainty of the measured no-load loss was 0.47%.

The declared uncertainty in no-load loss in the 160mm lamination width single phase, two limb core at 1.7 T is $\pm$ 13%. The uncertainties of the entire single packet, two limb cores are estimated in the same manner as described above.

IV. Single Phase, Epstein Size Cores

Table A30 Uncertainty Budget for B_{pk} in Single Phase, Epstein size HGO Core

Sources of Uncertainty	Value +/- %	Probability Distribution	Divisor	Ci	U(xi) +/- %	Vi or Veff
Accuracy of NI PCI 6120 DAQ Card	0.05	Normal	2.00	1.00	0.025	∞
Frequency setting	0.01	Normal	2.00	1.00	0.005	∞
Mass	0.01	Normal	2.00	1.00	0.005	∞
Density	0.03	Rectangular	1.73	1.00	0.005	
Sample Length	0.09	Rectangular	1.73	1.00	0.050	∞
Control of Bpk	0.02	Rectangular	1.73	1.00	0.012	∞
Control of Form Factor	0.02	Rectangular	1.73	1.00	0.012	∞
Type B uncertainty		Rectangular			0.059	∞
Type A uncertainty	0.01	Normal	1.00	1.00	0.010	2.00
Combined Uncertainty					0.060	∞
Expanded Uncertainty, k =2					0.119	
Declared uncertainty in B_{pk} at a confidence level of 95 %					0.12	

The uncertainties of B_{pk} in single phase, Epstein Size core detailed in table A-30 have been estimated based on the following calculations:

1)Accuracy of NI PCI-6120 DAQ – The accuracy of the voltage measurement range of ± 10 V is ± 4.94 mV. Therefore, the relative accuracy is 4.94 mV/10 V ×100 = 0.05 %.

2)Frequency setting – The frequency setting was 0.01%. This value was taken from the base clock accuracy of the NI PCI-6120 DAQ card.

3)Epstein strip mass measurement – The mass of the samples was measured using an Avery Berkel FB31 scale with a resolution of 0.01 g and accuracy of ±0.0002 g. Each sample was weighed three times and the expanded uncertainty of all samples was within ± 0.01 %.

4)Density – The manufacturer's quoted value is 7650 kg/m^3. The uncertainty can be half of the last two digits of the quoted value which is $\pm$ 25 kg/m^3. The relative value is around 0.03%.

5)Epstein strip length measurement – The length of every sample was measured using a metal ruler with a resolution of 0.5 mm. Its uncertainty was assumed as a half of the resolution resulting in 0.09 % of the nominal length of 290 mm. It was assumed to be 0.1 %.

6)Control of B_{pk} and form factor– The NI LabVIEW program was able to maintain the B_{pk} and form factor of secondary voltage within $\pm$0.02%.

7)Type A uncertainty – 0.01 % for three trials.

The declared uncertainty in B_{pk} in the single phase, Epstein Size HGO core at 1.7 T is $\pm$ 0.12%. The uncertainties of the entire single phase, Epstein size cores are estimated in the same manner as described above.

Table A31 Uncertainty Budget for No-load loss in Single Phase, Epstein size HGO Core at 1.7 T

Sources of Uncertainty	Value +/- %	Probability Distribution	Divisor	Ci	U(xi) +/- %	Vi or Veff
Frequency setting	0.01	Normal	2	1	0.005	∞
Dependence of loss on Bpk	0.12	Normal	2	3.86	0.23	∞
Density	0.03	Rectangular	1.73	1	0.02	
Type B uncertainty					0.23	∞
Type A uncertainty	0.5	Normal	1	1	0.5	2
Combined Uncertainty					0.55	∞
Expanded Uncertainty, k =2					1.10	
Declared uncertainty in No-load Loss at a confidence level of 95 %					1.10	

The uncertainties of no-load loss in single phase, Epstein size HGO core detailed in table A-31 have been estimated based on the following calculations:

1) Frequency setting – The frequency setting was 0.01%. This value was taken from the base clock accuracy of the NI PCI-6120 DAQ card.

2)The B_{pk} measurement uncertainty was obtained from tables A30

3)Dependence of no-load loss on B_{pk} - The sensitivity coefficient (Ci) was calculated to be equal to 3.86 from the measured no-load loss versus B_{pk} curves. At 1.7 T, the Ci is the ratio of the difference in no-load loss (measured at 1.8 T and 1.7 T) and the difference in B_{pk} (1.8 T -1.7 T =0.1T).

4)Type A uncertainty – The type-A uncertainty for no-load loss was 0.5 % for 3 trials.

The declared uncertainty in no-load loss in single phase, Epstein Size HGO core at 1.7 T is $\pm$ 1.1%. The uncertainties of the entire single phase, Epstein size cores are estimated in the same manner as described above.

Table A32 Uncertainty Budget for No-load apparent power in Single Phase, Epstein size HGO Core at 1.7 T

Sources of Uncertainty	Value +/- %	Probability Distribution	Divisor	Ci	U(xi) +/- %	Vi or Veff
Frequency setting	**0.01**	**Normal**	**2**	**1**	**0.005**	**∞**
Dependence of VA on Bpk	**0.12**	**Normal**	**2**	**10.31**	**0.61**	**∞**
Type B					**0.61**	**∞**
Type A uncertainty	**0.21**	**Normal**	**1**	**1**	**0.21**	**2**
Combined Uncertainty					**0.65**	**∞**
Expanded Uncertainty, k =2					**1.30**	
Declared uncertainty in No-load apparent power at a confidence level of 95 %					**1.30**	

The uncertainties of no-load apparent power in single phase, Epstein Size core detailed in table A-32 have been estimated based on the following calculations:

1) Frequency setting – The frequency setting was 0.01%. This value was taken from the base clock accuracy of the NI PCI-6120 DAQ card.

2)The B_{pk} measurement uncertainty was obtained from tables A30

3)Dependence of no-load apparent power on B_{pk} - The sensitivity coefficient (Ci) was calculated to be equal to 10.31 from the measured no-load apparent power versus B_{pk} curves. At 1.7 T, the Ci is the ratio of the difference in no-load apparent power (measured at 1.8 T and 1.7 T) and the difference in B_{pk} (1.8 T -1.7 T =0.1T).

4)Type A uncertainty – The type-A uncertainty for no-load loss was 0.5 % for 3 trials.

The declared uncertainty in no-load apparent power in single phase, Epstein Size HGO core at 1.7 T is $\pm$ 1.3%. The uncertainties of the entire single phase, Epstein size cores are estimated in the same manner as described above.